

IN THE QUEST OF MANIPULATING LIGHT-MATTER INTERACTIONS: COHERENT
CONTROL OF TWO-PHOTON INDUCED PROCESSES IN SOLUTION

By

DANIEL GUSTAVO KURODA

A DISSERTATION PRESENTED TO THE GRADUATE SCHOOL
OF THE UNIVERSITY OF FLORIDA IN PARTIAL FULFILLMENT
OF THE REQUIREMENTS FOR THE DEGREE OF
DOCTOR OF PHILOSOPHY

UNIVERSITY OF FLORIDA

2008

© 2008 Daniel Gustavo Kuroda

To the most important people in my life, my wife Fedra, my parents Laura and Yuji, my brother Marcelo, and my sister Fernanda.

ACKNOWLEDGMENTS

As I look back upon the years that have led to this dissertation, I have been lucky to be surrounded by such exceptional people. I would like to extend my warmest thanks to my research advisor Professor Valeria D. Kleiman for her scientific guidance and continuous motivation throughout my time in her group. She has been a great mentor and friend from whom I have learned a lot. It was her trust, understanding, enthusiasm, and tutoring that have led the Coherent Control project to completion.

I wish to thank my supervisory committee members, Prof. David Retize, Prof. Jeff Krause, Prof. Nicolás Omenetto, and Prof. Phillip Brucat for their guidance, fruitful collaborations, valuable discussions throughout my graduate studies, and for accompanying me in the final stage of my graduate career. I extend my thanks to Prof. Adrian Roitberg for his contribution in the theoretical work, to Prof. Nicolás Omenetto for teaching me the fundamentals of laser science, and to Prof. Sam Colgate for his teaching, trust, and support. I am also grateful to the Machine Shop people: Todd Prox and Joe Shalosky for the numerous hours that they have spent teaching me the art of machining. I also thank Prof. Zhonghua Peng from University of Missouri-Kansas for providing the unsymmetric dendrimers.

Many friends as well as coworkers have had an important role during my graduate studies in Gainesville with their discussions and companionship. The members of Kleiman Group provide a fun work environment. Thanks go out to Dr. Jürgen Müller for his friendship and tutoring on my first two years of graduate school. I thank Dr. Evrim Atas for her contagious energy and personal support. I would like to thank Dr. Lindsay Hardison for being a good friend/lab mate and for sharing both science and personal matters, and Mr. Derek LaMontagne for suffering to correct my English in this dissertation. I thank Dr. Chad Mair and Ms. Aysun Altan for their support and chats in the lab. The newest members of our group, Ms. Shiori

Yamazaki, Ms. Sevnur Komurlu, Dr. Chandra Pal Singh should also be thanked for their friendship. I also thank Mr. Montgomery and Prof. Damrauer for their contributions and help with the genetic algorithm. I especially thank Mr. Bob Letiecq and Mr. Mike Herrick from Spectra-Physics who provided day and night technical support.

My time here would not have been the same without the social diversions provided by all my friends in Gainesville. I am particularly thankful to Jorge, Sarah, Özge, Ece, Georgeos and Giovanni for their continuous friendship. I would like to thank Adrian and Valeria for being wonderful friends and great supporters since the day I arrived in the United States of America six years ago, and also for allowing me and my wife to teach them how to play burako. I reserve a very special thanks for Gustavo for his friendship and support, and for motivating me to improve my fitness.

My particular thanks go out to my friends from Argentina: Pablo H., Pablo E., German, Tamara, Ale C., Andres, Marcos, Flor, Ale L., Roby, and all the members of BWIM for their long distance friendship.

My most immense thanks go to my parents Laura and Yuji for their guidance and support in the decisions that I have made since I was a child. They always have believed and supported me in whatever I have been doing. I also thank my sister Fernanda and my brother Marcelo for sharing a very happy childhood together and for their long distance support and understanding.

Last but not least, I give a special thanks to my wife, Fedra, for her true love and understanding me without words. You are my soul mate and you bring happiness and peace to my life.

TABLE OF CONTENTS

	<u>page</u>
ACKNOWLEDGMENTS	4
LIST OF TABLES	10
LIST OF FIGURES	11
ABSTRACT	20
CHAPTER	
1 COHERENT CONTROL	22
Introduction.....	22
Single Parameter Quantum Control Schemes.....	23
Multiparameter Quantum Control Scheme: Optimal Control	26
Optimal Control in Solution	29
Single Parameter Control	31
Wavelength control	31
Spectral interference.....	31
Dynamics interference and pump and dump.....	33
Linear chirp control.....	34
Multiparameter Control	37
Control of selective electronic excitation.....	37
Control of vibrational excitation	39
Control of complex molecular processes	40
Optimal Control and Molecular Mechanism	42
Outline of the Dissertation.....	44
2 FEMTOSECOND LASER PULSES.....	47
Introduction.....	47
Femtosecond Laser Pulses.....	47
General Mathematical Description of a Femtosecond Laser Pulse.....	47
Pulse Propagation	51
Nonlinear Optical Effects.....	54
Femtosecond Laser Generation	56
Ti:Sapphire Oscillator	56
Femtosecond Amplifier	58
Femtosecond Pulse Characterization.....	59
Frequency Resolved Optical Gating Technique.....	59

3	FEMTOSECOND PULSE SHAPING	63
	Introduction.....	63
	Femtosecond Laser Pulse Shaping with Spatial Light Modulators.....	63
	Pulse Shaping in the Frequency Domain.....	64
	Zero Dispersion 4f Compressor.....	66
	Spatial Light Modulator	67
	Liquid crystal mask characteristics	68
	The spatial light modulator	70
	Pulse shaping with LC masks.....	72
	The Pulse Shaper	75
	Geometrical Configurations	75
	Reflective Mode Pulse Shaper.....	78
	Design Characteristics	79
	Reflective Mode Experimental Realization.....	81
	Pulse Shaper Phase Calibration	84
	Pulse Shaper Wavelength Dispersion Calibration.....	89
	Residual Phase.....	90
	Frequency Nonlinearity Correction.....	94
	Modulation Examples.....	95
	Spatial Light Modulation Limitations	97
	Summary.....	101
4	CLOSED LOOP OPTIMIZATIONS AND GENETIC ALGORITHMS	102
	Introduction.....	102
	Genetic Algorithms.....	103
	Genetic Algorithm Code.....	104
	Genetic Algorithm Implementation.....	105
	Parent selection	105
	Genetic operators.....	106
	Our algorithm code.....	110
	The role of the genetic algorithm parameters.....	112
	Optimization of Genetic Algorithm Parameters.....	113
	Mutation probability.....	116
	Number of elite parents	117
	Number of crossover children.....	118
	Number of cloned children.....	118
	Optimized Genetic Algorithm Parameters and Noise	119
	Summary.....	120
	Experimental Pulse Compression.....	121
	Implementation of Genetic Algorithms in Pulse Shaping Experiments.....	121
	Optimization Problem	121
	Setup and Optimization Conditions.....	121
	Results	123
	Summary.....	125

5	QUANTUM CONTROL OF TWO-PHOTON INDUCED FLUORESCENCE OF RHODAMINE 6G IN SOLUTION	126
	Introduction.....	126
	Molecular System and Control	126
	Experimental.....	129
	Results.....	131
	Fluorescence Efficiency Optimization	132
	Power Dependence	136
	Optimization Analysis	139
	Fluorescence Spectrum Control	141
	Relationship between Objective and the Genetic Algorithm Solutions	143
	Discussion.....	148
	Physical Interpretation of the Fitness	148
	Molecular Interpretation of the Fitness	149
	Perturbation Analysis	149
	Summary.....	152
6	COHERENT CONTROL OF ENERGY TRANSFER	154
	Introduction.....	154
	Donor Acceptor System.....	155
	Experimental Section.....	158
	Results.....	161
	Two-Photon Cross Section	161
	Closed Loop Experiments	162
	Open Loop Experiments.....	167
	Discussion.....	172
	Summary.....	176
7	STATISTICAL ANALYSIS OF THE RESULTS OF THE QUANTUM CONTROL OF ENERGY TRANSFER EXPERIMENTS	178
	Introduction.....	178
	Experimental.....	180
	Partial Least Squares Regression.....	181
	Genetic Algorithm Evolution Analysis	184
	Statistical Analysis	184
	Discussion.....	189
	Summary.....	191
	Variable Space Reduction.....	191
	Variable Space Size Effect	191
	Statistical Methodology Effect.....	193
	Theoretical Phase Unwrapping Effect.....	194
	Experimental Phase Unwrapping Effect	196
	Discussion.....	197
	Summary.....	198

8	AZOBENZENE EXCITED STATE DYNAMICS WITH TWO-PHOTON EXCITATION	199
	Introduction.....	199
	Azobenzene.....	200
	Experimental.....	204
	Results and Discussion	206
	Summary.....	208
APPENDIX		
A	PULSE SHAPER ALIGNMENT	209
B	TIME DEPENDENCE PERTURBATION THEORY	212
C	PARTIAL LEAST SQUARES.....	215
D	PARTIAL LEAST SQUARES ANALYSIS RESULTS.....	217
	Partial Least Squares Regression for The Autocorrelation Evolution.....	217
	Partial Least Squares Regression for the Spectral Evolution	219
	Partial Least Squares Regression for the Phase Evolution	222
E	SPATIAL LIGHT MODULATOR CHARACTERIZATION	225
	LIST OF REFERENCES.....	230
	BIOGRAPHICAL SKETCH	245

LIST OF TABLES

<u>Table</u>		<u>page</u>
3-1	Theoretical zero dispersion compressor characteristics.....	81
4-1	Initial genetic algorithm parameters.	116
4-2	Optimized genetic algorithm parameters.	119
4-3	Fitness results for simulations with noise. Set 1 represents the initial and set 2 the optimized genetic algorithm parameters.	120
4-4	Genetic algorithm parameters.	122
5-1	Power dependence linear fit results.	137
7-1	Root mean square for the different statistical methodologies.....	194
7-2	Experimental signal and fitness values for multiple components.....	197
7-3	Experimental normalized fitness values for multiple components.	197
8-1	Experimental and literature decay times.....	207

LIST OF FIGURES

<u>Figure</u>	<u>page</u>
1-1 Brumer-Shapiro phase control scheme. Adapted from work by Brumer et al. ¹⁵	24
1-2 Tannor-Kosloff-Rice time-domain control scheme.	24
1-3 Adiabatic rapid passage as proposed by Bergmann. Adapted from work by Gaubatz et al. ²²	25
1-4 Spectral sinusoidal phase creating a pulse train. A) Spectrum (solid line) and spectral phase (dotted line). B) Second order power spectrum comparison between the modulated pulse (solid line) and a transform limited pulse (dashed line).	32
1-5 Pump and dump scheme for linearly chirped pulses. Adapted from work by Cerullo et al. ²²	35
2-1 Temporal electric field representation of a Gaussian pulse. Temporal electric field, $E(t)$ (dash line), real amplitude, $A(t)$ (grey line), and intensity (black line).	49
2-2 Temporal electric field for phase modulated ultrafast laser pulses. A) Pulse with positive chirp ($a>0$). B) Pulse with negative chirp ($a<0$).	50
2-3 Experimental layout for a FROG apparatus using second harmonic generation.	60
2-4 Schematic of a generic FROG algorithm. Adapted from work by Trebino. ¹⁰⁰	61
3-1 Basic layout for a zero dispersion compressor. G: grating, L: lens, FP: Fourier plane. Adapted from work by Weiner et al. ²⁷	67
3-2 Cartoon of a nematic phase liquid crystal. ea: extraordinary axis.	68
3-3 Side view of a single nematic crystal pixel. A) Without electric field. B) With an external field applied. Adapted from work by Weiner et al. ¹⁰⁹	69
3-4 Schematic of spatial light modulator mask. A) Front view. B) Lateral cut. Adapted from work by Weiner et al. ²⁷	70
3-5 Setup for dual mask spatial light modulator.	73
3-6 Basic layout of a pulse shaper. A) Transmission mode configuration. B) Reflective mode configuration.	75
3-7 Top view of different design types for pulse shapers based on an optical Fourier transform.	76
3-8 Tilt in the Fourier plane produced by a mirror at 45 degrees with a vertical tilt.	77

3-9	Diagram of the experimental setup in a reflective mode configuration.....	78
3-10	Grating groove density and beam waist versus focal length. Grating groove density effect (solid line). Beam waist effect (dashed line).	81
3-11	Top and side views of the built pulse shaper. SM: spherical mirror; G: grating, M: mirror; P: polarizer; WP: $\lambda/2$ waveplate; FR: Faraday rotator, CP: cube polarizer.	82
3-12	3D Sketch of the built pulse shaper. SM: spherical mirror; G: grating, M: mirror; P: polarizer; WP: half waveplate; FR: Faraday rotator, CP: cube polarizer.	82
3-13	Polarization splitting of the incoming and the outgoing pulse. Incoming and outgoing polarizations are represented with a black and red arrow, respectively.	83
3-15	Experimental setup used for the masks calibration.....	86
3-16	Phase calibration curves of: A) front mask and B) back mask.	87
3-17	Phase at 700 counts (1.71 V) for: A) front mask and B) back mask.	87
3-18	Phase calibration of front mask. A) Corrected curves. B) Comparison between the average of all the curves and calibration curve at 799.66nm (inset: correction factor).....	88
3-19	Phase calibration of back mask. A) Corrected curves. B) Comparison between average of all the curves and calibration curve at 799.66nm (inset: correction factor).....	88
3-20	Dispersion calibration. A) Unmodulated and modulated spectra (red and black lines, respectively). B) Transimission produced by holes in the profile. C) Wavelength calibration curve.....	90
3-21	Pulse shaper setup using an external mirror. A) Without the spatial light modulator. B) With the spatial light modulator.	91
3-22	Phase mask effect on the temporal profile of the pulse for A) Zero dispersion compressor without the spatial light modulator in place. B) Zero dispersion compressor with the spatial light modulator in place.	91
3-23	SHG-FROG trace of the unmodulated pulse. A) Experimental trace. B) Retrieved trace. C) Temporal intensity (black line) and phase (red line). D) Spectral intensity (black line) and phase (red line).....	92
3-24	SHG-FROG trace of the phase corrected pulse. A) Experimental trace. B) Retrieved trace. C) Temporal intensity (black line) and phase (red line). D) Spectral intensity (black line) and phase (red line).....	93
3-25	Effect of the nonlinear frequency calibration in the pulse modulation. A) Sinusoidal phase pulse without frequency nonlinear correction. B) Sinusoidal phase pulse with nonlinear frequency correction.	94

3-26	Frequency calibration curve of the pulse shaper. Dots experimental points, dotted line linear fit, a solid line: second order polynomial fit.	95
3-27	Odd pulse (π step). A) Spectral intensity (black line), retrieved phase (red squares), and target phase (red line). B) Temporal intensity (black line) and phase (red squares).	95
3-28	Sinusoidal phase modulation. A) Spectral intensity (black line) retrieved phase (red squares), and target phase (red line). B) Temporal intensity (black line) and phase (red squares).	96
3-29	Quadratic phase pulse (4607 fs^2). A) Proposed phase (red line), and retrieved spectral intensity (black line) and phase (red squares). B) Temporal intensity (black line) and phase (red line).	96
3-30	Temporal double pulse with a 200 fs separation. A) Proposed temporal intensity (open circles) and phase (red line), retrieved temporal intensity (black line) and phase (red line). B) Spectral intensity (black line) and phase (red line).	97
3-31	A) Phase unwrapped. B) Phase wrapped.	97
3-32	Quadratic phase of $10^{-3} \text{ pixel}^2/\text{rad}$ A) Sampled every 10 pixels B) Sample every 10 pixels (black squares) and every pixel (black line).	98
4-1	Roulette wheel. Adapted from work by Xiufeng et al. ¹²⁹	105
4-2	Crossover operation.	108
4-3	Cloning operator.	109
4-4	Mutation operation.	109
4-5	Implemented genetic algorithm.	111
4-6	Simulated experimental setup. The femtosecond pulse is modulated in the glass rod (BK7) and its second harmonic intensity is produced in a non-linear crystal (NLC).	114
4-7	Influence of probability of gene mutation on the achieved fitness. Average best fitness (black squares). Overall best fitness (open circles). Overall worst fitness (open triangles).	116
4-8	Influence of the number of elite parents on the achieved fitness. Average best fitness (black squares). Overall best fitness (open circles). Overall worst fitness (open triangles).	117
4-9	Influence of the number of individuals generated by crossover on the achieved fitness. Average best fitness (black squares). Overall best fitness (open circles). Overall worst fitness (open triangles).	118

4-10	Experimental setup used in pulse compression.	122
4-11	Evolution of the two-photon induced current as a function of the generation. Average (open triangles), best (full squares), and worst (open circles) fitness values for each generation are plotted.....	123
4-12	Uncompressed pulse. A) Spectral intensity (black line) and phase (red line). B) Temporal intensity (black line) and phase (red line).	124
4-13	Compressed pulse. A) Spectral intensity (black line) and phase (red line). B) Temporal intensity (black line) and phase (red line).	124
5-1	A) Rhodamine 6G molecular structure. B) Absorption spectrum (black line) and emission spectrum (dashed line). Inset contains a zoom of the absorption spectrum from 360 to 445 nm.....	127
5-2	Jablonski diagram of Rhodamine 6G.....	128
5-3	Experimental setup for controlling molecular fluorescence. L: lens. NLC: nonlinear crystal. PD: photodiode. PMT: photomultiplier tube.....	129
5-4	A) Fitness evolution of typical experiments of maximization of fluorescence efficiency. B) Experimental convergence reproducibility.....	132
5-5	A) Optimal autocorrelation for different experiments. B) Typical SHG-FROG trace of the optimum pulse.	133
5-6	A) Fitness evolution of typical experiments of minimization of fluorescence efficiency. B) Experimental convergence reproducibility.....	134
5-7	A) Optimal autocorrelation. B) Typical SHG-FROG trace of the optimal pulse.	135
5-8	Power dependence of the different pulses. Top panel, fluorescence intensity dependence. Lower panel, second harmonic intensity dependence.....	137
5-9	Power dependence in fluorescence-second harmonic space. Fluorescence maximization (squares). Fluorescence efficiency maximization (stars) and minimization (triangles). Zoom of the lower left corner of the plot (inset).....	138
5-10	Variable space. A) All individuals of each experiment: maximization of fluorescence (blue squares), maximization of fluorescence efficiency (green triangles), and minimization of fluorescence efficiency (grey circles). B) Fitness for the best individuals on each generation of each experiment and fitness for individuals with random phases.....	139
5-11	Variable space in using ratio and difference of signals. Inset shows a zoom of the left corner of the plot. Individuals corresponding to the fluorescence efficiency maximization (triangles) and minimization (circles).....	140

5-12	Spectrum measured with the cutoff filter (grey area).....	142
5-13	FROG traces for different experiments. A) Maximization of fluorescence efficiency when the whole spectrum is collected. B) Maximization of red side fluorescence over second harmonic.	142
5-14	FROG traces for different experiments. A) Minimization of fluorescence efficiency minimization when the whole spectrum is collected. B) Minimization of red side fluorescence over second harmonic.....	143
5-15	A) Fitness evolution of maximization of spectral control. B) Evolution of the cost function for minimization of spectral control.	143
5-16	A) Fitness evolution of the cost function $(F_R - F_B)F_R/F_B$ (black line) and simulated evolution of the cost function $(F_R - F_B)F_R/F_B$ with the data corresponding to maximization of $(F_B - F_R)F_B/F_R$ (red line). B) Fitness evolution of minimization of spectral control (black line).	145
5-17	Signal of fluorescence spectral control experiments. A) Maximization, fluorescence (black line) and second harmonic signals (red line) B) Minimization, fluorescence (black line) and second harmonic signals (red line).	146
6-1	A) Chemical structures of phenylene ethynylene dendrimer: 2G2-m-Per. B) 3D model of the 2G2-m-Per. C) Absorption (green line) and emission (grey area) spectra of 2G2-m-Per, and absorption of 2G2-m-OH (black line) and ethylene perylene (red line).....	156
6-2	Energy diagram and dynamics of 2G2-m-Per. τ_1 , τ_2 , and τ_3 are ~ 0.4 ps, ~ 0.5 ps, and ~ 0.8 ps, respectively.	157
6-3	Coherent control setup.	158
6-4	A) Two-photon cross section of 2G2-m-Per (squares) and excitation laser spectrum (gray area). B) Spectral windows used to measure the two-photon cross section.....	162
6-5	Best individual evolution for the different optimizations: maximization of fluorescence (red squares), maximization of the ratio (green squares) and minimization of the ratio (blue squares). Inset shows an expanded view of the maximization region.	163
6-6	Fitness evolution for the maximization of fluorescence over two-photon induced current. Open squares and full circles represent the best individual for the ratio maximization and the calculated fitness using the values of the FL only maximization, respectively.	164
6-7	Retrieved (A) Temporal intensity and phase and (B) Spectrum and spectral phase.	165

6-8	Autocorrelation of the pulse observed after the minimization and of the transform limited pulse.....	166
6-9	Variable space for acceptor and donor-acceptor system. Full squares and black stars correspond to the optimization experiments on the donor-acceptor system and using those phase modulated that optimize 2G2-m-Per to induced excitation on the acceptor molecules alone, respectively.....	167
6-10	A) Fluorescence second harmonic ratio versus the step size of the spectral phase for 2G2-m-Per (stars), 2G2-m-OH (open triangle), Perylene (crossed circle). Inset shows the applied phase. B) Experimental (squares) and calculated (line) TPIC.....	168
6-11	Spectrally modulated pulses. A) Spectrum (red line) and spectral phase. B) Second harmonic spectrum (blue line). C) Temporal intensity (black line). From top to bottom: transform limited, 0.4π step, 1.4π step, linearly chirped 2000 fs^2 , and linearly chirped -2000 fs^2 pulses.....	170
6-12	A) Temporal autocorrelation of the pulse codified with a zero phase difference, where each color represent pulses separated by a different delay. B) Ratio of fluorescence over two-photon induced current versus the time delay between subpulses for zero phase relation (black line) and π phase relation (red line).....	171
6-13	Fluorescence-TPIC ratio versus variable quadratic phase for 2G2-m-Per.....	172
7-1	Variable space evolution and sampling for 2G2-m-Per energy transfer optimal control. A) Typical representation of the molecular signal versus two-photon signal. B) Ratio versus two-photon induced current for each experiment. Red line (grey dots) and green line (dark grey dots) lines correspond to the best (all) individual for each generation of the ratio of fluorescence over two-photon signal and the fluorescence, respectively.....	184
7-2	Generational correlation between fluorescence and two-photon induced current (full squares) and between the ratio and two-photon induced current (open squares) for energy transfer efficiency maximization (red) and fluorescence maximization (black).....	186
7-3	Pulse characteristics for the fluorescence for generation 1, 10, 20, 50, 100, and 200. A) Second harmonic spectra. B) Autocorrelations. C) Fourier transforms of the autocorrelations.....	187
7-4	Correlation between Fourier frequency amplitude and fitness. Three regions with correlation are observed: between $0\text{-}20 \text{ cm}^{-1}$ (negative), $40\text{ to }130 \text{ cm}^{-1}$ (positive), and $190\text{ to }250 \text{ cm}^{-1}$ (positive).....	188
7-5	A) Latent variable 1 (black line). B) Latent variable 2 (black line). Spectrum of the excitation (grey area) pulse.....	189

7-6	Latent variables for the best individuals of each of the 200 generations (red line) and total population (black line and squares). A) Latent variable 1. B) Latent variable 2. C) Latent variable 3. D) Latent variable 4.	192
7-8	Comparison of the model predicted by different statistical methodologies and the optimal phase. A) Energy transfer optimization. B) Fluorescence maximization. Each graphs shows: original data (black line and squares), the partial least squares model (green line), and the principal component analysis model (red line).....	193
7-9	Comparison between the model of the optimal phase (red line) and the experimental optimal phase (black line and points). A) Without phase unwrapping. B) With phase unwrapping.	195
7-10	Comparison among modeling of the optimal phase without unwrapping (red line) and with unwrapping (blue line), and the experimental optimal phase (black line).....	196
8-1	A) Isomerization of azobenzene. B) Ground state absorption of azobenzene samples: <i>trans</i> (black line) and <i>cis</i> (red line).	200
8-2	Rotation and inversion pathways of azobenzene isomerization. Adapted from work by Diau. ¹⁷⁶	201
8-3	Experimental setup for transient absorption experiment probing with UV. nIR pump pulses are obtained from the residual fundamental of the OPA. A chopper wheel is used to compare the signal with and without pump.....	205
8-4	Transient evolution of the absorption changes for azobenzene where open circles and black line represent the data and fitting model and the grey plots show the instrument response function. A) Probe at 440 nm. B) Probe at 480 nm.	206
A-1	Scheme of the setup with the apertures and translation stages. S1 and S2: translation stages; RS: rotation stage; A1, A2, A3, A4, and A5: iris apertures; M1, M2 steering mirrors; FM, folding mirror.	211
C-1	Geometrical representation of partial least squares model.	216
D-1	A) Variance explained by each latent variable. B) Cumulative variance explained. Autocorrelation model (Blue bars). Fitness model (red bars).....	217
D-2	A) RMSE error and B) Linear correlation (R^2) for the fitness model versus the number of latent variables used in the model. Autocorrelation model (Blue bars). Fitness model (red bars).	217
D-3	Error of the fitness model: A) Linear correlation and B) Chi square.	217
D-4	Chi square error of the autocorrelation model.	218
D-5	Autocorrelation latent variables: A) First and B) Second.....	218

D-6	Autocorrelation latent variables: A)Third and B) Forth.	218
D-7	Fitness (blue line) and PLS linear model (green line). A) With one latent variable. B) With two latent variables.	219
D-8	Fitness (blue line) and PLS linear model (green line). A) With three latent variables. B) With four latent variables.	219
D-9	A) Variance explained by each latent variable. B) Cumulative variance explained. Spectral model (Blue bars). Fitness model (red bars).....	219
D-10	A) RMSE error and B) Linear correlation (R^2) for the fitness model versus the number of latent variables used in the model. Spectral model (Blue bars). Fitness model (red bars).	220
D-11	Error of the fitness model: A) Linear correlation and B) Chi square.	220
D-12	Chi square error of the spectral model.	220
D-13	Spectral latent variables: A) First and B) Second.	221
D-14	Spectral latent variables: A) Third and B) Forth.	221
D-15	Fitness (blue line) and PLS linear model (green line). A) With one latent variable. B) With two latent variables.	221
D-16	Fitness (blue line) and PLS linear model (green line). A) With three latent variables. B) With four latent variables.	222
D-17	A) Variance explained by each latent variable. B) Cumulative variance explained. Phase model (Blue bars). Fitness model (red bars).....	222
D-18	A) RMSE error and B) Linear correlation (R^2) for the fitness model versus the number of latent variables used in the model. Phase model (Blue bars). Fitness model (red bars).	222
D-19	Error of the fitness model: A) Linear correlation and B) Chi square.	223
D-20	Chi square error of the phase model.	223
D-21	Phase latent variables: A) First and B) Second.	223
D-22	Phase latent variables: A) Third and B) Forth.	224
D-23	Fitness (blue line) and PLS linear model (green line). A) With one latent variable. B) With two latent variables.	224
D-24	Fitness (blue line) and PLS linear model (green line). A) With three latent variables. B) With four latent variables.	224

E-1	Spatial light modulator mask pixel inhomogeneity for mask 1 at level 4095 and mask 2 and level 600.....	225
E-2	Spatial light modulator mask pixel inhomogeneity for mask 1 at level 600 and mask 2 and level 4095.....	226
E-3	Spatial light modulator mask pixel inhomogeneity for mask 1 at level 3500 and mask 2 and level 4095.....	227
E-4	Spatial light modulator mask pixel inhomogeneity for mask 1 at level 4095 and mask 2 and level 3500.....	228
E-5	Spatial light modulator mask pixel inhomogeneity for mask 1 at level 4095 and mask 2 and level 4095.....	229

Abstract of Dissertation Presented to the Graduate School
of the University of Florida in Partial Fulfillment of the
Requirements for the Degree of Doctor of Philosophy

IN THE QUEST OF MANIPULATING LIGHT-MATTER INTERACTIONS: COHERENT
CONTROL OF TWO-PHOTON INDUCED PROCESSES IN SOLUTION

By

Daniel Gustavo Kuroda

May 2008

Chair: Valeria D. Kleiman

Major: Chemistry

During the late 80's, Brumer-Shapiro¹ and Rice-Tannor² proposed the use of quantum interference of molecular processes to control the outcome of chemical reactions. With the development of femtosecond lasers and pulse shapers, it has become possible to experimentally select a specific reaction pathway from a pool of possibilities and consequently, to control the outcome of a photochemical process. This thesis focuses on controlling processes initiated by light and on the understanding of the dynamics that lead to the control.

Many systems have been recently studied using closed loop optimization techniques. Most of them show only the proof of principle. In here the focus is rather on the understanding of the investigated process. The first part involves the design, construction, and characterization of the apparatus for carrying out optimal control experiments and the second part concerns the adaptive control of two-photon induced fluorescence, energy transfer, and molecular rearrangement in solution.

In the first investigated topic, I present the adaptive control of the two-photon fluorescence of Rhodamine 6G in solution. The second topic of quantum control addresses the energy transfer within a dendritic macromolecule with light-harvesting properties in solution. In this study, we show the optimal control of energy flow between coupled energy-donor and energy-acceptor

chromophores. We utilize phase tailored near IR excitation pulses to optimize the energy transfer process and amplitude tailored excitation pulses to learn about the nature of the involved pathways. In addition, statistical correlation analysis is used to investigate control mechanisms based on coherent superposition of states present in the dendritic molecule. This analysis provides information regarding pulse parameters that are critical to optimal control of excitation and energy transfer.

The last topic describes preliminary measurements on azobenzene. It focuses on establishing if a two-photon excitation of azobenzene is possible and on the possible changes in the excited state dynamics caused by multiphoton excitation. The ultimate goal of this study is to set the foundation for a two-photon excitation for coherently controlling the photoisomerization of azobenzene with a modulated 800 nm excitation source.

CHAPTER 1 COHERENT CONTROL

Introduction

Since ancient times, humans have been trying to control the transformation of matter; to some degree this has been achieved by chemistry. In order to produce the desired molecule, chemists know how to shift the equilibrium by varying thermodynamic properties of the system, such as temperature (average kinetic energy of the molecules) or solvent (interaction energy). These techniques involve synthesizing the proposed molecule by modifying the system energy on a macroscopic level. However, the reaction outcome depends upon the way in which energy is injected into the system, i.e. certain reactants attack specific molecular bonds.

In principle, a similar methodology can be utilized in photochemical reactions. Vibrational spectroscopy reveals resonant frequencies associated with specific periodic motions of bonds in molecules. It is possible to think about selectively transferring energy to the molecules using these resonant frequencies. This concept, known as “mode-selective” chemistry, represents the first proposed way to control photochemical phenomena. This approach was experimentally realized by tuning a monochromatic laser light to the vibrational frequency associated with the bond where the rupture is expected.^{3,4} Although the idea sounded plausible, those experimental trials only worked when the selected bond was the weakest in the molecule.⁵⁻⁷ The failure of the scheme was due to the coupling between the different vibrational modes which lead to a very efficient and fast intramolecular vibrational redistribution of the supplied energy.⁸ Scientists then understood that to control photochemical reactions it would be essential to know all of the processes affecting the dynamics.

Time resolved and steady state spectroscopies are well established techniques that have been effectively applied to investigate the dynamical behavior of many molecular systems.

Today, countless molecular systems have been dynamically characterized from its early dynamics times (femtosecond time scale) to the end of the dynamics (microsecond/millisecond time scale). Thus, the paradigm of molecular spectroscopy has shifted from purely observing to observing and controlling the system dynamics. This perspective differs from the proposed mode selective chemistry because it takes into consideration not only specific molecular degrees of freedom, but the system as a whole.

Atoms and molecules, like photons, present a wave-like behavior. This implies that interference phenomena observed in Young's double slit experiments can be extended to molecules, opening the possibility to produce very interesting effects in matter, i.e. interference.⁹ For instance, the population of a quantum state created simultaneously with two connected pathways will depend on the phase difference between the pathways used to generate it.¹ Recent efforts have focused on using the coherent properties of laser radiation to produce these interference phenomena in matter.

Single Parameter Quantum Control Schemes

Based on spectral-temporal properties of coherent laser fields, quantum interference can be used to adjust the system from the initial to the desired final quantum state, i.e. quantum control. Since the introduction of the concept in 1978 by Yablonovitch, many different schemes for achieving this goal have been proposed and realized.

One of the first schemes, as proposed by Brumer and Shapiro in 1986, is a frequency domain approach that uses the interference between two different excitations reaching the same excited state to manipulate the photoprocess.^{1,10} Quantum control is experimentally produced by shining two continuous wave lasers with different center frequencies which simultaneously induce different excitations on the quantum system. Hence the population of the excited state has two dependent components, which are related through a phase term imposed by the phase

difference of the two excitation processes and the molecular phase associated with the final state. The modification of the relative phase between the two excitation pathways affects via interference the final population observed in the excited state (Figure 1-1). This scheme was first experimentally demonstrated by Elliot and coworkers with atomic mercury.¹¹ Later, Gordon's group used a similar concept to control the dissociation product of polyatomic molecules and ionization of polyatomic molecules.¹²⁻¹⁴

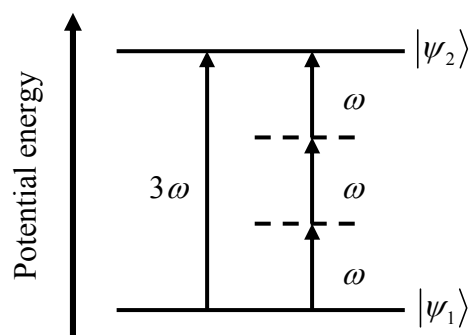


Figure 1-1. Brumer-Shapiro phase control scheme. Adapted from work by Brumer et al.¹⁵

A different approach was proposed by Tannor, Kosloff, and Rice in 1985. This methodology exploits the wave packet propagation in the time domain.^{2, 16} The scheme principle is based on creating a wave packet and modifying its evolution on the excited state potential energy surface (Figure 1-2).

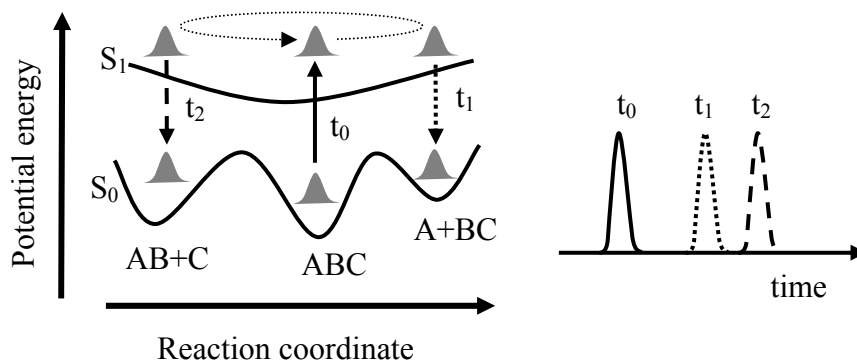


Figure 1-2. Tannor-Kosloff-Rice time-domain control scheme.

Tannor, Kosloff, and Rice's scheme can be illustrated as follows. Upon excitation with a temporally short pulse, a wave packet is generated on an excited potential energy surface. After its formation, the wave packet starts to evolve in this potential well according to its specific shape. During its trajectory the wave packet covers many different molecular conformations. When the wave packet is localized in a point on the potential energy surface where the molecular conformation corresponds to that of the desired product, a second pulse is used to transfer the wave packet back to the ground state where no molecular rearrangement can occur. To achieve control with this scheme, the time delay between the two ultrafast laser pulses must be correctly timed. Gerber's, Zewail's and Wilson's groups were the first groups able to demonstrate its feasibility for controlling small molecules in gas phase.¹⁷⁻¹⁹

Tannor, Kosloff, and Rice's scheme was further developed by Fleming and coworkers.²⁰ Fleming's methodology not only uses the time difference between the two pulses, but also maintains a fixed phase relationship between the pulses to coherently control photochemical processes. Using this improved scheme, Fleming and coworkers demonstrated wave packet interference on molecular iodine.²¹

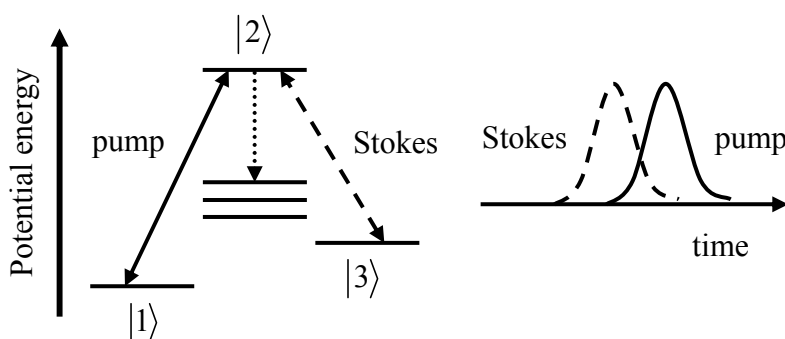


Figure 1-3. Adiabatic rapid passage as proposed by Bergmann. Adapted from work by Gaubatz et al.²²

The third scheme is based on the adiabatic passage technique. Laser induced rapid adiabatic passage was first demonstrated in a population inversion experiment by Loy in 1974.²³

Later, Bergmann and coworkers applied this finding to show theoretically and experimentally the possibility of transferring a whole initial quantum state to a different final state using stimulated Raman adiabatic passage in a three state Λ -type quantum system.²²

This concept is illustrated in Figure 1-3. The aim is to directly transfer all the population situated in quantum state 1 to final state 3. If the population of the initial quantum state is first optically promoted to state 2, a dissipative process occurring in 2 will removed a part of the population decreasing the population that can be later transferred to state 3. Using Bergmann scheme, the problem is avoided because states 1 and 3 are optically coupled before transferring the population to any other state. When states 1 and 2 are optically coupled, the coupling directly promotes the population from 1 to 3 without any transient population in 2. This total population transfer only occurs if the adiabatic conditions are fulfilled and if the time ordering of the laser pulses is the appropriate (Figure 1-3).

Multiparameter Quantum Control Scheme: Optimal Control

All these methodologies have been optimized and many different examples can be found in the literature.²⁴ In a more refined version of the Tannor-Kosloff-Rice scheme, the double femtosecond phase locked lasers are replaced with a single femtosecond laser including complex electric field features which enable control of a chemical reaction.² Ideally, a more complex pulse can be constructed such that it can continuously interact with the wave packet and progressively modify its trajectory until it reaches the desired destination, or equivalently, the desired product. Moreover, this envisioned complex pulse could allow one to combine the wave packet interference with pump and dump or pump and pump schemes through the specific time ordering and phase relationship of its components. To produce these intricate electric fields, the

different components of the electric field must be codified with many independent and controllable parameters.

Considering the ambition of this seminal scheme, it is not evident whether this control is possible in any complex molecular system and if so, how the electric field characteristics and correct femtosecond pulse parameterization can be obtained. The first indication of this approach's feasibility was introduced by Clark and coworkers in 1983.²⁵ Theoretically studying a quantum system with discrete spectral features, this group showed the possibility of transferring the quantum system to any proposed target state with a specifically designed electric field. However, they did not provide a way for finding the complex electric field necessary to achieve quantum control.

The theoretical calculations of electric field components required to manipulate a wave packet during its evolution in the potential energy surfaces are not simple. They require a very precise knowledge of the molecular Hamiltonian. If the coupling to the environment is negligible a theoretical calculation might be possible for small molecule, but for large molecules in condensed phase where strong coupling with the environment is evident, the possibility of making such a detailed calculations are, up to date, impossible.

To overcome the problem of knowing in advance the complex electric field components, Judson and Rabitz suggested a novel scheme where the complex electric field needed to reach a particular product is obtained experimentally without prior knowledge of the Hamiltonian of the system.²⁶ Based on a closed loop optimization, this scheme uses an optimization algorithm and molecular signals to find the electric field arrangement capable of controlling the molecular system. By varying simultaneously many parameters of the laser field, the algorithm creates different electric fields which are tested on the quantum system. The signals produced by the

system for a given electric field, known as pulse parameterization, are sent back to the algorithm where they are evaluated. Following this evaluation, feedback is provided by the algorithm which suggests new and improved electric fields. After applying this process successively, the algorithm manipulates the many different electric field components to control the quantum system. This results in a shaped electric field with optimal pulse parameterization suitable for controlling the system under investigation. This concept is usually referred to in the literature as “optimal control” or “adaptive control.” Optimal control can be applied to any system as long as there is a signal characteristic of the desired product. The drawback of an input free optimization is the rather complicated arrangement of the electric field components, one from which the type of control scheme applied during the optimization is not easy to infer. This methodology leaves the possibility of producing any of the previously mentioned single parameter control scenarios and eventually new ones.

To make optimal control possible, it is necessary to generate of numerous different electric fields in a very flexible manner. This has become possible with the advent of pulse shapers. Available pulse shapers can modulate the spectral²⁷ and/or amplitude²⁷ and/or polarization²⁸ characteristics of the electric field of laser pulses. The number of different fields that they can generate by current pulse shapers is on the order of 10^{1000} , making this technique suitable for studying the coherent light matter interactions in a systematic way with single parameter schemes as well as in an the adaptive way with a multi-parameter scheme.

The first experimental demonstration of an optimal control study was performed by Wilson and coworkers in 1997.²⁹ Later, different groups working in different areas demonstrated the control of other processes that include, but are not limited to, selective bond cleavage,³⁰

molecular emission in solution,³¹ two-photon transitions in atoms,³² and high harmonics generation.³³

Optimal Control in Solution

In the last decade many different coherent control experiments have been carried out for studying a variety of molecular systems in gas phase as well as in condensed phase.^{9, 15, 30, 34-39} Despite the impressive number of controlled systems, the vast majority of them have been focused on molecules in gas phase. Therefore, solution phase control experiments are a natural area to investigate. Specific issues related to condensed phase limit the application of different approaches successfully; principally among these problems is the nonlinear response produced by the solvent in the presence of intense electric fields.

In optimal control with strong laser fields, an intense electric field is employed to drastically change the potential energy surfaces of the quantum system with the goal of modifying its shape and therefore the wave packet dynamics. Several examples of this type of control in gas phase have been published.⁴⁰ When this approach is used in the condensed phase the nonlinear susceptibility of the solvent induces effects that can hide or destroy the control quantum system signal. For instance, an intense laser pulse generates white light in condensed media. The white light generation threshold is given by the power required for self-focusing and by the material band gap, which in the case of water corresponds to an intensity on the range of 10^{13} to 10^{14} W/cm².⁴¹ Thus if any electric field is applied to a water solution, its intensity can not overpass the constraint previously mentioned. This problem limits the possibility of producing strong field effects to control the dynamics or photoproducts of molecules in condensed phase. White light supercontinuum generation also detrimentally affects detection techniques commonly used for feedback.

Another challenge that has to be overcome in condensed phase is the rapid decoherence produced by the coupling of the molecular system with the solvent. Molecules in the gas phase are coupled to the environment through intermolecular collisions. Mean free paths on the order of meter, or equivalently milliseconds, are commonly found. In contrast, molecules in condensed phase are highly coupled to the environment through intra and intermolecular interactions and certain coherent processes can be rapidly destroyed by those interactions. Nevertheless, not all the coherences are quickly lost in solution phase. For example, the time scale of rovibrational molecular coherences is greatly diminished with the presence of a chaotic environment, but studies have shown rovibrational coherences lasting more than few picoseconds even under those conditions.²⁴

To achieve control over molecular dynamic processes in solution, the dephasing times of the photoinduced process have to be comparable to the temporal features produced in the modulated pulse. Systems undergoing very fast relaxations compared to the time scale of the pulse features will not be sensitive to the temporal pulse shape. At the other extreme, a system which relaxes to a state with very long residence time will lose all the coherences initially imprinted on it.

Since the introduction of the concept of quantum control, many different studies have shown the possibility of controlling the behavior of matter. Most experiments are based on the modulation of the excitation source, although the number of electric field parameters modified to achieve control (single or multiple parameters) varies. Single parameter experiments are very valuable and many times they can provide a more intuitive picture of the process being controlled.

Single Parameter Control

Wavelength control

Wavelength control was the first proposed method to achieve selective bond cleavage, but because of the intramolecular energy redistribution this methodology did not work as expected.⁵⁻⁷ Although, in some cases the correct selection of the excitation wavelength can still be used to control the photoproducts.²⁴ Wavelength excitation control is produced when the ground state population is transferred to different places in the manifold of the excited potential energy surfaces. Considering the distinct shape of each potential energy surface, a different initial positioning of the wave packet will affect the evolution of the system. The probability of producing the excitation to different parts of the potential energy surfaces is given only by the Franck-Condon coefficients; therefore one can not acknowledge the change in wavelength as a quantum control scheme because no coherences are involved. The problem changes when the coherent properties of the excitation are intentionally modified to produce an effect in the molecular response.

Spectral interference

Another possibility involves the creation of spectrally interfered pulses. For example, a pulse sequence created by applying a sinusoidal spectral phase to a broad band transform limited pulse will not create interference fringes in its spectrum (Figure 1-4(A)), but will visibly do so on its second order power spectrum (Figure 1-4(B)). Spectral modulation will affect the excitation processes initiated via two-photon absorption, as the second order power spectrum is changed by the new phase function (Figure 1-4(B)).⁴²

The first experiment displaying spectral interference effects was performed by Silberberg's group in 1998.³² In this work the effect of an odd pulse with a π step spectral phase function was investigated for the two-photon absorption process in cesium gas. In cesium, a system with

narrow absorption bands, the odd pulse with the π step centered at half the frequency of the transition gives the same emission as a transform limited pulse in a system with narrow absorption lines.

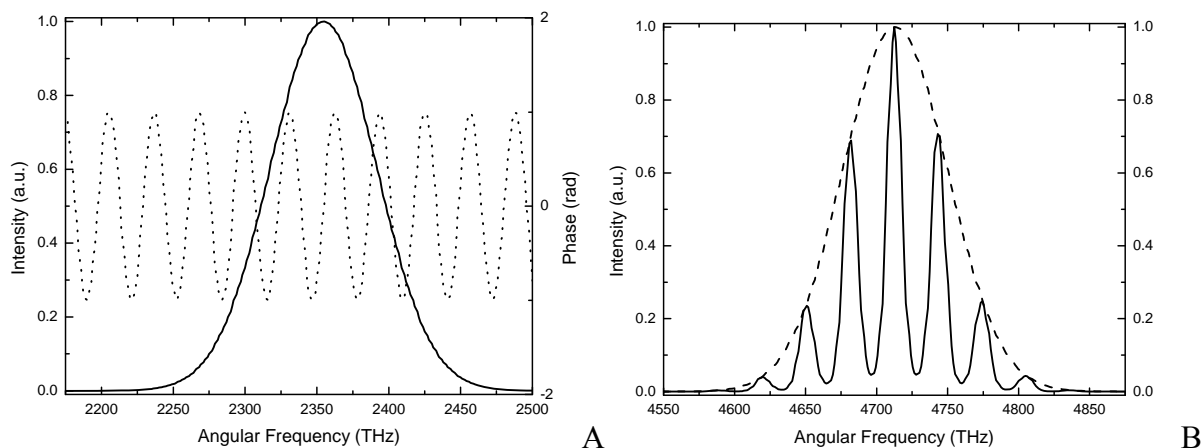


Figure 1-4. Spectral sinusoidal phase creating a pulse train. A) Spectrum (solid line) and spectral phase (dotted line). B) Second order power spectrum comparison between the modulated pulse (solid line) and a transform limited pulse (dashed line).

This can be explained by observing the second order power spectrum. Positioning the π step at half the frequency of the transition, the second order power spectrum has its maximum in resonance with the electronic transition and consequently will produce the same effect as the transform limited pulse. In a later experiment, the same group showed that a similar pulse applied to a dye in solution does not induce the same effect as in the atom in gas phase.⁴² The difference between the two results was explained in terms of the width of the band involved in the transition. While in the cesium atoms there is only one defined resonant transition, in solvated molecules the bands are broad, which implies that many transitions simultaneously contribute to the excitation. Hence, in a system with broad absorption bands a change in the second order power spectrum will always lower emission compared to that observed for the transform limited pulse in which its second order power spectrum covers the maximum number

of possible transitions. These studies show that when the spectrum has broad inhomogeneous line shapes, the pulse intensity is the driving force in the two-photon initiated process.

These results were confirmed by Joffree's group in a study involving two-photon emission of different dyes in solution.⁴³ By removing the intensity dependence of the excitation process, they showed that the fluorescence efficiency can be modulated by changing the second order power spectrum of the femtosecond pulse. Since the excitation is decoupled from the intensity, the emission will be given by the molecular population reaching the excited state. Thus, maximization of the emission efficiency will imply a maximization of the excitation efficiency.

Two-photon excitation efficiency can be optimized by shaping the excitation source such that its second order power spectrum maximizes the overlap between the excitation source and the two-photon excitation spectrum of the molecule under investigation.⁴³ This optimization scheme was used to explain the results obtained in an optimal control experiment involving the two-photon induced emission of a ruthenium complex in solution.⁴⁴ It is interesting to note that this was a multiparameter experiment, which was reduced to a single parameter optimization to understand the photophysical process.

Dynamics interference and pump and dump

Although the interference effect has been used in phase modulation studies to shape the second order power spectrum of the pulse, most studies focus its application on modifying the excited state wave packet dynamics rather than matching the excitation source to the shape of the potential energy surfaces.

One way of modifying the system dynamics is by using a double pulse with a particular time separation. The parameter used to produce and modify the wave packet interference is the time delay between the pulses in the sequence.

Early ultrafast studies in stilbene,⁴⁵ retinal,⁴⁶ and yellow protein⁴⁷ show that this manipulation is possible, but those studies were intended for studying the system dynamics and they did not emphasize the time delay as a source for controlling the outcome of the photochemical reaction. While this scheme has been extensively used in solids,⁴⁷⁻⁴⁹ only a few examples have been observed in solution photoprocesses.⁵⁰

One demonstration of coherent control using a wave packet interference scheme was performed by Wohlleben et al. in 2002.⁵¹ In this case, parameterization of pulses in the time domain was used after an early multivariable control experiment suggested that the system could be controlled with a train of femtosecond pulses.^{51, 52} The phase of the pulse was modulated to generate an equally spaced pulse sequence. After scanning the time delay and phase between pulses, they concluded that a 160 cm^{-1} frequency of the sinusoidal function was necessary for matching the vibrational deactivation coordinates in a natural light harvesting complex.

Another example was performed by Gerber and coworker to study the control landscape of IR140.⁵³ By searching the control landscape with colored double pulses, they show the possibility of controlling the molecular induced fluorescence in a similar manner as that observed with linear chirp.

Linear chirp control

Linear chirp has shown to be an important parameter in modulating the excited state population of many molecular systems in solution. In early experiments the quadratic spectral chirp, linear chirp, was generated either by two-grating compressors or simply by passing the femtosecond pulse through material with known index of refraction.

The first experiments applying this effect to control a process in solution were performed by the Shank group in 1996.⁵⁴ Using high intensity femtosecond pulses, the authors showed that the excited state population can be substantially enhanced or suppressed depending on the linear

chirp imposed on the pulse. This observation was interpreted within the pump and dump model. In molecules with different minimum positions on the ground state and excited state potential energy surfaces (Figure 1-5), the wave packet is created on the Franck-Condon region, located on one side of the excited potential energy surface (S_1). When the non-equilibrium population evolves on the excited state, a dynamics Stokes' shift where the population migrates from higher to lower energies is produced. This temporal evolution of the population causes a time-dependent change of the energy gap between the surfaces. An intense laser field exploits this energy shift by dynamically matching the frequencies components of the pulse with the temporal evolution of energy separation between the states. Since the energy gap between the potential energy surfaces decreases as the wave packet evolves on S_1 , the chirp necessary to produce this effect must be negative. Furthermore the matching of instantaneous energy implies that neither a transform limited nor a positively chirped pulse can exert this molecular response. Similar observations were obtained in many molecules as well as biomolecular complexes.²⁴

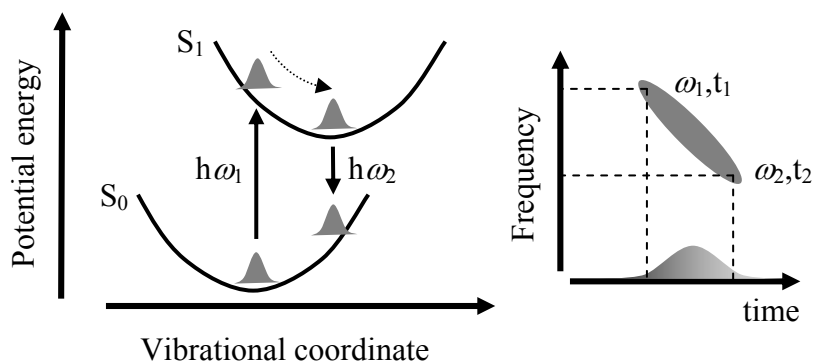


Figure 1-5. Pump and dump scheme for linearly chirped pulses. Adapted from work by Cerullo et al.²²

Modulation of two-photon excitation with linearly chirped intense laser fields has also been shown to work. The emission enhancement obtained in those experiments is produced via self phase modulation of the pulse in the sample.⁵⁵

Other controllable processes using this type of mechanism have been demonstrated in coherent anti-Stokes Raman scattering (CARS). Besides the resolution improvement using femtosecond pulses with non-zero second order phase,^{56, 57} chirped pulses also permit the selective excitation of vibrational modes in CARS experiments. The Maternity and Kiefer groups presented a selective excitation study where the population in one mode of a diacetylene single crystal was varied by the amount of chirp present on the femtosecond laser pulse.⁵⁸

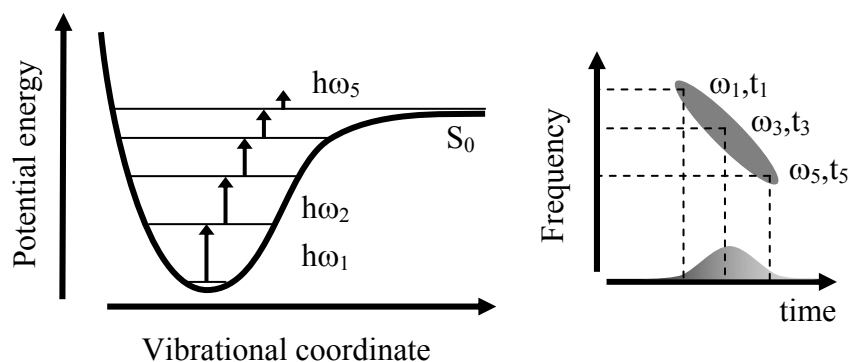


Figure 1-6. Ladder climbing scheme with tailored mid-infrared pulses.

A totally different application of chirp control in solution involves selective excitation of vibrational modes in the ground electronic state to promote population to excited vibrational states within the same electronic surface. “Ladder climbing” in the condensed phase was first introduced by Heilweil’s group on tungsten hexacarbonyl in n-hexane solution.⁵⁹ Using chirped infrared pulses, they showed the modulation of population transfer up to the second vibrational level by climbing the vibrational overtone ladder. While transform limited pulses transfer a smaller population to the second vibrational level, positively chirped pulses leave the population in the ground vibrational level. Later experiments extended the ladder climbing up to the seventh level.⁶⁰

In addition, it has been shown experimentally in the gas phase that a selective bond cleavage is produced by populating the ladder vibrational levels above the dissociation barrier.^{61,}

⁶² Although dissociation using ladder climbing in solution samples with chirp pulses has not been demonstrated yet, these experiments leave open the possibility of producing this dissociation.

Multiparameter Control

After the proposal by Judson and Rabitz²⁶ of using a multiparameterized electric field and closed loop optimization to control photochemical processes, the first multiparameter control experiment to study a molecular process in condensed phase was presented by the Wilson group in the late 1990s.²⁹ This induced an avalanche of experimental studies in the following years.

To simplify the description of these studies, they are divided according to their objective in three different groups: selective electronic excitation, vibrational dynamics, and complex molecular photoprocesses.

Control of selective electronic excitation

In the very first multiparameter control experiment, Wilson and Warren studied the electric field phase and amplitude effect on the excitation/emission of a dye molecule (IR125) using a closed loop feedback.²⁹ The controllable parameters of this experiment were amplitude, second order phase, third order phase, center frequency, and spectral width of the femtosecond laser pulse. This study aimed to control two different objectives: maximization of fluorescence over the excitation energy ratio and of the fluorescence intensity. The first objective, maximization of the fluorescence for a minimum laser excitation power, was achieved by modulating the laser excitation source such that its spectrum matched the absorption features of the dye spectrum. The second objective, maximization of fluorescence regardless of laser excitation power, was attained with a modulated pulse with a strong positive chirp without any noticeable amplitude modulation. While the first experiment is a demonstration of a selective excitation control scheme, the second experiment represents the mechanism of intrapulse “pump and dump”.

A later study of two-photon induced emission in a ruthenium complex was carried out by Gerber and coworkers in 1996.³¹ They used intensity independent optimization objectives to perform the optimal control experiment and retrieve molecular information about the system. These objectives were generated by dividing the emission intensity with a second order intensity dependent process, thus removing the intensity dependence inherent to the two-photon excitation. The optimizations acknowledged the intensity decoupling by converging to modulated electric fields different from the most effective fields obtained for a non-linear excitation, a transform limited pulse.⁴² The particularities observed in the tailored femtosecond pulse were assigned to the molecular and dynamical properties of the system. A recent study performed by Damrauer's group showed that the actual control mechanism of those experiments is based on matching the two-photon excitation spectrum of the complex rather than on dynamically controlling the system.⁴⁴

In 2001, Gerber's group also examined the selective excitation of two different dyes in solution.⁶³ Their results indicated the possibility of selectively controlling a system consisting of components with very similar one and two-photon spectra using specially designed femtosecond pulses. Many different groups have exhibited in recent years the usage of this concept for many practical applications.^{64,65} For example, Dantus' group showed the possibility of modifying the emission ratio in biological tissue⁶⁶ and in samples with different pH environments.⁶⁷

Another example of selective excitation was performed by Wada and coworkers. In this work, the two-photon excitation of α -perylene in a monocrystal, as well as an aggregated solution, was optimized.^{68,69} A closer look of the two-photon excitation spectrum reveals that the temporal response is the product of modifying the excitation second order power spectrum to match the excitation spectrum of the aggregated system.

Control of vibrational excitation

The use of simple parameter schemes in the mid-infrared region was successfully demonstrated in different quantum systems, i.e. $W(CO)_6$,⁵⁹ carboxyhemoglobin,⁷⁰ and chloroform.⁷¹ Due to the lack of direct modulation in the mid-infrared spectrum, early coherent control experiments aiming to manipulate the vibrational excitation were performed with mid-infrared shaped pulses in which the tailoring of the pulse was produced by transferring the chirp during the generation of the mid-infrared pulse, which only permit single variable studies.⁵⁹

In the late 1990s, Bucksbaum's group performed multiparameter control experiments on stimulated Raman scattering of liquid methanol with a self phase modulated femtosecond source.⁷² Using a closed loop optimization, they effectively controlled the Raman scatter spectrum of liquid methanol corresponding to symmetric and antisymmetric carbon-hydrogen stretching modes. The optimization accomplished a high degree of control on the system, which permitted the suppression or enhancement of both modes simultaneously as well as individually. Following experiments on benzene, deuterated benzene, and deuterated methanol they concluded that the control mechanism was intramolecular coupling rather than a change of the self modulated spectrum.^{38, 73} The optimal pulse was a pulse sequence whose separation coincided with the beating period of the two modes. This suggested that the control can occur by initially exciting a beat of the two modes followed by the impulsive redistribution of the energy.

Materny and coworkers studied the improvement of the excitation step in coherent anti-Stokes Raman spectroscopy by multidimensional adaptation. These optimal control studies produced, among other results, mode-selective excitation and suppression of certain modes.^{74, 75}

Very recently Zanni's group presented an acoustic optical modulator specifically designed for shaping the mid-infrared region of the spectrum.⁷⁶ They used this pulse shaper to perform the first closed loop learning control experiments using shaped mid-infrared femtosecond pulses.⁷⁷

The group reported the selective population of the excited vibrational levels in tungsten hexacarbonyl. The multidimensional searching iteration was successful in finding optimal pulses for populating specific vibrational levels by following the stimulated emission peaks as parameters of population inversion.

Control of complex molecular processes

With the advance of the optimal control field, the degree of complexity of the systems under study has increased too. In the last five years many optimal control experiments have been performed in very complex systems, i.e. biomolecular complexes.

In 2002, Motzkus and coworkers published a study presenting the control of the energy flow in the bacterial photosynthetic system LH2.⁵¹ LH2 antenna complex presents well known dynamics:⁷⁸⁻⁸⁰ upon excitation with 525 nm light three different channels are opened. While two channels are responsible for the energy transfer from the periphery to the reaction center, the third is a deactivation channel given by internal conversion. Monitoring the transient absorption signals corresponding to internal conversion and energy transfer, shaped pulses obtained in a closed loop optimization changed the internal conversion to energy transfer ratio by more than 30 %. This change in the ratio was produced with a modulated femtosecond excitation consisting of equispaced pulse sequences. Based on these results, an equispaced multipulse parameterization of the excitation revealed an anticorrelation between the energy transfer and the internal conversion channels when the phase relationship among the subpulses was varied.

Other studies involving different biological complexes can also be found in the literature, e.g. green fluorescence protein⁸¹ and living organisms.⁶⁴

Besides the intense attention that biomolecules have drawn from the optimal control field, the quest of producing new photoproducts with shaped pulses is still to be demonstrated. Recent

demonstrations of control of molecular rearrangement in different system seriously support the possibility of achieving this goal.

The first adaptive control experiment targeting isomerization in condensed phase was demonstrated in Gerber's group on a dye molecule (NK88) in 2005.⁸² To modulate the isomerization, the excitation source was produced by doubling the near infrared tailored pulse. Detecting two different absorption signals, this experiment showed that the correct pulse modulation can enhance or suppress the isomerization efficiency. These experiments were done under intense laser fields inevitably inducing multiphoton interactions during the excitation; thus preventing the interpretation of the pulse temporal shape in terms of the induced dynamics on the system. A later computational study of this isomerization process produced similar modulated electric fields as in the experiment.⁸³

In 2006, a study on the isomerization control of a cyanine dye was performed by the Yartsev group.⁸⁴ This study verified the controllability of the absolute quantum yield of isomerization which was achieved by modifying the initial momentum distribution of the wave packet on an excited state potential energy surface. The optimal pulse presented Fourier components of the torsional coordinate which is responsible for keeping the wave packet evolution parallel to the conical intersection. This coordinate induces the isomerization process and avoids the wave packet relaxation to the ground state before the isomerization, maximizing the isomerization. To decrease the isomerization the wave packet was pushed to evolve in the coordinates that drives the system to the conical intersection, avoiding its passage through the torsional coordinate.

Another example of optimal control of isomerization was performed by Miller's group, who investigated the retinal in bacteriorhodopsin.⁸⁵ Using a closed loop control scheme with

phase and amplitude modulation, the group succeeded in enhancing or diminishing the amount of formed photoproduct by 20 %. These experiments were performed in a linear regime (low field intensities) in which the observed change corresponds to the optimization isomerization efficiency.

The same system was also studied by Gerber and coworkers.⁸⁶ Employing an unmodulated pump and a modulated dump, they investigated the deactivation rather than the excitation process. The study focused on modifying the wave packet dynamics close to the conical intersection since the tailored dump had a lower energy than the corresponding transition from the ground state of either isomer. Their results show that a delay of 200 fs in the tailored dump pulse was the most effective way to bring the system back to the ground state, preventing the isomerization. However, a question that the authors did not address is whether the time delay between excitation and dumping pulses or both delay and phase are the critical parameters for exerting control.

All the presented studies show the significant progress achieved in the optimal control field in condensed phase. Now it is clear that the electric field can be obtained with a multidimensional optimization, but the challenge of understanding the process under control in terms of its molecular properties still remains.

Optimal Control and Molecular Mechanism

Closed loop experiments have been shown to be suitable techniques to control any molecular systems that generate a signal for the desired product, but they have a major drawback: only a few of those experiments lead to results that are explained in terms of the molecular properties of the system under investigation. The main reasons for this disadvantage are: a) the intricate relationship between the variables to be optimized and the molecular response, b) the arbitrary and random pathway followed by the optimal closed loop to produce

the manipulation, and c) the large number of parameters used for the generation of arbitrarily modulated pulses. In addition to the vast amount of data produced by the searching algorithm, optimization data can contain redundancies, i.e. same pulses tested more than once in the closed loop optimization, and/or physically meaningless variables, i.e. phase parameter without any important weight in the fitness. In addition, if we include the experiments performed using high intensity fields, an unknown number of multiphoton interactions prevent the correct correlation of the molecular response with the characteristic magnitudes of the field.

An ultimate goal in optimal control is to develop a procedure for gaining molecular information from the molecules under study, especially in processes where the photophysical or photochemical mechanism is unknown. A few research groups (including us) have taken the initial steps towards the development of general tools for inferring the control mechanism using the closed loop optimization data.^{33, 87-90}

One proposed way to extract the molecular information encoded on the data is by finding the parameters directly involved in the optimization procedure. The idea is to express all the independent electric field parameters used in the closed loop optimization as a collective set directly related to the studied molecular process and at the same time filter out or discard those variables with negligible or no effect on the molecular response. This is a commonly established problem in many different research areas and it is usually solved by statistical analysis.

Bucksbaum's group used principal component analysis to study the pulse parameterization space produced in the optimal control experiment of stimulated Raman scattering of liquid methanol.⁹⁰ The authors demonstrated the possibility of simplifying the representation of the electric field by removing variables with no connection to the achieved control. They concluded

that statistical analysis can be used to extract the effective degrees of freedom optimized during the experiment.

Damrauer's group used partial least squares technique to explain the observations produced in a previously performed experiment of two-photon induced emission in solution.⁸⁸⁻⁹⁰ With this methodology they extracted the collective variables and they linked them to the observed molecular response. In addition, they were able to reduce a 208 phase parameter problem into 7 fundamental dimensions in the phase space,⁸⁸ and to simplify the multivariable control experiment into a single control parameter experiment.⁸⁹

Taking a completely different approach, Weinacht's group has published two recent studies showing the viability of the parameter space reduction using simple algebra transformations.^{87, 89, 91} The first study focuses on reducing the complexity of the problem by including the parameters variability in the fitness of the experiment.⁸⁷ The authors showed that a nonlinear change of basis can significantly reduce the dimension of the search space. The second study presented a simple linear transformation of used variables to transform the multidimensional space into a set of globally independent variables. The authors test successfully the transformation in closed-loop molecular fragmentation experiments.⁹¹

Rabitz's group presented a statistical correlation analysis to explain the attosecond dynamics of high harmonic generation.³³ By examining the correlation behavior between the different harmonics produced and the optimization objective, the researches show that the experimental evidence corroborates the proposed theoretical mechanism for this phenomenon.

Outline of the Dissertation

The main scope of this work is to investigate coherent light matter interactions of molecular systems in solution. For this research study, we had developed and built a phase modulator apparatus and a pulse characterization apparatus. Using this novel apparatus, we have

conducted experimental studies to show the possibility of controlling different two-photon induced process in solution. These studies are not intended to be only a proof of principles, but a new way to understand the dynamics and electronic structure of the molecules under investigation.

Chapter 2 summarizes the theoretical description of a femtosecond laser, its implementation in our laboratory, and the techniques necessary for its characterization.

Femtosecond pulse shaping is described in Chapter 3. This chapter provides a theoretical description as well as the experimental implementation of femtosecond pulse shaping using a spatial light modulator. Different examples of shaped pulses are presented to show the capabilities of our design.

Chapter 4 describes the closed loop optimization and the genetic algorithm used in all the optimal control studies presented in this dissertation. Besides describing the genetic algorithm and its implementation, this chapter evaluates the best algorithm parameters that can be used to optimize a 128 phase parameter space. In addition, a simple closed loop experiment involving pulse compression is presented.

In Chapter 5, we study the phase effect on the two-photon induced emission on Rhodamine 6G. In this particular system, a fitness parameterization is examined.

Chapter 6 focuses on the control of energy transfer in dendritic macromolecular structures with light-harvesting properties. This chapter not only includes a closed loop optimization, but also a series of single parameter studies to discern which coherent control mechanisms are produced in the optimization. Chapter 6 presents an understanding of the energy transfer photophysics that could not be obtained via any other method.

The first part of Chapter 7 describes how variable space analysis, in conjunction with statistical analysis (correlation and multivariate), is used to extract a linear regression model of the genetic algorithm evolution during the optimization. The second part focuses on understanding what requisites are necessary for using statistical techniques to reduce the optimization variable space dimensionality.

Chapter 8 addresses feasibility of the two-photon excitation of azobenzene, and outlines possible changes in the excited state dynamics caused by this type of excitation.

CHAPTER 2 FEMTOSECOND LASER PULSES

Introduction

Since the first realization of a laser system by Maiman in 1960,⁹² scientists have been interested in producing the shortest laser pulse for studying the dynamics of processes that occur in very fast times scales, being femtoseconds the time scale of nuclear motion. Recent technologic and scientific breakthroughs, such as modelocking,⁹³ have changed laser technology. Today, it is possible to generate and characterize high power, high energy, and tunable femtosecond laser pulses. Hence, a broad spectrum of new spectroscopic applications has been opened in different fields of science including chemistry, physics, and biology.

This chapter provides a brief introduction to the theory of femtosecond laser pulses and their realization followed by a short description of the femtosecond laser system used in our laboratory. At the end of this chapter, the two main characterization techniques of femtosecond pulses and our implementation are presented.

Femtosecond Laser Pulses

General Mathematical Description of a Femtosecond Laser Pulse

The temporal and spatial dependence of a femtosecond laser pulse can be represented by its electric field, given by $E(x, y, z, t)$.⁹⁴ To simplify the description of an ultrafast pulse, the spatial dependence of the electric field is assumed to be polarized in one dimension.

$$E(x, y, z, t) = E(z, t) = E(t) \hat{z} = E(t) \quad (2-1)$$

The electric field is a real physical quantity, but in many calculations a complex representation simplifies considerably the mathematical treatment. Thus, the complex spectral

intensity ($\tilde{E}(\omega)$) is defined as the complex Fourier transform of the real temporal electric field ($E(t)$)

$$\tilde{E}(\omega) = \int_{-\infty}^{\infty} E(t) e^{-i\omega t} dt = |\tilde{E}(\omega)| e^{i\varphi(\omega)}. \quad (2-2)$$

Here, $|\tilde{E}(\omega)|$ denotes the spectral amplitude and $\varphi(\omega)$ its spectral phase. By definition of the Fourier pair, $E(t)$ is computed through the inverse Fourier transform of $\tilde{E}(\omega)$

$$E(t) = \frac{1}{2\pi} \int_{-\infty}^{\infty} \tilde{E}(\omega) e^{i\omega t} d\omega. \quad (2-3)$$

The trade off of modeling the electric field in a complex form is that the complex spectrum ($\tilde{E}(\omega)$) has positive and negative frequencies with nonzero values. Negative frequencies have not physical meaning, so a more convenient representation ($\tilde{E}^+(t)$) is employed,

$$\tilde{E}^+(t) = \frac{1}{2\pi} \int_0^{\infty} \tilde{E}(\omega) e^{i\omega t} d\omega. \quad (2-4)$$

Note that in this representation the Fourier transform is restricted to only positive frequencies. To further simplify the electric field description ($\tilde{E}^+(t)$) is usually expressed in terms of amplitude and phase terms (Equation 2-5).

$$\tilde{E}^+(t) = \frac{1}{2} A(t) e^{i\Gamma(t)}, \quad (2-5)$$

where $A(t)$ is the envelope and $\Gamma(t)$ is the phase term.

Generally the spectral amplitude is centered around the mean frequency, ω_0 , and it has nonzero values in a small frequency interval compared to the center frequency ($\Delta\omega \ll \omega_0$). This allows one to decompose the electric field in terms of an envelope and a carrier frequency (Equation 2-6).

$$\tilde{E}^+(t) = \frac{1}{2} A(t) e^{i\varphi(t)} e^{i\omega_0 t} = \frac{1}{2} \tilde{A}(t) e^{i\omega_0 t} \quad (2-6)$$

where ω_0 is the carrier frequency, $\varphi(t)$ the time-dependent phase, and $A(t)$ and $\tilde{A}(t)$ are the real and complex field envelop, respectively. An example of this representation can be found in Figure 2-1.

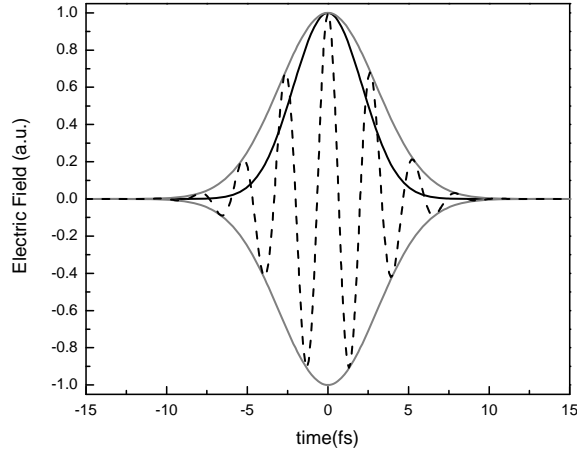


Figure 2-1. Temporal electric field representation of a Gaussian pulse. Temporal electric field, $E(t)$ (dash line), real amplitude, $A(t)$ (grey line), and intensity (black line).

This description is only valid when $\Delta\omega \ll \omega_0$ or equivalently, $\Delta\omega/\omega_0 \ll 1$. It is important to highlight that in pulses with few optical cycles this approximation might not be valid, and the electric field will not be described correctly in this representation. For pulses with carrier frequencies in the visible region of the spectrum, this assumption breaks down when their time duration is on the order of 2 fs.⁹⁴

Another important property to describe the electric field is its instantaneous frequency. Instantaneous frequency is defined as the first derivative of the phase term, $\Gamma(t)$ (Equation 2-5),

$$\frac{d\Gamma(t)}{dt} = \omega_0 + \frac{d\varphi(t)}{dt} \quad (2-7)$$

With this definition the carrier frequency is uniquely defined as the frequency that minimizes the time variation of the temporal phase. The time dependence of the phase

component, $\varphi(t)$, defines whether the frequency has a time evolution or not. For example, if $d\varphi(t)/dt = f(t)$, the carrier frequency changes with time and the pulse is said to be frequency modulated or chirped. In Figure 2-2, examples of the electric field modulation produced when $d\varphi(t)/dt = at^2$ are depicted.

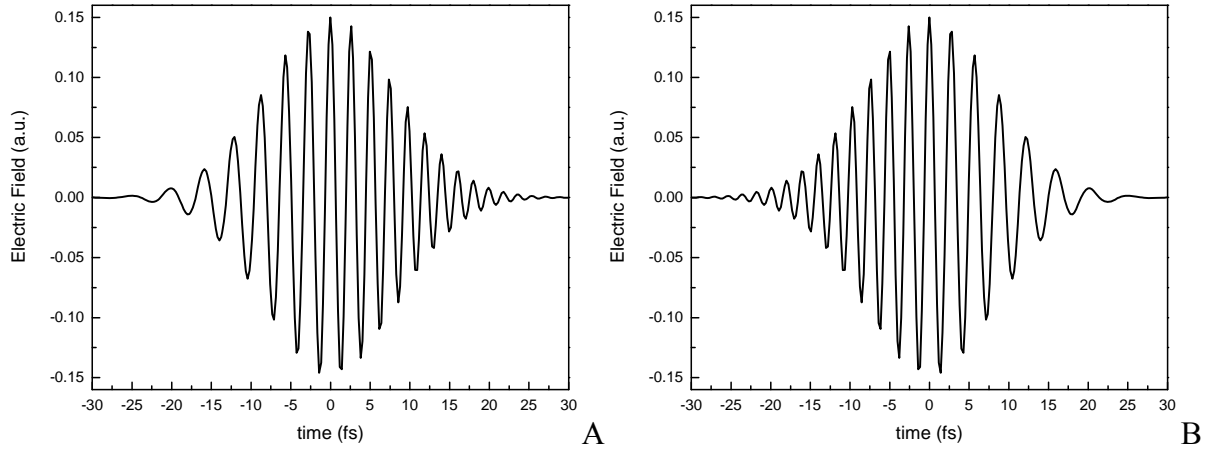


Figure 2-2. Temporal electric field for phase modulated ultrafast laser pulses. A) Pulse with positive chirp ($a > 0$). B) Pulse with negative chirp ($a < 0$).

A similar decomposition of the electric field in terms of carrier frequency and a field enveloped can be performed in the frequency domain. The spectral envelope of the electric field can be calculated from its Fourier pair ($\tilde{A}(t)$)

$$\tilde{A}(\omega) = \int_{-\infty}^{\infty} \tilde{A}(t) e^{-i\omega t} dt. \quad (2-8)$$

Many times the measured observable is not the electric field, but the intensity and spectrum. These physical quantities are related to field envelopes with the following expressions:

$$S(\omega) = \frac{\epsilon_0 c n}{4\pi} |\tilde{A}(\omega - \omega_0)|^2 \quad (2-9)$$

$$I(t) = \frac{\epsilon_0 c n}{2} \tilde{A}(t) \tilde{A}^*(t). \quad (2-10)$$

In femtosecond pulses, the most commonly used envelope is a Gaussian profile (Equation 2-11).

$$\tilde{A}(t) = \tilde{A}_0 e^{-(t/\tau_G)^2} \quad (2-11)$$

In this representation, τ_G is defined as the full width at half maximum (FWHM) of the intensity profile (Equation 2-10). Similarly, $\Delta\omega_G$ represents the FWHM of its corresponding spectral intensity (Equation 2-9).

For a given laser pulse, its temporal and spectral fields are related to each other through Fourier transforms. Because of this interconversion, the bandwidth, $\Delta\omega_p$, and the pulse duration, τ_p , cannot change independently. This relation is expressed by the time-bandwidth product.

$$\Delta\omega_p \tau_p \geq 2\pi c_B \quad (2-12)$$

Here, c_B is a constant that depends on the shape of the pulse. The lower limit for this expression is observed in pulses without frequency modulation, $d\varphi(t)/dt = 0$, which for Gaussian pulses corresponds to $c_B = 0.441$.

A very important consequence of the time-bandwidth product is that temporally short pulses will have very broad spectra. Since matter has different refraction index values for different wavelengths, a spectrally broad ultrafast pulse propagating through matter will suffer changes in its electric field characteristics.

Pulse Propagation

To describe the effect of the pulse propagation through matter, spatial and temporal dependence of the electric field are necessary. Considering the electric field linearly polarized

and propagating in the z direction as a plane wave, the following wave equation for the electric field can be derived from Maxwell equations⁹⁴

$$\left(\frac{\partial^2}{\partial z^2} - \frac{1}{c^2} \frac{\partial^2}{\partial t^2} \right) E(z, t) = \mu_0 \frac{\partial^2 (\mathbf{P}(z, t))}{\partial t^2}. \quad (2-13)$$

Here μ_0 is the magnetic permeability on vacuum, and \mathbf{P} is the polarization. The implication of this equation is that induced polarization is responsible for the effect of the medium over the incident electric field as well as for the medium's response. Polarization can be decomposed in two terms: linear and nonlinear polarization.⁹⁴

$$\mathbf{P} = \mathbf{P}^L + \mathbf{P}^{NL} \quad (2-14)$$

While the first term (\mathbf{P}^L) is responsible for effects such as diffraction and dispersion, the second term (\mathbf{P}^{NL}) is responsible for nonlinear phenomena such as harmonic generation.

The pulse propagation through a medium is described by the linear term of the polarization, \mathbf{P}^L . The general solution of the wave equation (Equation 2-13) constrained to a linear polarization term is

$$\tilde{E}(\omega, z) = \tilde{E}(\omega, 0) e^{-ik(\omega)z}. \quad (2-15)$$

Here, $k(\omega)$ is the wave vector and contains properties of the material in which the pulse is propagating, i.e. index of refraction, $n(\omega)$.

$$k^2(\omega) = \frac{\omega^2 n^2(\omega)}{c^2} \quad (2-16)$$

The wave propagation vector, $k(\omega)$, can be expressed as a Taylor series around the central frequency, ω_0 ,

$$k(\omega) = k(\omega_0) + \left. \frac{dk}{d\omega} \right|_{\omega_0} (\omega - \omega_0) + \left. \frac{d^2k}{d\omega^2} \right|_{\omega_0} (\omega - \omega_0)^2 + \dots = k_0 + \delta k \quad (2-17)$$

where δk contains all the Taylor terms except the constant k_0 .

The temporal counter part of $\tilde{E}(\omega, z)$ can be calculated through Fourier transform, assuming that the envelope slowly varies in time and space.

$$\tilde{E}(t, z) = \frac{1}{2} \underbrace{\left[\frac{1}{\pi} \int_{-\infty}^{\infty} E(\omega, 0) \exp(-i\delta k z) \exp(-i(\omega - \omega_0)t) d\omega \right]}_{\tilde{A}(t, z)} e^{-i(\omega_0 t - k_0 z)}. \quad (2-18)$$

From this result (Equation 2-18) and using the Fourier transform it is easy to demonstrate that if only the linear term of the Taylor expansion of the wave vector is included, the resulting electric field will have the following representation,

$$\tilde{E}(t, z) = \frac{1}{2} \tilde{A} \left(t - \left. \frac{dk}{d\omega} \right|_{\omega_0}, z, 0 \right) e^{-i(\omega_0 t - k_0 z)}. \quad (2-19)$$

Therefore in the time domain, the presence of a linear term in the wave vector propagation implies a temporal delay in the pulse which is proportional to the distance of propagation.

The term responsible for the delay is the group velocity,

$$v_g = \left(\left. \frac{dk}{d\omega} \right|_{\omega_0} \right)^{-1}. \quad (2-20)$$

In the case where the quadratic term in the Taylor expansion of the wave vector is not zero, the group velocity will not be the same for all the frequencies. Hence, the different frequency components will be travelling at different speeds with respect to the group velocity producing a broadening in the pulse temporal profile, i.e. chirping the pulse (Figure 2-2). This effect, group velocity dispersion, is defined as

$$\frac{dv_g}{d\lambda} = \frac{\omega^2 v_g^2}{2\pi c} \frac{d^2 k(\omega)}{d\omega^2} = \frac{\omega^2 v_g^2}{2\pi c} \left(\frac{\lambda^3}{2\pi c^2} \frac{d^2 n}{d\lambda^2} \right) \quad (2-21)$$

and represents the second or higher order terms effect on the change in the group velocity. Since the wave propagation vector and the index of refraction are related (Equation 2-16), the group velocity dispersion can be interpreted as the change produced in the group velocity of the pulse due to a non constant change in the refraction index of the medium.

Equivalently, the group velocity dispersion can be expressed in the frequency domain of the electric field as previously done. Discarding the first term of the Taylor series of the propagation vector (the delay in the pulse) we obtain

$$\begin{aligned}\tilde{E}(\omega, z) &= \tilde{E}(\omega, 0) \exp(ik(\omega)z) \\ &= \tilde{E}(\omega, 0) \exp \left[-iz \left(\frac{1}{2!} \frac{d^2k}{d\omega^2} \Big|_{\omega_0} (\omega - \omega_0)^2 + \frac{1}{3!} \frac{d^3k}{d\omega^3} \Big|_{\omega_0} (\omega - \omega_0)^3 + \dots \right) \right].\end{aligned}\quad (2-22)$$

The group velocity dispersion produces a quadratic term in the spectral phase, which in the time domain gives also a quadratic term. This explains why temporal pulse broadening is observed when an initially transform limited pulse travels in a material where $d^2n/d\lambda^2 \neq 0$, or equivalently group velocity dispersion is not zero.

Nonlinear Optical Effects

In the last section, we analyze the interaction of the linear polarization term with the electric field. However, when short and intense pulses propagate through material, the non-linear polarization produces very interesting effects, such as Kerr's effect. These the nonlinear terms must be taken into consideration when solving the wave equation (Equation 2-13).

$$\mathbf{P} = \mathbf{P}^L + \mathbf{P}^{NL} = \varepsilon_0 \left(\chi^{(1)} E + \chi^{(2)} E^2 + \dots \right) \quad (2-23)$$

The second order induced polarization can be written in terms of $E(t, z)$.

$$\mathbf{P}^{(2)} = \varepsilon_0 \chi^{(2)} E^2(t, z), \quad (2-24)$$

and since $E(t, z)$ is

$$E(t, z) = \frac{1}{2} \tilde{E}(t, z) e^{-i(\omega_0 t - k_0 z)} + \frac{1}{2} \tilde{E}^*(t, z) e^{i(\omega_0 t - k_0 z)}. \quad (2-25)$$

The effect of the second order induced polarization in a nonlinear medium can be seen as:

$$\begin{aligned} \mathbf{P}^{(2)} &\propto E^2(t, z) \\ &\propto \left[\frac{1}{2} \tilde{E}(t, z) e^{-i(\omega_0 t - k_0 z)} + \frac{1}{2} \tilde{E}^*(t, z) e^{i(\omega_0 t - k_0 z)} \right]^2 \\ &\propto \tilde{E}_0^2(t, z) \cos^2(-\omega_0 t + k_0 z) \\ &\propto \frac{\tilde{E}_0^2(t, z)}{2} (1 + \cos[2(-\omega_0 t + k_0 z)]). \end{aligned} \quad (2-26)$$

This result implies that the nonlinear polarization induced by two waves interacting in a medium produces two terms: a constant term and a term with double the frequency of the original waves. This second term is called the second harmonic of the incident wave. A similar derivation can be done for higher order nonlinear effects.

The derivation of the second harmonic intensity in terms of the non-linear polarization and phase matching conditions is not a trivial demonstration, but it can be found in any non-linear optics book.⁹⁵ The intensity of the second harmonic is given by

$$I^{2\omega} = \frac{\eta_0 \omega^2 (\chi^{(2)})^2 (I^\omega)^2 L^2}{2c_0^2 n^3} \text{sinc}^2\left(\frac{\Delta k L}{2}\right). \quad (2-27)$$

This result exhibits the second harmonic's dependence on the intensity of the fundamental wave, I^ω , the second order susceptibility, $\chi^{(2)}$, the optical path, L , and the wave vector change Δk . Since the dependence of the wave vector change is through a *sinc* function square, the maximum second harmonic conversion that can be produced in a given material is obtained when Δk is close to zero. In second harmonic generation produced by two collinear beams, Δk can be expressed as

$$k_3(2\omega_0) = k_1(\omega_0) + k_2(\omega_0). \quad (2-28)$$

Using its relation with the index of refraction (Equation 2-16), the condition can be rewritten as

$$n(\omega_0) = n(2\omega_0). \quad (2-29)$$

To produce second harmonic, the fundamental wave and its second harmonic must travel with their relative phase constant inside the nonlinear medium. In most materials, this condition can not be fulfilled. However, birefringent materials can meet this constraint. Birefringent crystals are anisotropic mediums with two different optical axes, each characterized with its own index of refraction. If fundamental and second harmonic waves travel through the different optical axis of the materials, the phase match condition is fulfilled and second harmonic will be generated.

Femtosecond Laser Generation

Ultrafast laser pulses are generated with a mode-locked laser. Since its introduction in 1986, Ti:Sapphire lasers have replaced dye lasers as source of femtosecond laser pulses because of their tunability, stability, excellent mode quality, high output power, and ultrashort laser generation.⁹⁶ Today it is possible to buy commercially available Ti:Sapphire femtosecond laser sources with pulses as short as 6 fs and several watts of power output.⁹⁷ Two main components are necessary to produce amplified femtosecond laser pulses: a femtosecond laser seed (Ti:Sapphire oscillator) and an amplifier (in our case, a chirped regenerative amplifier).

Ti:Sapphire Oscillator

Ti:Sapphire oscillators can produce pulses as short as 4.5 fs. Ultrashort pulses are generated by keeping all the longitudinal modes of a cavity with a fixed phase relationship, i.e. phase-lock or modelocked. Modelocked can be attained with two different techniques: active and passive mode locking. Active modelocking is produced by acousto-optical or electro-optical modulation

of the longitudinal modes inside the cavity.⁹³ Passive modelocking can be achieved with saturable absorbers or by Kerr's effect.⁹³

Briefly, modelocking with an acousto-optical modulator consists on producing phase locked modes by introducing an acousto-optic transducer into the cavity. This component has a small fused silica element with a piezo-electric transducer attached to it. The piezo-electric transducer produces a standing wave in the crystal, creating a transmission grating perpendicular to the longitudinal modes of the cavity. A fundamental mode passing through the optical resonator is amplitude modulated such that new modes appear in the cavity. These new modes have frequencies of the fundamental mode frequency plus/minus the frequency introduced by the transducer, typically MHz. The interaction of these new modes with the crystal produces more modes. After many passes, the different modes are phase locked and they add up coherently to form the femtosecond pulse.

This modelocking technique adjusts the acousto-optical modulator frequency continuously to match the cavity round trip time, avoiding the necessity of a fixed cavity size.⁹⁸ However, as the number of modes increases their relative phases start to change due to the intrinsic dispersion of the cavity elements. To avoid this problem, oscillator cavities also included a prism pair compressor and negatively chirped mirrors to keep all the longitudinal modes phase locked.

In our laboratory, the Ti:Sapphire oscillator is a commercially available system (Tsunami Spectra Physics ®). The Ti:Sapphire rod is pumped with the second harmonic of a continuous wave Nd:YVO₄ laser (Millennia Spectra Physics®). The oscillator cavity is actively modelocked with a regenerative modelocking mechanism. The Tsunami provides ultrashort pulses (>35 fs) in the near infrared region (tuning range from 710 to 980 nm) with a 80 MHz repetition rate. Since

the oscillator pulses have low energy (~ 5 nJ per pulse), its output is used as a seed for the chirped femtosecond amplifier.

Femtosecond Amplifier

Laser amplification is usually achieved by pumping an optically active material with a pump source. In the case of femtosecond laser amplification this process cannot be produced by direct amplification because the gain medium of the amplifier will be damaged by the peak intensities of an amplified femtosecond pulse. To produce the amplification of a pulse from the oscillator, a chirped regenerative pulse amplifier is used.⁹⁹

The chirped pulse amplifier uses a Ti:Sapphire medium pumped with the second harmonic of a Nd:YLF Q-switched laser. The oscillator serves as a seed for the amplification process. To avoid damaging the active medium, the oscillator femtosecond pulse is temporally broadened (chirped) in a stretcher, before coupling it with the amplifier cavity. In a regenerative amplifier, a pair of Pockels' cells are used to trap the seed pulse in the amplifier cavity until it reaches maximum amplification. Once inside the cavity, the amplification of the seed occurs with each pass through the Ti:Sapphire crystal. Upon reaching saturation, the pulse is released from the amplification process with the second Pockel cell and a polarization beam splitter. After the pulse amplification, the pulse is temporally compressed to the femtosecond time duration with a double pass grating compressor.

In our laboratory, the Ti:Sapphire amplifier is a commercially available system (Spectra Physics, Spitfire®). The gain medium, a Ti:Sapphire rod, is pumped with a 7 W Nd:YLF Q-switched laser (Spectra Physics, Evolution®) and seeded with the Ti:Sapphire oscillator previously described. The amplifier delivers ultrashort amplified pulses (45 fs) in the near infrared region (25 nm FWHM at 800 nm) with 1 KHz repetition rate. The amplification in this

chirped regenerative amplifier is more than 6 orders of magnitude yielding pulse energies up to 850 μJ .

Femtosecond Pulse Characterization

To study light-matter interactions, it is necessary to have a correct description of the laser electric field, i.e. amplitude and phase. Two different types of diagnostic techniques are commonly employed to characterize completely the femtosecond electric field. The first type is the frequency resolved optical gating (FROG) technique which involves a frequency resolved autocorrelation.¹⁰⁰ The second type is spectral phase interferometry for direct electric field reconstruction (SPIDER), and as its name indicates the technique is based on interferometry to measure the time-frequency profile of the laser pulse.¹⁰¹ The main advantages of each technique are: SPIDER is a real time characterization technique, and FROG is a technique with a simple implementation. Thus if the priority is to characterize in real time the ultrashort pulse SPIDER should be chosen and when the real time characterization is not a experimental priority, the FROG technique should be selected. The FROG technique was implemented since in our experiments the real-time characterization of the laser pulse is not mandatory.

Frequency Resolved Optical Gating Technique

Frequency resolved optical gating is based on measuring the spectrally resolved signal of an autocorrelation. As in the autocorrelation, the pulse is divided into two identical replicas which are recombined in a nonlinear medium. The signal produced in the nonlinear medium is later spectrally resolved with a spectrometer. Many different nonlinear properties of materials can be use, e.g. Kerr's effect, second harmonic, third harmonic, self diffraction, etc. The FROG technique based on second harmonic generation, SHG-FROG, is the most widely used because unlike any other nonlinear processes the signal depends on the second order susceptibility

coefficient of the nonlinear medium, which is usually large. This makes SHG-FROG an extremely sensitive technique that can be used to characterize pulses down to 1 pJ of energy.

The main limitation of SHG-FROG is that due to the time symmetry of the traces the time direction is unknown. In cases where the electric field consists of two or more pulses, the relative phase of the pulses has an ambiguity. Specifically, double pulses with a phase relationship between them of φ or $\varphi + \pi$ will have the same FROG trace.

It is important to note that the FROG technique was created to analyze well behaved pulses, close to transform limited pulses. For complex electric fields one should be careful in the interpretation of the phase retrieved by this technique.

The usual realization of this technique is shown in Figure 2-3.¹⁰⁰

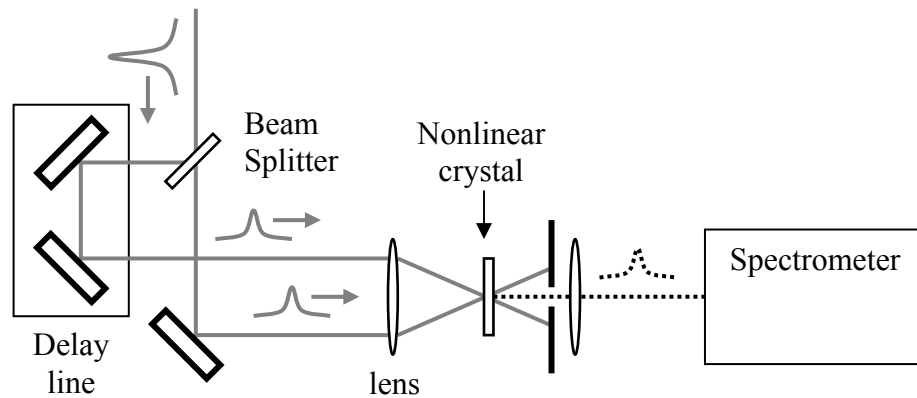


Figure 2-3. Experimental layout for a FROG apparatus using second harmonic generation.

The FROG trace corresponds to

$$I_{FROG}^{SHG}(\omega, \tau) = \left| \int_{-\infty}^{\infty} E(t) E(t - \tau) \exp(-i\omega t) dt \right|^2. \quad (2-30)$$

A phase retrieval algorithm is used to retrieve the phase out of this trace. The phase retrieval problem is not a simple problem because it does not have an analytical solution and it gets even more complicated when the pulse gates itself, like in SHG-FROG. This problem is generated because the retrieval algorithm needs the gate function to retrieve the phase. Many

different algorithms have been developed to solve this problem. In fact, the commercially available program used to retrieve the phase and amplitude of a pulse out of its SHG-FROG trace implements various different algorithms.

The basic idea of the two dimensional phase retrieval algorithm can be seen in Figure 2-4. This algorithm uses two constraints for solving the problem, i.e. it uses mathematical and data constraints.¹⁰⁰ The mathematical constraint is related to the nonlinear property used to generate the trace. In SHG-FROG this constraint is represented by

$$E_{sig}(t, \tau) \propto E(t)E(t - \tau). \quad (2-31)$$

The data constraint is implemented by replacing the square root of the amplitude of the experimental trace with the new field trace without modifying its phase, generating a new electric field.

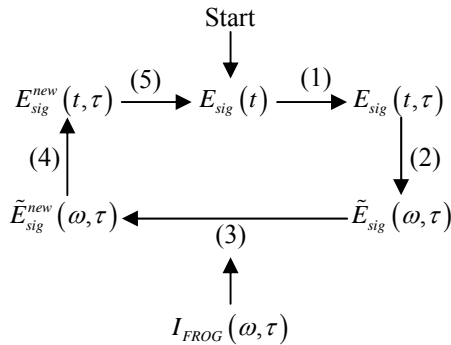


Figure 2-4. Schematic of a generic FROG algorithm. Adapted from work by Trebino.¹⁰⁰

The FROG algorithm starts with an initial guess of the electric field in the time domain. Using the experimental FROG trace and the Fourier transform of the guess into the frequency domain, a new and improved electric field is generated. This field is back transformed to the time domain. The last step of the cycle consists on using this new electric field to generate a new guess. The process is repeated until convergence has been reached, which is evaluated in terms of the root mean square difference of the measure traced and the trace obtained by the algorithm.

The program used for retrieving the phase of the SHG-FROG in our laboratory is the commercially available software FROG 3.2.2 by Femtosoft Technologies.

CHAPTER 3 FEMTOSECOND PULSE SHAPING

Introduction

Envisioned two decades ago, one of the latest applications of femtosecond lasers is to control photochemical process.²⁴ The manipulation of the temporal and spectral components of the ultrafast laser electric field is required to produce quantum control of molecular photophysics. Due to the lack of fast electronics, it is currently impossible to modulate a femtosecond pulse in the time domain. Modern technology takes advantage of the time-frequency inversion by modulating pulses in the frequency domain. Optical devices capable of synthesizing different ultrafast pulse waveforms in the frequency domain have been proposed and realized, e.g. spatial light modulators, acoustics optics modulators, deformable mirrors, etc.^{27, 102, 103}

Originally developed by Weiner and coworkers, pulse shaping with spatial light modulators is a widespread technique because of its high transmission and its capability of shaping amplified laser pulses.

Femtosecond Laser Pulse Shaping with Spatial Light Modulators

The first spatial light modulator was experimentally realized by Weiner and coworker using a zero dispersion pulse compressor with a fixed mask in its Fourier plane.¹⁰⁴ Later, the same group developed the first programmable spatial light modulator using a voltage controlled multi-element liquid crystal mask.¹⁰⁵

Nowadays, pulse shaping with liquid crystal masks has become a major methodology for tailoring femtosecond pulses because it allows for the arbitrary modulation of the “individual” frequency components of an ultrafast laser field.

In this section, a brief description of the basic principles of pulse shaping with spatial light modulator is provided, followed by the experimental realization of the pulse shaper in our laboratory and examples of its capabilities.

Pulse Shaping in the Frequency Domain

The concept of femtosecond pulse shaping is based on the application of a linear, time-invariant filter.²⁷ Linear filtering can be described either in the time or frequency domain. In the frequency domain, the filter's frequency response function, $H(\omega)$, characterizes the effect produced by the filter on the input electric field, $E_{in}(\omega)$, so the output electric field, $E_{out}(\omega)$, is defined as

$$E_{out}(\omega) = E_{in}(\omega) \cdot H(\omega) . \quad (3-1)$$

The time domain filter response can be computed using the Fourier transform of the filter's frequency response function, $H(\omega)$.

$$H(\omega) = \int_{-\infty}^{\infty} H(t) e^{-i\omega t} dt , \quad (3-2)$$

consequently

$$H(t) = \frac{1}{2\pi} \int_{-\infty}^{\infty} H(\omega) e^{i\omega t} d\omega . \quad (3-3)$$

The modulated output of the electric field in the time domain is

$$E_{out}(t) = E_{in}(t) \otimes H(t) = \int E_{in}(u) \cdot H(u-t) du , \quad (3-4)$$

where the \otimes denotes the convolution of the two functions. In the case where the input pulse is a delta function in the time domain, the input spectrum is unity

$$E_{in}(\omega) = \int_{-\infty}^{\infty} E_{in}(t) e^{-i\omega t} dt = \int_{-\infty}^{\infty} \delta(t) e^{-i\omega t} dt = 1 \quad (3-5)$$

and the output spectrum is equal to the frequency response of the filter.

$$E_{out}(\omega) = E_{in}(\omega) \cdot H(\omega) = 1 \cdot H(\omega) = H(\omega). \quad (3-6)$$

For short pulses, specific temporal output pulses can be generated by calculating the linear filter with the proposed impulse response. A complex frequency response of the filter is given by

$$H(\omega) = T(\omega) e^{-i\psi(\omega)} \quad (3-7)$$

where $T(\omega)$ and $\psi(\omega)$ are the real and imaginary parts of the filter response, respectively. The filtered electric field is then

$$E_{out}(\omega) = E_{in}(\omega) T(\omega) \exp(-i\psi(\omega)). \quad (3-8)$$

In the previous section, it was shown that a pulse propagating in a medium suffers a change in its electric field (Equation 2-15) given by

$$E(\omega, z) = \tilde{E}(\omega, 0) \exp\left(-i \frac{\omega \cdot n(\omega)}{c} z\right). \quad (3-9)$$

If we compare the effect of propagation (Equation 3-9) with the output of the electric field when a filter is imposed on it (Equation 3-8)

$$E_{in}(\omega) T(\omega) = \tilde{E}(\omega, 0), \quad (3-10)$$

$$\psi(\omega) = \frac{\omega \cdot n(\omega)}{c} z. \quad (3-11)$$

This result is the basis for pulse shaping with spatial light modulators. It shows that by controlling the filter's refractive index for the input frequency components it is possible to arbitrarily modify its phase, and hence its temporal shape. Moreover, changing the real part of the filter function, $T(\omega)$, will produce spectral amplitude modulation on the input field.

The phase of the filter can be expressed as a Taylor series around the pulse central frequency of the pulse (ω_0)

$$\psi(\omega) = \sum_{n=0}^{\infty} \frac{1}{n!} \left. \frac{d^n \phi(\omega)}{d\omega^n} \right|_{\omega_0} (\omega - \omega_0)^n. \quad (3-12)$$

An arbitrary pulse in the time domain can be calculated from the electric field in the spectral domain (Equation 2-3) and filtered electric field (Equation 3-8).

$$E_{out}(t) = \frac{1}{2\pi} \int_{-\infty}^{\infty} E_{in}(\omega) T(\omega) e^{i\psi(\omega)} e^{i\omega t} d\omega. \quad (3-13)$$

Replacing the imaginary part of the filter's response with the Taylor series, we obtain

$$E_{out}(t) = \frac{1}{2\pi} \int_{-\infty}^{\infty} E_{in}(\omega) T(\omega) \exp \left(i \sum_{n=0}^{\infty} \frac{1}{n!} \left. \frac{d^n \phi(\omega)}{d\omega^n} \right|_{\omega_0} (\omega - \omega_0)^n \right) e^{i\omega t} d\omega. \quad (3-14)$$

This expression shows that many different temporal pulses can be created depending on the function applied to filter the electric field in the frequency domain. Spectral filters capable of producing totally arbitrary functions, not necessarily smooth functions like the Taylor series, can produce pulses with the most unthinkable temporal shapes.

To experimentally realize the pulse shaping of a femtosecond pulse in the frequency domain two important components are necessary: a zero dispersion compressor and a spatial light modulator.

Zero Dispersion 4f Compressor

A zero dispersion compressor consists of two gratings and two lenses arranged in a line (Figure 3-1).¹⁰⁵ Each grating is located in the front focal plane of one lens and the distance between both lenses is twice their focal length. An incident beam is dispersed in its frequency components and then focused into the back focal plane of the first lens. In this plane, the Fourier plane, all the frequency components are spread along the horizontal axis. A second lens grating pair recombines all the pulse components into a single pulse. This spatial arrangement can be understood as the first lens-grating pair performing the spatial Fourier transform on the incident

pulse and the second grating-lens pair performing the inverse Fourier transform on the components located at the Fourier plane.

Any phase or amplitude filter placed at the Fourier plane will modulate the individual frequency components of the input pulse. As a result, after the inverse Fourier transform the output pulse will be modulated in phase and/or amplitude.

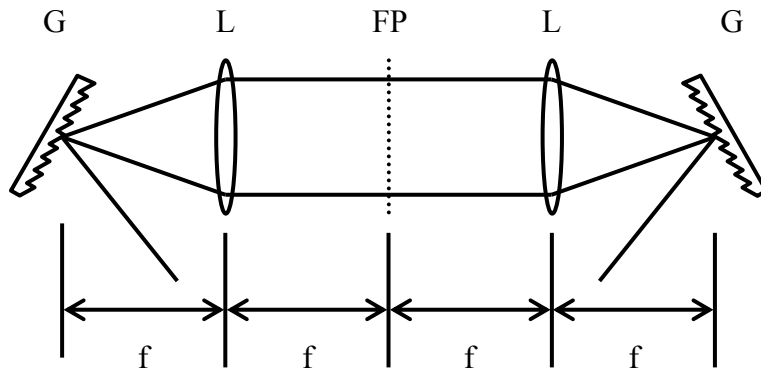


Figure 3-1. Basic layout for a zero dispersion compressor. G: grating, L: lens, FP: Fourier plane. Adapted from work by Weiner et al.²⁷

Without a filter in the Fourier plane, this type of optical arrangement produces an output pulse with the same temporal shape as the input pulse (zero dispersion compressor). This configuration is the standard setup used to compress ultrafast pulses because the displacement of the second grating compensates for the second order phase component of an input chirped pulse.¹⁰⁶

Spatial Light Modulator

The spatial light modulator used in this work is based on utilizing a liquid crystal to produce a filter function in the Fourier plane of the zero dispersion compressor. To understand the basic functioning characteristics of our spatial light modulator a brief introduction on liquid crystal mask properties is provided in the next subsection.

Liquid crystal mask characteristics

The liquid crystal mask consists of a linear array of independent pixels. Each pixel has its own control which permits the generation of totally arbitrary filter responses. One of the most important characteristics of these devices is their operation over an extensive range of temperatures without the need of a temperature controller.¹⁰⁷

A liquid crystal can present different phases, e.g. smectic, nematic, and chiral.¹⁰⁷ Each different phase is characterized by the type of ordering in its cell volume. Liquid crystal masks use the properties of the nematic phase to control the index of refraction of the pixels.

Liquid crystal molecules are elongated rods. In a nematic liquid crystal phase, all the rods are vertically oriented without any type of ordering in the other two axes, i.e. distance between rods is not constant (Figure 3-2). Due to its elongated shape, these nematic materials are optically anisotropic leading to birefringence. These birefringent materials are optically characterized by their anisotropic dielectric tensor, in which the extraordinary index of refraction coincides with the long axis of the rod. Their dielectrically anisotropic tensor makes the nematic molecules' orientation susceptible to the presence of an external electric field.¹⁰⁸ Hence, liquid crystals are materials with a controllable birefringence.

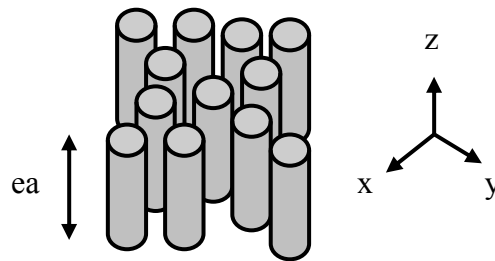


Figure 3-2. Cartoon of a nematic phase liquid crystal. ea: extraordinary axis.

Liquid crystal masks are fabricated by rubbing a window substrate with a fine polishing compound along one specific direction. When liquid crystal molecules are sandwiched in between one rubbed and one flat surface, they automatically align in the rubbing direction.¹⁰⁷ By

coating the two surfaces of the containing cell with a thin, transparent, and electrically conductive film of indium tin oxide (ITO), the liquid crystal orientation can be controlled with an externally applied field between the electrodes.

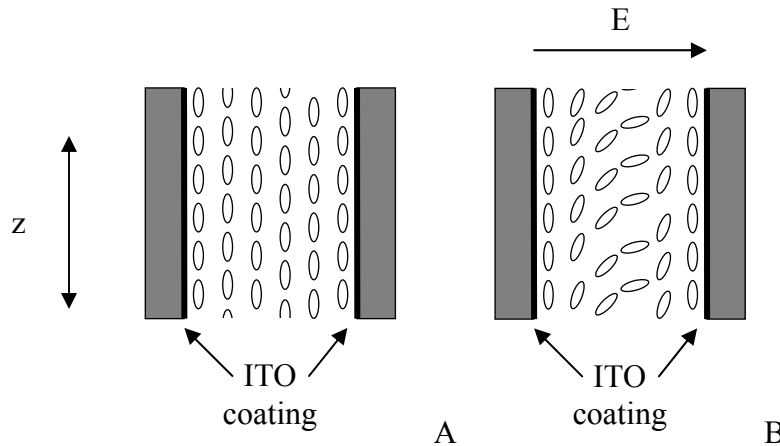


Figure 3-3. Side view of a single nematic crystal pixel. A) Without electric field. B) With an external field applied. Adapted from work by Weiner et al.¹⁰⁹

The liquid crystal mask operates as follows (Figure 3-3): when no electric field is applied, the liquid crystal molecules are oriented with their long axis parallel to the grooves (z axis) created in the window (Figure 3-3(A)). When the electric field is turned on, the molecules rotate so that their long axis is aligned parallel the direction of the field (Figure 3-3(B)). This rotation changes the refraction index along the rotation axis (z axis). For light propagating through the mask with a polarization at 45 degrees with respect to the liquid crystal elongated axis, the component along the extraordinary optical axis will be delayed with respect to the component propagating parallel to the ordinary axis.

The change in the index of refraction, or retardation, can be calculated using the following relation:¹¹⁰

$$\frac{1}{n^2(\theta(V))} = \frac{\cos^2(\theta(V))}{n_o^2} + \frac{\sin^2(\theta(V))}{n_e^2} \quad (3-15)$$

where, θ represents the angle of inclination of the liquid crystal which is a function of the external applied field, V .¹¹¹

A series of consecutive pixels form a discrete variable retarder perfectly suitable for filtering the electric field of an ultrafast pulse in the Fourier plane of a zero dispersion compressor. In addition, the use of a double mask with a special configuration permits the modulation of the electric field in phase and amplitude.

The spatial light modulator

The liquid crystal based spatial light modulator used in this work is a commercially available model (CRI Inc. SLM-640-D-VN®). The mask consists of two linear arrays with 640 pixels each (Figure 3-4(A)). Each liquid crystal array is composed of two glass substrates coated with ITO. While one substrate acts as ground, the other is lithographically patterned into a linear array of 640 electrodes each with 5 mm height and 97 μm width. Each electrode is connected to its own voltage controller, which produces 640 independent pixels on the mask. The separation between pixels is 3 μm and as no electric connector is present in this region the refraction index can not be controlled, leading to an interpixel gap.

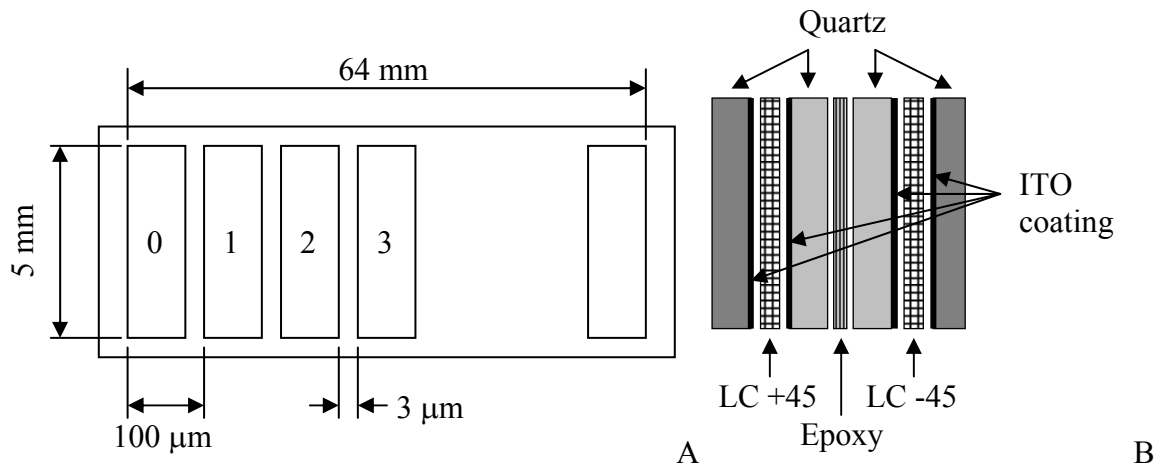


Figure 3-4. Schematic of spatial light modulator mask. A) Front view. B) Lateral cut. Adapted from work by Weiner et al.²⁷

To make the phase and amplitude spatial light modulator, two liquid crystal arrays are glued together such that the pixels of the first array spatially coincide with the pixels in the second array. The space between masks is held constant (1.02 mm) by adding little quartz rods in between the arrays (Figure 3-4(B)). The glue used is a refraction index matching epoxy to minimize losses due to surface reflections.

The spatial light modulator is controlled with an electronic driver located inside the housing of the apparatus, which provides an independent voltage control for each of the pixels in the mask. This driver is computer controlled through a USB port. The voltage adjustment dynamic range of the driver is 12 bit or 4096 discrete levels, where the maximum level corresponds to 10 V (level 4095) and the minimum to 0 V (level 0). To avoid electromigration effects produced by DC sources, the controller source is an alternating current source (3.3 kHz square waveform).¹¹² The usual response time of the liquid crystal mask in our system is close to 50 milliseconds.

In each side of the double mask there is a thin polarizer limiting the use of the mask to the 488-900 nm region. The damage threshold for 900 nm is 200 $\mu\text{J}/\text{cm}^2$ (50 fs pulse, repetition rate 1kHz). If the mask is used without the polarizers the spectral working range extends up to 1620 nm. In addition, by replacing the output polarizer with a specially designed mirror the spatial light modulator can be used in a reflective mode, which presents many important advantages.

This spatial light modulator operates onto the polarized incident light. In our system, the extraordinary index of refraction of each mask is +45 degrees and -45 degrees with respect to the entrance horizontal polarizer, which permits phase and amplitude modulation of the incident light.

Pulse shaping with LC masks

Introduced in previous chapters, the phase produced by ultrafast pulses propagating in a material is (Equation 2-22)

$$\phi(\omega) = \frac{\omega \cdot n(\omega)}{c} z \quad \text{or} \quad \phi(\lambda) = \frac{2\pi \cdot n(\lambda)}{\lambda} z . \quad (3-16)$$

The index of refraction in a liquid crystal can be modulated by applying an external voltage, thus

$$\phi(\lambda, V) = \frac{2\pi \cdot n(\lambda, V)}{\lambda} z . \quad (3-17)$$

The difference in phase, $\Delta\phi$, produced by a change in voltage (ΔV) is

$$\Delta\phi(\lambda, \Delta V) = \frac{2\pi \cdot \Delta n(\lambda, \Delta V)}{\lambda} z , \quad (3-18)$$

where Δn is the change in index of refraction due to a ΔV change in voltage. This change in refraction index of a liquid crystal can be expressed in terms of its ordinary and extraordinary components

$$\Delta n(\lambda, \Delta V) = n_{LC}(\lambda, V) - n_{LC}^o(\lambda, 0) \quad (3-19)$$

where n_{LC} is

$$\frac{1}{n_{LC}^2(\lambda, V)} = \frac{\cos^2(\theta(V))}{n_{LC}^o{}^2(\lambda)} + \frac{\sin^2(\theta(V))}{n_{LC}^e{}^2(\lambda)} . \quad (3-20)$$

The change in phase, or retardation, is only applied to the polarization component of the incident wave parallel to the optical axis of the liquid crystal pixel. In the spatial light modulator, the liquid crystal optical axis on each mask is at +45 and -45 degrees with respect to the vertical axis of the array (Figure 3-5).¹¹³

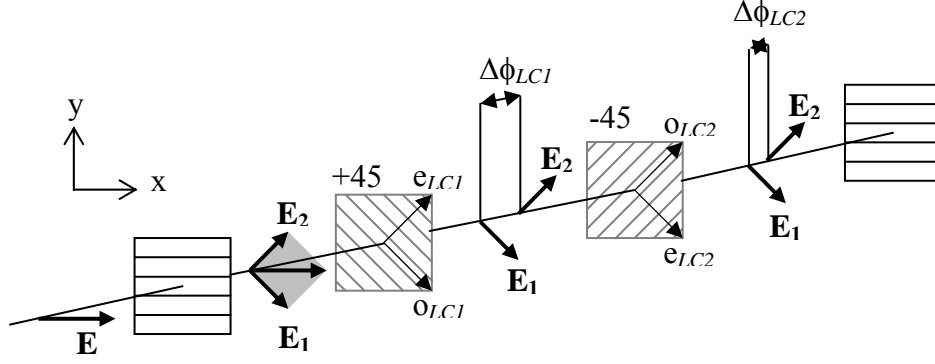


Figure 3-5. Setup for dual mask spatial light modulator.

The extraordinary and ordinary axes of the liquid crystal for each mask can be expressed as

$$\vec{e}_{LC1} = \frac{1}{\sqrt{2}}(\vec{X} + \vec{Y}) \text{ and } \vec{o}_{LC1} = \frac{1}{\sqrt{2}}(\vec{X} - \vec{Y}) \quad (3-21)$$

and

$$\vec{e}_{LC2} = \frac{1}{\sqrt{2}}(\vec{X} - \vec{Y}) \text{ and } \vec{o}_{LC2} = \frac{1}{\sqrt{2}}(\vec{X} + \vec{Y}), \quad (3-22)$$

where \vec{e} and \vec{o} are the extraordinary and ordinary axis, and $LC1$ and $LC2$ are the first and second liquid crystal masks, respectively. For an incident electric field, \vec{E}_0 , polarized in the \vec{X} direction, its electric field can be expressed in terms of the extraordinary axis of both masks

$$\vec{E}_0 = E_0 \vec{X} = \frac{E_0}{\sqrt{2}}(\vec{e}_{LC1} + \vec{e}_{LC2}). \quad (3-23)$$

The retardation and the electric field observed after passing both masks will be

$$\vec{E}_1 = \frac{E_0}{\sqrt{2}}(\vec{e}_{LC1} \cdot e^{i\Delta\phi_{LC1}} + \vec{e}_{LC2} \cdot e^{i\Delta\phi_{LC2}}), \quad (3-24)$$

where $\Delta\phi_{LCi}$ is the retardation produced by the i^{th} mask. Expressing the electric field back in terms of the \vec{X} and \vec{Y} axis

$$\vec{E}_1 = \frac{E_0}{2}(\vec{X}(e^{i\Delta\phi_{LC1}} + e^{i\Delta\phi_{LC2}}) + \vec{Y}(e^{i\Delta\phi_{LC1}} - e^{i\Delta\phi_{LC2}})). \quad (3-25)$$

By Euler's formula, it can be expressed as

$$\vec{E}_1 = E_0 \exp\left(i \frac{\Delta\phi_{LC1} + \Delta\phi_{LC2}}{2}\right) \left(\vec{X} \cos\left(\frac{\Delta\phi_{LC1} - \Delta\phi_{LC2}}{2}\right) + i\vec{Y} \sin\left(\frac{\Delta\phi_{LC1} - \Delta\phi_{LC2}}{2}\right) \right). \quad (3-26)$$

In the spatial light modulator the input and output polarizer set the polarization in the x axis, thus

$$\vec{E}_x = E \exp\left(i \frac{\Delta\phi_{LC1} + \Delta\phi_{LC2}}{2}\right) \cos\left(\frac{\Delta\phi_{LC1} - \Delta\phi_{LC2}}{2}\right). \quad (3-27)$$

The output electric field, which is tailored after propagating through both masks, has two terms: the first one, an exponential function, is imaginary, while the second one, a cosine function, is real. While the imaginary term will only change the phase of the transmitted electric field, the real term will produce amplitude modulation over the spectrum of the pulse. Phase and/or amplitude modulation will be imprinted on the pulse depending on the applied voltage on each mask. This modulation can be expressed in terms of the filter's frequency response (Equation 3-8)

$$E_{out}(\omega) = E_{in}(\omega) T(\omega) \exp(i\psi(\omega)) \quad (3-28)$$

where $\psi(\omega)$ is the phase filter function and $T(\omega)$ is the transmission filter function. Comparing with the above result (Equation 3-36) we obtain

$$\psi = \frac{(\Delta\phi_{LC1} + \Delta\phi_{LC2})}{2} \quad (3-29)$$

$$T = \cos\left(\frac{(\Delta\phi_{LC1} - \Delta\phi_{LC2})}{2}\right). \quad (3-30)$$

Note that this result present two special cases, $\Delta\phi_{LC1} + \Delta\phi_{LC2} = 0$ and $\Delta\phi_{LC1} - \Delta\phi_{LC2} = 0$.

While the former case corresponds to amplitude modulation only, the latter corresponds to phase modulation only.

If the transmission and phase filter functions to produce a certain pulse are known, the phase applied to each mask can be calculated as

$$\Delta\phi_{LC1} = \psi + \arccos(T) = \psi + \arccos(\sqrt{A}) \quad (3-31)$$

$$\Delta\phi_{LC2} = \psi - \arccos(T) = \psi - \arccos(\sqrt{A}). \quad (3-32)$$

The Pulse Shaper

Geometrical Configurations

Pulse shapers can be implemented in several different configurations. The first proposed configuration is depicted in Figure 3-6(A). In this configuration, the beam propagates through the Fourier plane to the other side of the pulse shaper, which is a mirror image of the first side. If a mirror is positioned at the Fourier plane of the pulse shaper, another possible configuration is obtained, Figure 3-6(B). The former implementation, transmission mode, is the most standard methodology found in the literature; the later, reflective mode, provides unmatched advantages such as smaller footprint size and lower cost.

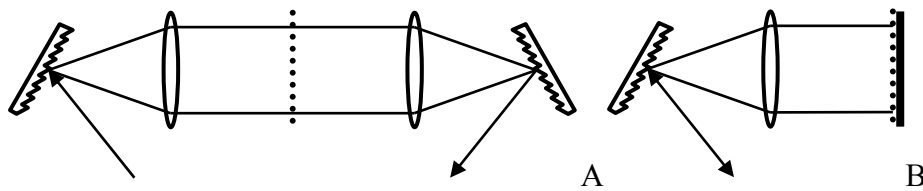


Figure 3-6. Basic layout of a pulse shaper. A) Transmission mode configuration. B) Reflective mode configuration.

Figure 3-7 shows many previously implemented^{27, 114-117} and newly proposed pulse shaper geometries.¹ Each of these configurations has its advantages and drawbacks. A detailed analysis of each of the possible implementations was used to determine the most suitable realization for our pulse shaper.

¹ All configurations can be converted to reflective mode by setting a mirror in their corresponding Fourier plane.

The first setup (Figure 3-7(A)) has the advantage of having all the optics positioned along a line, but the use of lenses introduces chromatic aberrations especially in pulses with very broad spectrums (temporally short), thus a configuration with reflective focusing optics is preferred.

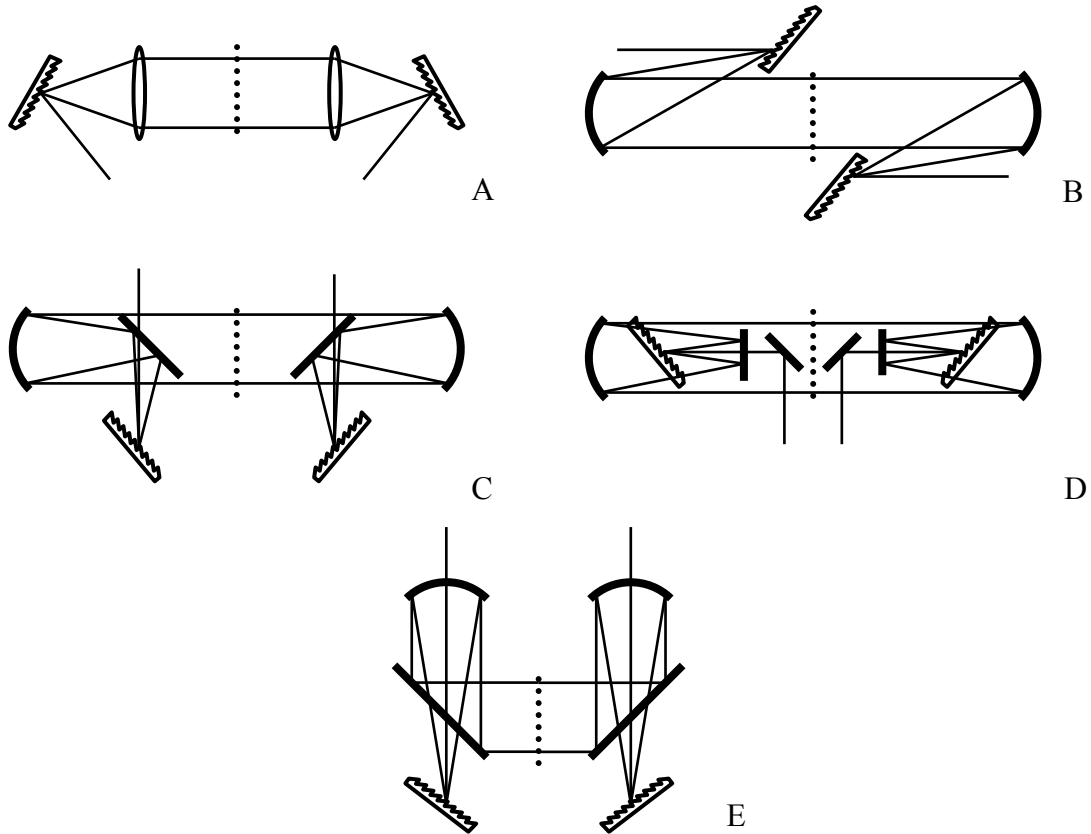


Figure 3-7. Top view of different design types for pulse shapers based on an optical Fourier transform.

The remaining configurations (Figure 3-7(B)-(E)) can be categorized in two groups: those with (B) and those without (B,C) a folding mirror. A pulse shaper without a folding mirror creates spatial aberrations since its focusing element reflects the beam in a direction out of its optical axis, producing astigmatism. This type of aberration is very difficult to compensate.

The remaining configurations introduce at least one folding mirror (Figure 3-7(C)-(E)). When the dispersed beam is reflected such that the angle between incident and reflected beam is

non zero and the height of the reflected beam is also changed (Figure 3-8(C),(E)), a tilt on the beam in the Fourier plane is observed (Figure 3-8).

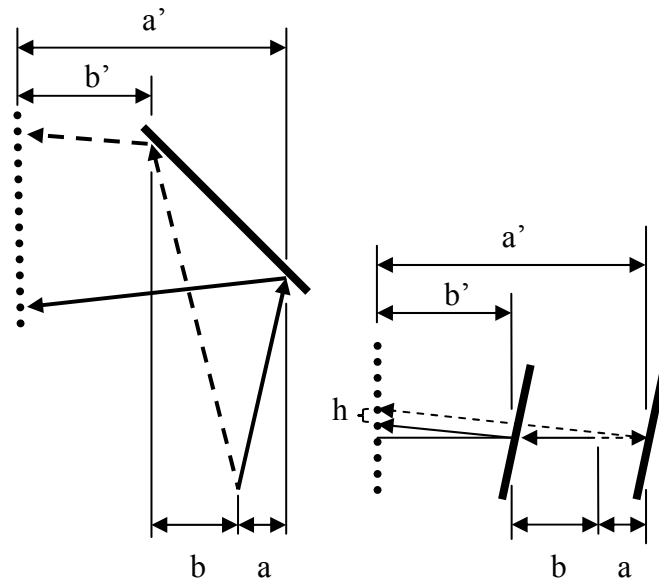


Figure 3-8. Tilt in the Fourier plane produced by a mirror at 45 degrees with a vertical tilt.

The other two possibilities (Figure 3-7(D)-(E)) are very similar. In both cases the tilt of the Fourier plane is minimized either because the reflection angle is zero and only the height is changed (Figure 3-8(D)) or a very small angle is used in the folding mirror (Figure 3-8(E)). The apparatus depicted in Figure 3-7(E) needs a bigger folding mirror than the one observed in Figure 3-7(D). Large good quality mirrors are usually more expensive and difficult to get. For these reasons, we chose the design in Figure 3-7(D) for constructing our experimental setup.

To increase the input power in the pulse shaper, cylindrical optics are preferable to spherical optics. In cases where the output power of the pulse shaper is not critical or is not required, the use of spherical lenses is preferable because they have smaller fabrication aberrations than cylindrical optics. We choose to use spherical mirrors because of the above reasons and because our studies do not need high energy pulses.

Reflective Mode Pulse Shaper

Due to the difficulties in its implementation, only the transmission mode configuration had been successfully realized with liquid crystal mask based pulse shapers. With the recent development of large mirrors (needed for a 64 mm spatial light modulator) the experimental realization of the reflective mode geometry setups is possible. We demonstrate the feasibility of a reflective mode configuration using the new 640 pixels CRI's spatial light modulator. One limitation of the reflective mode geometry is the required separation between input and output beams. Since both beams must travel through the same optics, it is necessary to develop a way to separate the beams. One possibility is to change the height of the input and output beams. As it was mentioned before, this can lead to aberrations on the beam focusing. To minimize beam aberrations and front wave tilt, we have developed a new geometry that uses collinear input/output beams. This innovative geometry uses polarization to separate input and output beams. To our knowledge, it is the first reflective mode collinear phase and amplitude modulator setup constructed to date (Figure 3-9).

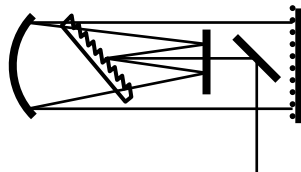


Figure 3-9. Diagram of the experimental setup in a reflective mode configuration.

Our setup presents important advantages over the transmission mode. First, the number of optical components is reduced to half: one spherical mirror, one folding mirror, one back mirror, and one grating. Second, the total phase achieved in our setup is higher than any transmission mode setup because the beam travels twice through each phase mask. Third, the collinear geometry simplifies the alignment reducing the distortions produced by misalignment. Fourth,

there is only one grating angle to align. Last but not least, the footprint size of this setup is half of that observed in a transmission pulse shaper which is a critical constraint for a large mask.

Design Characteristics

In the design of the pulse shaper, the objective is to have the maximum spectral resolution so more complex filters can be produced without significantly cutting the spectrum of the laser pulse. To find what are the best components for constructing the pulse shaper, we will assume that the mask needs to hold at least three times the spectral FWHM maximum of our laser source and that the incident and diffracted angles are the same (Littrow configuration). While fitting three times the spectral FWHM of the laser spectrum warrants that the mask can accept 98.8% of the spectrum, it loses only frequencies with intensities of less than 0.2% of the maximum intensity. The Littrow configuration keeps the diffracted beam centered on the spherical optic, avoiding astigmatism.

Our femtosecond laser source delivers pulses with a temporal duration (FWHM) of 42 fs and a bandwidth of 25 nm (FWHM), thus the necessary spatial dispersion is given by

$$\frac{d\lambda}{dx} = \frac{75\text{nm}}{64\text{mm}} = 1.1 \frac{\text{nm}}{\text{mm}}, \quad (3-33)$$

where 75 nm corresponds to the three spectral FWHM and the 64 mm to the width of the mask.

The grating equation establishes that for Littrow configuration the angle of diffraction is¹¹¹

$$\theta = \arcsin\left(\frac{G \cdot \lambda}{2 \cdot o}\right), \quad (3-34)$$

where G is the groove density in mm^{-1} , λ is the wavelength diffracted, and o is the diffraction order. The linear spatial dispersion in the Fourier plane of the compressor is given by¹⁰⁵

$$\frac{d\lambda}{dx} = \frac{\cos(\theta_d)}{G \cdot f} \quad (3-35)$$

where θ_d is the diffraction angle and f is the focal length of the focusing optic.

The relationship between the grating groove density and the focal length becomes

$$f = \frac{\cos\left(\arcsin\left(\frac{G \cdot \lambda}{2 \cdot o}\right)\right)}{G \cdot \frac{d\lambda}{dx}}. \quad (3-36)$$

An additional important parameter that needs be taken into consideration in this design is the spot size of each wavelength at the Fourier plane. Each wavelength of the pulse spectrum produces an image on the Fourier plane of the compressor. The size of this spot must be similar to the pixel size, neither smaller nor larger. If the spot size of a given wavelength is larger than the pixel size (97 μm), the pulse shaper will lose resolution as each wavelength will be spread over more than one pixel. If the spot size is comparable to the gap between pixels (3 μm) some wavelengths will not be modulated. For a spot size of 40 μm only 7 % of its intensity will not be modulated. It is therefore critical to consider this parameter when choosing the focusing optics. For a Gaussian beam, the spot size at the focus plane as a function of the focal length for a given optic is¹¹⁰

$$\omega_0 = \frac{f \lambda}{\omega_s \pi} \quad (3-37)$$

where ω_s is the waist spot at the focusing optic, f is the focal length, and λ the wavelength.

Both effects, resolution and spot size, must be considered in the design. We find that using the relationship between grating groove density and beam waist versus focal length gives the possible combinations for a grating lens pair.

For a Gaussian input beam with 3 mm beam diameter a beam waist size from 40 to 70 μm is produced with a focal length of 200 to 400 cm (see Figure 3-10). The corresponding grating groove density necessary to keep the spatial dispersion close to 1.1 nm/mm is between 1750 and

2100 mm⁻¹. A combination of grating lens in that range is suitable for building a high resolution pulse compressor.

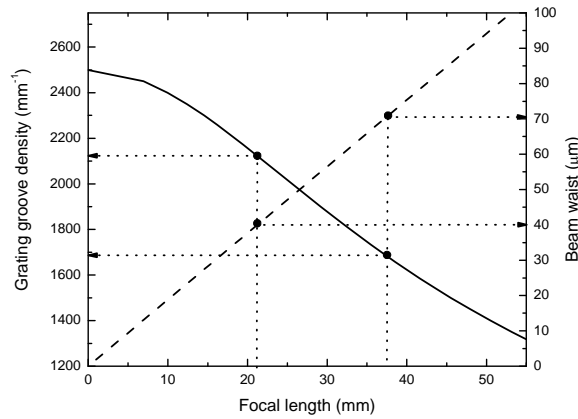


Figure 3-10. Grating groove density and beam waist versus focal length. Grating groove density effect (solid line). Beam waist effect (dashed line).

In our designed, we selected a grating of 1800 mm⁻¹ groove density in combination with a focusing optic of 300 mm. The selection took into consideration the commercial availability of the parts. The summary of the theoretical pulse shaper characteristics for this configuration is presented in Table 3-1.

Table 3-1. Theoretical zero dispersion compressor characteristics.

Parameter	Value
Grating groove density	1800 mm ⁻¹
Grating Littrow angle	46.05 degrees
Mirror focus	300 mm
Theoretical spatial dispersion	1.285 nm/mm
Theoretical spectral window accepted by the SLM	82.24 nm
Raleigh length	32 mm
Beam waist	56.6 μm

Reflective Mode Experimental Realization

Our reflective mode phase and amplitude pulse shaper is presented in Figures 3-11 and 3-12. To obtain phase modulation in the frequency domain the optical setup is arranged in a folded zero dispersion compressor (Figure 3-11). This type of configuration reduces the setup size by half.

In our folded configuration, the zero dispersion compressor is composed of: a gold spherical mirror (Edmund Optics, $f=300$ mm), one folding gold mirror (half of a two inch diameter mirror, CVI Inc), one inch diameter gold steering mirror, one gold-coated holographic grating (Richardson Gratings, 1800 groves/mm 30x30 mm), and the mask back mirror (CRI Inc.).

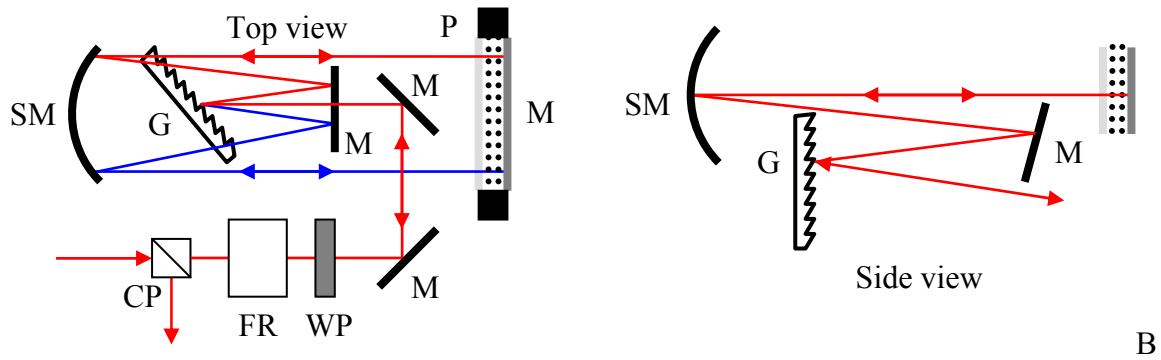


Figure 3-11. Top and side views of the built pulse shaper. SM: spherical mirror; G: grating, M: mirror; P: polarizer; WP: $\lambda/2$ waveplate; FR: Faraday rotator, CP: cube polarizer.

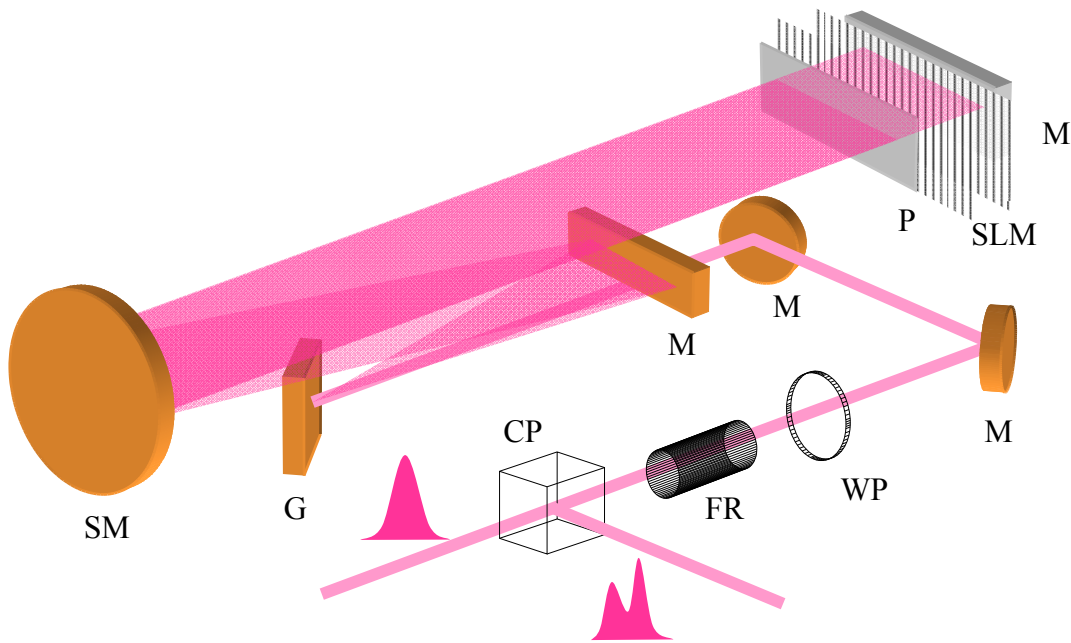


Figure 3-12. 3D Sketch of the built pulse shaper. SM: spherical mirror; G: grating, M: mirror; P: polarizer; WP: half waveplate; FR: Faraday rotator, CP: cube polarizer.

This optical configuration provides a spectral resolution of 0.129 nm per pixel with a bandwidth window of approximately 83 nm (see wavelength calibration section). All the compressor elements are arranged in a line with the beam traveling slightly out of the plane parallel to the optical table to avoid spatial distortions in the mask (Figure 3-11, side view). While the folding mirror is mounted on a standard mirror mount, the rest of the components are mounted on special custom-made mounts to meet the necessary degrees of freedom (see alignment procedure, Appendix A).

A critical component of our apparatus is its collinear optical path. This configuration requires a polarization method to separate the unmodulated (incoming) from the modulated (outgoing) pulse. Based on the same principle of pulsed regenerative amplifier cavities, the experimental arrangement uses a cube polarizer (Optics for Research, PH-8), a Faraday rotator (Electro-Optics Technology, BB8-8R), and a $\lambda/2$ waveplate (Karl Lambrecht, MWPA2-22-HEAR800) (Figure 3-13). The cube polarizer acts as a polarization beam splitter, the Faraday rotator as a cumulative retarder, and the $\lambda/2$ waveplate as a polarization corrector.

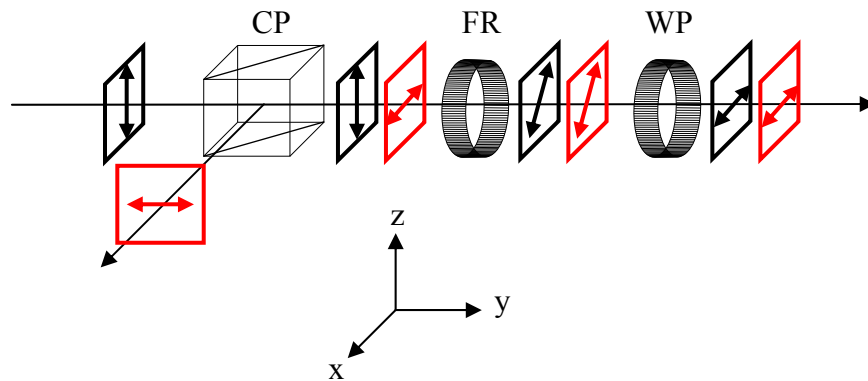


Figure 3-13. Polarization splitting of the incoming and the outgoing pulse. Incoming and outgoing polarizations are represented with a black and red arrow, respectively.

Its operation can be described as follows: the incoming beam (black arrow, +90 degrees) crosses the Faraday rotator and its polarization is tilted by +45 degrees. Since the waveplate

produces the same effect over the pulse as the Faraday rotator, the electric field accumulates +45 degrees yielding an electric field with a 0 degree orientation inside the pulse shaper. The outgoing beam (gray arrow, +0 degree) crosses the waveplate and its polarization changes to +45 degrees. However, when the pulse propagates through the Faraday rotator the polarization changes -45 degrees to 0 degrees and the cube polarizer splits the different polarization, separating the incoming (unmodulated, 90 degree polarization) from the outgoing (modulated, 0 degree polarization) beam.

This arrangement allows a collinear path, simplifies the alignment procedure, minimizes temporal dispersions, and provides a very compact and less expensive setup instead of the large setup usually used in high-resolution pulse shapers.

Our dual mask system has a high average transmission (>94%). Our setup is configured to produce amplitude and phase modulation using an entrance polarizer (transmission <80% from 750 to 850nm) and a returning mirror (transmission <95%). Due to the double pass, these components reduce the overall transmission to less than 55 %.

The overall pulse shaper transmission is 30%, which is mainly determined by all the polarization optics and the efficiency of the grating.

Pulse Shaper Phase Calibration

The spatial light modulator should be placed at the Fourier plane of the $4f$ compressor to modify the temporal and spectral characteristics of the incident pulse. The phase control in the modulator is obtained by changing the applied voltage to each pixel in the individual mask. Before an experiment, a calibration of the pixel response using applied voltage must be performed to control precisely the phase imposed by each pixel.

The index of refraction of the liquid crystal is voltage and wavelength dependent. A pixel by pixel calibration can take too long to be performed as a daily routine, since there are 1280

(640 in each mask) independent pixels. Instead, all pixels of each mask of the spatial light modulator are calibrated simultaneously with the corresponding wavelength by measuring the spectrum of the modulated pulse with a spectrometer, greatly reducing the time of the phase calibration and avoiding the individual pixel by pixel calibrations.

The phase introduced by a change in the applied voltage is given by Equation 3-18. Assuming that the dependence on wavelength and voltage can be treated independently, the change of refractive index can be written as

$$\Delta n(\lambda, V) = \Delta n(\lambda, 0) \cdot f(V), \quad (3-38)$$

where the first term ($\Delta n(\lambda, 0)$) represents the change in the index of refraction as a function of wavelength alone and the second term ($f(V)$) models the voltage response for a liquid crystal pixel. If the mask pixel inhomogeneity is negligible, a calibration of one pixel as a function of wavelength can be used to extrapolate to the rest of the pixels in the array. The change of the refraction index as a function of wavelength can be calculated from the corresponding ordinary and extraordinary index of refraction (Equation 3-20).

While characterizing the spatial light modulator we found that the pixels in both masks are not truly uniform. From one pixel to the next there are changes on their refractive index even for the same wavelength when no voltage is applied. This complicates the calibration of our spatial light modulator. The same model (Equation 3-38) can be used to calibrate the birefringence of the mask, considering that $\Delta n(\lambda, 0)$ is an effective refraction index. To achieve the spatial light modulator calibration a spectrometer is set at the output of the pulse shaper and the whole spectrum of the beam is measured after passing through the masks. This calibration not only includes the wavelength dependence of the refractive index, but also takes into consideration the pixel inhomogeneity. The calibration setup is depicted in Figure 3-15.

To perform the calibration a home written program in Labview (National Instrument TM) is used. This program measures the output pulse spectrum while the voltage of one of the masks is varied every 10 bit (2.5 mV) and the other mask voltage is kept constant at the value of maximum transmission.

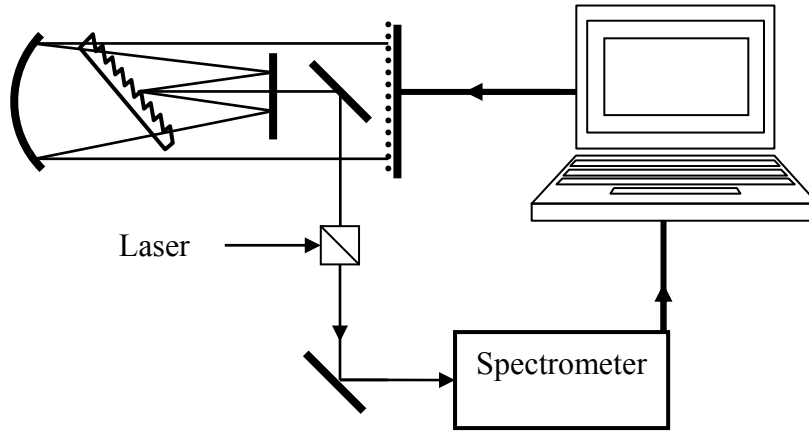


Figure 3-15. Experimental setup used for the masks calibration.

When the spectrum is measured, only the real part of the spectral filter response is measured:

$$S_{out}(\lambda) = S_{in}(\lambda) \cdot T^2(\lambda), \quad (3-39)$$

where $T(\lambda)$ is the real part of the filter response function (Equations 3-7 and 3-30).

Under these conditions, the transmission $A(\lambda)$ is

$$A(\lambda) = T^2(\lambda) = \frac{S_{out}(\lambda)}{S_{in}(\lambda)}, \quad (3-40)$$

and the difference in phase applied by the mask is

$$\Delta\phi_{LC1} - \Delta\phi_{LC2} = 2 \arccos(\sqrt{T(\lambda)}). \quad (3-41)$$

Since only one mask is modulated during the phase calibration, the phase produced by the this mask is

$$\Delta\phi_{LCi} = 2 \arccos\left(\sqrt{T(\lambda)}\right) + \Delta\phi_{LCj}^{\max}, \quad (3-42)$$

where $\Delta\phi_{LCi}$ is the change in phase produced at each wavelength of the spectrum for a given voltage, and $\Delta\phi_{LCj}^{\max}$ is a phase constant. This phase constant will be discarded by setting the phase of the calibrated mask at zero when the voltage applied is 10 V.

The phase curve for each wavelength is calculated using Equation 3-42. The calibration results are shown in Figures 3-16 and 3-17.

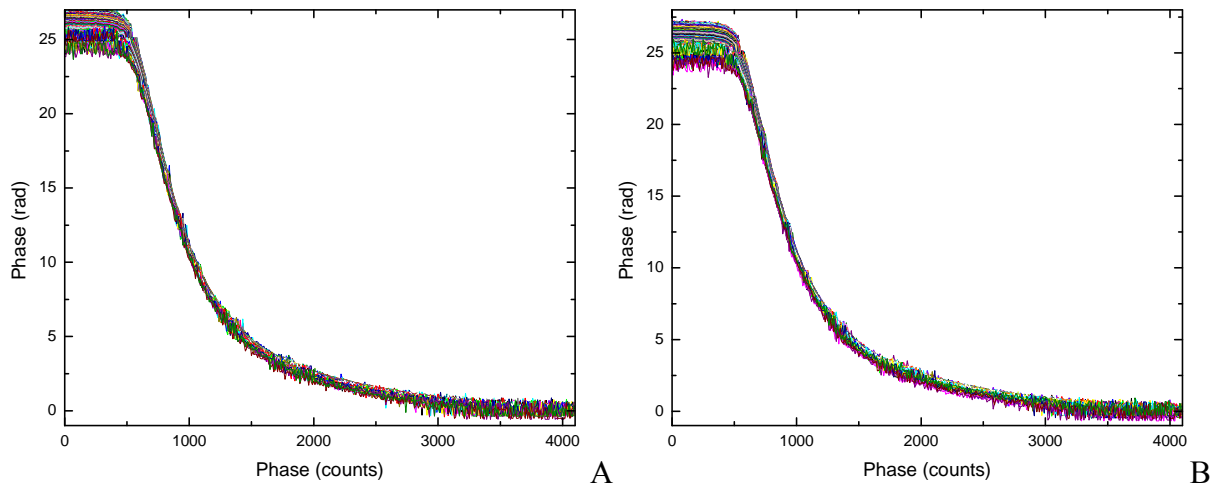


Figure 3-16. Phase calibration curves of: A) front mask and B) back mask.

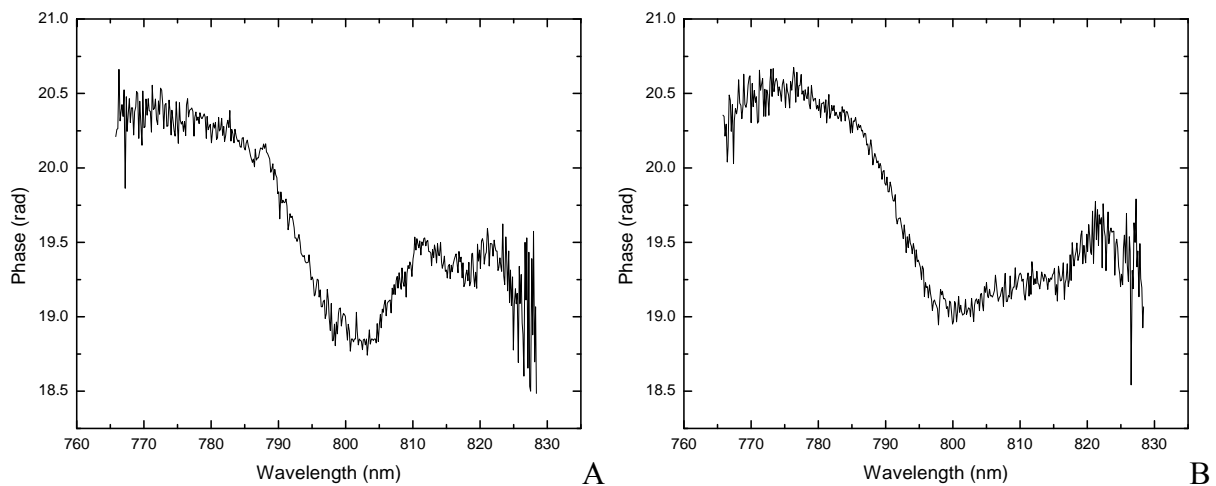


Figure 3-17. Phase at 700 counts (1.71 V) for: A) front mask and B) back mask.

Since the phases corresponding to different wavelengths at a given voltage do not follow the expected Sellmeirs' refractive index behavior (Figure 3-17), the phase values for each curve at 700 counts (1.71 V) are normalized with respect to the phase of 799.666 nm and used as a correction factor for the phase curves. The phase at 799.666 nm is used as the only phase calibration curve and its phase correction factor is used to correct the deviation to the calibration curve of other pixels due to pixel inhomogeneity and wavelength index of refraction dependence.

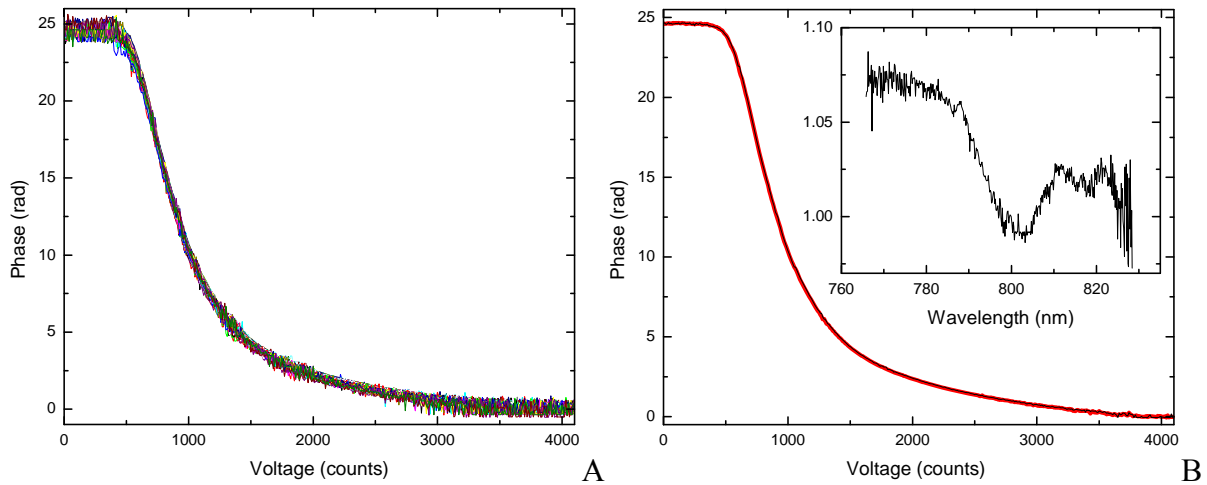


Figure 3-18. Phase calibration of front mask. A) Corrected curves. B) Comparison between the average of all the curves and calibration curve at 799.66nm (inset: correction factor).

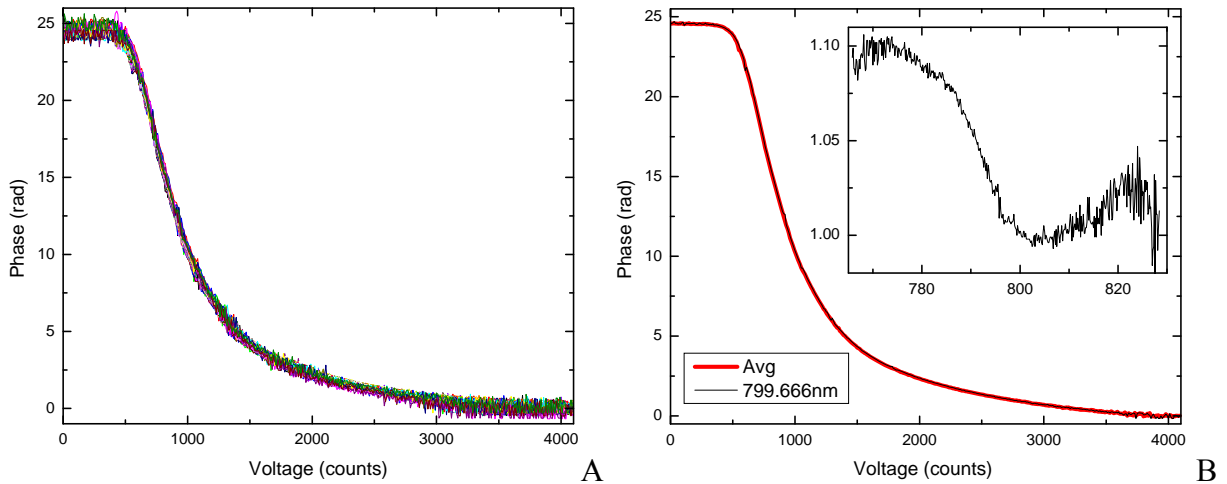


Figure 3-19. Phase calibration of back mask. A) Corrected curves. B) Comparison between average of all the curves and calibration curve at 799.66nm (inset: correction factor).

The corrected phase calibration shows a maximum retardation of 8π (25 radians) for both masks. The maximum dynamic range for a 2π modulation is produced between 1250 and 4095 driver counts (corresponding to 2.5 V and 10 V, respectively). The wavelength correction factor does not show the expected dependence for the index of refraction versus wavelength (Sellmeier's equation). This difference can be attributed to the inherent inhomogeneity of the mask. The maximum change in the retardation for a 1.71 V (700 counts) observed on either mask is on the order of 10 % with respect to the normalization wavelength (center wavelength, 799.666 nm). The inhomogeneity of the mask has enormous consequences on the performance of the pulse shaper setup because it imposes a residual phase on the input pulse which reduces the dynamic range of the spatial light modulator. In addition, this residual phase must be compensated to produce transform limited pulses and to relate the output pulse modulation of an arbitrary pulse to the applied voltage.

Pulse Shaper Wavelength Dispersion Calibration

A wavelength calibration of the spatial light modulator must be performed to assign the wavelength correction factor to each pixel. The way to produce this calibration is similar to the voltage calibration, but in this case instead of varying the voltage of both masks, the pulse shaper is set to produce amplitude modulation. By imposing in some pixels of the first mask a retardation of π and leaving the other entire mask at a retardation of 0 radians (10 V), holes will be observed in the spectrum of the output pulse. Since the position of the pixels with π phase is known, the holes in the spectrum are directly assigned to them.

The wavelength versus pixel calibration curve is

$$\lambda(p) = \lambda_0 + p \cdot \frac{d\lambda}{dp} , \quad (3-43)$$

where the observed experimental values are: $\lambda_0 = 843.36$ nm and $d\lambda/dp = -0.12896$ nm/pixel.

Since the pixel size is 100 μm , the spatial dispersion in the Fourier plane is 1.29 nm/mm which agrees with the theoretical spatial dispersion for this zero dispersion compressor apparatus (Table 3-1).

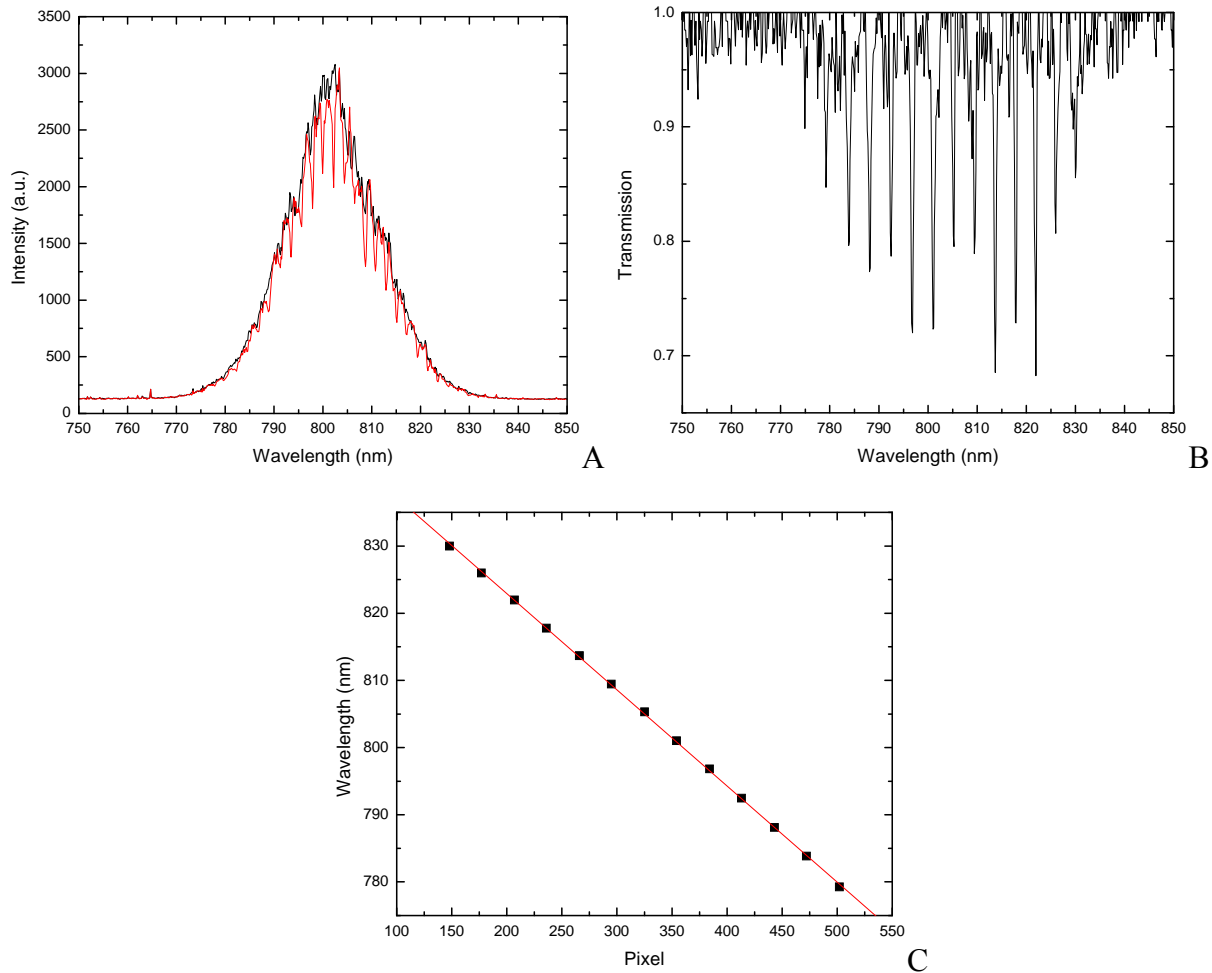


Figure 3-20. Dispersion calibration. A) Unmodulated and modulated spectra (red and black lines, respectively). B) Transmission produced by holes in the profile. C) Wavelength calibration curve.

Residual Phase

The pixel inhomogeneity in each mask produces a residual phase in the modulator. This background phase is amplified in our double pass implementation of a reflective mode configuration setup. To observe, characterize, and correct this effect, the zero dispersion

compressor was modified by replacing the spatial light modulator back mirror with an external, independent mirror (Figure 3-21). The effect produced by putting the double mask in the zero dispersion compressor could be observed with this modified configuration. The modulator's residual phase was measured by collecting the pulse autocorrelation with and without the mask.

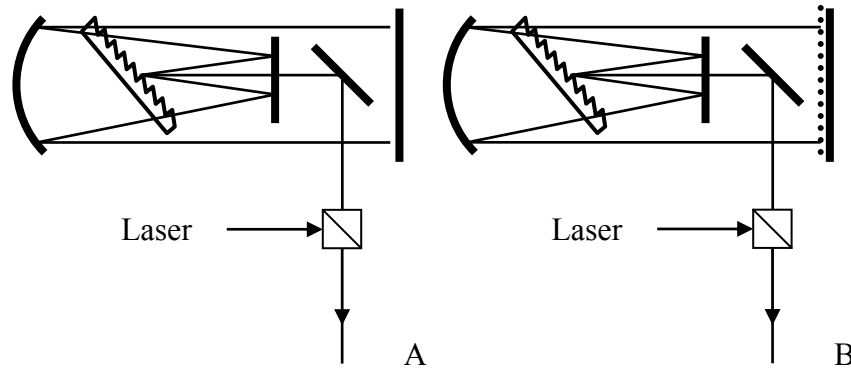


Figure 3-21. Pulse shaper setup using an external mirror. A) Without the spatial light modulator. B) With the spatial light modulator.

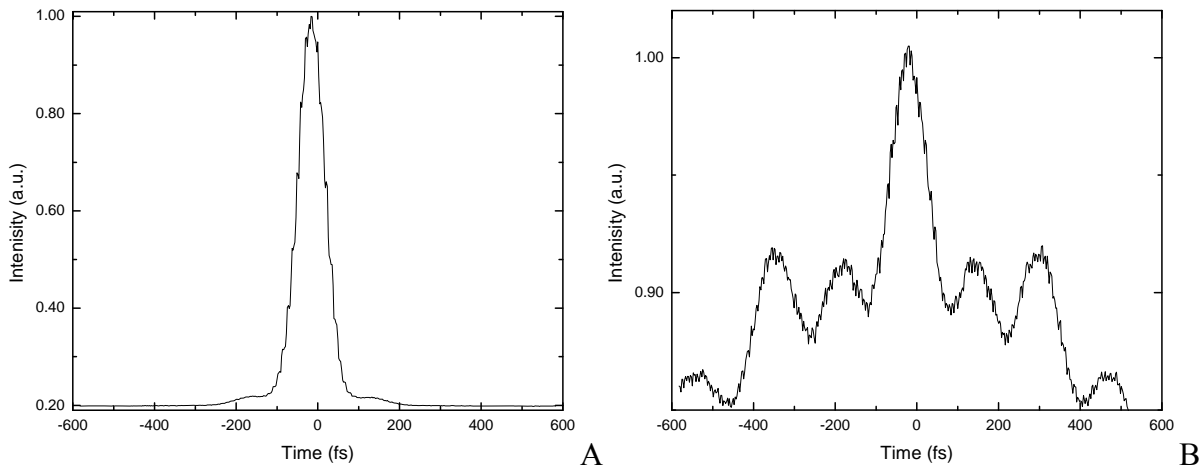


Figure 3-22. Phase mask effect on the temporal profile of the pulse for A) Zero dispersion compressor without the spatial light modulator in place. B) Zero dispersion compressor with the spatial light modulator in place.

Figure 3-22 shows that the spatial light modulator has an important residual phase that should be compensated to modulate pulses. One way to compensate for this residual phase is by measuring the phase of the output pulse and imposing the same phase, but with opposite sign on the pulse shaper.

We use multishot SHG-FROG and commercially available software (Femtosoft FROG 3.2) to retrieve the phase out of the generated FROG trace.

Figure 3-23 shows the SHG-FROG trace measured for the output pulse shaper pulse with no phase applied. The retrieved trace of this pulse presents a good agreement with the experimental SHG-FROG trace (Figure 3-23(A) and (B)). From the retrieved electric field we can extract the phase needed to achieve the residual phase correction in the spatial light modulator. Knowing the phase needed to generate a transform limited pulse, we use the previous calibration to generate the voltages required at each pixel. After applying the phase opposite in sign to the one measured, we collect the SHG-FROG traces again (Figure 3-24).

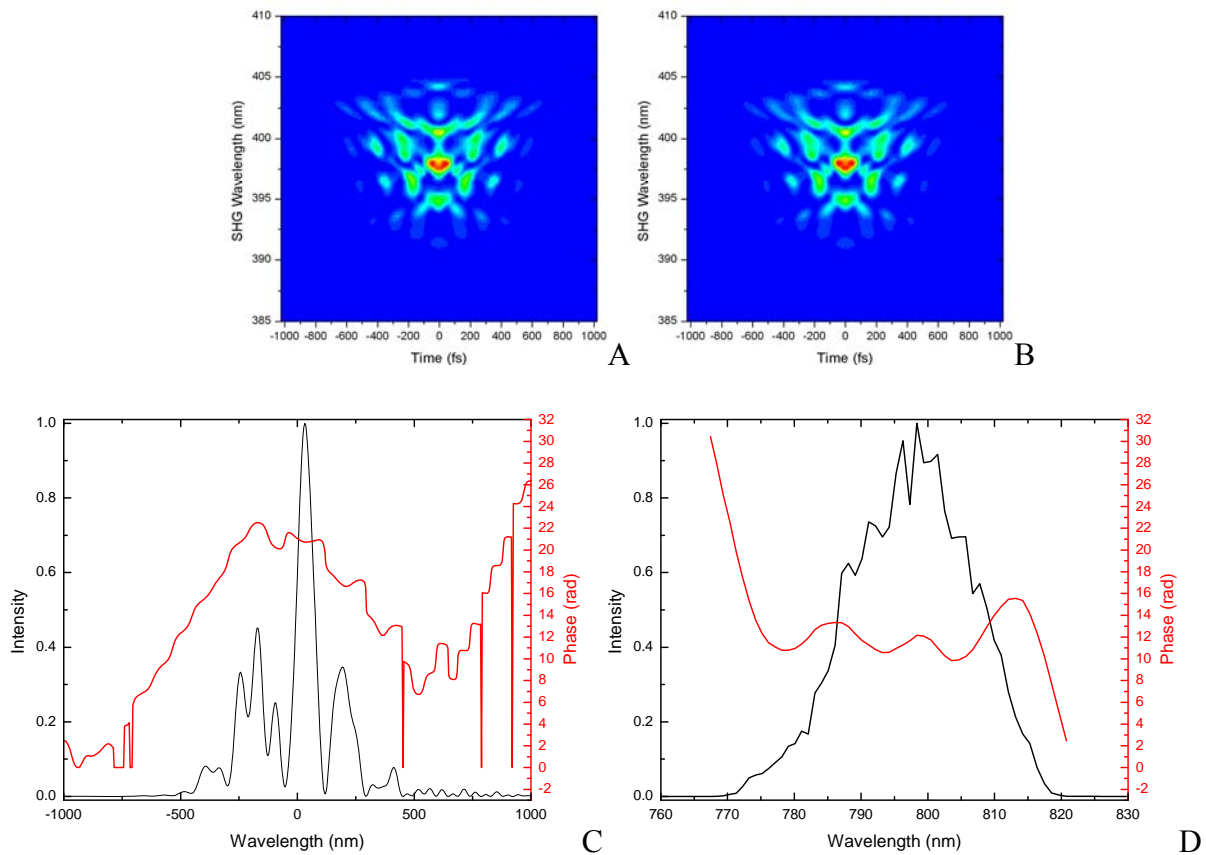


Figure 3-23. SHG-FROG trace of the unmodulated pulse. A) Experimental trace. B) Retrieved trace. C) Temporal intensity (black line) and phase (red line). D) Spectral intensity (black line) and phase (red line).

Figure 3-24 shows that the phase can be successfully reduced from 20 radians to less than 1 radian by applying the opposite phase in the pulse shaper. The new SHG-FROG trace and the retrieved electric field show pulses very close to the transform limited pulse with an almost flat phase across the spectrum.

The lack of zero residual phase in the corrected pulse is a product of the phase determination via FROG. To improve this phase retrieval a technique like MIIPS can be used.¹¹⁸ This technique has been shown to produce transform limited pulses with a phase error of less than 0.01 rad. The other possibility is to compress the pulse with a closed loop optimization. Implementation of this technique will be shown in the following chapter.

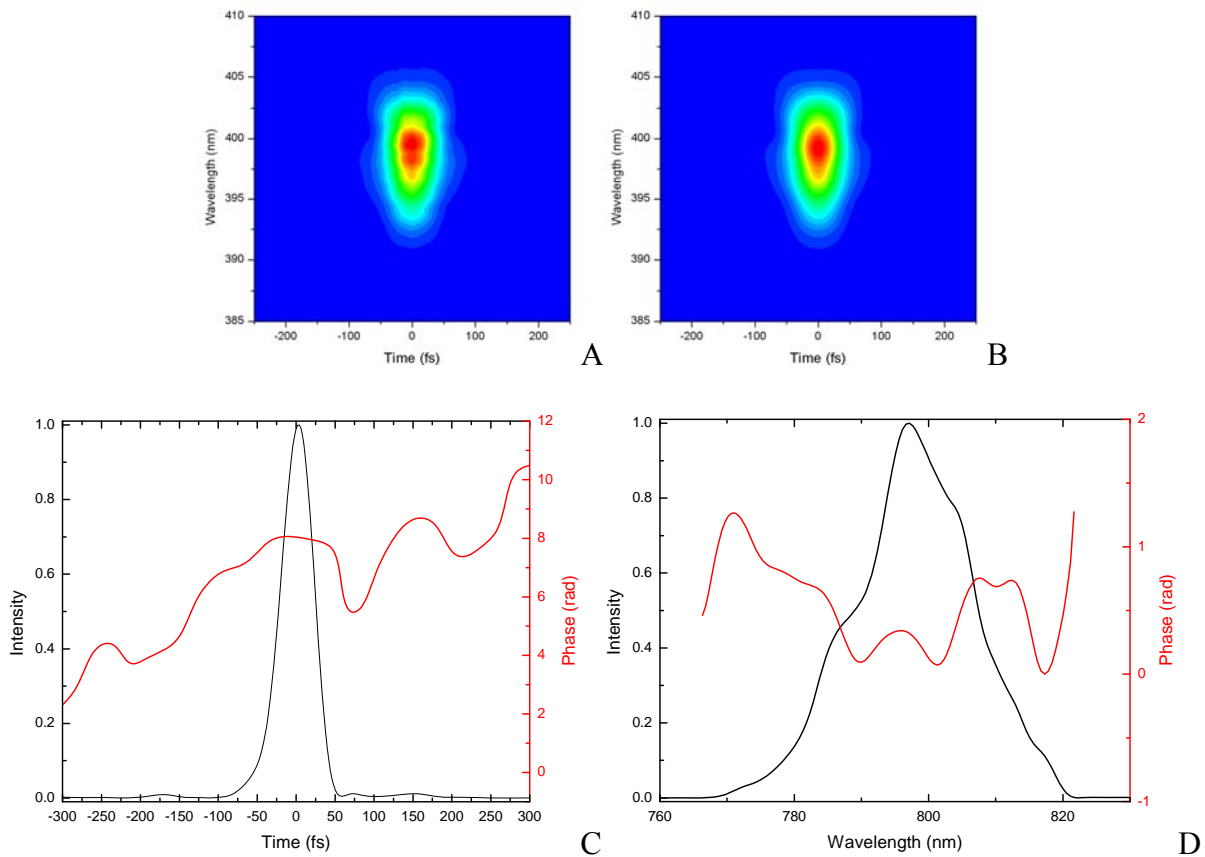


Figure 3-24. SHG-FROG trace of the phase corrected pulse. A) Experimental trace. B) Retrieved trace. C) Temporal intensity (black line) and phase (red line). D) Spectral intensity (black line) and phase (red line).

Frequency Nonlinearity Correction

For the sake of simplicity, a linear change of frequency from one pixel to the next is assumed in the pulse shapers (Figure 3-26, dotted line). For non-complex pulses, this assumption works well. However, when the output phase modulated pulses are very complicated, this assumption fails and leads to spatio-temporal distortions which deviate the results from the theoretical prediction. Figure 3-25(A) show the SHG-FROG trace of a sequence of pulses generated by applying a sine function to the spectral phase. This type of modulation creates equispaced subpulses. The SHG-FROG trace in panel A shows an additional distortion with tilted traces that are also broader in time (phase modulated).

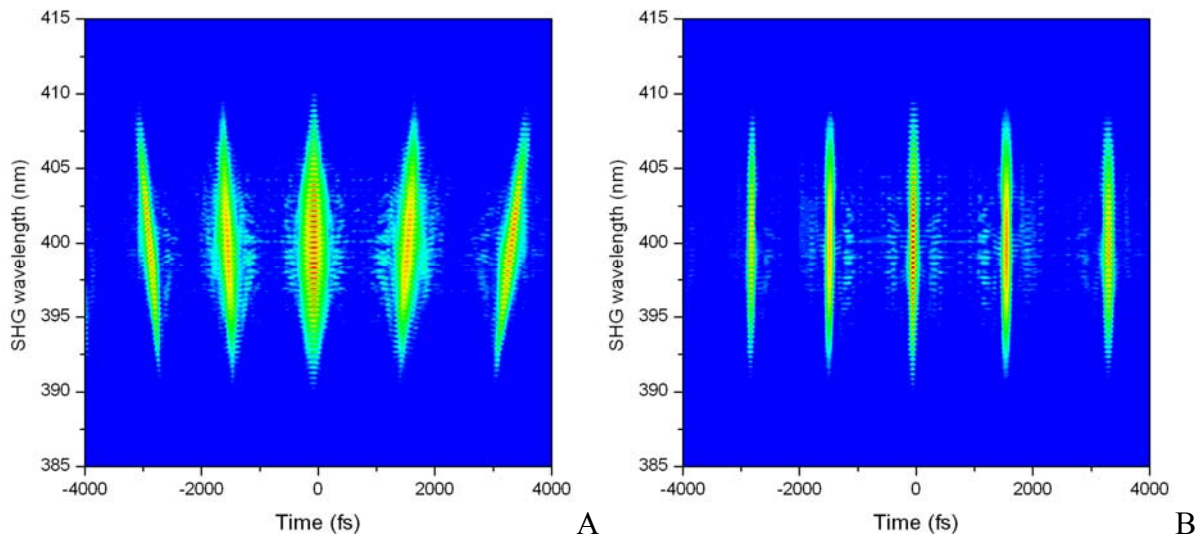


Figure 3-25. Effect of the nonlinear frequency calibration in the pulse modulation. A) Sinusoidal phase pulse without frequency nonlinear correction. B) Sinusoidal phase pulse with nonlinear frequency correction.

The pixel versus frequency plot presented in Figure 3-26 shows a small non-linearity that needs to be taken into account. The periodicity in time is no longer constant for all the frequencies, and the output pulse presents broader replica pulses with more time delay.

When this correction is accounted for and the pulses are codified linearly in frequency, the same modulated pulse does not present any distortions on its replica pulses. This can be observed in Figure 3-25(B) where all the replicas are narrower and the tilt is removed.

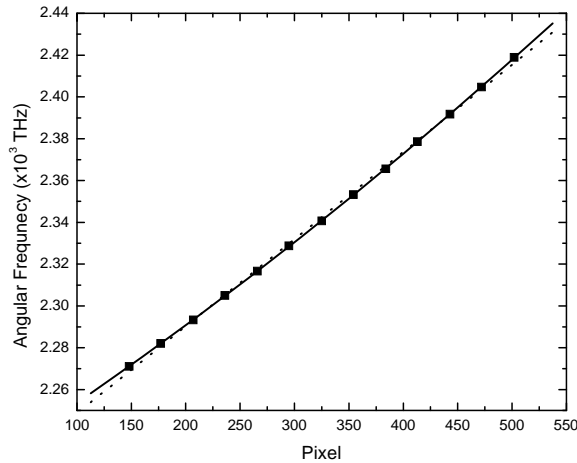


Figure 3-26. Frequency calibration curve of the pulse shaper. Dots experimental points, dotted line linear fit, a solid line: second order polynomial fit.

Modulation Examples

Finally, we chose some masking operations using amplitude and phase modulation to check the performance of our experimental setup. An example of a pulse with π step phase modulation is presented in Figure 3-27.

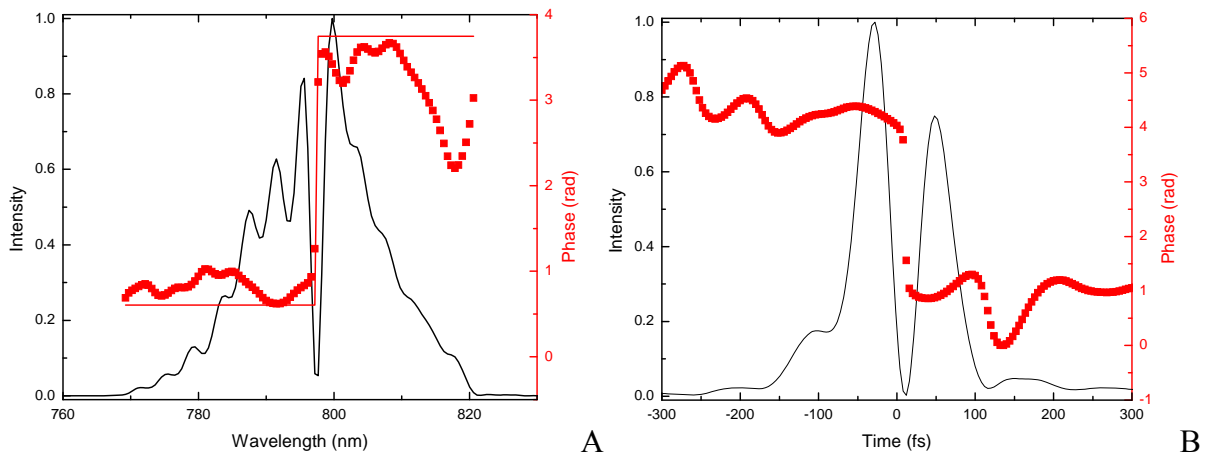


Figure 3-27. Odd pulse (π step). A) Spectral intensity (black line), retrieved phase (red squares), and target phase (red line). B) Temporal intensity (black line) and phase (red squares).

In Figure 3-27, red squares correspond to the experimental results, whereas the red line is the proposed target phase. In all cases, the calculated waveforms agree with the experimental pulses. Nevertheless, the difference between the analytical waveform and the experimental results shows some temporal pulse distortions. This difference can be attributed to uncertainties in the compensation of the residual phase in our modulator and/or mask calibration errors.

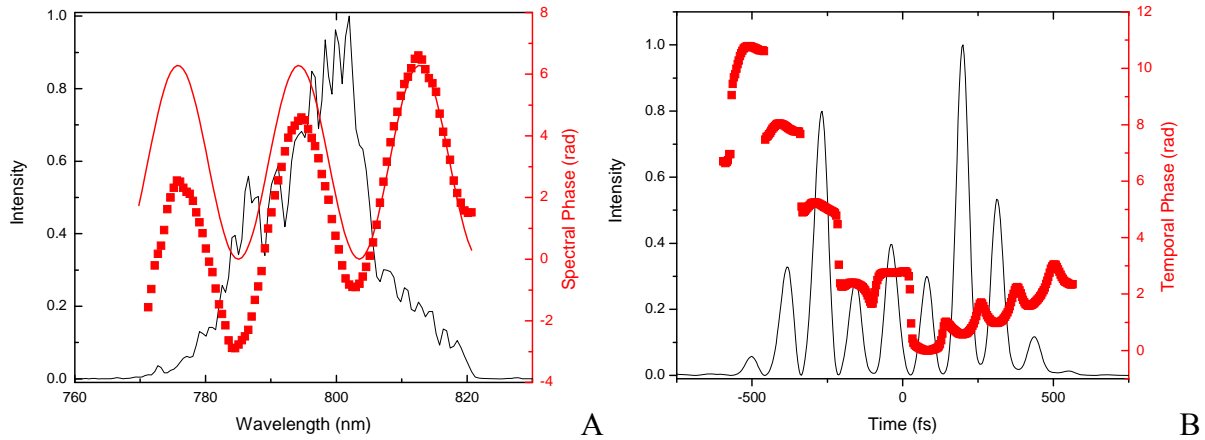


Figure 3-28. Sinusoidal phase modulation. A) Spectral intensity (black line) retrieved phase (red squares), and target phase (red line). B) Temporal intensity (black line) and phase (red squares).

Other examples using only phase modulation were successfully implemented: sinusoidal spectral phase pulse, quadratic phase pulse, and zero phase double pulse.

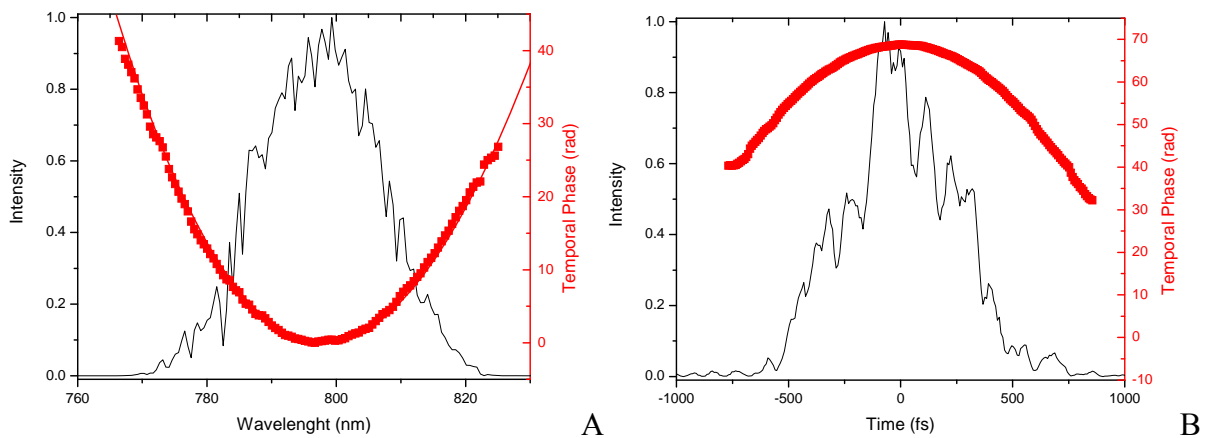


Figure 3-29. Quadratic phase pulse (4607 fs^2). A) Proposed phase (red line), and retrieved spectral intensity (black line) and phase (red squares). B) Temporal intensity (black line) and phase (red line).

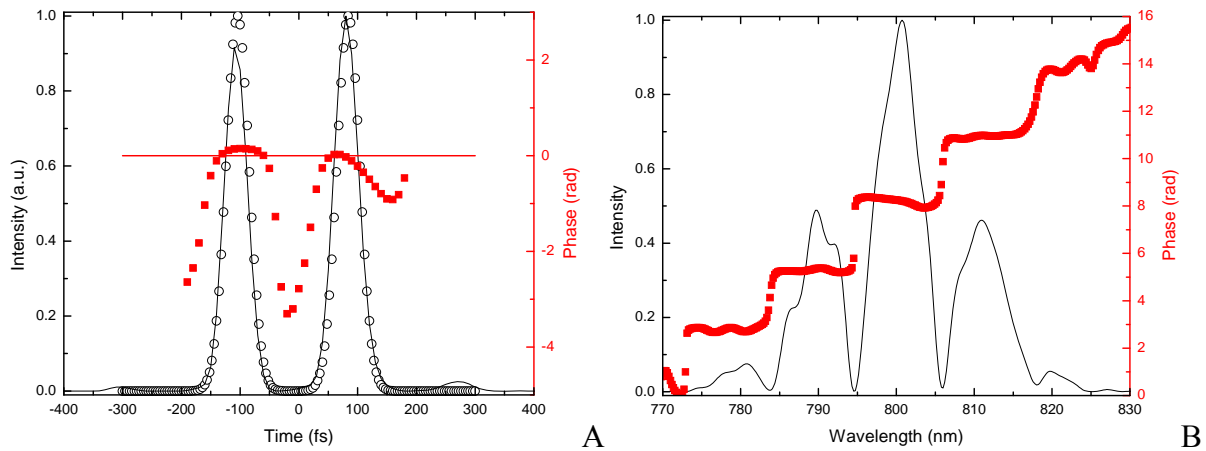


Figure 3-30. Temporal double pulse with a 200 fs separation. A) Proposed temporal intensity (open circles) and phase (red line), retrieved temporal intensity (black line) and phase (red line). B) Spectral intensity (black line) and phase (red line).

Spatial Light Modulation Limitations

The physical limit of the maximum phase modulation of the spatial light modulator is given by the thickness of the liquid crystal used in the mask (Equation 3-18). In our pulse shaper, this limit is ~ 25 radians (see phase calibration curves, Figures 3-16 and 3-17). To overcome this physical limitation, phase wrapping is used. Due to the definition of phase, it is possible to arbitrarily add or subtract any multiple of 2π without physically affecting its value (phase wrapping). An example of phase wrapping is presented in Figure 3-31.

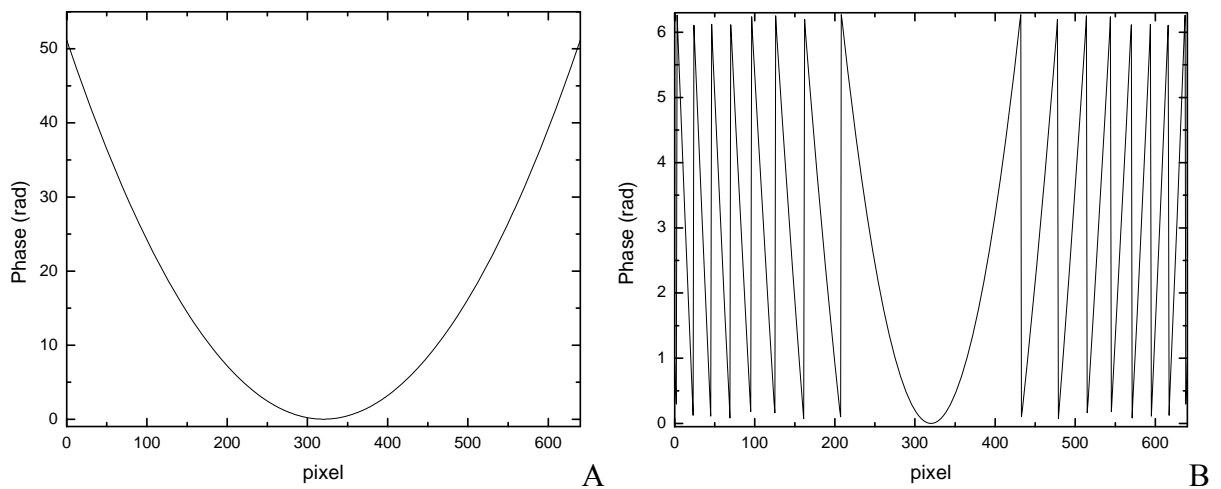


Figure 3-31. A) Phase unwrapped. B) Phase wrapped.

Figure 3-31(A) shows phase values that cannot be achieved with our pulse shaper. Using the phase wrapping treatment, the new phase (Figure 3-31(B)) is physically equivalent to the unwrapped phase (Figure 3-31(A)) which then can be applied with our pulse shaper because its values do not pass the pulse shaper phase limits. Phase wrapping solves the limited dynamic range produced by birefringent materials utilized in spatial light modulators.

Another limitation of the spatial light modulator is given by the discrete nature of the spatial light modulator masks. This constrains the accessible phase modulations to the Nyquist's limit. The Nyquist theorem states:¹¹⁹

“If a function $f(t)$ contains no frequencies higher than W cycles per second, it is completely determined by giving its ordinates at a series of points spaced $1/(2W)$ seconds apart”

This theorem implies that the sampling must be made twice per period, or twice in the working phase interval. Since the phase working interval for the spatial light modulator is from 0 to 2π , the maximum change phase that can be produced without aliasing is

$$\Delta\phi < \pi \tag{3-44}$$

An example of the aliasing effect is presented in Figure 3-32.

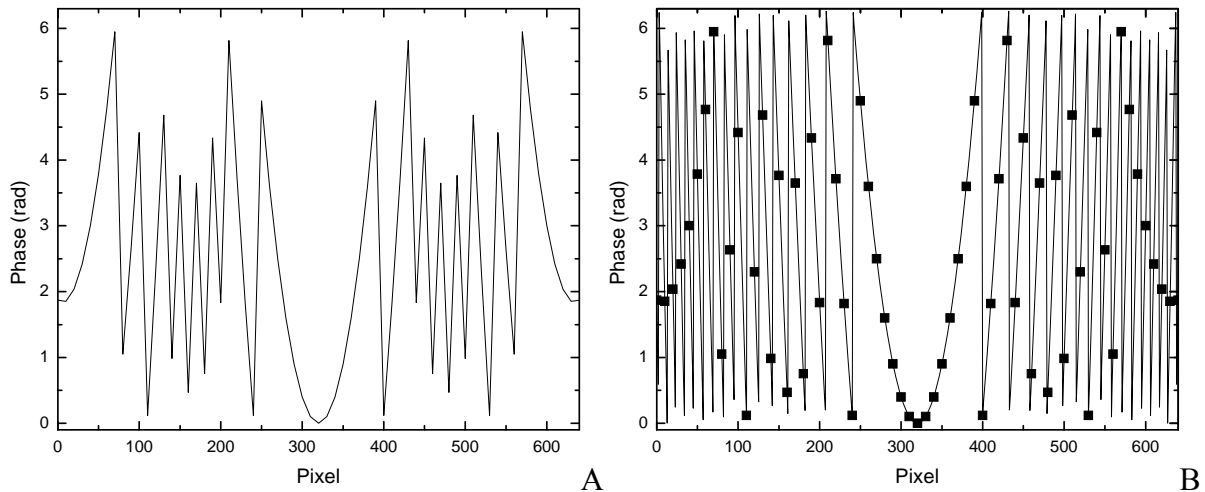


Figure 3-32. Quadratic phase of 10^{-3} pixel²/rad A) Sampled every 10 pixels B) Sample every 10 pixels (black squares) and every pixel (black line).

Figure 3-32(A) shows that for a sampling of 10 pixels a quadratic phase of 10^{-3} pixel²/rad starts to be undefined below the pixel 200 and above the pixel 440. A comparison with the phase sampled at every pixel (Figure 3-32(B) black line) reveals that outside the 200-440 pixel range only one point is used for defining the phase within each 2π phase interval, producing aliasing on the phase.

Using the limits imposed by the Nyquist limit, it is possible to calculate the maximum phase coefficients that can be applied if the phase is codified using a Taylor expansion. The different terms of a Taylor expansion of the phase in the frequency are

$$\phi_n^{(i)} = \frac{b_i}{i!} \cdot (\omega - \omega_0)^i, \quad (3-45)$$

where ω is the frequency, ω_0 is the frequency at the center of the array, and i is the Taylor polynomial order. Using the frequency calibration of the pulse shaper at each pixel the Taylor coefficients are expressed in terms of the discrete pixel number

$$\phi_n^{(i)} = \frac{b_i \cdot \Delta\omega^i}{i!} \cdot \left(n - \frac{N}{2}\right)^i, \quad (3-46)$$

where $\Delta\omega$ is the linear frequency change in each pixel, n is the pixel number, and N is the total number of pixels (640 in our spatial light modulator). The phase difference between two consecutive pixels is

$$\Delta\phi_n^{(i)} = \phi_{n+1}^{(i)} - \phi_n^{(i)} = \frac{b_i \cdot \Delta\omega^i}{i!} \cdot \left[\left(n+1 - \frac{N}{2}\right)^i - \left(n - \frac{N}{2}\right)^i \right]. \quad (3-47)$$

For the linear coefficient of the expansion, the Nyquist limited coefficient is

$$\Delta\phi_{\max}^{(1)} = \pi = b_1^{\max} \cdot \Delta\omega, \quad (3-48)$$

where

$$b_1^{\max} = \frac{\pi}{\Delta\omega} = \frac{\lambda_0^2}{2c \cdot \Delta\lambda}. \quad (3-49)$$

Similarly the second order phase coefficient is

$$\Delta\phi_{\max}^{(2)} = \pi = \frac{b_2^{\max}}{2} \cdot \Delta\omega^2 \cdot (2n-1-N). \quad (3-50)$$

Since discrete polynomial functions present their maximum changes for the highest values of the independent variable, the maximum difference will be obtained for pixels N and $N-1$, thus the Nyquist limited coefficient is

$$\Delta\phi_{\max}^{(2)} = \pi = \frac{b_2^{\max}}{2} \cdot \Delta\omega^2 \cdot (N-1), \quad (3-51)$$

$$b_2^{\max} = \frac{2\pi}{\Delta\omega^2 (N-1)} = \frac{\lambda_0^4}{2c^2 \cdot \pi \cdot \Delta\lambda^2 (N-1)}. \quad (3-52)$$

All the other Nyquist limited coefficients can be calculated in a similar manner. The calculated Nyquist's limits for the linear and quadratic phase for our setup configuration parameters (Table 1) are ± 8269 fs and ± 68010 fs², respectively. By applying a linear phase to the incident pulse, pulses are shifted in time (see Chapter 2). Within the Nyquist's limit of ~ 8 ps the linear modulations will not distort the original pulse structure. This limit constrains the modulator to an effective delay range of 16 ps (± 8 ps) with a resolution of 18 fs (minimum slope created by changing the minimum phase step in our phase modulator). This time resolution (18 fs or 5.4 μ m) is comparable with the time step resolution of any commercially available stepper motor translation stage used for optical delay lines. As a result, the pulse shaper can be used as a delay generator for pump and/or probe experiments with the capabilities of phase and amplitude modulation of its pump pulse.

In addition, the Nyquist's theoretical predictions state that the designed pulse shaping apparatus can stretch pulses from 42 fs (FWHM) to close to 4.5ps (maximum quadratic phase possible) without producing any measurable distortion.

The Nyquist theoretical limits in our pulse shaper apparatus are constrained by the residual phase of the mask, thus the real Nyquist limits must be calculated numerically including this residual phase term.

Summary

We have constructed a state of the art pulse shaper with many important improvements with respect to literature implementations. Among those improvements, it is important to highlight its small footprint and easy alignment achieved without compromising its high resolution. In the following chapters this apparatus coupled to a genetic algorithm is used for scientifically relevant problems.

CHAPTER 4 CLOSED LOOP OPTIMIZATIONS AND GENETIC ALGORITHMS

Introduction

Femtosecond laser pulse shaping has been shown to be the most promising technique to produce quantum control because it can create electric fields capable of affecting the molecular excited state wave packets during their evolution in their molecular potential energy surfaces.^{2,}

120

Since molecular evolution is governed by the system Hamiltonian, the possibility of knowing which laser field parameters can control a certain molecular system is very limited for all but few very simple systems. In particular for strongly coupled systems, such as large molecules in condensed phase, the complete Hamiltonian is either unknown or too complicated to use for electric field calculations. Researchers have been using optimal control experiments to control photoinduced processes without prior knowledge of the molecular quantum properties.

First proposed by Judson and Rabitz, optimal control involves an iterative closed loop optimization with feedback signals arising from the molecular process to be controlled (see chapter 1).²⁶ Ideally, closed loop optimization will optimize the electric field without requiring any prior knowledge of the molecular system, requiring only a measurable signal from the desired photoproduct. Closed loop optimizations require an optimization algorithm capable of optimizing many independent variables simultaneously. This algorithm should be able to find the optimum solution in surfaces with many different local optima and in the presence of experimental noise. Genetic algorithms can fulfill these requirements because they are non local searching algorithms capable of handling rough variable spaces in the presence of noise.¹²¹

In this section, an introduction to genetic algorithm is provided, followed by a description of its implementation to compress chirped femtosecond pulses.

Genetic Algorithms

Genetic algorithms are an heuristic search technique used to find approximate or exact solutions to given problems. These searching procedures are suitable for problems where the solution space is too large for exhaustive search. They have been successfully applied in many different research areas to solve a great variety of problems involving a large number of variable parameters.¹²²

Based on the principle of biological evolution, genetic algorithms rely on inheritance, natural selection, and variability to search the solution space.^{123, 124} In nature, a given species has a certain number of individuals from which new offspring is born. The natural selection principle states that only those individuals who by random variations on their genome become adapted to the environment will, on average, leave more offspring. Less apt individuals will not survive long enough to be involved in the reproduction process. Natural selection does not provide all the necessary ingredients for biological evolution, inheritance and variability are also needed.

Inheritance is the individual's capacity of transmitting part of the individual characteristics to his offspring. As demonstrated by Mendel and Watson and Crick,¹²⁵ the characteristics of each individual that pass from generation to generation are encoded in their genome. Variability is responsible for maintaining the diversity of the population genome, otherwise, inbreeding will take place and the population will be stacked in terms of evolution. There are two sources of variability: crossover and mutation. Crossover represents descendant's genome as combination of pieces from both parents genome. Mutation symbolizes the variability in the genome of individuals due to errors in the duplication and occasional random alterations of the genome.

Genetic Algorithm Code

The basic idea of a genetic algorithm is to mimic natural evolution in a computer algorithm. During the optimization, the algorithm simulates natural selection, inheritance, and variability. A pseudo code of this algorithm is presented below:

```
0 Begin genetic algorithm;
1     If generation=0;
2         Initialize population P(generation);
3     While not optimized do;
4         Get population P(generation) fitness;
5         generation = generation +1;
6         Select parents from population P(generation -1);
7         Generate offspring P(generation);
8     End while;
9 End GA;
```

This algorithm can be summarized as follows; the solutions (individuals) to particular problems are represented as a one-dimensional array of parameters (genes). An initial population of random solutions with random parameters is generated and the fitness (adaptability) of each individual is measured. Those solutions (individuals) with the highest fitness (adaptability) will be selected for reproduction (natural selection) and they will pass to the next iteration loop (natural selection). Since the new set of solutions (offspring) is generated from the solution of the previous round, the new solutions will have better optimization parameters for a particular trait (phenotype) than its predecessors. Each new solution is generated by recombination (crossover) of the fittest solutions. Since cloning is allowed, the new solutions will have to compete with the best solutions of the previous generations to be allowed to reproduce and/or to pass to the next

optimization loop step. The new set of solutions is passed through a mutation step, where some of the parameters of each solution are changed. In principle, this new solution set has the best variables for solving the problem; and in terms of fitness, they will probably outperform the old solutions (evolution). This new generation is evaluated and the cycle continues until a certain termination criterion is met, e.g. maximum number of generations, a given value for the measured fitness, etc.

Genetic Algorithm Implementation

Since the initial implementation of genetic algorithm for quantum control,²⁹ several different optimization algorithms have been implemented.¹²⁶⁻¹²⁸ Our genetic algorithm code is based on previously published algorithms.¹²⁹ It uses roulette wheel parent and elitism for parent selection, random initial population, and special floating point genetic operators for reproduction. Among the various advantages, these genetic operators yield a fast convergence with a small number of individuals per generation.

Parent selection

In genetic algorithms, the parent selection provides individuals with higher fitness a greater probability of reproducing. There are several different ways to implement this selection. In our algorithm, the roulette wheel parent selection is used to select from the elite population those individuals apt for reproduction.

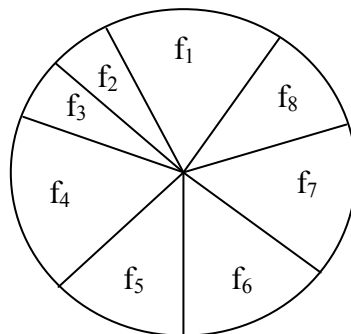


Figure 4-1. Roulette wheel. Adapted from work by Xiufeng et al.¹²⁹

The roulette wheel is composed of slots sized according to the fitness of each individual (Figure 4-1). Elitism is achieved by including only the best individuals in the roulette wheel. In Figure 4-1, f_i represents the fitness of each individual and the size of the wheel slots is proportional to the fitness value. The roulette wheel is constructed as follows,

1. Determine the fitness, f_i , of the i^{th} individual in one generation.
2. Calculate the total fitness of the elite population:

$$F = \sum_i^{epop} f_i . \quad (4-1)$$

3. Calculate the probability of selection for each individual according to,

$$p_i = \frac{f_i}{F} . \quad (4-2)$$

4. Calculate the cumulative probability of selection for each individual, q_i , of the elite pool.

$$q_i = \sum_i^{epop} p_i \quad (4-3)$$

The selection process is based on spinning the wheel as many times as there are individuals in the elite population; each time one parent is selected in the following manner,

1. Generate a random number, r , from 0 to 1.
2. If $r < q_1$ then select the first individual; otherwise select the i^{th} individual such that q_i .

$$i < r < q_i .$$

Genetic operators

Genetic operators represent the different forms of reproduction. While numerous genetic operators are found in the literature,¹²² only a few of them have been demonstrated to be highly

efficient. The classical genetic operators can be divided in three: cloning, crossover, and mutation.

The first operator, cloning, represents an exact copy of the individual and it is mainly used because of its robustness against experimental noise.

Crossover involves the creation of a new individual with the genetic code of two parents. In our algorithm, two types of crossover operators are used: two-point crossover and two-point arithmetical crossover.

The last operator, mutation, is utilized to provide new individuals to the population avoiding the inbreeding problem found in a closed population. Inbreeding leads to unwanted convergence towards a local minimum. Three different mutation operators are used: uniform mutation, non-uniform mutation, and non-uniform arithmetical mutation. While the first type of mutation produces a real change of the population, the other two operators are important for the fine tuning capabilities of the algorithm.

An individual G^i in generation k is represented with a vector of n parameters (genes)

$$G_{generation}^{ind} = (g_1, g_2, g_3, \dots, g_n). \quad (4-4)$$

Here, each gene is represented with a number from the domain of the corresponding parameter $[L, U]$, where L and U represent the lower and upper limit of the domain, respectively. The number of parameters codified in one individual depends on the problem itself and not on the algorithm.

Each genetic operator can be represented as follows:

1- Crossover: It occurs when parts of the parent's genomes are swapped in randomly selected points, generating two new individuals with a mixture of the parent's genotypes (Figure 4-2).

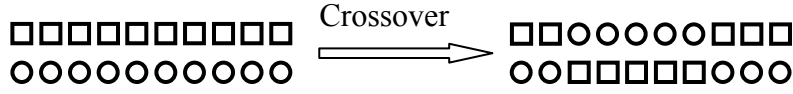


Figure 4-2. Crossover operation.

Two-point crossover involves the selection of two random numbers from 1 to the size of the parameter space (n). To avoid copying the whole genome from a single parent (cloning) the random numbers are selected such they are not equal and their sum is bigger than $n+1$. The individuals are generated as follows,

$$G_{old}^1 = (g_1^1, g_2^1, g_3^1, \dots, g_{parm}^1) \quad (4-5)$$

$$G_{old}^2 = (g_1^2, g_2^2, g_3^2, \dots, g_{parm}^2) \quad (4-6)$$

for $1 \leq i < j \leq n$, where i and j are random numbers delimiting the position of gene swapping in each individual. This leads to two new individuals of the form

$$G_{new}^1 = (g_1^1, \dots, g_{i-1}^1, g_i^2, \dots, g_j^2, g_{j+1}^1, \dots, g_n^1) \quad (4-7)$$

$$G_{new}^2 = (g_1^2, \dots, g_{i-1}^2, g_i^1, \dots, g_j^1, g_{j+1}^2, \dots, g_n^2). \quad (4-8)$$

Two-point arithmetical crossover is similar to the two-point crossover, but instead of directly replacing the genes, the genes are calculated as a linear combination of the parental genes. Starting from the same parent (Equation 4-5), the individuals are generated as follows:

$$G_{new}^1 = (g_1^1, \dots, g_{i-1}^1, g_i^a, \dots, g_j^a, g_{j+1}^1, \dots, g_n^1) \quad (4-9)$$

$$G_{new}^2 = (g_1^2, \dots, g_{i-1}^2, g_i^b, \dots, g_j^b, g_{j+1}^2, \dots, g_n^2) \quad (4-10)$$

where each element g_i^a and g_i^b is calculated as a linear combination of the old genes,

$$g_i^a = a g_{i,old}^1 + (1-a) g_{i,old}^2 \quad (4-11)$$

$$g_i^b = a g_{i,old}^2 + (1-a) g_{i,old}^1. \quad (4-12)$$

The parameter a is calculated as in the non-uniform mutation

$$a = \left(\frac{t}{T} \right) 0.8 \quad (4-13)$$

2- Cloning: this operator is responsible for passing old individuals to the new generation by directly copying the individual without changing its genetic material (Figure 4-3).

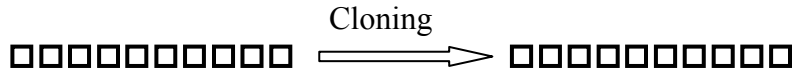


Figure 4-3. Cloning operator.

A mathematical description is

$$G_{old} = G_{new} = (g_1, g_2, g_3, \dots, g_n) \quad (4-14)$$

3- Mutation: when this operator is applied over an individual, one of its genes is changed to a different number (Figure 4-4).

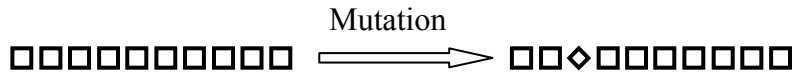


Figure 4-4. Mutation operation.

Mathematically it can be represented as follows:

$$\text{Individual before mutation: } G_{old} = (g_{1,old}, g_{2,old}, \dots, g_{i,old}, \dots, g_{n,old}) \quad (4-15)$$

$$\text{Individual after mutation: } G_{new} = (g_{1,old}, g_{2,old}, \dots, g_{i,new}, \dots, g_{n,old}) \quad (4-16)$$

While all mutation operators consist of replacing a gene with a new one, each mutation operator produces a different new gene.

Uniform mutation consists on replacing the old gene with a new random number, r , belonging to the domain of the parameter, where

$$g_{i,old} \rightarrow g_{i,new} = r \quad \text{and} \quad r \in [L, U] \quad (4-17)$$

This operator is responsible for searching vast regions of the variable space, since this mutation produces a stochastic operation.

A secondary type of mutation is the non-uniform mutation in which a random number, r , from $[0,1]$ is selected, followed by the calculation of the new gene,

$$g_{i,new} = \begin{cases} g_{i,old} + \Delta(t, U - g_{i,old}) & \text{if } r < 0.5 \\ g_{i,old} - \Delta(t, g_{i,old} - L) & \text{if } r > 0.5, \end{cases} \quad (4-18)$$

where the function $\Delta(t,y)$ returns a value within $[0,y]$ such that the probability of a smaller change of the gene increases with the generation number. This function, $\Delta(t,y)$, is defined as

$$\Delta(t, y) = y(1 - r^{(1-t/T)}), \quad (4-19)$$

where r is a new random number from $[0,1]$, t is the generation number, and T is the total number of generations used in the optimization. Since its action is linked to the generation number, at the beginning of the optimization this mutation will act as a random operator. As the optimization proceeds, this operator will only produce small changes in the genome leading to fine tuning of the overall solution.

Finally, non uniform arithmetical mutation is also designed for local tuning. The gene mutation is generated as follows:

$$g_{i,new} = ag_{i,old} + (1-a)r, \quad (4-20)$$

where r is a random number from the domain $[L,U]$ and a is a generation variable parameter

$$a = \left(\frac{t}{T}\right)0.8. \quad (4-21)$$

Our algorithm code

Our adapted genetic algorithm has been implemented in a LabView (National Instrument) programming environment. A representation of its code can be observed in Figure 4-5.

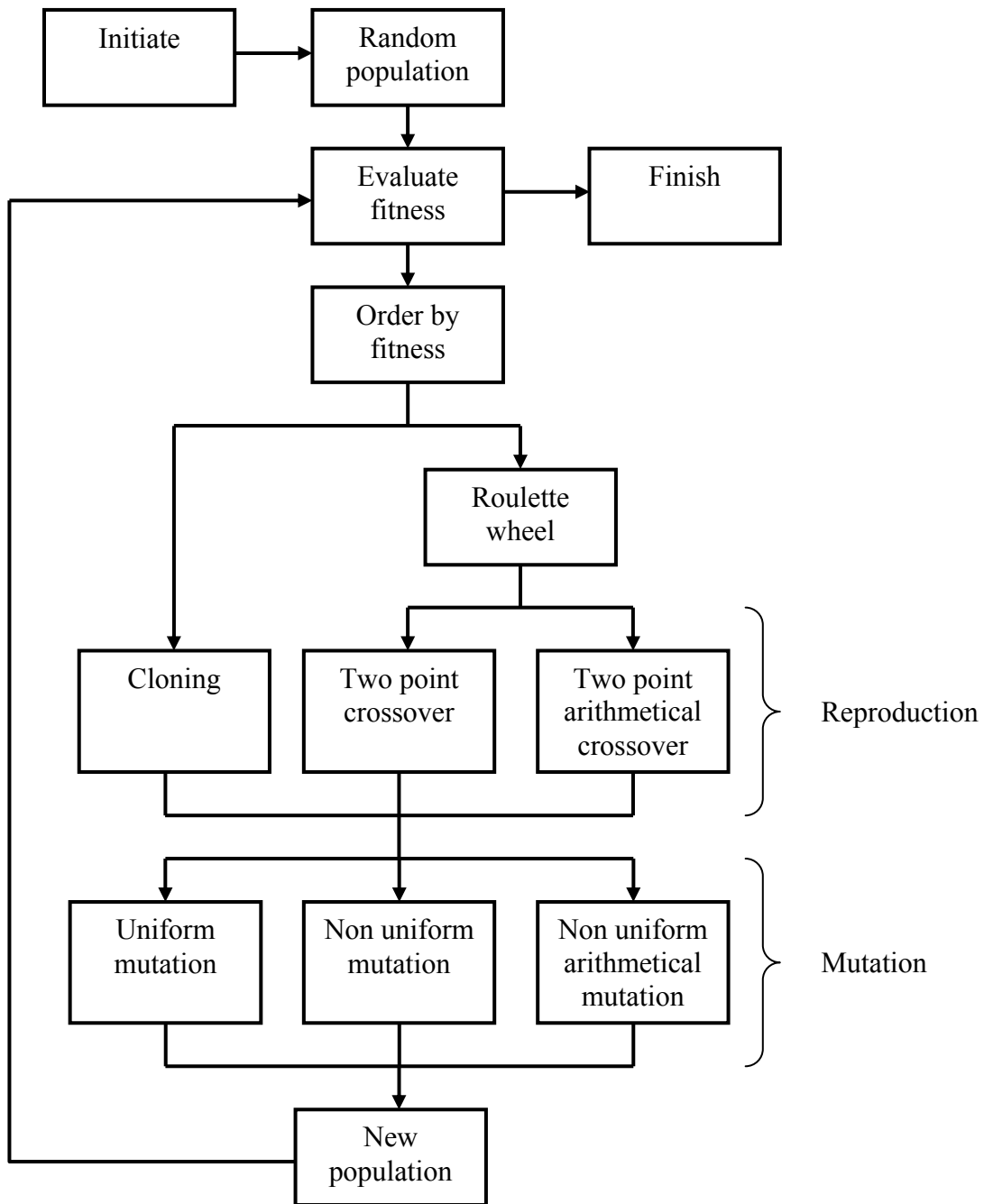


Figure 4-5. Implemented genetic algorithm.

Some special rules are included in this algorithm:

- The total number of generations is a user defined parameter.
- The initial random population is produced by randomly selecting the initial genes for each individual, although a starting point with a particularity designed individual can also be used.

- The population size is a user defined parameter.
- The number of crossover children is a user defined parameter
- Parent selection is performed with elitist roulette wheel.
- Two parents form two children via crossover, but only one, randomly selected, will form the offspring kept for the new generation.
- The number of cloned individuals is calculated from the difference between population size and number of crossover children.
- All the individuals are subject to mutation.
- The probability of mutating one of the genes is defined by the user.
- The mutation operator is randomly selected among the three possibilities.
- The termination of the algorithm is defined by the number of generations.

The role of the genetic algorithm parameters

Our adapted algorithm presents the following controllable parameters: number of generations, number of individuals, number of elite parents, number of cloned kids, and probability of gene mutation.

The number of generation depends upon how long experimentally it takes to run each optimization loop and how long it takes to reach convergence. Since genetic algorithms are nothing but an optimized variable space sampler, the higher the number of trials the higher the possibility of finding a true maximum. Thus, the number of generations should neither be too small nor too big.

During the optimization loop, the time for finding the fitness of one individual is limited by the time that it takes to transfer a phase from the computer to the spatial light modulator (~300 ms), and the number of average laser shots used for the feedback signals (~150 ms). It takes approximately 450 ms to evaluate each individual. Since the reproducibility of the result is very important in these experiments, many successive repetitions have to be performed for each

optimization. The stability of our laser system can be maintained for approximately 24 hours straight, limiting the number of experiments that can be performed. An optimization lasting for 3 hours, 180 min, implies that 8 to 9 experiments can be performed while the laser system remains stable. This 3 hour limit is a reasonable time only if the achieved answer is reproducible. With a 180 min optimization, the algorithm can try approximately 24000 individuals. Usually, the number of individuals used in one population is 80. Thus in 180 min, 300 generations can be evaluated. To restrict the problem to shorter times, in this work the selected number of generations is 200 or 120 min. This time constraint can be modified for special cases where noisy signals are used or when more laser shots need to be averaged.

For this selected time, it is possible to optimize the remaining parameters to produce maximum achievable fitness. As stated before, each experimental optimization will take 120 minutes, making it unfeasible to optimize the remaining parameters experimentally. Therefore, the rest of the parameters are optimized using a theoretical simulation of the experiment. The advantages of the optimization simulations are: short run time, usually between 1 or 2 min, and independence from environmental conditions, e.g. temperature change.

Optimization of Genetic Algorithm Parameters

The aim of this simulation is to find the optimal genetic algorithm parameters to perform real optimization experiments. A simulation of pulse compression using our genetic algorithm with different algorithm parameters was performed to find the best set of conditions yielding the best optimization performance of the algorithm within an experimentally reasonable time.^{II} The experiment consists of compressing a chirped pulse back to its transform limited form (Figure 4-6).

^{II} The software to perform this simulation can be freely obtained in www.lab2.de.

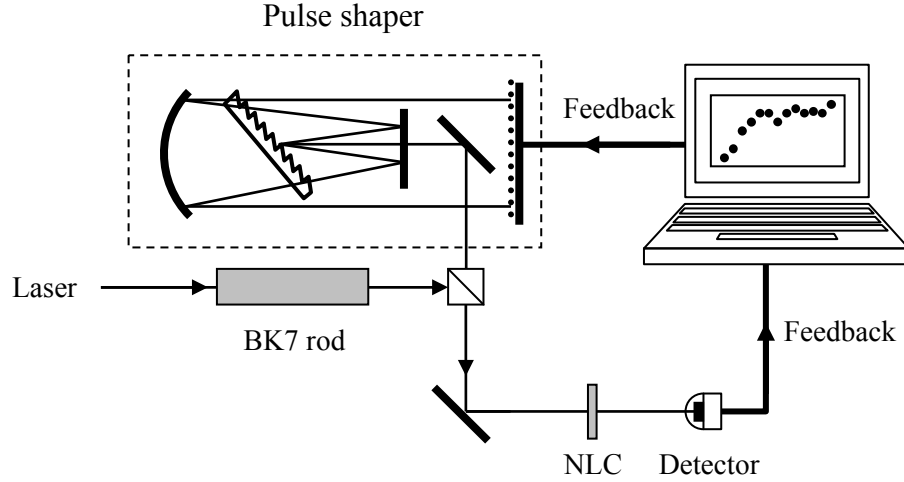


Figure 4-6. Simulated experimental setup. The femtosecond pulse is modulated in the glass rod (BK7) and its second harmonic intensity is produced in a non-linear crystal (NLC).

The chirped pulse is obtained by passing a transform limited pulse with a known Gaussian temporal shape through 10 cm of glass (BK7). As presented in Chapter 3 (Equation 3-9), propagation through this glass produces a modulation of the incident electric field:

$$E(\omega) = \tilde{E}(\omega, 0) e^{i\omega t} \exp\left(-i \frac{\omega \cdot n(\omega)}{c} z\right), \quad (4-22)$$

consequently the pulse gets broader in time. Assuming that the BK7 glass only impose quadratic chirp, the following expression can be derived¹³⁰

$$\Delta t = \Delta t_0 \sqrt{1 + \frac{16 \ln^2(2) \varphi^2}{\Delta t_0^4}} \quad (4-23)$$

where Δt_0 is the FWHM pulse duration of the transform limited pulse, φ is the second order spectral coefficient, and Δt is the FWHM of the pulse after propagating through the glass. The signal used for feedback is the second harmonic generation produced by the pulse. Since second harmonic generation is proportional to the integrated intensity squared (Equation 2-26 and 4-23)

$$I_{SHG}(\Delta t) \propto I^2(\Delta t) \propto \left(|E(\Delta t)|^2 \right)^2 \propto \left(E_0 \exp\left(\frac{-2t^2}{\Delta t} \right) \right)^4. \quad (4-24)$$

A chirped pulse generates less second harmonic signal than a transform limited pulse.

After the BK7 glass, the pulse is sent into the ideal pulse shaper where the quadratic phase can be compensated. Considering Equation 3-8 for the pulse shaper as a filter mask in a zero dispersion compressor, the output is

$$E_{out}(\omega) = \tilde{E}(\omega, 0) e^{i\omega_0 t} \exp\left(i \left(-\frac{\omega \cdot n_{BK7}(\omega)}{c} z_{BK7} + \psi_{applied}(\omega) \right) \right), \quad (4-25)$$

where $\psi_{applied}$ is the phase applied by the filter mask, and n_{BK7} and z_{BK7} are the refractive index and thickness of the glass, respectively.

In the case where

$$\psi_{applied} = \frac{\omega \cdot n_{BK7}(\omega)}{c} z_{BK7}, \quad (4-26)$$

the output pulse will have the same second harmonic signal as the transform limited pulse.

The idea of this simulation is to find the best phase variables that maximize second harmonic generation, or equivalently find the necessary phase to compensate the glass dispersion. The spectral phase is codified in 128 discrete variables that can vary from 0 to 2π . Genetic algorithms can produce similar but not identical solutions for consecutive optimizations; thus each optimization is performed five times and the fitness values of the best individual fitness are recorded. For comparison, the average, best, and worst fitness corresponding to the best five individuals in each set of simulations are presented.

The initial conditions for this optimization are summarized in Table 4-1.

Table 4-1. Initial genetic algorithm parameters.

Parameter	Value
Number of individuals	80
Number of elite parents	16
Number of crossover kids	75
Number of cloned kids	5
Probability of gene mutation	0.03

Mutation probability

The mutation effect on the optimization of second harmonic is studied. This parameter is optimized by changing the mutation probability while keeping all the other initial parameters constant. The effect produced by the different mutation probabilities on the achieved fitness is illustrated in Figure 4-7.

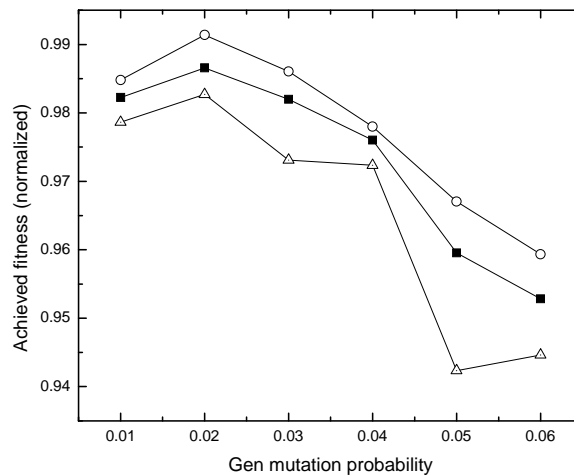


Figure 4-7. Influence of probability of gene mutation on the achieved fitness. Average best fitness (black squares). Overall best fitness (open circles). Overall worst fitness (open triangles).

As observed in Figure 4-7, the optimal mutation probability is found to be close to 0.02. The achieved fitness is very similar (>98 %) for the mutation rates from 0.01 to 0.03 and is greatly reduced when the mutation probability becomes larger. These results agree well with the expected behavior for the operator. When the mutation probability is too small only a few numbers of genes will be changed in each individual and the population variability will rapidly

decrease, leaving the algorithm stacked in a local minimum. In contrast, a large gene mutation probability produces too many new individuals in each generation removing the population inheritance and transforming the genetic algorithm in a trial and error search.

Number of elite parents

We performed similar simulations varying this parameter while keeping all the others constant to choose the optimal number of elite parents. Figure 4-8 presents the effect produced on the best individual fitness by selecting different numbers of elite parents.

The plot shows that the fitness is a decreasing function of the number of elite parents. This dependence is produced because increasing the number of elite parents includes individuals with lower fitness values in the roulette wheel of parent selection, resulting in a less apt offspring.

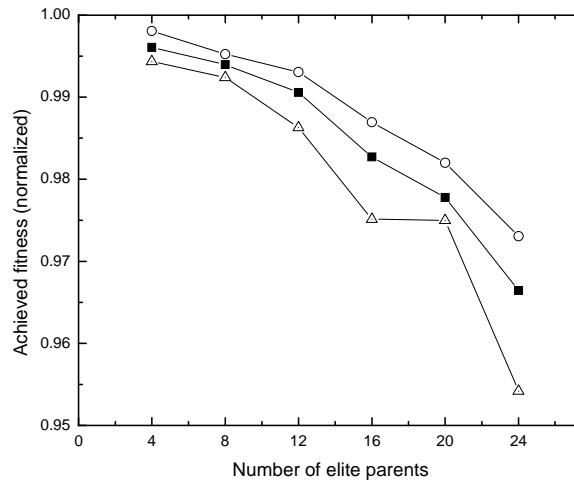


Figure 4-8. Influence of the number of elite parents on the achieved fitness. Average best fitness (black squares). Overall best fitness (open circles). Overall worst fitness (open triangles).

For less than 12 elite parents, the algorithm recovers 99 % of the second harmonic independently of the number of selected parameter. Thus, any number of elite parents of less than 12 produces almost equal results. If the number of elite parents is too small, the roulette wheel selection will be formed with individuals of very similar genomes. This type of elitism will transform some operators like two-point crossover into a cloning operator.

Number of crossover children

In this optimization the number of crossover kids is changed while keeping all the other genetic algorithm parameters at their initial values. Figure 4-9 shows the fitness as a function of the number of children for this simulation.

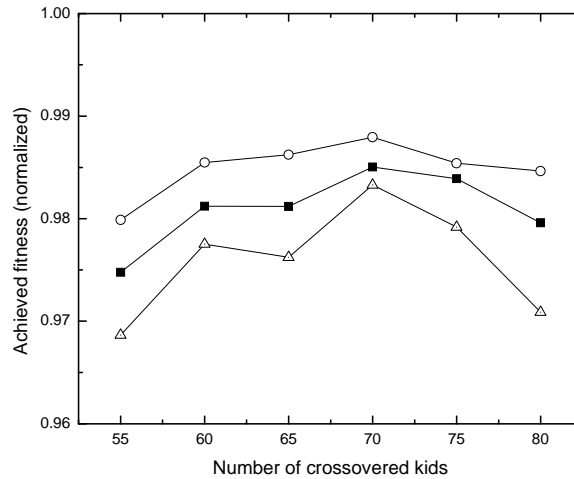


Figure 4-9. Influence of the number of individuals generated by crossover on the achieved fitness. Average best fitness (black squares). Overall best fitness (open circles). Overall worst fitness (open triangles).

Comparing with other genetic algorithm parameters, the effect on achieved fitness for different numbers of crossover children is not very pronounced (Figure 4-9). We conclude that this parameter does not change substantially the result of the optimization and that the specific chosen value is not critical.

The optimal number of crossover children is 70, but its difference with the fitness obtained using 75 elite parents is not considerable (<0.2 %). Therefore either one of them can be used.

Number of cloned children

Since the number of cloned children is obtained from the difference between the population size and the number of crossover children, this parameter is optimized simultaneously with the number of crossover children.

Optimized Genetic Algorithm Parameters and Noise

From the previous results, it is possible to extract the best genetic algorithm parameters for compressing a pulse (Table 4-2) with an initial population of 80 individuals.

Table 4-2. Optimized genetic algorithm parameters.

Parameter	Initial values	Optimal values
Number of individuals	80	80
Number of elite parents	16	4
Number of crossover kids	75	70
Number of cloned kids	5	10
Probability of gen mutation	0.03	0.02
Average Fitness	98.7	99.8

An optimization with the chosen values is performed to confirm the correct selection of parameters. In this case the achieved fitness is more than 99.8 % (Table 2), which shows that the chosen values are excellent for phase compensation. In general the algorithm has a remarkable performance because even for initially selected parameters, such as those of the above experiments, the optimization always compresses the pulse to 95 % of its transform limited pulse.

The limitation with these simulations is the lack of noise. Noise is one the biggest constraints in closed loop optimizations.¹³¹ Rabitz and coworkers studied the noise effect in several two-photon processes. The main conclusion of that work is that noise can significantly change the quality of the achieved objective. We decided to investigate the noise effect produced on the achieved fitness with the parameters chosen before by performing optimizations in which the fitness values have noise (as it would be for experimental data). The fitness is calculated using

$$f_{noise} = f(1 \pm r \cdot noise) \quad (4-27)$$

where f is second harmonic signal and r is a random number from 0 to 1. The investigated noise values are: 5 % and 10 %.

Each optimization is performed five times and the fitness value of the best individual fitness is recorded. For comparison, the average, best, and worst fitness corresponding to the best five individuals in each set of simulations are presented.

Table 4-3. Fitness results for simulations with noise. Set 1 represents the initial and set 2 the optimized genetic algorithm parameters.

Fitness	Noise		
	0.00	0.05	0.10
	Average Best Fitness	Average Best Fitness	Average Best Fitness
Set 1	98.7	96.8	94.4
Set 2	99.8	97.0	96.1
ANOVA test ^{III}	Statistically no different	Statistically no different	Statistically no different

Table 4-3 shows the results obtained in the pulse compression simulation with noise. The noise in this simulation does not change significantly the performance of the algorithm: for a 10 % noise the recovered pulse has ~95 % of the second harmonic observed for the transform limited pulse (Table 4-3). However it is important to notice that when the noise is included with the first set of coefficients (set 1 for initially chosen values) we have the same performance as with the optimized parameters. This is confirmed with the ANOVA statistical test which shows that with 99.0 % confidence the two results are not statistically significantly different.

Summary

From this part we can conclude that this genetic algorithm is very impressive in terms of efficiency and robustness in the presence of noise. Laser amplifiers usually have a noise less than 2 %, thus the intensity squared noise is approximately 4 %, either set of parameters (1 or 2) found in this optimization can be used in a closed loop optimization. It is important to note that from the number obtained in Table 4-3, the larger the noise the more critical is the correct

^{III} This test was performed using the best five fitness for each set of parameters.

selection of the optimization parameters. Thus for experimental situations with large noise these optimization parameters should be reevaluated.

Experimental Pulse Compression

Implementation of Genetic Algorithms in Pulse Shaping Experiments

In pulse shaping experiments, the individual genetic code is represented by an array of spatial light modulator voltages or phases. Given the large size of the parameter space (640 pixels per mask) simultaneous optimization of all parameters becomes impossible to pursue (and provides no physical insight into the dynamics of the molecular system). Instead we parameterize each array with a function of 128 variables. The same parameterized function (linear or spline interpolation among 128 pixels) is applied to both masks to produce a phase only modulated pulses. The selection of feedback signals used to generate the fitness and the fitness function chosen in each optimization procedure depends on the desired experimental objective.

Optimization Problem

The spatial light modulator in our laboratory produces temporal distortions to the input pulse because of the inhomogeneity of the pixels. To test our genetic algorithm, we performed an optimization experiment with the aim of compensating this residual phase and achieving a transform limited pulse. As we showed in the previous section, the pulse compression problem is equivalent to the maximization of a second order dependent signal (Equation 4-24).

Setup and Optimization Conditions

The used experimental setup is shown in Figure 4-10. In this experiment, the feedback signal is a two-photon photoinduced current, which is obtained by softly focusing a laser beam on a GaAsP photodiode with a 100 mm focal lens. Since GaAsP band gap is 680nm and our laser beam has a spectrum centered at 790 nm, the photocurrent generate is a two-photon intensity dependent process.¹³² In contrast to the second harmonic generation in doubling crystals, the

generated electric signal does not have the constraints observed in nonlinear materials, such as short pulses' bandwidth phase matching and acceptance angles.¹¹⁰ Two-photon induced current signal is processed with a boxcar integrator and acquired with a PC based data acquisition card.

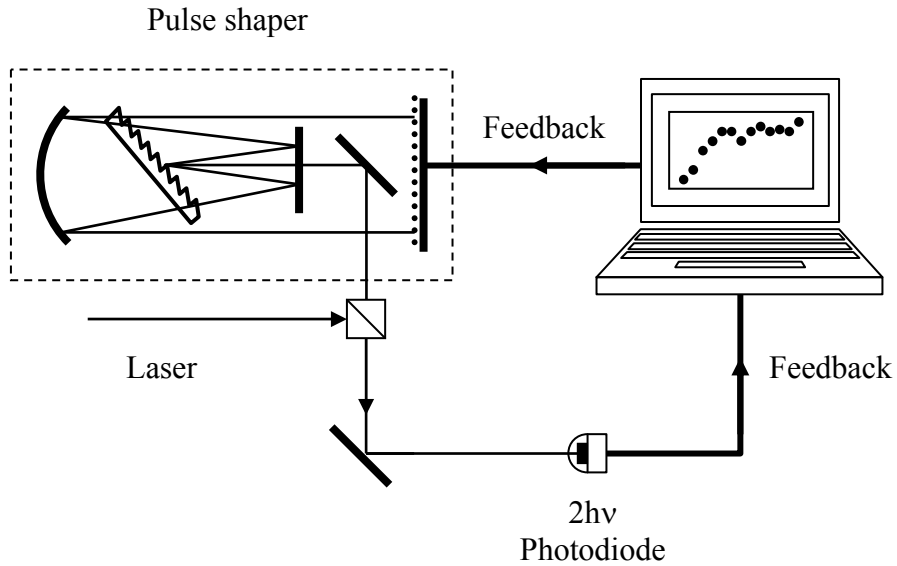


Figure 4-10. Experimental setup used in pulse compression.

An average of 150 laser shots is used to generate the fitness value of each individual in each generation, and since the noise to signal ratio for our laser system is better than 3 %, no corrections are made for energy fluctuation.

The genetic algorithm parameters used in this experiment are presented in Table 4-4.

Table 4-4. Genetic algorithm parameters.

Parameter	Value
Number of generations	200
Number of individuals	80
Number of elite parents	16
Number of crossover kids	75
Number of cloned kids	5
Probability of gen mutation	0.03

Multishot SHG-FROG is used to fully characterize the optimization results. The electric field is retrieved from the experimental traces with commercially available software (FROG Femtosoft Technologies®).

Results

Figure 4-11 shows the fitness evolution curves obtained by optimizing the two-photon process at the photodiode.

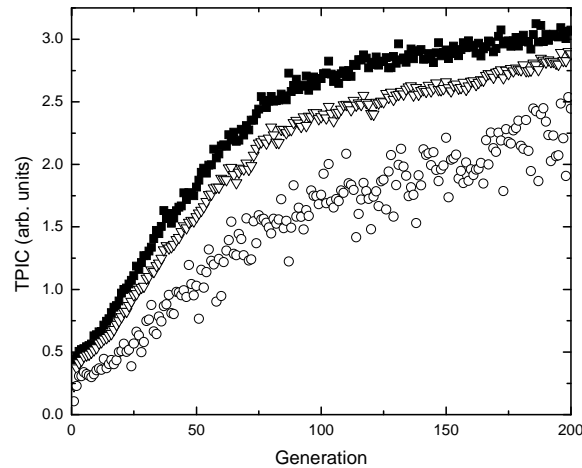


Figure 4-11. Evolution of the two-photon induced current as a function of the generation. Average (open triangles), best (full squares), and worst (open circles) fitness values for each generation are plotted.

Three different evolution curves are presented corresponding to the best, average and worst individual's fitness for each generation. All these fitness curves show a monotonic increase of the fitness value during the optimization. Starting from a photocurrent signal of 0.5 the best fitness of the individuals evolves to a signal value of 3 after 200 generation. This change represents an increment of the two-photon current intensity of approximately 600 %. From these plots we can also observe that at ca. 100 generations the best individual fitness reaches 83 % of the optimized value suggesting that the genetic operators providing the fine tuning are critically important on the 100 final generations of the optimization.

To confirm the quality of the optimization results, SHG-FROG traces of the initial and final pulses are analyzed. The initial pulse is shown in Figure 4-12 in which a strong modulation is observed. Figure 4-13 shows the temporal and spectral characteristic of the pulse retrieved from the analysis of the experimental traces.

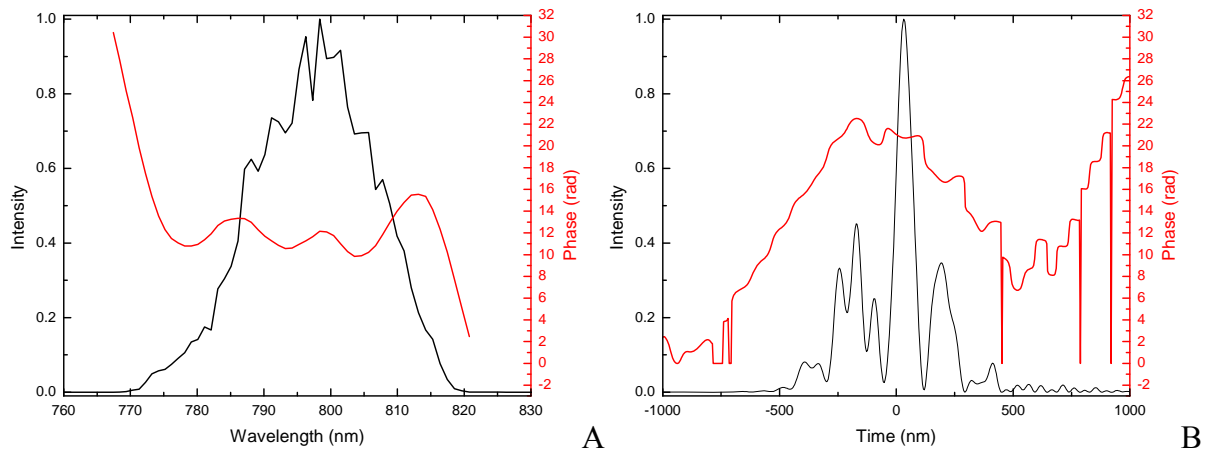


Figure 4-12. Uncompressed pulse. A) Spectral intensity (black line) and phase (red line). B) Temporal intensity (black line) and phase (red line).

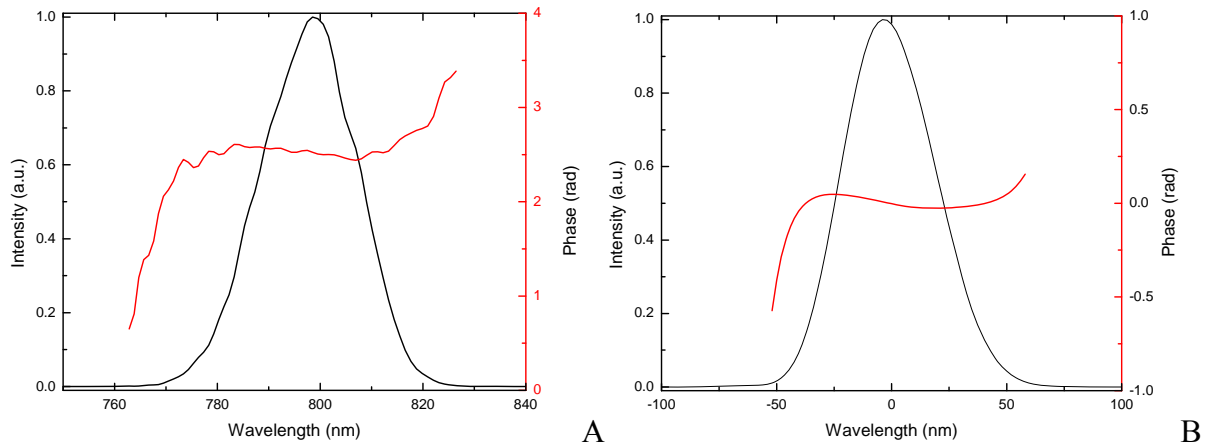


Figure 4-13. Compressed pulse. A) Spectral intensity (black line) and phase (red line). B) Temporal intensity (black line) and phase (red line).

As seen in the temporal and spectral intensities of the optimized pulse, the phase change in both domains in less than half a radian for the spectral and temporal FWHM. This indicates that the algorithm is capable of compressing the pulse to a transform limited one, starting from a very

far position in the phase variable space (Figure 4-12). Some residual phase is observed after the optimization. This residual phase is probably produced by the lack of compensation of the different dispersive optics presented in the FROG and second order intensity signal setups. The pulse temporal FWHM is 47 fs, which is only 5 fs away from the theoretical limit for a 25 nm FWHM spectral bandwidth pulse.

Summary

From all the above results we conclude that our home-written algorithm is suitable for performing experiments involving a large number of variables in closed loop optimizations. Moreover, this compression is substantially better than the phase compensation presented in the previous chapter.

CHAPTER 5 QUANTUM CONTROL OF TWO-PHOTON INDUCED FLUORESCENCE OF RHODAMINE 6G IN SOLUTION

Introduction

Many systems have recently been studied using the closed loop optimization technique.²⁴ Most of them have been focused on a proof of principle rather than on an understanding of the process investigated. In this chapter, we present the adaptive control of the two-photon fluorescence of Rhodamine 6G in solution.

Rhodamine 6G is a relatively simple quantum system in which both molecular dynamics and electronic structure¹³³ are well known, making it a good candidate to find the components of the optimal laser field directly related to its molecular properties. The motivation for these experiments is not only to show control over a simple system, but also to gain molecular information about the possible excited state processes occurring in Rhodamine 6G. To achieve these goals, adaptive control experiments are performed in our home-built femtosecond pulse shaping setup.

Molecular System and Control

Rhodamine 6G is a yellow emitting dye with a xanthane core structure (Figure 5-1(A)). Among its various molecular properties, it has high photo-stability, high extinction coefficient, and high fluorescence quantum yield. Due to these properties, Rhodamine 6G is commonly used as a laser dye¹³⁴ and as a biomolecular probe in microscopy studies.¹³⁵

Steady state spectroscopy of Rhodamine 6G is presented in Figure 5-1(B). The absorption spectrum shows two distinct absorption maxima at 350 and 530 nm, and a third absorption band at 390 nm with a low extinction coefficient (inset Figure 5-1(B)). The emission spectrum manifests the typical mirror image observed in molecules with similar potential energy surfaces in the ground and first electronic excited states. A fluorescence excitation anisotropy study

performed by Eggeling et al. reveals the presence of three distinctive electronic transitions at 450 to 550 nm, 375 to 425 nm, and 325 to 375 nm, confirming the band assignment made in the absorption spectrum.¹³⁶ This assignment shows that the first two bands, 350 and 530 nm, are one photon allowed and the third, 390 nm, is one photon forbidden (two-photon allowed).

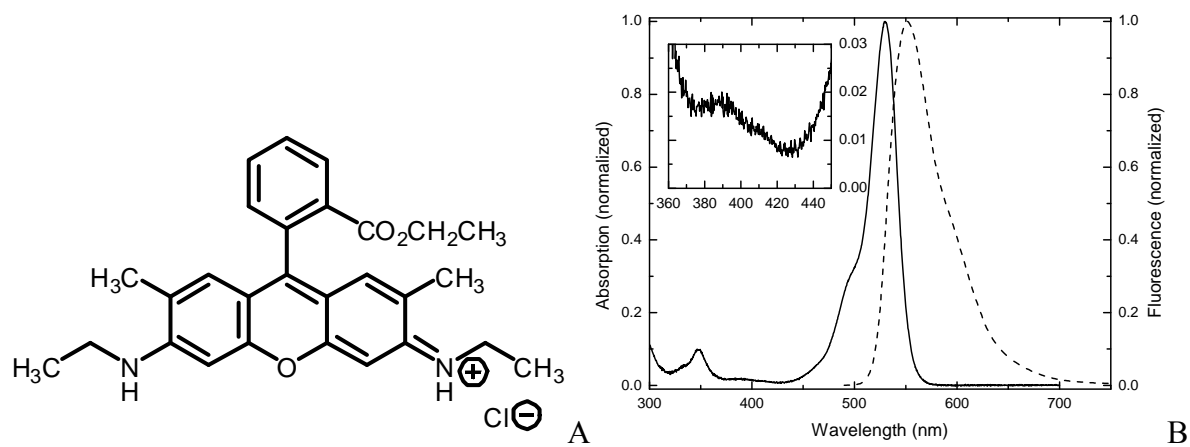


Figure 5-1. A) Rhodamine 6G molecular structure. B) Absorption spectrum (black line) and emission spectrum (dashed line). Inset contains a zoom of the absorption spectrum from 360 to 445 nm.

Rhodamine 6G two-photon cross section in the 700 to 850 nm spectral region has been measured by different authors.^{135, 137} All these studies show a large and featureless cross section in that region of the spectrum.

Fluorescence studies show that the fluorescence spectrum shape and quantum yield are excitation wavelength independent,¹³⁷ indicating a strong coupling between different excited states, S_n , and the first excited state, S_1 . No evidence of phosphorescence is found in the emission spectrum, thus ruling out the possibility the presence of intersystem crossing leading to triplet states. Rhodamine 6G's quantum yield of triplet state formation was measured to be less than 0.005.¹³⁸

A Jablonski diagram of Rhodamine 6G is represented in Figure 5-2. Disregarding triplet states, this diagram shows four electronic states, S_0 to S_3 , with fluorescence arising exclusively from the S_1 state.

Time-resolved experiments show a simple deactivation mechanism (Figure 5-2).¹³⁹⁻¹⁴⁵ Upon excitation to $S_{n>1}$, the system relaxes to the vibrational ground state of S_1 in a subpicosecond time scale. Strong coupling among the excited states leads to an ultrafast internal conversion.¹³⁹ Once in the first excited state, the system relaxes from S_1 to S_0 via emission or internal conversion.¹³⁹ The quantum yield of the emission from S_1 is 95 %, ¹⁴⁶ and its life time is 3.9 ns.¹³⁶

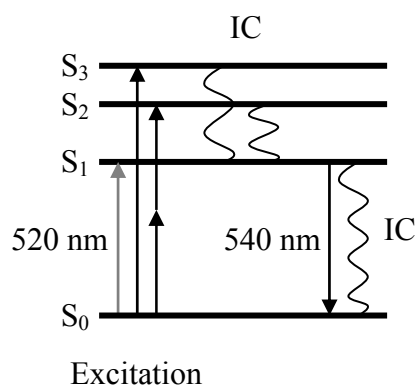


Figure 5-2. Jablonski diagram of Rhodamine 6G.

The emission quantum yield from $S_{n>1}$ depends on the coupling between the $S_{n>1}$ and S_1 states and on the non-radiative deactivation pathways that directly transfer the system to the ground state. This study aims to control the coupling between S_2 - S_1 using the phase-modulation of the two-photon excitation pulses thus controlling the quantum yield. If quantum control of the process is achieved, it will indicate a control over the coupling between S_2 - S_1 and/or S_1 - S_0 states. The motivation for this experiment is not only to show control over a simple system but also to gain molecular information of the various deactivation processes occurring in Rhodamine 6G's excited states.

Experimental

The experiment setup used in the optimal control experiments is depicted in Figure 5-3. This apparatus consists of a femtosecond laser source (described in Chapter 2), a pulse shaper to produce arbitrary phase-modulation (described in Chapter 3), a detection system to reveal the molecular response to the tailored pulses, and a genetic algorithm to modify the pulses according to the molecular response (described in Chapter 4).

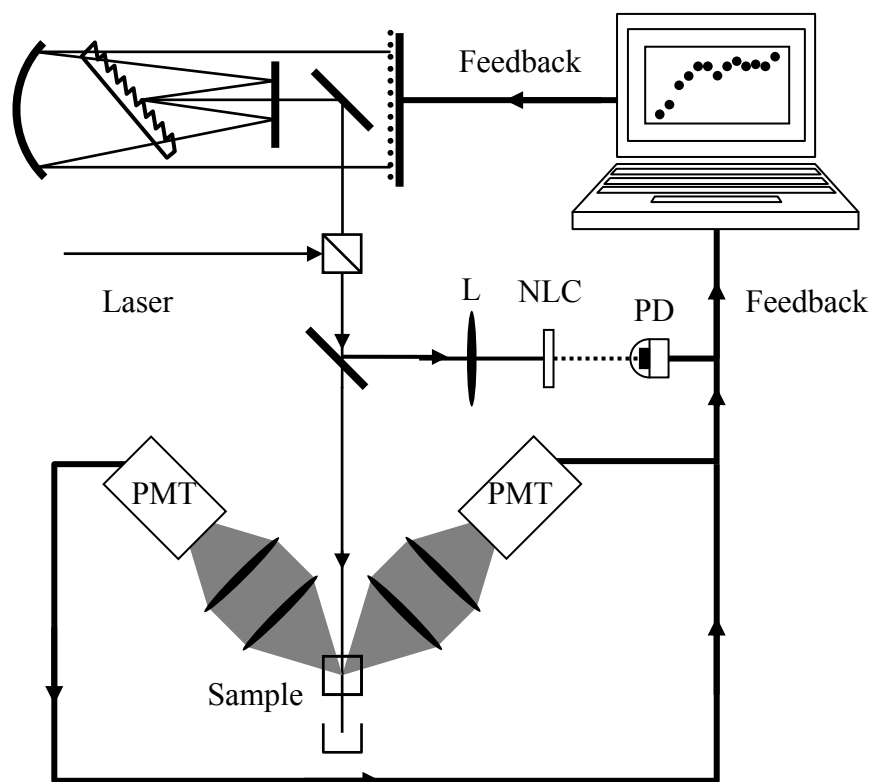


Figure 5-3. Experimental setup for controlling molecular fluorescence. L: lens. NLC: nonlinear crystal. PD: photodiode. PMT: photomultiplier tube.

Rhodamine 6G sample was purchased from Exciton. Samples are prepared in methanol (spectroscopy grade) with concentrations below 10^{-5} M (OD of 0.25 mm^{-1} at 520 nm) to avoid any aggregation.¹⁴⁷ The sample's photo-stability is checked by steady state absorption before and after each set of experiments.

In this study two signals are monitored simultaneously, namely the two-photon induced emission from the sample and the second harmonic generated in a nonlinear crystal. The phase modulated beam is split into two new beams with one beam used to excite the chromophore and the other one to generate the second harmonic.

To induce excitation the sample, pulses with 300 nJ of energy are focused on the sample with a 100 mm lens to c.a. a 40 μm diameter spot size. The sample is held in a 2 mm path length quartz cell with magnetic stirring to ensure identical experimental conditions for each laser excitation pulse. Two different photomultiplier tubes (Hamamatsu H5783), each at 45 degrees with respect to the excitation beam, collect the two-photon induced emission of Rhodamine 6G. Two-photon absorption is a nonlinear process that will occur at the focus of the excitation beam. The sample is correctly placed at the focus of the lens by maximizing the fluorescence signal. BG-39 color filters are used to avoid having straight excitation light hit in the detector.

Simultaneously, second harmonic signal is produced with a collimated 30 nJ beam on a 100 μm β -BBO crystal and detected with a photodiode (Thorlabs DET210). As with the other detectors, a BG-39 filter is used to eliminate residual fundamental light.

The two signals, fluorescence and second harmonic, are used as feedback in the closed-loop optimization. A boxcar integrator (Stanford Research System, SR250) and PC based data acquisition card (National Instrument, PCI-MIO-16E-4) are used to integrate and digitalize the signals, allowing coupling between the signals and the genetic algorithm. The genetic algorithm uses the average of the signal produced by 150 laser shots.

In the genetic algorithm, the pulse shaper phase is codified by 128 independent parameters, which are transformed into the corresponding 1280 mask pixel phases by linear interpolation between adjacent points. The algorithm starts the iterative search with a population of 80 random

individuals, each consisting of 128 genes, and finishes the search optimization after 200 iterative loops.

Due to the large size of the search space, experimental reproducibility is used as a way of demonstrating that the system evolved to a global extreme of the searched space. Optimization experiments are reproduced at least three times; also for each experiment the laser stability is followed by simultaneously measuring the raw feedback signals for the unmodulated pulses (phase coefficients in zero phase).

In order to fully characterize the modulated pulses obtained in the closed loop experiments, a second harmonic FROG trace is collected after each experiment. This trace is acquired in a home-built FROG setup with a 12-bit resolution fiber optic spectrometer (Ocean Optics).

Results

Emission maximization can always be produced with a transform limited pulse. In samples with broad absorption bands this effect occurs because the transform limited pulse has the broadest spectrum leading to the maximum overlap between its second order power spectrum and the molecular absorption coefficients for the two-photon transition.⁴² In addition, two-photon processes depend on the intensity squared: the maximum value of which is achieved with transform limited pulses. In this work, the aim is to control the two-photon induced emission of Rhodamine 6G in methanol beyond this trivial solution. The intensity dependence of the excitation is removed by experimentally working with the ratio of two signals with the same intensity dependence.⁶³

The process utilized to represent the two-photon excitation intensity dependence is second harmonic generation. As any second order intensity process, second harmonic generation is sensitive to the change of the phase of the electric field. In addition, second harmonic conversion

efficiency is wavelength independent for many nonlinear materials in the spectral window of our laser excitation (770-830 nm).¹⁴⁸

Fluorescence Efficiency Optimization

The first set of experiments aims to optimize fluorescence efficiency, which is defined as the ratio of fluorescence over second harmonic signals. This ratio physically represents the fluorescence intensity normalized by the intensity used to induce it.

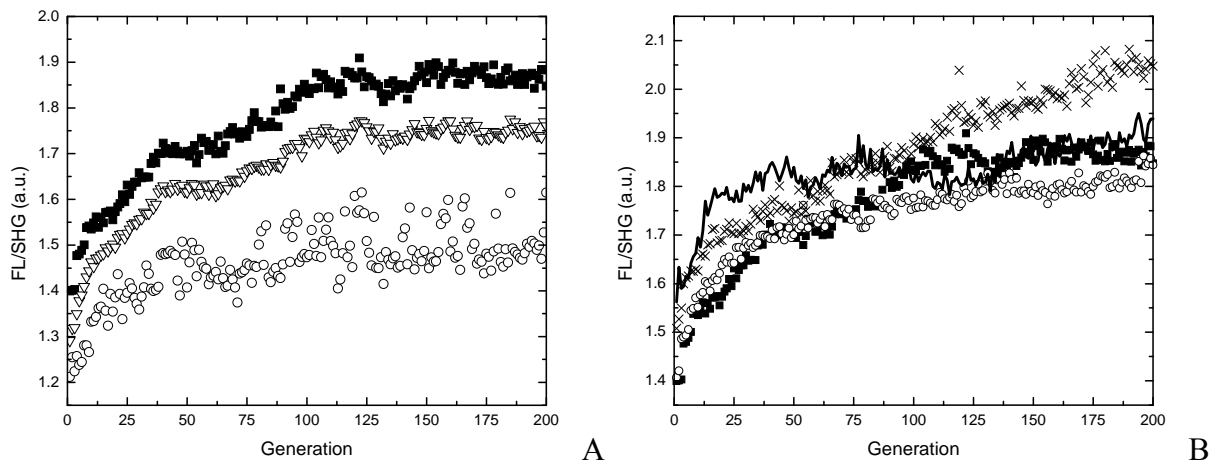


Figure 5-4. A) Fitness evolution of typical experiments of maximization of fluorescence efficiency. B) Experimental convergence reproducibility.

Figure 5-4(A) shows typical evolution curves obtained during the maximization of fluorescence efficiency, where solid black squares, open triangles, and open circles correspond to the fitness measured for the best individual, the average of all individuals, and the worst individual fitness in each generation, respectively. Starting with low ratio values (for pulses with randomly generated phases), the curves exhibit an improvement of the ratio after 200 generations. In contrast to the smooth changes observed for the individuals with the average and best fitness values as a function of generation, fitness values for the worst individuals show strong oscillations. This is a normal effect exhibited in genetic algorithms where very unfit individuals are created by the different reproduction operators in each generation.

In heuristic searches, the convergence of the optimization is given by the stability of the solution. This stability is represented by the evolution of the average of the fitness for all individuals, because ideally, the average fitness values should asymptotically reach the solution. Figure 5-4(A) shows that stability is reached in the 125th generation indicating the presence of a possible maximum in the fluorescence efficiency. This maximum reaches a value for the fitness 35 % higher than that obtained when exciting with a transform limited pulse (FL/SHG~1.4).

Figure 5-4(B) shows the convergence reproducibility. Three different experiments show a good reproducibility in terms of the achieved objective, but a fourth experiment deviates by 10 % from the average. Since the stability of the laser did not show any important fluctuation, this difference can not easily be explained.

The autocorrelation of the best excitation pulse for all the experiments is also examined as an independent check of convergence reproducibility (Figure 5-5).

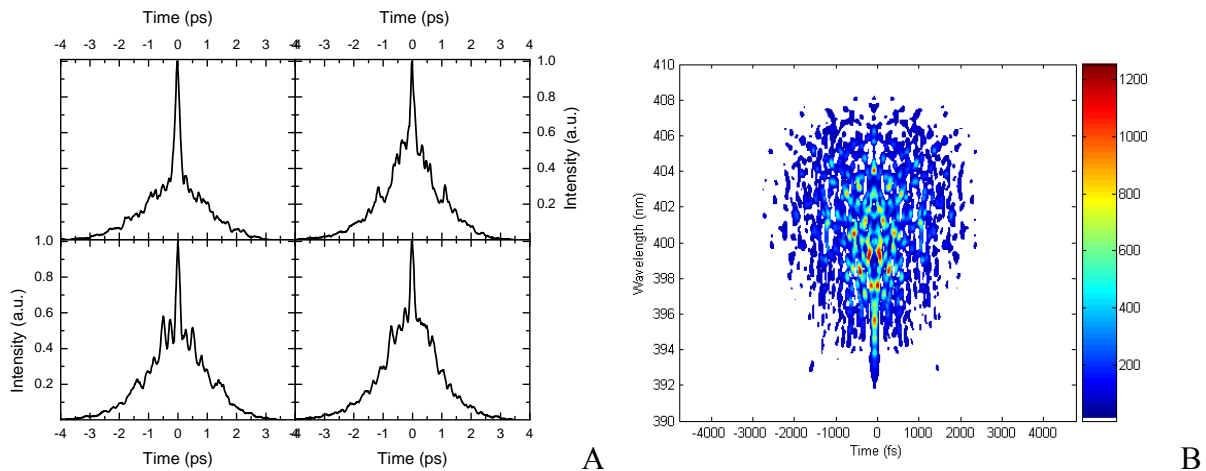


Figure 5-5. A) Optimal autocorrelation for different experiments. B) Typical SHG-FROG trace of the optimum pulse.

All autocorrelations present similar complex temporal structures (pulses with a subpulse structure) indicating a convergence towards a non-trivial solution. The similar resemblance of the pulse temporal shapes reveals that the outlier optimization did not reach a new solution, but a

solution similar to the rest. This is also observed in their corresponding SHG-FROG traces (not shown), confirming the reproducibility of the global solution.

The second experiment presented here focuses on the minimization of fluorescence efficiency. As in the previous experiment, the ratio shows an evolution of the fitness of the individual pulses with the generation. A typical fitness evolution plot with the FL/SHG ratio of the best individual (black full squares), the one for the worst individual (open circles), and the ratio average over all individuals of a given generation (open triangles) as a function of generation is presented in Figure 5-6(A). From the initial random phase to the optimized pulse, the efficiency ratio for the best individual of each generation decreases to a value close to 1.15, which compared to the transform limited pulse (~ 1.4) represents a reduction of 20 %.

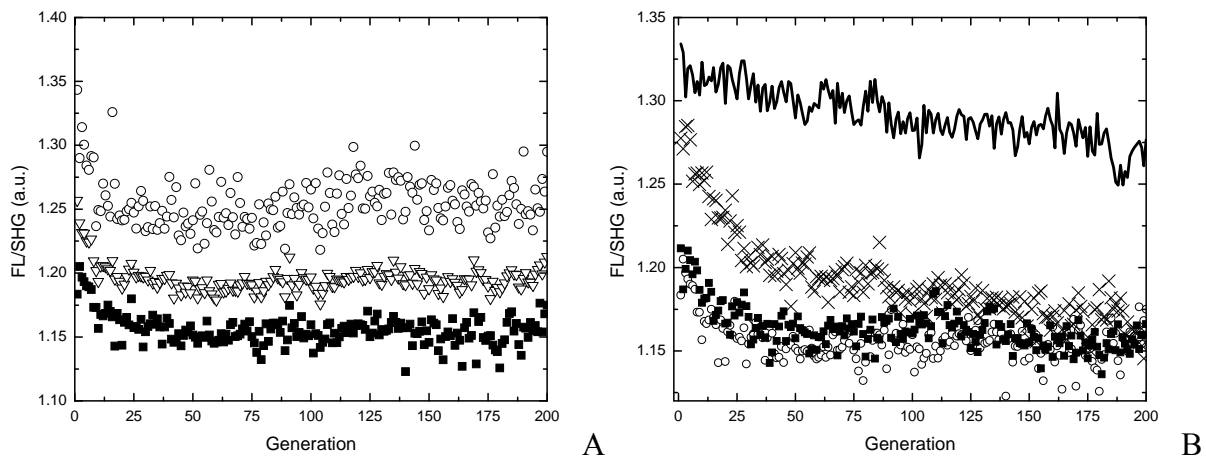


Figure 5-6. A) Fitness evolution of typical experiments of minimization of fluorescence efficiency. B) Experimental convergence reproducibility.

In the evolution curves, the average ratio becomes constant after approximately 50 generations, indicating that the algorithm found a minimum. When compared to the previous experiment, the curve corresponding to the ratio values of the best individuals shows a larger noise to signal ratio. This could suggest a solution trapped in a local minimum. However, the analysis of the convergence reproducibility (Figure 5-6 (B)) for experiments starting with very

different pulses (different fitness) clearly shows that another optimization produces the same effect excluding the previous possibilities. Again, one experiment did not converge to the same objective, although no laser stability issues were observed during the optimization.

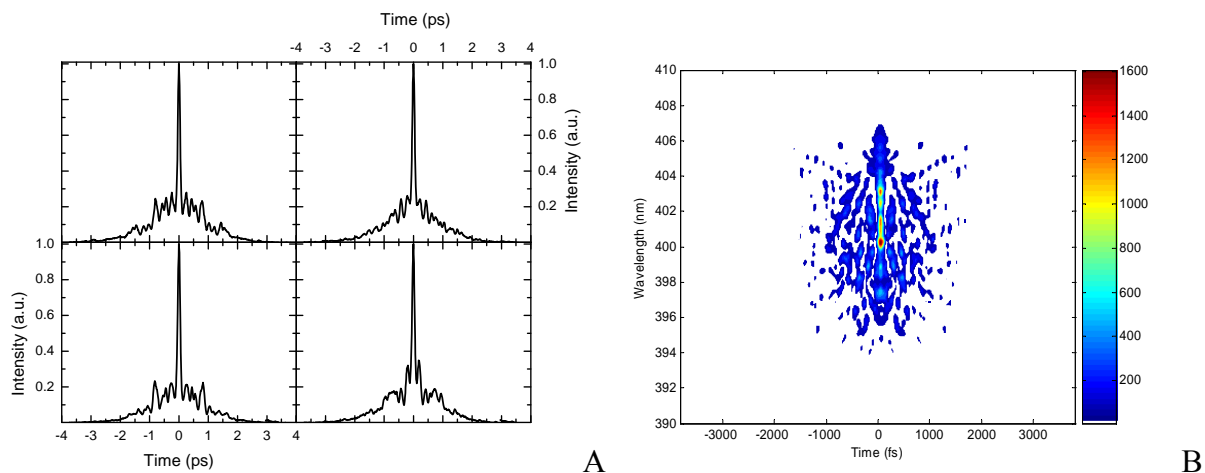


Figure 5-7. A) Optimal autocorrelation. B) Typical SHG-FROG trace of the optimal pulse.

Agreeing with the observed convergence, the autocorrelation of the optimal pulse shows that the minimization of the fluorescence efficiency is not achieved by modulating the pulse to a very long featureless pulse, instead, by modulating it such it converge to a relatively short complex pulse. Similar to the fluorescence maximization experiments, the optimal pulses present a subpulse structure.

Interestingly, a comparison between the optimal pulse for the maximization or minimization of fluorescence efficiency reveals a counter intuitive result: the pulses that maximizes efficiency is significantly longer than the one that minimizes the process, suggesting solutions specifically designed to match molecular properties of Rhodamine 6G. A similar effect has been observed in an analogous study performed by Brixner et al.³¹

The optimal control of the fluorescence efficiency manipulates the photophysics of Rhodamine 6G, but it does not provide direct information about the process(es) being controlled. To understand where or how the quantum control is achieved, it is necessary to investigate the

nature of the states involved in the photoprocess, which can be inferred from power dependence studies.

Power Dependence

Since this study is based on populating an excited state via multi-photon absorption, a power dependence study will reveal which singlet state is initially populated. It is important to note that even in the case of third interaction with the electric field, the power dependence will not show this interaction, if the 3rd interaction follows a two-photon resonant process. The intensity of the excitation source is enough to produce high order interactions, considering that excited electronic state populations usually have a large and reachable manifold of higher electronic excited states where they can be further transferred. In this case the excitation energy is not in resonance with the S_1 to S_0 transition, so a third interaction will only promote the already excited state to a higher excited state, but it will not increase or decrease the population in the initially excited state. Another case, contemplates the possibility of creating two or more wave packets in the same excited state. As stated before the formation of those wave packets depends on the square of the excitation and so does the emission produced after their interaction. The two-photon stimulated emission is not considered to play a major roll in this process because it has only been observed at very high field intensities.⁵⁵

The states that can be reached with this source are only those whose energies are resonant with two or three photon transitions since the near infrared source can only induce the emission of Rhodamine 6G through a multi-photon excitation. The laser intensity on the sample is high enough to produce a three photon excitation, therefore we measure the power dependence of each of the optimized pulses. For comparison purposes, the power dependence corresponding to a transform limited pulse is also investigated.

Figure 5-8 shows the dependence of the fluorescence and the second harmonic signal to power of the excitation pulse for the experiments performed with a transform limited pulse (open triangles), the pulse obtained after maximization of fluorescence efficiency (solid black squares), and the pulse obtained after minimization of fluorescence minimization (black stars).

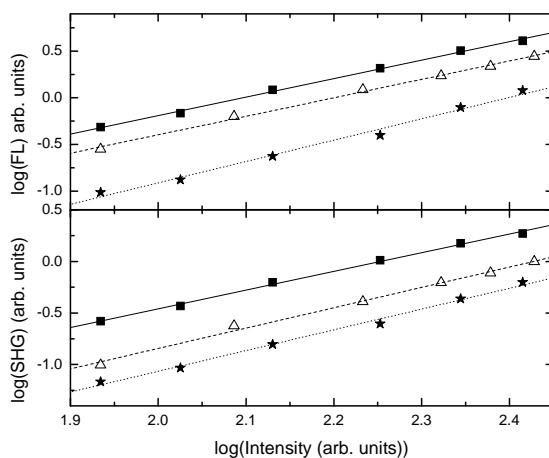


Figure 5-8. Power dependence of the different pulses. Top panel, fluorescence intensity dependence. Lower panel, second harmonic intensity dependence.

A linear fitting of the intensity dependence trend for each curve exhibits slopes always close to 2 (Table 5-1), confirming the two-photon behavior in both fluorescence and second harmonic signals for each particular pulse.

Table 5-1. Power dependence linear fit results.

Pulse	Linear fit		y intercept		$10^{\log(a/b)}$
	Slope		FL (a)	SHG (b)	
	FL	SHG			
Transform limited	1.97	1.81	-4.14	-4.09	0.89
Maximization experiment	1.97	1.97	-4.35	-4.79	2.75
Minimization experiment	2.29	2.01	-5.49	-5.09	0.25

This second order intensity dependence confirms that the state reached with the 800 nm excitation corresponds to a state located at 25000 cm^{-1} above S_0 , which is the dark state S_2 .

In contrast to the slope values, y-interceptions of the linear fittings (Table 5-1) have different values for each curve, showing a change in the response between the investigated signals of fluorescence and second harmonic. A second order response can be expressed as

$$r^{(2)} = aI^2, \quad (5-1)$$

where a represent a proportionality constant which is strictly related to the process and the detection, and I is the intensity of the excitation pulse. In the log-log plot, the intercept is the $\log(a)$ and is represented by the y interception. When the two responses are plotted against each other, the obtained slope is given by the ratio of these proportionality constants. Those slopes can be evaluated using the intercepts from the linear fit of the power dependence.

The different y intercepts indicates that the optimum pulses should have different slope in a fluorescence-second harmonic representation.

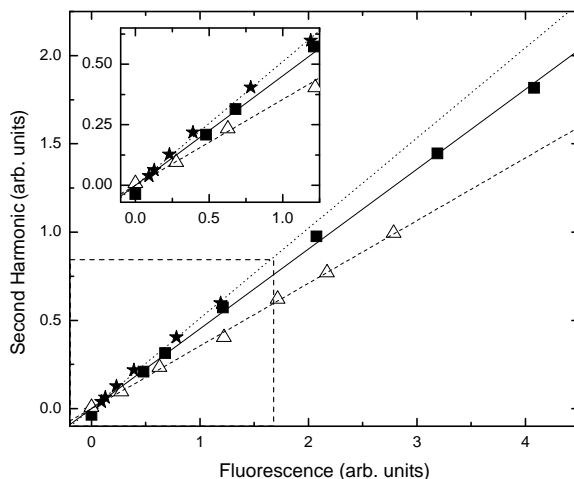


Figure 5-9. Power dependence in fluorescence-second harmonic space. Fluorescence maximization (squares). Fluorescence efficiency maximization (stars) and minimization (triangles). Zoom of the lower left corner of the plot (inset).

The representation of the optimal pulses in the [SHG, FL] space is shown in Figure 5-9. It shows that each optimization of a different goal presents a different slope, and that they evolve in different zones of this variable space. Since these signals represent the molecular and field responses, the magnitude of the slope provides insight into the optimization process. For

instance, comparison of maximization and minimization of the fluorescence efficiency reveals that the former explores a region of higher intensity of the laser field while the latter stays within regions of lower electric field intensities and emission.

Optimization Analysis

As shown in the previous section, a good representation to study the evolution of the optimization process is the fluorescence versus second harmonic signal space. Figure 5-10 shows the second harmonic signal and fluorescence intensities for all the tailored pulses tested in the optimization of the fluorescence efficiency. In addition to these two optimizations, the experiment in which only the fluorescence is optimized (equivalent to pulse compression) is also included.

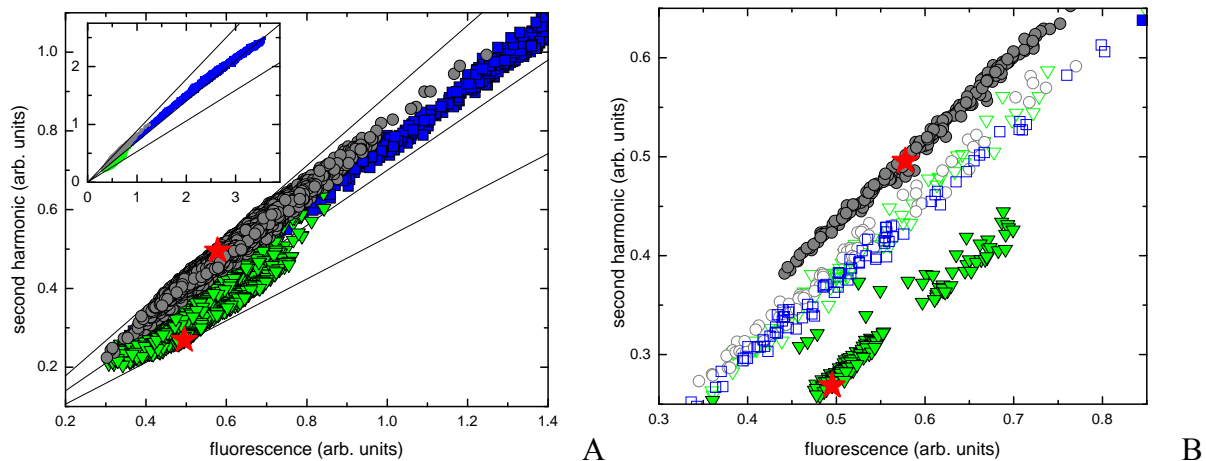


Figure 5-10. Variable space. A) All individuals of each experiment: maximization of fluorescence (blue squares), maximization of fluorescence efficiency (green triangles), and minimization of fluorescence efficiency (grey circles). B) Fitness for the best individuals on each generation of each experiment and fitness for individuals with random phases.

Looking at Figure 5-10(B), the data presented in this variable space can be separated in three distinctive regions. The center region corresponds to fitness arising from pulses with random phases and pulses leading to the optimization of fluorescence alone. Below that region are the best individuals corresponding to the optimization in which a maximum of fluorescence

over second harmonic signal ratio was sought and above all are the individuals corresponding to an evolution in which the goal was the minimization of the ratio. These three regions denote the physical limits of the searched space because each fitness goal is specifically designed to reach the extremes of this space. In addition, it confirms that each optimization reaches an independent solution (red stars). The extreme slopes show in Figure 5-10 are related to the optimization improvement with respect to the experiment with a transform limited pulse.

Although this representation shows the correlation between the variables and the achieved objective it does not reflect either the attained convergence or the generational evolution of the optimization variables. The region explored by each optimization appears as a delocalized area where more than one solution for each problem can be found. A new representation is necessary to better understand the evolution of the fitness. We plot the ratio of fluorescence over second harmonic signal (fitness) value versus the difference in the signals.

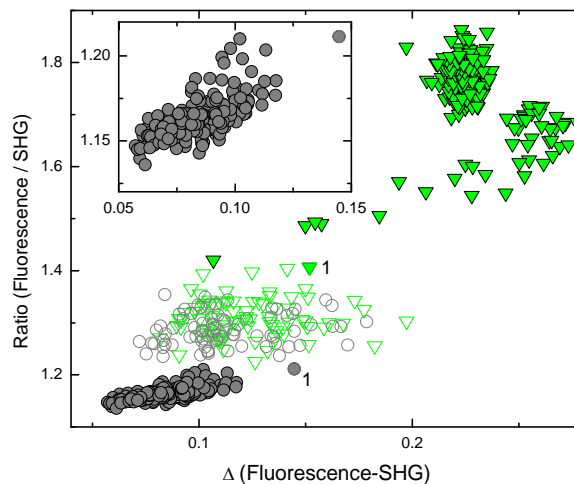


Figure 5-11. Variable space in using ratio and difference of signals. Inset shows a zoom of the left corner of the plot. Individuals corresponding to the fluorescence efficiency maximization (triangles) and minimization (circles).

Figure 5-11 shows the new space for the coordinates of the best individual in each generation (solid shapes) and for the coordinates of random initial pulses (open shapes).

The evolution of the chosen variables for both experiments displays different optimization mechanisms. The pathway corresponding to the maximization exhibits a complex optimization route: starting with a random pulse (see label 1 on Figure 5-11) the data moves horizontally with changes occurring mainly on the “difference” axis. This is followed by a simultaneous change in both axes reaching an area in which the difference in signals is not pronounced, but in which the ratio has been improved. In contrast the minimization shows evolution only on the difference axis while keeping the ratio constant. This implies that both variables are changing their magnitude approximately by the same amount in the minimization.

Although the optimization starts in the same area of the explored space (open circles, Figure 5-11), the convergence zones for each objective are clearly delimited in opposite regions. Also, the convergence zone for the maximization of the fluorescence efficiency is localized and the zone reached by the minimization is not. This suggests that the variable space landscape has local extremum zones with different shapes: the maximization falls into a well while the minimization remains in a more shallow area.

Fluorescence Spectrum Control

In this thesis we shall try to develop new experiments that can provide insight into the quantum control mechanism. With this goal in mind, we performed an optimization experiment with the objective of controlling the final Franck-Condon state localization in the first excited state. The proposed experiments optimize selectively the low energy region of the emission spectrum. The new fitness function, defined as the ratio of the intensity of the red side fluorescence (Figure 5-12) over second harmonic, biases the optimization towards those transitions with lower energies. The fluorescence spectrum shape is given by the overlap of the wavefunction of the vibrational ground state of the first electronic excited state with the various wavefunctions of the vibrational states of the electronic ground state. An optimization of only the

red side of the emission spectrum could only be produced by an important modification of the potential energy surfaces (strong field control) or by affecting the wave packet evolution such that the internal vibrational relaxation promotes the excited state to a different region of the excited state inevitably changing the Franck-Condon coefficients and consequently the fluorescence spectrum.

To acquire only the red side of the emission spectrum (grey area, Figure 5-12), a 550 nm long-pass filter is placed in front of the photomultiplier.

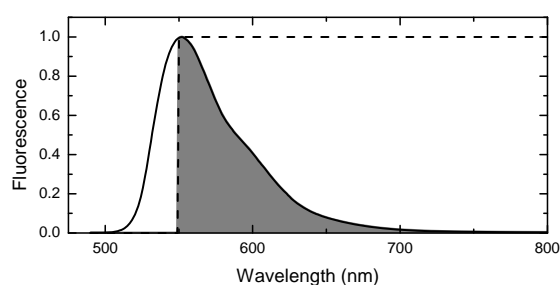


Figure 5-12. Spectrum measured with the cutoff filter (grey area).

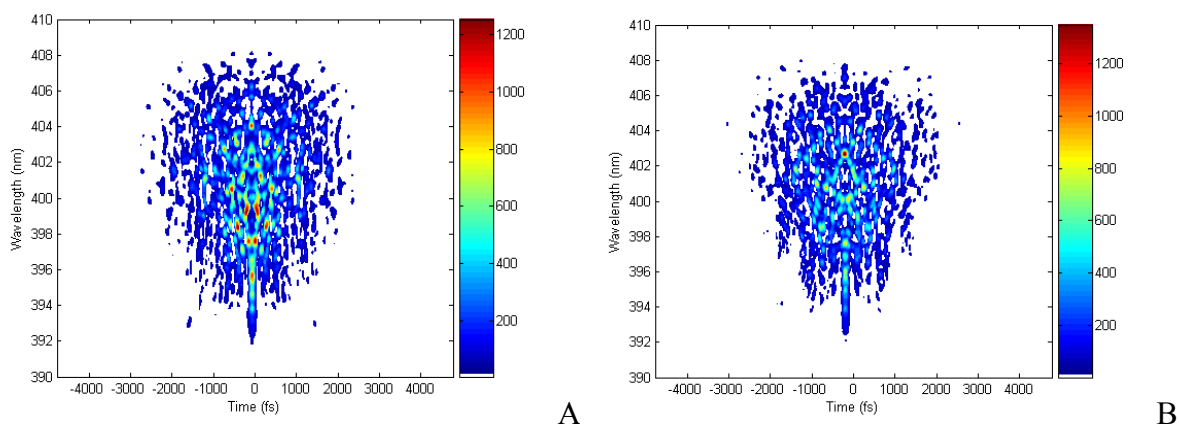


Figure 5-13. FROG traces for different experiments. A) Maximization of fluorescence efficiency when the whole spectrum is collected. B) Maximization of red side fluorescence over second harmonic.

These experiments produce ratio performances similar to those optimizations in which the total fluorescence over second harmonic is measured. Also, the FROG traces of the optimal pulses have a strong resemblance to their counterpart on the experiments with the total

fluorescence. Therefore, we discard a control mechanism based on changing the final position of the wave packet or a strong field control.

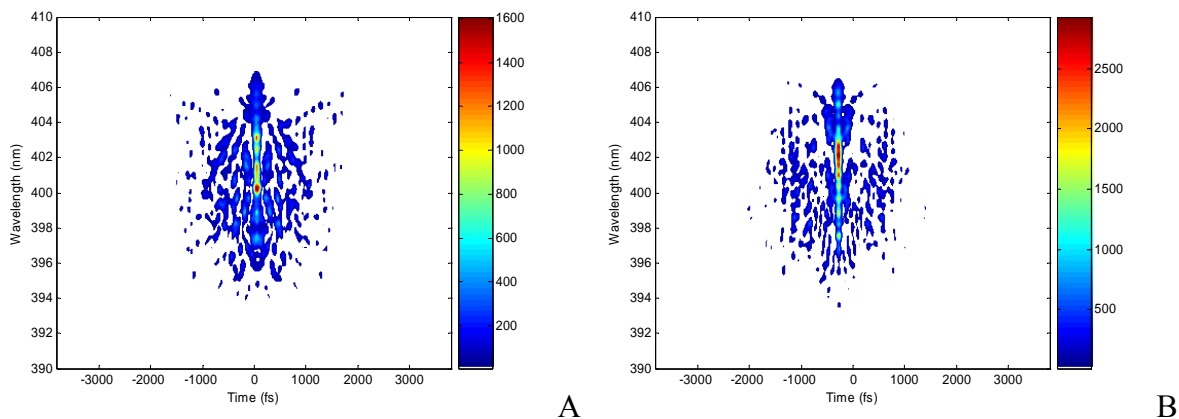


Figure 5-14. FROG traces for different experiments. A) Minimization of fluorescence efficiency minimization when the whole spectrum is collected. B) Minimization of red side fluorescence over second harmonic.

Relationship between Objective and the Genetic Algorithm Solutions

We performed an experiment in which the cost function only includes signals from different regions of the emission spectrum to confirm the lack of control over the spectrum. The proposed fitness is the intensity of the red side of the emission spectrum over the total fluorescence intensity.

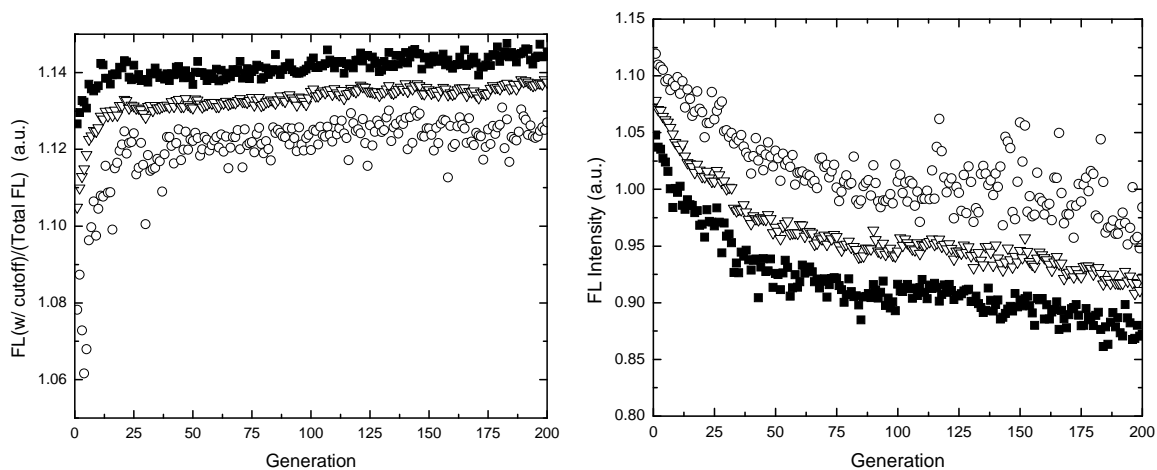


Figure 5-15. A) Fitness evolution of maximization of spectral control. B) Evolution of the cost function for minimization of spectral control.

Two photomultiplier detectors with different combinations of band pass filter are employed to collect the different signals. Due to the lack of control over the spectrum observed in the previous experiment, we expected that the fitness function will oscillate and change randomly without ever converging to any solution.

Instead, both experiments present an optimization of the fitness which contradict our initial speculations (Figure 5-15). Two possible scenarios can be occurring during the optimization. The first involves an actual optimization of the spectrum, which is discarded due to the results previously obtained. The second possibility concerns the role of noise and its optimization in an evolution process. The cost function used is

$$f = \frac{F_{red}}{F_{total}}, \quad (5-2)$$

where F_{red} , F_{total} represent the low energy region of the fluorescence and the overall fluorescence, respectively. The error in the cost function is

$$\Delta f = \frac{1}{F_{total}} \Delta F_{red} + \left| -\frac{F_{red}}{F_{total}^2} \right| \Delta F_{total}. \quad (5-3)$$

The fitness error function might explain the pseudo optimization achieved in these experiments. In Equation 5-2 and 5-3, it is observed that as the fluorescence is either minimized(maximized), the fitness noise is increased(decreased). Assuming a constant error in all the ranges of fluorescence integrated intensity, this error optimization is due to the inverse relation with the fluorescence value, which produces the above inverse relationship in the error function.

To avoid this problem a function where the noise does not increase when the magnitude of the signals goes to zero is created. The new cost function is

$$f = (F_i - F_j) \frac{F_i}{F_j}. \quad (5-4)$$

Note that the error function for this fitness function is

$$\Delta f = \left| \frac{2F_i}{F_j} - 1 \right| \Delta F_i + \left| -\frac{F_i^2}{F_j^2} \right| \Delta F_j. \quad (5-5)$$

Comparing with the other fitness error (Equation 5-3), this fitness error is not maximized(minimized) when fluorescence signals decrease(increase).

Two experiments are performed with this new noise independent cost function. Here the feedback signals are the blue and red side intensities of the emission spectrum. In the first optimization F_i is the blue side and F_j is the red side, and in the second their role is reversed. Since the optimization aims to optimize one side of the spectrum at the expense of the other, both experiments seek the maximization of this new cost function.

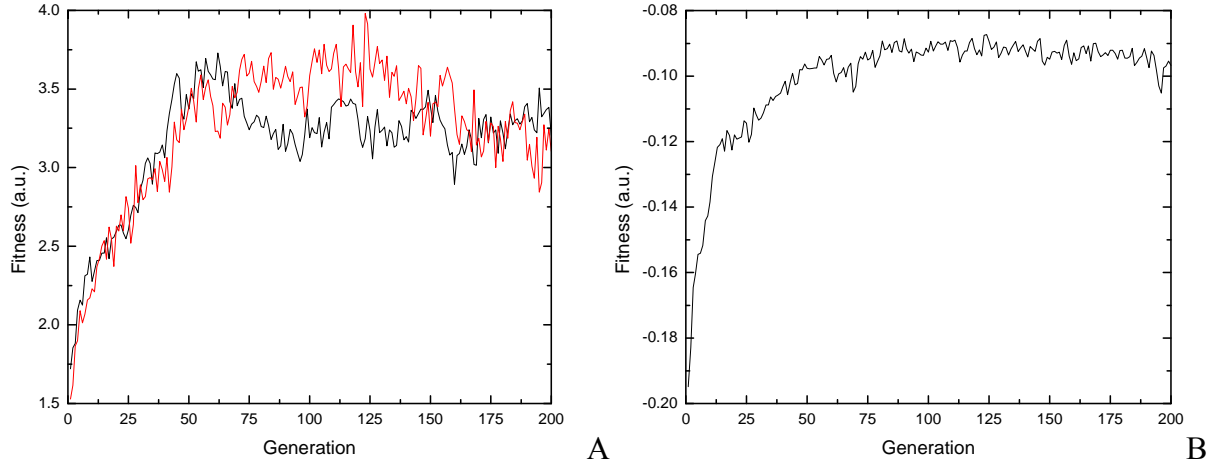


Figure 5-16. A) Fitness evolution of the cost function $(F_R - F_B)F_R/F_B$ (black line) and simulated evolution of the cost function $(F_B - F_R)F_B/F_R$ (red line). B) Fitness evolution of minimization of spectral control (black line).

Again, the experimental results using the new fitness function (Equation 5-4) show optimization, i.e. an increase in the value of the cost function (black lines, Figure 5-16(A) and

(B)). To understand which process is being optimized, we use the raw data collected in the optimization of $(F_R - F_B)F_R/F_B$ and use it to simulate the evolution of the function $(F_B - F_R)F_B/F_R$. A perfect agreement between both fitness is found (red line, Figure 5-16(A)). This implies that even though we discard fitness noise optimization during the experiments, two different optimizations with opposite objectives are producing the same effect.

To find out why the fitness is optimized in all these experiments, the raw signal corresponding to the first spectral control (cost function intensity of the red side over the whole spectral intensity) experiment is analyzed (Figure 5-17).

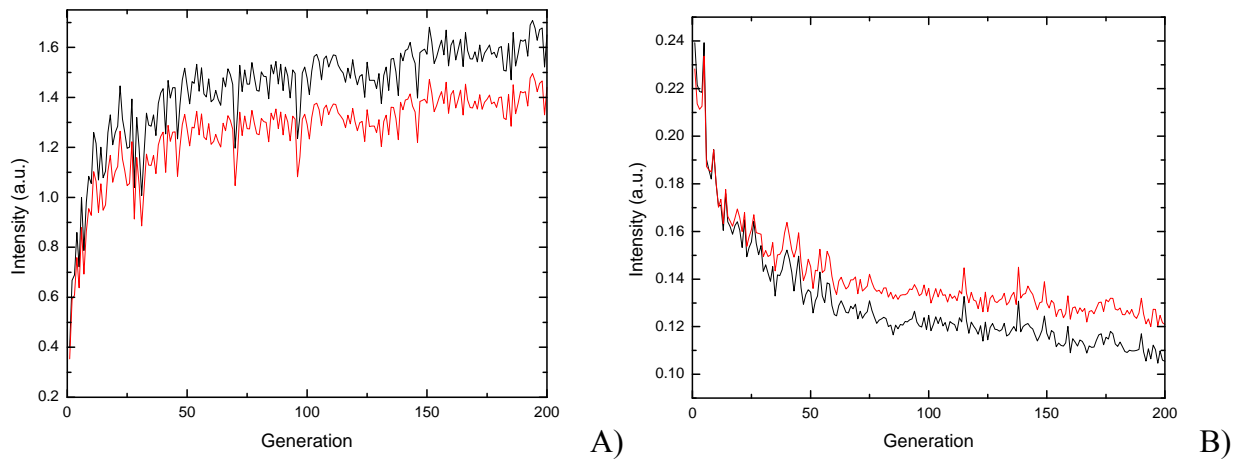


Figure 5-17. Signal of fluorescence spectral control experiments. A) Maximization, fluorescence (black line) and second harmonic signals (red line) B) Minimization, fluorescence (black line) and second harmonic signals (red line).

From Figure 5-17, it is possible to observe that both signals have exactly the same noise. As expected, these signal trends contradict the noise optimization model because for noise maximization the minimization of both variables is required, and vice versa. Depending on the experiment, second harmonic signal presents higher values than the red side for the maximization, and vice versa. This implies that a crossing in the magnitude of the signals is taking place.

A simple mathematical model can be used to describe the optimization effect. The fluorescence signal can be expressed as

$$F_i(I) = a_i + b_i I^2, \quad (5-6)$$

where I represents the intensity of the excitation laser, a is the response of the detector for zero intensity, and b is a parameter that includes the detector response, the transmission of the color filter, and the two-photon fluorescence quantum yield. Using that the intensity is the same for both fluorescence signals (red and total), and a mathematical relationship between the fluorescence signals is obtained

$$F_{total} = a_{total} - \frac{a_{red} b_{total}}{b_{red}} + \frac{b_{total}}{b_{red}} F_{red} = a' + b' F_{red}. \quad (5-7)$$

Since the fitness is defined by the ratio of fluorescence intensities (Equation 5-2), replacing the relation between the detector signals we obtain

$$f = \frac{F_{red}}{F_{total}} = \frac{F_{red}}{a' + b' F_{red}}. \quad (5-8)$$

This fitness function depends on the value of the red fluorescence intensity. To understand its behavior the limits of the function can be analyzed.

$$\lim_{F_{red} \rightarrow 0} \frac{F_{red}}{a' + b' F_{red}} = 0 \quad (5-9)$$

and

$$\lim_{F_{red} \rightarrow \infty} \frac{F_{red}}{a' + b' F_{red}} = \frac{1}{b'}. \quad (5-10)$$

These limits show that the fitness is modulated by the intensity of the red fluorescence and the actual cause of the optimization is the a' term in the fitness, which is given by the difference in background signals produced by both detectors. This simple model explains the observed

trends of the fitness and the crossing between the signals with different intensities. To avoid this pseudo optimization, it is necessary to make the background signals as close to zero as possible and to maintain both detectors in similar gains.

Discussion

Physical Interpretation of the Fitness

Besides the mathematical description of the fitness of the fluorescence efficiency, we can also try to interpret fitness in terms of the physics of the process. Since fluorescence and second harmonic signals depend on the square of the intensity, a long temporal pulse not only leads to small fluorescence signals, but also minimizes the second harmonic signal. When the ratio of these signals is minimized, the changes are compensated preventing the system from evolving towards a long structureless pulse. A similar conclusion is observed with the maximization of second harmonic signal and the effect of pulse compression. If no molecular property of the system is involved in the optimization, the fluorescence efficiency cannot be optimized because both fluorescence and second harmonic signal follow the same intensity dependence. This can be observed using the model previously described (Equation 5-6). Consider a simple case in which the detectors do not have a background signal ($a=0$) and the measured signals are fluorescence and second harmonic; the fluorescence over second harmonic fitness becomes:

$$f = \frac{S_{FL}}{S_{SHG}} = \frac{a + bI^2}{a + b'I^2} = \frac{bI^2}{b'I^2} = \frac{1}{b''}. \quad (5-11)$$

Thus no matter what type of optimization is performed all the solutions will be located in a line with constant fitness. As observed in the variable space as well as in the power dependence experiments, a slope change in the fluorescence-second harmonic optimization is observed when this fitness function (Equation 5-11) is optimized, confirming the control of molecular properties of Rhodamine 6G.

Molecular Interpretation of the Fitness

All the experimental evidence points to a control of the fluorescence efficiency with pulses specifically adapted to match certain molecular properties of Rhodamine 6G. It is useful to describe fluorescence/second harmonic fitness in terms of molecular and laser field properties to understand the molecular manipulation produced in the optimization. Using perturbation analysis, a simple model can be derived. This perturbation model was first developed by Silberberg et al.⁴² and later extended by Gerber et al..³¹

Perturbation Analysis

Time dependent perturbation theory can describe the two-photon absorption process. A quantum system originally located in the stationary state $|g\rangle$ can be promoted to the final state $|f\rangle$ with an electric field interaction at time t_0 . In the limit of a small perturbation and assuming no resonance with any real intermediate or final state, the amplitude of the final state can be expressed as (see Appendix B for full derivation)⁴²

$$a_{|f\rangle}(t) = -\frac{1}{\hbar^2} \sum_n \langle f|\mu|n\rangle \langle n|\mu|g\rangle \int_{-\infty}^t \int_{-\infty}^{t_1} E(t_1) E(t_2) e^{i(\omega_f t_1 + \omega_n t_2)} dt_1 dt_2 . \quad (5-12)$$

Here, $\langle i|\mu|j\rangle$ are the dipole matrix elements between the $|i\rangle$ and $|j\rangle$ states, and ω_{ij} is the corresponding energy difference between those states,

$$\omega_{ij} = (E_i - E_j)/\hbar . \quad (5-13)$$

In the case of short interaction, the coherent contribution of all intermediate levels will also be short, hence it is possible to approximate the summation term in the amplitude (Equation 5-11) by

$$\sum \mu_{fn} \mu_{ng} \exp[iE_n(t_2 - t_1)/\hbar] = \begin{cases} \sum_n \langle f | \mu | n \rangle \langle n | \mu | g \rangle, & |t_2 - t_1| < (\omega_{ng} - \omega/2)^{-1} \\ 0, & |t_2 - t_1| \geq (\omega_{ng} - \omega/2)^{-1}. \end{cases} \quad (5-14)$$

The transition probability for the two-photon process is

$$p_{TPA} = \frac{1}{\hbar^4} \left| \sum \frac{\langle f | \mu | n \rangle \langle n | \mu | g \rangle}{\omega_{ng} - \omega_{fg}/2} \right|^2 \left| \int_{-\infty}^{\infty} E^2(t) \exp(i\omega_{fg}t) dt \right|^2. \quad (5-15)$$

The frequency domain representation of the probability is

$$p_{TPA} = \frac{1}{\hbar^4} \left| \sum \frac{\langle f | \mu | n \rangle \langle n | \mu | g \rangle}{\omega_{ng} - \omega_{fg}/2} \right|^2 \left| \int_{-\infty}^{\infty} E(\Omega) E(\omega_{fg} - \Omega) d\Omega \right|^2. \quad (5-16)$$

This last expression shows that the two-photon absorption process can be decomposed in two independent factors.

$$g_{TPA} = \frac{1}{\hbar^4} \left| \sum \frac{\langle f | \mu | n \rangle \langle n | \mu | g \rangle}{\omega_{ng} - \omega_{fg}/2} \right|^2 \quad (5-17)$$

$$S_2 = \left| \int_{-\infty}^{\infty} E(\Omega) E(\omega_{fg} - \Omega) d\Omega \right|^2 \quad (5-18)$$

While the former represents the properties of the molecule, the later shows the electric field characteristics. The presence of the electric field in Equation 5-18 is one of the most important results of the perturbation model because it demonstrates that the two-photon transition probability can be modulated by varying the second order power spectrum of the excitation source, S_2 .

In the limit of very broad inhomogeneous lines, the transition probability is the summation over all the possible states⁶³

$$p_{TPA} \approx \int g_{TPA} \rho(\omega) S_2(\omega) d\omega, \quad (5-19)$$

where $\rho(\omega)$ is the excited state density of states.

Second harmonic intensity as a function of the fundamental electric field can be expressed as¹¹⁰

$$I_{SHG}(2\omega) = \left(\frac{\chi^{(2)} \omega_2^2 L}{4c^2 k_2} \right)^2 \text{sinc}^2 \left\{ \left[\left(\frac{1}{v_2} - \frac{1}{v_1} \right) \omega - \Delta k \right] \frac{L}{2} \right\} \left| \int_{-\infty}^{\infty} E(\Omega) E(\omega - \Omega) d\Omega \right|^2, \quad (5-20)$$

where $\chi^{(2)}$ is the second order susceptibility, L is the crystal length, ω is the fundamental frequency between the fundamental and second harmonic fields, Δk is the phase mismatch, and v_1 and v_2 are the group velocities of the fundamental and second harmonic wave, respectively.

Similarly to the two-photon absorption probability, second harmonic generation can be decomposed into two terms: g_{SHG} and S_2 :³¹

$$g_{SHG}(\omega) = \left(\frac{\chi^{(2)} \omega_2^2 L}{4c^2 k_2} \right)^2 \text{sinc}^2 \left\{ \left[\left(\frac{1}{v_2} - \frac{1}{v_1} \right) \Omega - \Delta k \right] \frac{L}{2} \right\} \quad (5-21)$$

and

$$S_2 = \left| \int_{-\infty}^{\infty} E(\Omega) E(\omega_{fg} - \Omega) d\Omega \right|^2. \quad (5-22)$$

The first term depends on the properties of the nonlinear material while the second term is the integrated second order power spectrum. The signals measured in this experiment are then

$$I_{FL}(\omega) = N_m \cdot p_{TPA} \cdot \Phi_{FL} \quad (5-23)$$

and

$$I'_{SHG} = \int I_{SHG}(\omega) d\omega, \quad (5-24)$$

where N_m is the total number of molecules present in the irradiated volume, p_{TPA} is the two-photon absorption probability, Φ_{FL} is the quantum yield of two-photon induced fluorescence, and I'_{SHG} is the second harmonic intensity integrated over the fundamental wave. The fitness becomes

$$f = \frac{I_{FL}}{I'_{SHG}} = \frac{N_m P_{TPA} \Phi_{FL}}{I'_{SHG}} = \frac{N_m \Phi_{FL} \int g_{TPA} \rho(\omega) S_2(\omega) d\omega}{\int g_{SHG} S_2(\omega) d\omega}. \quad (5-25)$$

Removing all the constants and assuming the second harmonic generation efficiency (g_{SHG}) to be constant across the laser excitation spectrum, the fitness can be described by

$$f \propto \frac{\int g_{TPA} \rho(\omega) S_2(\omega) d\omega}{\int S_2(\omega) d\omega}. \quad (5-26)$$

This model of the fitness expresses the possibility of controlling the molecular system by changing the second order power spectrum, $S_2(\omega)$.

The validity of this simple model was demonstrated by Joffre and coworkers using a second order interferometric autocorrelator in different dye samples in solution.⁴³ They prove that the two-photon excitation spectrum ($g_{TPA} \rho(\omega)$) is the main controllable feature within the optimization process.

There is experimental evidence that supports a flat two-photon cross section of Rhodamine 6G in the spectral region of our excitation source.^{135, 137} If this is the case, this optimization step can be discarded from the control steps because it will imply a constant $g_{TPA} \rho(\omega)$. This suggests that control over the two-photon absorption is not the critical component. Furthermore, our spectral control experiments confirm the lack of control in the relaxation process in S_1 , which agrees with the ultrafast internal vibrational relaxation times observed in this system.

Summary

In this work, Rhodamine 6G two-photon induced emission is successfully controlled using phase modulated femtosecond pulses. In the performed experiments, the closed loop optimization produces phase adapted femtosecond pulses. The adaptation can be driven by stationary, two-photon excitation spectra, as well as dynamic properties of the system.

Interestingly, the pulses that optimize the fluorescence efficiency are not necessarily the shortest ones. The presence of a specific time distribution of the different frequencies within each excitation pulse might signify the control over the wave packet dynamics in the excited state. The multipulse structure observed in the optimization of the fluorescence efficiency might be associated with the optimization of a specific deactivation channel (vibrational mode) in the molecular electronic manifold, indicating that when the power dependence is removed, the algorithm finds a new solution which contains molecular properties. To confirm this possibility, different studies using pulse sequences are necessary.

Finally, spectral control experiments have shown how important the selection of the fitness and the conditioning of the feedback signals are to avoid fake optimizations.

CHAPTER 6 COHERENT CONTROL OF ENERGY TRANSFER

Introduction

Optimal control using pulses with phase, and/or amplitude, and/or polarization modulation, has been successfully used to govern a variety of processes.^{24, 51, 77, 85} Many of these experiments involved the simultaneous measurement of two signals arising from independent processes.⁶³ In this work, we explore the optimal control of energy transfer between donor and acceptor moieties. Moieties with efficient energy transfer must have a strong electronic coupling; thus their states can not be independently modulated, but one state can be modulated at the expenses of the other.

Resonance energy transfer involves Coulombic coupling between an excited state donor and an acceptor. The relative strength of the coupling between donor and acceptor compared to their spectral overlap (the resonance condition) defines the efficiency and mechanism of the energy transfer process.¹⁴⁹ Arbitrary preparation and manipulation of the donor's excited state can then influence the coupling strength, and therefore manipulate the energy flow. One possible way of influencing the donor's excited state is by negatively interfering those relaxations pathways that do not contribute to the energy transfer, indirectly increasing the coupling efficiencies. Depending on the control objective, optimal control can be used to enhance the system's absorption or to prepare a particular coherent superposition of states that will optimize (maximize/minimize) the moieties coupling. However, molecular systems with energy transfer present other properties that can change the energy transfer efficiency and consequently make its manipulation difficult. One important property is the rigidity of the donor-acceptor system. Energy transfer efficiency depends on the donor-acceptor distance and their transition dipole moment orientation. Many molecular systems including those generally used for fluorescence

resonant energy transfer (FRET) have flexible backbones, thus their energy transfer efficiency is also governed by their molecular dynamics. To prevent this problem, a molecule with a constant donor-acceptor distance should be used. The other important property is the acceptor excitation cross section. To avoid direct excitation, the acceptor cannot have a significant one or two-photon cross section in the wavelength region of the excitation source or, if excited, it has to be uncontrollable. This guarantees that the acceptor emission (and its modulation) is arising exclusively from energy transfer. These two properties are intrinsic to the molecule, so special care should be taken when choosing a system to perform quantum control.

This study is focused on controlling the energy transfer process in 2G2-m-Per using phase modulated two-photon excitation pulses. We investigate the control of the energy transfer process by preparing and controlling those coherent states that lead to the coupling from donor to acceptor purposely avoiding optimization of the absorption process. The motivation for these experiments is not only to prove that control over the energy transfer process is feasible, but also to understand the important frequency and time domain parameters that induce the change in the energy transfer process. In addition, we use the results from a closed loop experiment to find the crucial parameters to be explored in an open loop experiment.

Donor Acceptor System

The system under investigation is a phenylene ethynylene dendrimer, 2G2-m-Per,^{IV} which was specifically designed to mimic light harvesting systems.¹⁵⁰ Phenylene ethynylene dendrimers are rigid donor/acceptor macromolecules with an extremely high quantum yield for energy transfer.^{150, 151} 2G2-m-Per architecture is designed such that the donor is the dendrimer,

^{IV} 2G2-m-Per a second generation dendrimer with two monodendron on *meta* positions and a ethynylene perylene trap.

and the acceptor is an ethynylene perylene covalently bond to the dendritic backbone (see Figure 6-1(A)).¹⁵²

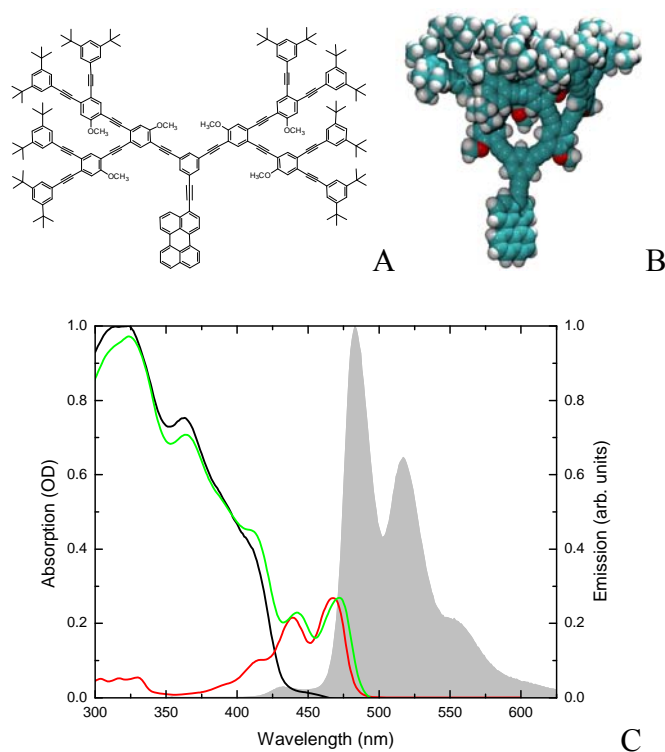


Figure 6-1. A) Chemical structures of phenylene ethynylene dendrimer: 2G2-m-Per. B) 3D model of the 2G2-m-Per. C) Absorption (green line) and emission (grey area) spectra of 2G2-m-Per, and absorption of 2G2-m-OH (black line) and ethylene perylene (red line)

The dendrimer presents a folded spatial arrangement with all the dendritic branches packed in a bouquet-like 3D spatial arrangement.¹⁵¹ The energy transfer donor consists of two identical and indistinguishable monodendrons that in the ground state are electronically decoupled because of their *meta* connectivity. However, within the monodendron the different length phenylene ethynylene units are bonded in *ortho* and *para* substitution creating extended π conjugated electronic states with broad absorption bands.¹⁵¹ A phenylethynylene perylene acceptor is bonded to the donor's backbone in *meta* position, which creates donor and acceptor moieties with only a weak coupling in the ground state. This weak coupling results in an

absorption spectrum for the whole molecule which is approximately equal to the sum of absorption spectra of its moieties (Figure 6-1(C)).¹⁵¹

In 2G2-m-Per, an initial excitation is delocalized within each monodendron and the donor-acceptor *meta* connectivity confines the exciton within the monodendrons until it is further transferred to the acceptor. Time resolved spectroscopy previously performed in our group showed that upon single photon excitation the exciton migrates from the initially excited state through two different pathways to the acceptor (Figure 6-2).¹⁵¹ While one pathway consists of an initial step within the dendrimer backbone and a final transfer to the acceptor, a parallel, direct energy transfer involves direct exciton migration from donor to acceptor. Both pathways are completed in a subpicosecond time scale.¹⁵¹ Indirect energy transfer (a funnel type process) involves an incoherent process, but the direct pathway is not understood and it might involve a different initially excited state. This initial state might be a coherent state originated by superposition of spatially close phenylene ethynylene states of the donor.

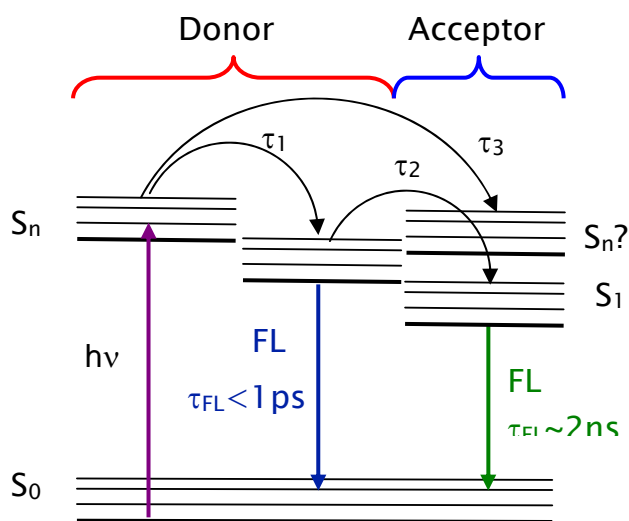


Figure 6-2. Energy diagram and dynamics of 2G2-m-Per. τ_1 , τ_2 , and τ_3 are ~ 0.4 ps, ~ 0.5 ps, and ~ 0.8 ps, respectively.

The calculated quantum yield for energy transfer, using experimental kinetics times of 2G2-m-Per is greater than 99 %, where approximately 60 % and 40 % of the energy transfer occurs via the direct and the indirect processes, respectively.¹⁵¹

Experimental Section

Our experimental setup (Figure 6-3) produces the shaping of pulses generated by a femtosecond amplified laser. The laser source is a Ti:Sapphire amplified system (Spectra Physics, Spitfire®) pumped by a Ti:Sapphire oscillator (Spectra Physics, Tsunami®), operated at 1 kHz repetition rate. This source delivers pulses with 25 μJ energy, Gaussian spectrum centered at 800 nm, a pulse width of 28 nm (FWHM), and temporal duration of 45 fs (FWHM). To avoid energy loss generated by small apertures in some pulse shaper components, a Galilean telescope is used to reduce the beam size to a final 3 mm diameter.

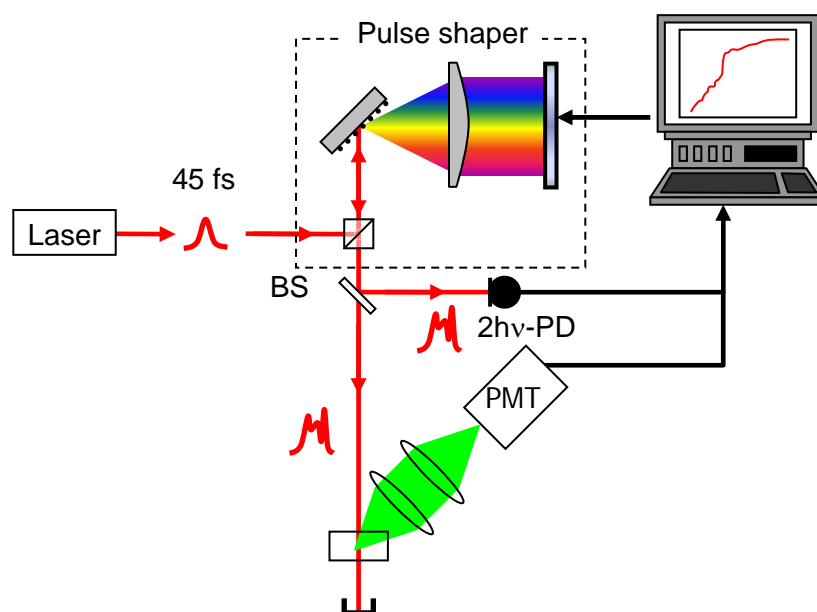


Figure 6-3. Coherent control setup.

Arbitrary phase and amplitude modulation is achieved with a spatial light modulator based pulse shaper. Our pulse shaper setup is arranged in a folded zero-dispersion compressor, and it has been described elsewhere.¹⁵³ The compressor is constructed in a quasi Littrow configuration

(46 degrees for 800 nm) with a 300 mm spherical lens and an 1800 groves/mm holographic grating. This optical configuration has a resolution of 0.13 nm/pixel and a maximum spectral window of ca. 84 nm.¹⁰⁵ The spatial light modulator is a CRI Inc., SLM-640-D-VN®, which has 640 individual pixels, and phase and amplitude modulation capabilities.

Figure 6-3 shows the experimental configuration. Tailored pulses are split twice: a small amount (<4%) is used to generate two-photon induced current in a GaAsP photodiode and the rest is used either to produce the sample excitation or to characterize the pulse's electric field in a multishot SHG-FROG setup. Modulated excitation pulses with an energy of 330 nJ per pulse are focused on the sample with a 50 mm lens which yields a experimental $\sim 24 \mu\text{m}$ diameter and a Rayleigh length of $420 \mu\text{m}$, and produces intensity of $6.8 \times 10^{11} \text{ W/cm}^2$ on the sample. The lens position is carefully set to maximize the emission produced by the sample.

The sample is held in a 2 mm optical path quartz cell with a magnetic stirrer to ensure fresh sample for each excitation pulse. Since the two-photon cross section is much smaller than the linear cross section, higher sample concentrations (OD=0.4) are used in the region equivalent to one photon excitation (400 nm). The emission signal is collected front face at 45 degrees with respect to the excitation beam with a photomultiplier tube (PMT) to avoid self absorption. A two-photon induced signal is obtained by focusing the laser beam on a GaAsP photodiode. Since GaAsP's band gap is 680nm, the generated photocurrent is a two-photon intensity dependent process similar to second harmonic generation.¹⁵⁴ In contrast to the second harmonic generation in doubling crystals, the generated photocurrent does not have the constraints present in these nonlinear mediums, such as short pulses' bandwidth phase matching and acceptance angles. Fluorescence and two-photon induced currents are processed with a boxcar integrator and acquired with a PC based data acquisition card.

A home written genetic algorithm is used to produce the closed-loop optimization. Our genetic algorithm is based on previously published algorithms and uses roulette wheel for parent selection, random initial population, and special floating point genetic operators for reproduction.¹²⁹ Among their various advantages, these genetic operators yield a fast convergence with a small number of individuals per generation. We used 80 individuals per generation, from which 16 are selected as parents for the next generation. Each new generation is originated through crossover (75 individuals) and cloning (5 individuals). All the individuals are subject to a possible mutation after their creation. Each individual has codified 128 genes (phase parameters) and the 640 phase pixel values are generated through linear interpolation. The genetic pool is optimized for 200 generations.

In the following experiments, the feedback signals are fluorescence and two-photon induced current. The fitness or objective function is defined in the experiments as either the emission or the ratio of emission over two-photon photodiode response. An average of 150 laser shots is used to generate the fitness value of each individual in each generation. Since the noise to signal ratio from our laser system is lower than 3 %, no corrections are made for energy fluctuation when fluorescence is used as fitness. When the ratio of emission over two-photon photodiode response is used, no corrections for power fluctuations are necessary because the two-photon induced current and the fluorescence have the same quadratic intensity dependence. Optimization experiments are repeated at least three times to assure experimental reproducibility. During each experiment we monitor the laser stability by collecting the signals for an extra individual with all its phase coefficients set to zero. This individual is not included in the optimization of the population.

A multishot SHG-FROG is used to fully characterize the optimization pulses (phase modulated pulses) and their electric field is retrieved with commercially available software, FROG Femtosoft Technologies®.¹⁵⁵

Dendrimer samples, 2G2-m-Per and 2G2-m-OH, were synthesized by Z. Peng (University of Missouri, KA) and their synthesis has been described elsewhere.¹⁵² Perylene sample was purchased from Sigma Aldrich Corporation. All the samples are prepared by making dichloromethane (spectroscopy grade) solutions at concentrations below 10^{-6} M (OD less than 0.2 mm^{-1} at 470nm, acceptor's wavelength) to avoid any aggregation or excimer formation.^{156, 157} The sample's photostability is checked by steady state absorption spectrum before and after each set of experiments.

Results

Two-Photon Cross Section

This work is focused on studying the quantum control of energy transfer using a modulated two-photon excitation. Since the spectrum of the laser source is in the near IR region (760 nm to 840 nm) and selection rules are different for one and two-photon transition, the accessible electronic states reached after a two-photon excitation could be different from those accessed by a one photon transition with equivalent transition energy (400 nm). We evaluate the two-photon excitation response using the two-photon fluorescence over second harmonic technique presented by Montgomery and Damrauer.⁴⁴

Figure 6-4(A) shows the two-photon excitation response of 2G2-m-Per. The macromolecule presents a flat two-photon excitation response, which agrees with early experiments performed by Melinger and coworkers on a family of similar phenylene ethynylene dendrimers.¹⁵⁰ That study showed that the two-photon cross section for different phenylene ethynylene dendrimers varies with the structure and connectivity of the dendrons. Interestingly,

up to the third generation they all present a flat two-photon cross section in the region of our excitation source (760 nm to 840 nm) regardless of their internal coupling and conjugation length.¹⁵⁰

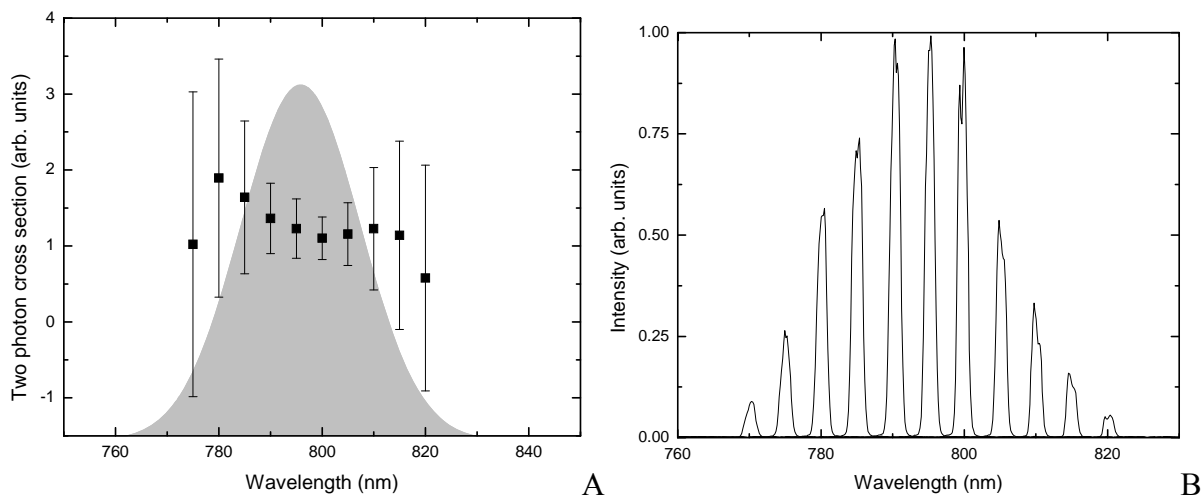


Figure 6-4. A) Two-photon cross section of 2G2-m-Per (squares) and excitation laser spectrum (gray area). B) Spectral windows used to measure the two-photon cross section.

Investigation of the perylene's two-photon cross section shows that the trap does not contribute significantly to the system's two-photon cross section, since the integration of its two-photon induced fluorescence (after excitation with a transform limited pulse) is more than nine times smaller than that for 2G2-m-Per for similar absorptions conditions (OD=0.21 and OD=0.22, respectively, at 470 nm, perylene absorption region), which for this decoupled system gives the same concentrations.

Closed Loop Experiments

Typical experiments compare the optimization of a pure excitation process (pulse compression) on 2G2-m-Per with the optimization of the combined excitation-dynamics-relaxation process. Figure 6-5 presents the fluorescence signal emitted from the energy acceptor in 2G2-m-Per as a function of the two-photon induced current generated by the excitation pulse. Each point corresponds to the best individual in a given generation of the optimization algorithm.

When the fitness function is the fluorescence intensity, the genetic algorithm will only optimize the excitation process. Since the dendrimer backbone is excited through two-photon absorption, the process of optimization is equivalent to compressing the excitation pulse.^{32, 158} When the fluorescence is plotted against the two-photon induced current signal, the best individuals follow a straight line with slope of 1.02. The result of this optimization is a transform limited pulse ($\tau_{FWHM} = 45$ fs).

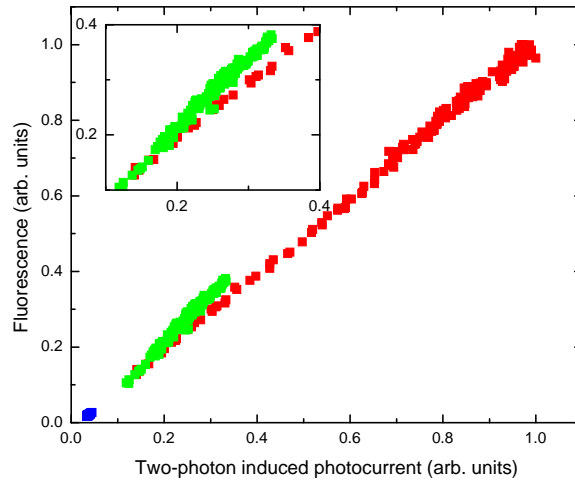


Figure 6-5. Best individual evolution for the different optimizations: maximization of fluorescence (red squares), maximization of the ratio (green squares) and minimization of the ratio (blue squares). Inset shows an expanded view of the maximization region.

We carry out optimizations where we use the fluorescence over the two-photon dependent GaAsP signal as the fitness function to explore the control of processes beyond the two-photon excitation.³¹ As expected, the plot of the best individuals as a function of the two-photon induced current signal reveals a new evolving pathway (Figure 6-5, green squares). This new path is significantly different from the first experiment as the evolution of the best individuals departs from the linear response obtained in the previous optimization. The best individual of the last generation has a fluorescence over GaAsP photodiode signals ratio close 1.17, and for an

excitation pulse that generates considerably less fluorescence and two-photon induced current intensities.

One way to differentiate an optimization due to pulse compression from the optimization of the overall process is seen in Figure 6-6. Figure 6-6 shows the ratio of the fluorescence to GaAsP two-photon signals for optimization based on two different fitness functions: fluorescence only and fluorescence over two-photon induced photodiode signal.

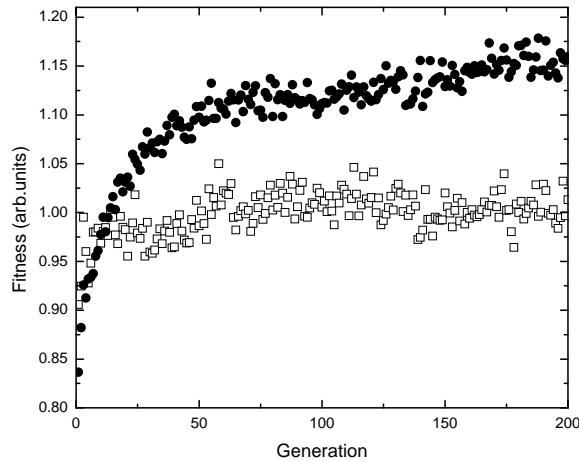


Figure 6-6. Fitness evolution for the maximization of fluorescence over two-photon induced current. Open squares and full circles represent the best individual for the ratio maximization and the calculated fitness using the values of the FL only maximization, respectively.

Open squares correspond to the ratio of fluorescence over two-photon induced current when the objective is chosen to maximize only the fluorescence. After approximately 10 generations, the ratio reaches a saturation point, which is the same ratio obtained for the last generation where the transform limited pulse is located and the total fluorescence signal is maximized. After the 10th generation, the intensity of fluorescence keeps increasing (see Figure 6-5). The final fluorescence is five times larger than the intensity in generation 10, but the ratio of fluorescence over two-photon induced current signals at generation 200 has the same value as in generation 10. These optimized pulses present almost the same ratio value of their pulse

spectral phase. The average and dispersion of the calculated ratio are approximately 1 and 0.05, respectively.

A more interesting case is observed when the objective is set to maximize the ratio of fluorescence over two-photon GaAsP signals (full circles). After 200 generations the fitness reaches a plateau zone indicating the existence of an optimum. This optimum represents a 15-20 % fitness increase with respect to the previous experiment. The intensity of fluorescence is about 60 % smaller than the intensity of fluorescence obtained before, but the efficiency of photon emitted per excitation pulse intensity has been improved. This experiment proves that the attained solution cannot be achieved by setting the genetic algorithm to maximize the emission alone, and that the optimal solution can not be a consequence of noise optimization.

FROG traces of critical pulses were measured and their spectral and temporal electric field profiles reconstructed (Figure 6-7). Figure 6-7 shows that the system did not converge to the trivial solution (a transform limited pulse), but to a pulse with a well defined temporal shape.

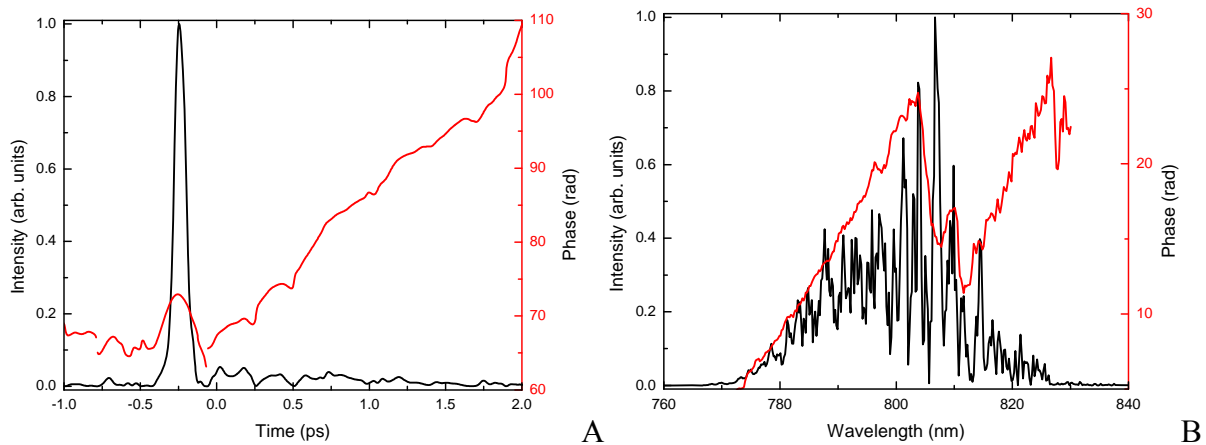


Figure 6-7. Retrieved (A) Temporal intensity and phase and (B) Spectrum and spectral phase.

This pulse temporal intensity (Figure 6-7(A)) has an asymmetric profile with two distinguishable main features: a spike component (~ 50 fs time scale) and a long component (~ 2 ps). The long component is temporally delayed with respect to the short component. In addition,

the spectral phase observed in the retrieved electric field presents a step, which is directly related to the control mechanism (see following section).

We also performed an optimization in which we tried to minimize the ratio of the fluorescence over two-photon induced current. A new zone of the variable space was explored by the individual pulses (Figure 6-5, blue squares), but no evolution of the optimization process was observed and the optimum zone reached fits within the linear dependence region.

Comparison of the autocorrelation of the optimal pulses with autocorrelation of the transform limited pulse shows that this optimization leads to a broad and featureless pulse (Figure 6-8).

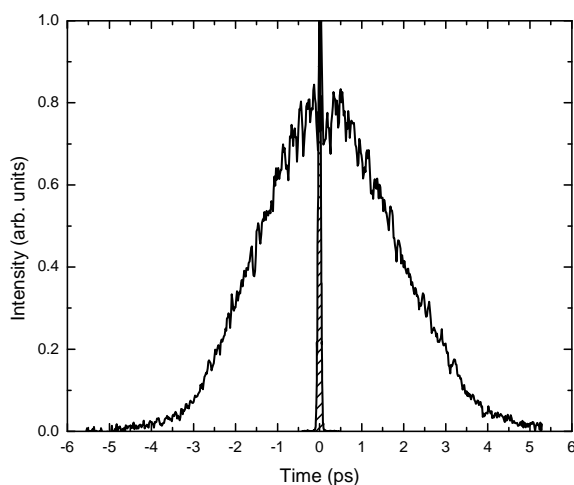


Figure 6-8. Autocorrelation of the pulse observed after the minimization and of the transform limited pulse.

We independently investigate the coherent control of acceptor and donor-acceptor molecules to further explore which process is being affected by the phase modulation of excitation pulses. A solution containing the acceptor moiety (perylene) in dichloro methane was excited at the same wavelength and the emission and two-photon induced current signals were recorded for excitation with pulses having the same modulated phase as those individuals that lead to the maximization of the emission over the GaAsP signal for the 2G2-m-Per molecule in dichloro methane. As stated before, the two-photon cross section of perylene is almost ten times

smaller than that of 2G2-m-Per, thus to obtain a reasonable noise to signal ratio we average over a larger number of shots. For comparison, signals are normalized with respect to the perylene fluorescence and two-photon induced signal obtained with a transform limited pulse.

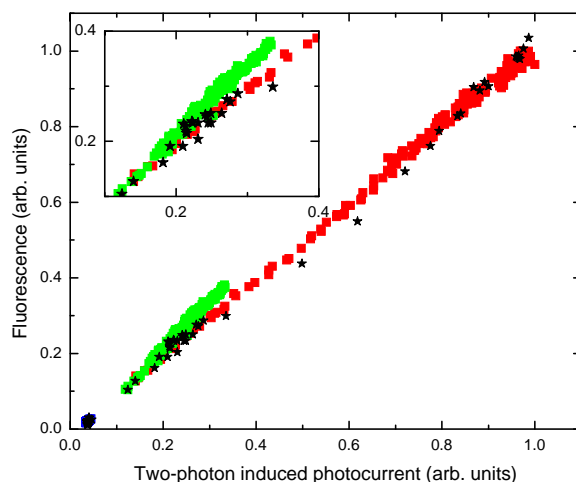


Figure 6-9. Variable space for acceptor and donor-acceptor system. Full squares and black stars correspond to the optimization experiments on the donor-acceptor system and using those phase modulated that optimize 2G2-m-Per to induced excitation on the acceptor molecules alone, respectively.

With these excitation pulses, the ratios lie within the linear region determined by the fluorescence maximization. This indicates that the deviation from a unity slope in the optimization of 2G2-m-Per obtained is not due to a direct excitation of the acceptor, but instead, it involves the excitation of the donor followed by energy transfer to the acceptor.

Open Loop Experiments

Genetic algorithms are an easy and fast way to optimize an ultrafast laser pulse to achieve a given goal, e.g. molecular energy transfer. The solution obtained in these types of experiments usually is an electric field with very complicated phase features (Figure 6-7); thus the possibility of gaining any molecular insight into the dynamics of the process is limited.⁸⁸ We will show here how certain features of the optimal pulse can be recognized and extracted to be used to simplify the solution with the goal of getting a single knob control system. Chapter 7 presents a series of

statistical analysis used to extract those phase components that most affect the optimal pulse. The experimental retrieved phase leads to Figure 6-7, while a deeper investigation including statistical analysis is presented in Chapter 7.

The spectral phase of the optimal pulse presents a step-like change at 810 nm (Figure 6-6). A step phase function produces an asymmetric temporal pulse. According to Brumer-Shapiro asymmetric time pulse profiles have an effect on closed systems interacting with two or more photons.⁵⁵ To explore the role of asymmetric electric fields on the excited state dynamics, we investigate the response of 2G2-m-Per to excitation with time asymmetric pulses (step-like phase) and time symmetric pulses (quadratic phase).

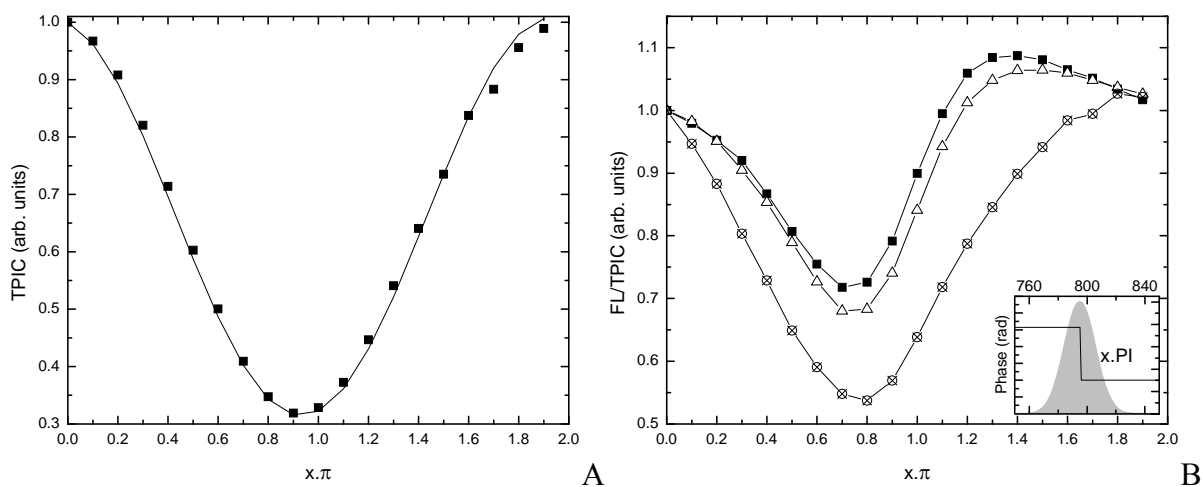


Figure 6-10. A) Fluorescence second harmonic ratio versus the step size of the spectral phase for 2G2-m-Per (stars), 2G2-m-OH (open triangle), Perylene (crossed circle). Inset shows the applied phase. B) Experimental (squares) and calculated (line) TPIC.

The experiment consists on measuring the ratio of emission over two-photon induced current signals following the two-photon excitation of the different samples. The excitation pulses are modulated with a step-like phase function in which the depth of the modulation is continuously varied. The experiments do not provide a feedback signal and they are not optimized in any way. They represent the testing of what we learned from the previous

optimization experiments. The experimental result is the raw response of the excited sample to an applied π phase. The choice of the phase function (step-like function from 0 to 2π radians) was governed by the result of the initial retrieved phase.

. Figure 6-10(A) exhibits the phase effect over the generation of the two-photon photodiode response. The two-photon absorption signal in GaAsP produces the expected symmetric well that can be modeled by calculating the two-photon absorption in the GaAsP photodiode of pulses with a step phase function plus a residual cubic phase.

Figure 6-10(B) shows the effect produced by a variable amplitude step function centered at a fixed wavelength (800 nm) on 2G2-m-Per (DA), 2G2-m-OH (D), and perylene (A). The perylene sample shows a symmetric response to the scanning of the applied phase. The emission over two-photon induced current ratio is maximum for an applied phase of 0 (or the equivalent 2π) and minimum for 0.8π . This is the expected response for a system in which the phase only affects the two-photon excitation process. The small shift of the position of the minimum of the response curve (0.8π instead of 1π) is probably due to solvent effects on the phase of the excitation.

Quite different is the response observed for the 2G2-m-OH and 2G2-m-Per samples. In both cases, the measured ratio does not follow the expected behavior for a simple two-photon process. The variable step function with step size between 1.2π and 1.8π clearly outperforms the response from the transform limited pulse (phase of 0π or 2π). For these particular phases, the ratio reaches values close to 1.1 and 1.05 for 2G2-m-Per and 2G2-m-OH, respectively. These differences represent a 10 and 5 % increase with respect to the transform limited pulse (ratio=1). It is important to highlight that the maximum position is located where the step size is ~ 4.5 rad

(1.4π) for both samples. This phase position not only represents a double pulse with a certain delay, but also determines their relative intensity.

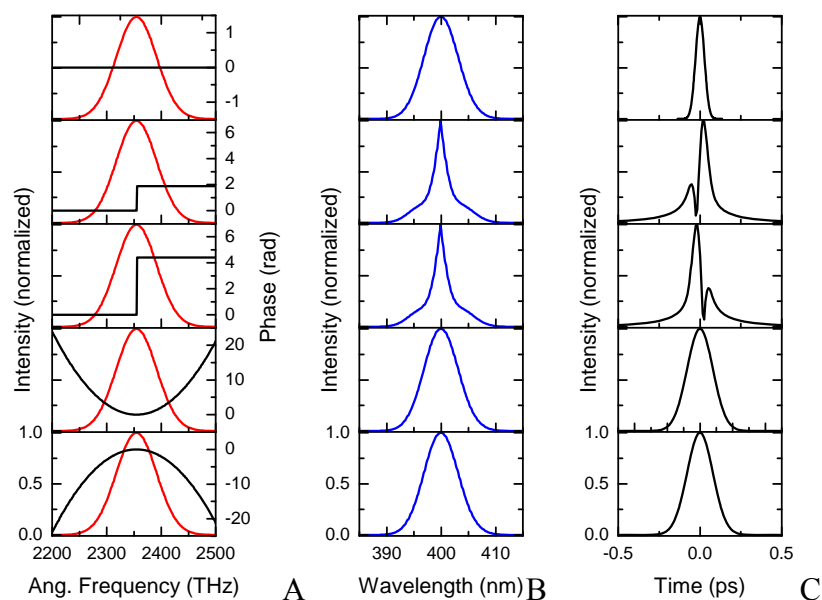


Figure 6-11. Spectrally modulated pulses. A) Spectrum (red line) and spectral phase. B) Second harmonic spectrum (blue line). C) Temporal intensity (black line). From top to bottom: transform limited, 0.4π step, 1.4π step, linearly chirped 2000 fs^2 , and linearly chirped -2000 fs^2 pulses.

The signal obtained for perylene and two-photon induced current trends can be explained with the theoretical treatment developed by Silberberg's group, where the absorption of a multiphoton transition without a resonant intermediate state only depends on the excitation intensity and not on its phase.³² 2G2-m-Per and 2G2-m-OH do not follow this model, strongly suggesting that a different mechanism must be taking place. This mechanism yields a fluorescence efficiency larger than the one obtained with a transform limited pulse, and the optimization is phase since the response at $\pi x(1-0.4)$ is opposite to the signal at $\pi x(1+0.4)$.

We also performed an experiment in which double pulses with different phase relationship between the pulses is codified to investigate the phase effect rather than the time ordering of the

pulses. In this experiment a double pulse with zero phase relation and a train of pulses with a π phase relation between the two consecutive pulses are examined.

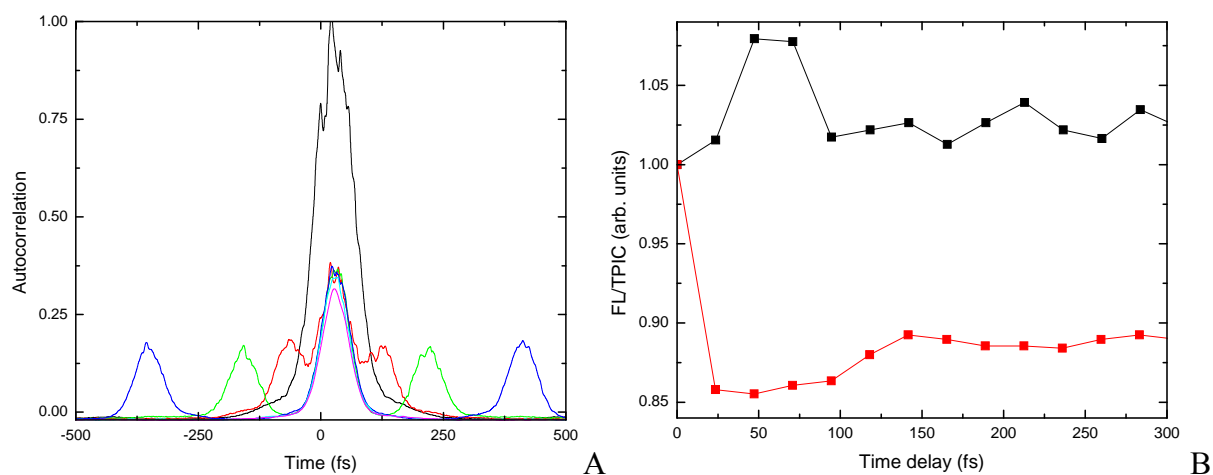


Figure 6-12. A) Temporal autocorrelation of the pulse codified with a zero phase difference, where each color represent pulses separated by a different delay. B) Ratio of fluorescence over two-photon induced current versus the time delay between subpulses for zero phase relation (black line) and π phase relation (red line).

Figure 6-12 presents the results of these experiments. In the case of pulses with zero phase relationship the ratio is increased (ratio ~ 1.07) above the value observed for the transform limited pulse (ratio 1). In contrast, when the pulses have a π phase relationship no improvement of the ratio is observed. It is interesting to note that the transform limited pulse does not yield the highest response. Also, the delay for the maximum response (~ 70 fs) coincides with the delay between pulses found in the step phase function experiments. Experiments with 2G2-m-OH yield a similar response.

To further prove the uniqueness of the step-like phase function we perform an experiment in which a different phase function is scanned, yielding always a symmetric temporal profile and a second harmonic spectrum similar to that observed for a transform limited pulse (Figure 6-13). Application of a quadratic phase only produces broadening of the pulse width while maintaining its symmetric temporal shape. We investigate the quadratic phase effect over the

donor-acceptor excited state dynamics with pulses with temporal widths (FWHM) ranging from 42 fs (0 fs^2 phase) to almost 600 fs (4600 fs^2 phase). Figure 6-13 shows the results of time symmetric pulses applied to the excitation of 2G2-m-Per.

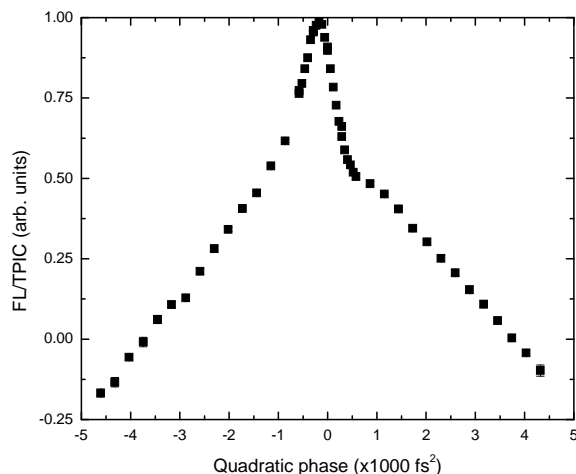


Figure 6-13. Fluorescence-TPIC ratio versus variable quadratic phase for 2G2-m-Per.

The fluorescence over second harmonic response of 2G2-m-Per is a nearly symmetric bell. In contrast to the phase response observed with the step phase function, the quadratic phase does not yield any improvement in the response with respect to the transform limited pulse. The small shift on the position of the maximum is due to the lack of compensation of the phase produced by the solvent. This behavior was predicted by Brumer-Shapiro theory and it agrees well with Silberberg's two-photon absorption theory and previously published results in Rhodamine B.^{32, 55}

Discussion

Closed loop and open loop experiments suggest that control of the energy transfer in 2G2-m-Per is exerted over the dynamics of the excited state. To confirm if the system is dynamically controlled, we must analyze all possible processes involved and whether these processes can be controlled or not within our experimental conditions. For instance, a mechanism in which the population is dumped from the excited state is not feasible because the respective emission wavelengths (420 nm for the donor and 520 nm for the acceptor) do not match with the spectrum

of the excitation laser (near IR, centered at 800 nm). Recent experiments on Rhodamine B performed in Dantus lab show that if the peak power density is smaller than 10^{15} W/cm²,⁵⁵ two-photon stimulated emission does not play an important role. Our experiments conditions provide a peak power density $\sim 7 \times 10^{11}$ W/cm², ruling out contribution from two-photon stimulated emission. Also, the experiments presented here for linearly chirped pulses present a symmetric response. This response would not be expected if stimulated emission played a role in the mechanism.⁵⁴ These considerations eliminate the possibility of producing a control mechanism base on a pump and dump scheme.

Another uncontrollable process is the last step of the dynamics: emission from the acceptor. In addition to the difference in energy between excitation and emission (1/2 eV), the population in this state has a decay time of 2 ns; thus all coherences initially created are completely erased by vibrational energy redistribution, and consequently no control can be exerted on this step.

The two-photon absorption process can be modeled in terms of two components: power spectrum of the second harmonic wave and two-photon excitation response (see Chapter 5 for a full description)⁶⁵

$$f \propto \frac{\int g_{TPA} S_2(\omega) d\omega}{\int S_2(\omega) d\omega} \quad (6-1)$$

where g_{TPA} is the two-photon excitation spectrum of the molecule and S_2 is the second harmonic spectrum of the laser. While the component S_2 is a property of the laser electric field, the g_{TPA} component is an intrinsic molecular property. Theoretically demonstrated by Silberberg and coworkers and experimentally realized by Gerber and coworkers, at a given energy and power spectrum the two-photon transition probability for molecules without any intermediate resonant

state is maximized by the pulse with the shortest time duration.^{32, 63} In addition the experiments presented here for linearly chirped pulses present a symmetric response. We observe this behavior when the optimization is set to maximize solely the 2G2-m-Per emission. The transform limited pulse produces the highest population transfer of the donor via two-photon excitation. As a consequence the energy transfer process and acceptor emission are increased, but not due to the control of the excited state dynamics. A smart choice for the fitness function can remove this dependence on the excitation source. In this thesis, it was accomplished by using the ratio of emission over two-photon induced current in a GaAsP photodiode. The optimization process is decoupled from the intensity dependence of the two-photon absorption and it evolves to a new distinct solution.

The new solution is independent of the peak power but it can still depend on the frequency response of the two-photon excitation process ($g(\omega)$, $\rho(\omega)$, see Chapter 5 for a complete description). In experiments involving two-photon emission processes from Damrauer's and Joffre's groups the maximization/minimization of the two-photon excitation response was responsible for most of the control mechanisms.^{43, 89} If the two-photon excitation response for a given molecule is not flat, the most effective excitation will be obtained with tailored pulses whose second harmonic spectrum matches the molecular regions of high two-photon cross section and will be minimum or negligible in those spectral regions with lower two-photon absorption cross section. In the closed loop maximization experiment presented in this thesis, we do not observe any significant changes in the spectrum of the second harmonic of the optimal pulse compared to the transform limited pulse. This lack of spectral selectivity in the excitation agrees well with flat two-photon cross section measured for 2G2-m-Per (Figure 6-4). An experiment that confirms the control beyond the trivial of spectral control mechanism is shown

in Figure 6-10 and 6-11. Pulses with identical second harmonic spectra yield very different signal values. For example, application of a 0.6π step-like function to a transform limited pulse generates the same second order spectrum as that with a 1.4π phase function (see Figure 6-11). However, the measured values for emission over two-photon induced current are strikingly different. The former yields a 0.725 signal whereas the later yields to optimum value of 1.08.

Since different pairs of pulses with “identical” second harmonic spectrum have different molecular response, the molecular response must be governed by time ordering and relative phase of the double pulse. A step phase function produces a pair of pulses, where the intensity relation between them depends on the size of the step. Modulation with a 0.6π step phase creates a double pulse in which the amplitude of the first pulse is smaller than the second. Modulation with 1.4π step phase creates the mirror image in time. A similar observation is made on the optimal pulse. The optimum temporal intensity presents a short time component followed by a long time component. The optimal pulse can be explained in terms of two separated and controllable processes occurring during the energy transfer: first the population transfer and then control over the excited state dynamics. Population transfer is directly controlled with a short early pulse. Control over the molecular energy transfer (represented by the temporal intensity’s long time component) strictly depends on the molecular properties of the system, e.g. vibrational relaxations channels, coherent states, etc. The single knob experiment clearly demonstrates that the time profile of the laser pulse is the one producing the effect. In addition, the double pulse experiments show that not only the time ordering of the pulse is important but also the phase relationship between the pulses. We conclude that both temporal and phase features of the electric field are the actual knob of the control mechanism.

Multipulse structure has been previously observed in other control experiments.^{51, 82, 85} Many of them have presented strong evidence of a control mechanism involving molecular coherences, e.g. vibrational mode selection.⁵⁰ In our case the dynamics is finished in a couple of hundred femtoseconds leaving the possibility of producing control on the coherences lasting hundreds of femtoseconds.

Last but not least, in our control experiment we rule out the possibility of producing control based on matching the second order power spectrum of the excitation source with the potential energy surface. To our knowledge this is the first experiment which uses the different pulse modulation to rule out this type of control mechanism.

Summary

We successfully control the energy transfer process of a 2G2-m-Per in solution. Using closed loop experiments we found that the optimal control mechanism is based on two different components: population transfer control and energy transfer control. These components represent different processes, but they do not have independent evolutions during the optimization, indicating a dependency between them. Moreover, we show that the features of the phase of the pulse leading to maximization of the energy transfer can be extracted and used to simplify the optimal control experiment into an open loop single variable experiment. The results of this open loop experiment show that the system has coherences which are controlled with specific tailored pulses. The single variable experiment presents strong indications of coherences present in the donor moiety only.

Although the optimal control pulse has been successfully simplified with phase step, a closed inspection of the optimal electric field phase shows two jumps in the phase profile suggesting that an experiment in which the pulse is codified with a double step phase function should produce a higher degree of quantum control of the energy transfer. Hence, a future

experiment using a phase function with a double step (centered at different wavelengths) could verify the degree of control achieved with the optimal solution in the closed loop optimization experiment.

CHAPTER 7

STATISTICAL ANALYSIS OF THE RESULTS OF THE QUANTUM CONTROL OF ENERGY TRANSFER EXPERIMENTS

Introduction

Adaptive quantum control, introduced by Judson and Rabitz,²⁶ has been proposed as an effective methodology to control a large number of photoprocesses without previous knowledge of the quantum properties of the system. Since its introduction in 1992, many molecular systems have been quantum controlled using this scheme. These breakthroughs range from selective bond cleavage of small molecules in gas phase to energy transfer control in complex biological systems in liquid phase.^{51, 84, 159} Nevertheless, only a few of those experimental demonstrations led to results explained in terms of the process under investigation.^{51, 160} The intricate relationship between the pulse parameterization variables and the molecular response, the arbitrary and random manipulation of the pulse parameterization during the optimization, and the large number of pulse parameterization variables available make the interpretation of the results difficult and challenge the application of simplified schemes, e.g. Taylor phase parameterization.

To infer from experimental data the molecular properties involved in the optimization, researchers must overcome the inherent heuristic character of the optimal control technique. For instance, optimization results contain not only redundancies, e.g. same pulses tested more than once in the closed loop optimization, but also phase parameters that do not contribute significantly to the optimal outcome. The question on how to gather molecular properties from the closed loop optimization data must be acknowledged, if optimal control is to be implemented to investigate properties of quantum systems.

Statistical analysis has been successfully used in many different areas to reduce the dimensionality, to remove unnecessary data and/or noise, and to extract important experimental parameters. Considering the similarities of problems solved by statistical analysis, these

exploratory approaches are logical methodologies to extract the molecular quantum information encoded in the optimal control data. Finding ultrafast pulse parameterization variables directly related to the molecular response opens the possibility of determining unknown molecular characteristics from the quantum control optimization.

A couple of examples of these methodologies have been recently implemented in the optimal control field.⁸⁸⁻⁹⁰ Using principal component analysis, Bucksbaum and coworkers extracted and explained what components of the phase parameterization are important in controlling stimulated Raman scattering in liquid methanol. The authors noted the capabilities of this exploratory analysis to remove extraneous phase features out of the optimal phase parameterization.⁹⁰ However, principal components analysis does not link the characteristic features of the experiment with the induced molecular response, e.g. Raman scattering.

Damrauer suggested the additional use of a partial least squares methodology to uncover a model that explains the optimization response in terms of the optimal electric field variables.^{88, 89} In their work, they used this statistical methodology to model the phase variable space in terms of a set of simple collective variables,⁸⁸ and to reduce a 208 variable optimal control problem into a single control knob experiment.⁸⁹

Analysis of statistical methodologies and their application to the energy transfer efficiency control on a dendritic macromolecule is presented in this chapter. We focus on the understanding of the genetic algorithm evolution during the optimization and on the reduction of the number of laser field variables needed to produce molecular control.

In the first part, we present a variable space analysis in conjunction with statistical correlation and multivariate analysis to model the evolution of the genetic algorithm during the optimization. The correlation analysis is used to uncover a characteristic pathway in optimal

control experiments and it is followed by partial least squares analysis to extract the principal laser field characteristics affecting the 2G2-m-Per fluorescence efficiency. The partial least squares method aims at reducing the optimization variable space dimensionality.

Several questions regarding the reduction of the space dimensionality have not yet been addressed and they can help us gain insight into these statistical methodologies. For example, is it necessary to use all the tested phase parameterizations to extract global variables from the experimental data? Do the answers change when different multivariate statistical techniques are used to reduce the complexity of the problem? In the case of phase parameterization, is it the same to analyze the phase in the 0 to 2π space (phase wrapped) as it is without constraints (phase unwrapped)?

Experimental

This study aims to model the data produced in the optimization of the energy transfer efficiency of 2G2-m-Per. This molecule harvests light with an extremely efficient energy transfer process (quantum yield >0.98).^{151, 152} Optimal control experiments were set to optimize the ratio of molecular emission over two-photon induced current in a semiconductor diode for different spectrally phase modulated pulses with a home written genetic algorithm.

The setup used in these experiments is described in detail in previous chapters. In brief, ultrafast laser pulses centered at 800 nm and modulated using a 640 pixels spatial light modulator are used to control the efficiency of the energy transfer process in 2G2-m-Per. Each pulse shape is codified with 128 phase parameters which cover the whole spatial light modulator array. The modulated excitation beam is split by a small amount ($>10\%$) is used to produce the two-photon induced current on a GaAsP photodiode. The rest is used to excite the dendritic sample in solution at room temperature. The integrated emission is recorded with a

photomultiplier tube. The second harmonic spectrum and autocorrelation of the modulated pulses are recorded to obtain the ultrafast pulse characteristics related to the two-photon process. While the second harmonic spectrum is measured with a spectrometer by generating second harmonic in a β -BBO 100 μm crystal, the autocorrelation of the modulated pulse is determined with a home made multi-shot SHG-FROG.

As previously discussed (Chapter 6), the control of energy transfer in this macromolecule is produced via modulated electric fields with phase steps at 805 and 810 nm which correspond to pulses with a short and a long temporal component.

Partial Least Squares Regression

Closed loop optimization experiments manipulate enormous femtosecond pulse parameterization spaces to induce different molecular photoresponses. Partial least squares can link the effective changes in the laser parameterization with the system photo-response. In partial least squares, the nexus is expressed on a set of latent variables, i.e. global variables. Latent variables represent the actual coordinates where the optimization algorithm is evolving because they are selected such that they provide the maximum correlation with the molecular response. Latent variables are abstracted entities that acquire physical meaning only when they are projected back to their original space. However, the features observed in these global variables do not depend on the projection coefficients. So they are useful to correlate the electric field modulation with the molecular property under control.

Optimal Control Theory establishes that the set of independent laser field variables which optimizes a given molecular or laser field property is the optimal solution.⁹⁰ This optimal solution contains the effective control Hamiltonian, which has encoded the molecular statistical and/or dynamical properties of the system.⁹⁰ Partial least squares can extract these molecular

components from the molecular response produced by the system. This methodology not only reduces the variable dimensionality but also removes any data redundancy by selecting the minimum number of latent variables that explains most of the phase parameterization and fitness evolution.

The closed loop experiment data can be modeled into independent (**X**) and dependent (**Y**) variables

$$\mathbf{Y} = \mathbf{A} + \mathbf{B}\mathbf{X}, \quad (7-1)$$

where **A** and **B** represent the coefficients of the linear model. Bold letters express the multidimensional nature of the variables. Implementing this representation to optimal control experiments, the variables in Equation (7-1) become

$$\mathbf{X} = [x_{ik}] = [\phi] \quad (7-2)$$

and

$$\mathbf{Y} = [y_{im}] = f, \quad (7-3)$$

where f represents the fitness and ϕ the phase parameterization. In phase modulated experiments, the phase is a matrix with [generations, phase parameters] dimensions and the fitness is a vector of [generations] dimension. The linear model attained with partial least squares is

$$f = \mathbf{B}[\phi] + \mathbf{A} = \sum_k \phi_{ik} \cdot b_{km} + a_{im}, \quad (7-4)$$

where **B** contains the model regression coefficients, and **A** contains the residuals of the linear model. In this expression (Equation 7-4), the index k represents the number of phase components which are used to produce the linear regression of the fitness.

The phase variables, ϕ_{ik} , can be expressed as a linear combinations of global variables

$$t_{ia} = \sum_k \phi_{ik} \cdot w_{ka}^\dagger, \quad (7-5)$$

where w_{ka} are the weight of each phase component ϕ_{ik} in the global variable, t_{ia} .

The aim of this linear combination (Equation 7-5) is to model simultaneously the phase parameterization and fitness; hence the new global vectors have to be good estimates of the phase parameterization and fitness

$$\phi_{ik} = \sum_a t_{ia} \cdot p_{ak} + e_{ik} \quad (7-6)$$

and

$$f_{im} = \sum_a t_{ia} \cdot c_{am} + g_{im} \quad (7-7)$$

where p_{ak} and c_{am} are coefficients of the linear decomposition and e_{ik} and g_{im} are the residuals of the decomposition.

Up to this point partial least squares and principal components analysis are the same. The difference between the methodologies arises from the way that the weight vectors (w_{ka}) are found. In principal component analysis, the weight vectors (w_{ka}) are selected to maximize only the covariance of the phase matrix. In contrast, partial least squares calculates the weight coefficients (w_{ka} and c_{am}) such that the covariance of the phase and the fitness are simultaneously maximized. As a consequence, the new basis set models both the phase variables and the fitness evolutions.

It is important to note that this statistical analysis can be extended to any problem in which a set of independent and dependent variables are to be linearly modeled. A more complex model can be obtained by purposely including nonlinear terms in the dependent variable rather than by assuming a simple linear model.¹⁶¹

Genetic Algorithm Evolution Analysis

Statistical Analysis

Maximization of the ratio of fluorescence over second harmonic and maximization of fluorescence directly are analyzed to find out which variables are controlling the energy transfer process. These experiments typically describe the optimization of the combined excitation-dynamics-relaxation on 2G2-m-Per and the optimization of the excitation process alone. Figure 7-1 shows all individuals (light and dark grey squares) and the individuals with the best fitness (red and green lines) for these experiments in two different spaces: fluorescence versus two-photon induced current (Figure 7-1(A)), and ratio of fluorescence over two-photon induced current versus two-photon induced current (Figure 7-1(B)).

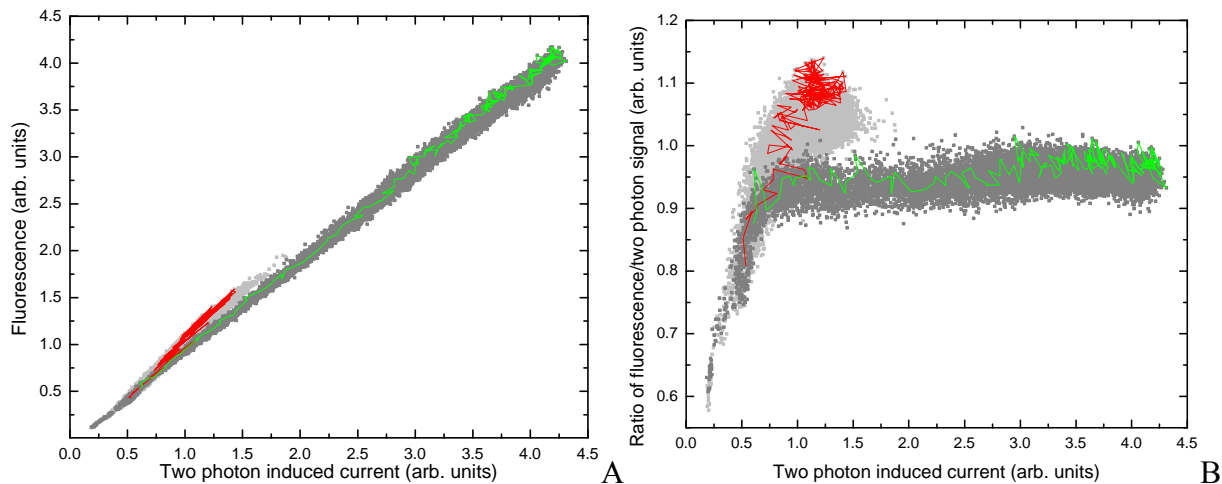


Figure 7-1. Variable space evolution and sampling for 2G2-m-Per energy transfer optimal control. A) Typical representation of the molecular signal versus two-photon signal. B) Ratio versus two-photon induced current for each experiment. Red line (grey dots) and green line (dark grey dots) lines correspond to the best (all) individual for each generation of the ratio of fluorescence over two-photon signal and the fluorescence, respectively.

The usual representation of the fluorescence versus two-photon induced current space (Figure 7-1(A)) does not provide enough information of the pathway followed by the genetic algorithm to produce the desired objective. Although the slopes of both experiments are different

(see Chapter 5) the change is not that pronounced and the evolution is not clear. The difference in the pathways followed during each optimization is better described when the space is represented in terms of the ratio of fluorescence over two-photon induced current versus two-photon induced current. In this new representation, the fluorescence maximization experiment (when the two-photon signal is measured but not included in the cost function) evolves by essentially keeping the ratio constant. Although the intensity of the excitation source keeps increasing, the ratio remains constant because the gain in the fluorescence is solely due to the increase in of the number of excited molecules without controlling the excited state dynamics. In contrast, the maximization of energy transfer efficiency achieves its objective by modifying mainly the ratio and only slightly increasing the two-photon induced current. During the first fifteen generations both optimizations share a common pathway although after that they diverge. This behavior suggests that the optimizations make similar changes to the initial random pulse phase to achieve their respective objectives. After the separation of the pathways, each optimization modifies distinctively the phase parameterization to proceed towards its own optimum region on the surface. The final attained position in this space is unique for each optimization, corroborating the idea that fluorescence and fluorescence over two-photon induced current maximization aim to control very different molecular processes.

Analysis of the correlation between fluorescence and two-photon induced current for all the individual pulses within one generation gives signals which remain highly correlated for all generations (Figure 7-2, full squares). Similar results are observed whether optimizing fluorescence (black squares) alone or fluorescence over two-photon signal (red squares). This strong correlation agrees with the second order intensity dependence of both signals. A similar correlation study using the ratio and the two-photon induced current exhibits a completely

different behavior (Figure 7-2, open squares). Initially, the optimizations have similar correlations, but as the generation number increases, the correlation between the energy transfer efficiency experiments remains constant (Figure 7-2, red open squares), while the correlation in the fluorescence maximization spreads in the range of 0.6 to -0.4 and in the last 10 generations has negative values (Figure 7-2, open black squares). Again, this agrees with the different pathways followed by each population in the different experiments.

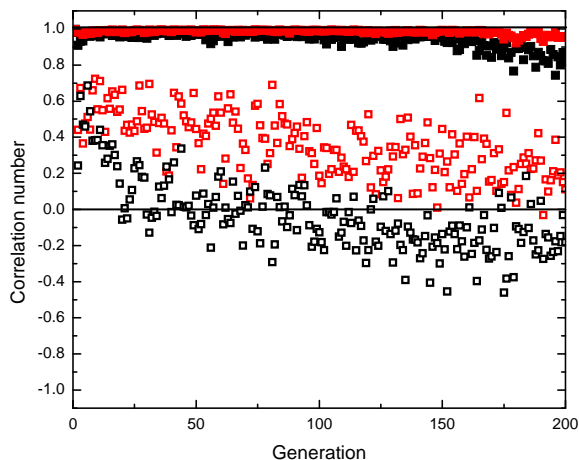


Figure 7-2. Generational correlation between fluorescence and two-photon induced current (full squares) and between the ratio and two-photon induced current (open squares) for energy transfer efficiency maximization (red) and fluorescence maximization (black).

The pathway for the optimization of the energy transfer efficiency has a clear evolution in the 50 first generation, and after that we do not observe major changes in this space, indicating the presence of a local optimum (Figure 6-6 and 7-1). This trend is also observed in the electric field characteristics, i.e. second harmonic spectrum and temporal pulse autocorrelation presented in Figure 7-3.

Spectra of the second harmonic produced by the excitation source and autocorrelations of the fundamental pulses suffer their greatest changes during the first 20 generations. After the 20th generation, neither their second harmonic spectrum nor their corresponding autocorrelations show substantial variations of their profiles. The second harmonic spectrum remains center at

~403 nm during most of the optimization steps. This does not directly correspond with the fitness evolution for this experiment (Figure 7-2) where the fitness suffers the major changes (~40%) in the first 50 generations and later only small adjustments are produced. In the 20th generation, the autocorrelation already has the main feature found in the last generation, but the fitness values still show a significant change, going from ~1.03 in the 20th generation to ~1.15 in the 200th generation.

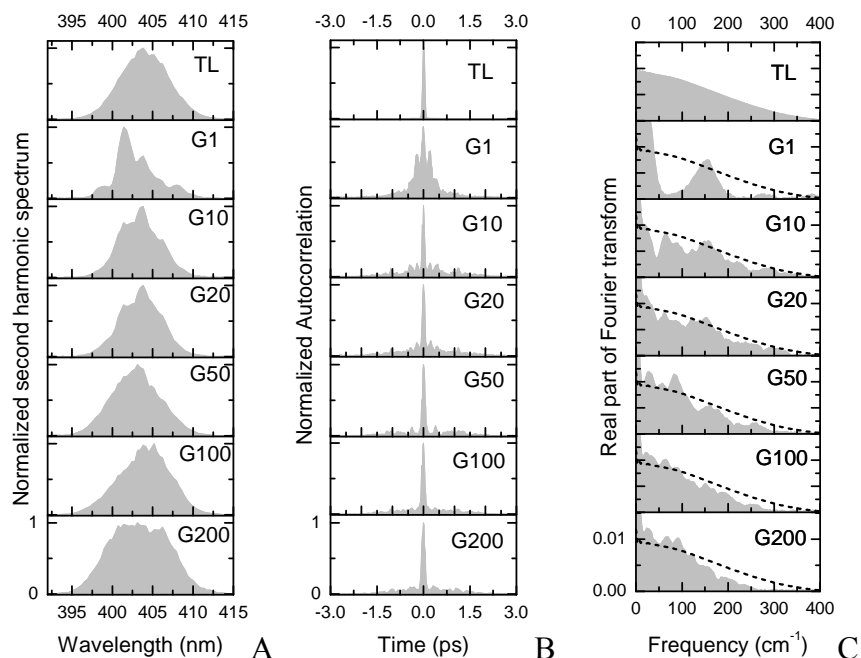


Figure 7-3. Pulse characteristics for the fluorescence for generation 1, 10, 20, 50, 100, and 200. A) Second harmonic spectra. B) Autocorrelations. C) Fourier transforms of the autocorrelations.

In contrast to the autocorrelation of the fundamental pulse and the second harmonic spectra, the evolution of the Fourier transform of the autocorrelation (Figure 7-3(C)) exhibits an initial recovery of the missing frequencies and then a narrowing in the frequency spectrum with some of 300 cm⁻¹ contributions disappearing after 100 generations. This change indicates that the fine structure of the autocorrelation is still changing in the generations where the autocorrelation and second harmonic are not significantly varied, i.e. from the 50th generation and above. A

correlation between the fitness of the optimization and the real amplitude of the frequency components (Figure 7-4) reveals three main regions of the frequency domain correlated with the evolution of the fitness. The frequency components between 40 to 130 cm^{-1} and between 190 to 250 cm^{-1} are positively correlated with the fitness function. There is also a negatively correlated region with frequencies between 0 to 20 cm^{-1} .

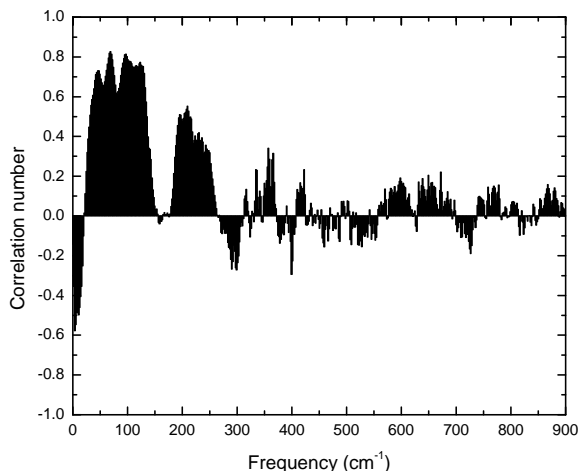


Figure 7-4. Correlation between Fourier frequency amplitude and fitness. Three regions with correlation are observed: between 0-20 cm^{-1} (negative), 40 to 130 cm^{-1} (positive), and 190 to 250 cm^{-1} (positive).

Partial least squares analysis of the evolution of the spectrum of the second harmonic displays one latent variable explaining almost 100 % of the spectrum and fitness variances (Appendix D). This implies that the optimization can be described within a very good degree of approximation as a system evolving through only one dimension. However, the predicted linear model of the fitness with only this latent variable is very poor ($R^2=0.1$), and it can be greatly improved with the addition of a second latent variable ($R^2=0.8$). While the first latent variable is a featureless broadband second harmonic spectrum very similar to the transform limited pulse spectrum, the second latent variable is a non symmetric broad spectrum with a 5 nm dip in the center (see Appendix D). A similar result is obtained when the autocorrelation evolution is statistically modeled with partial least squares.

Partial least squares analysis of the phase evolution displays once more an explained variance of almost 100 % using only the first global variable. Figure 7-5 shows the first and second latent variables.

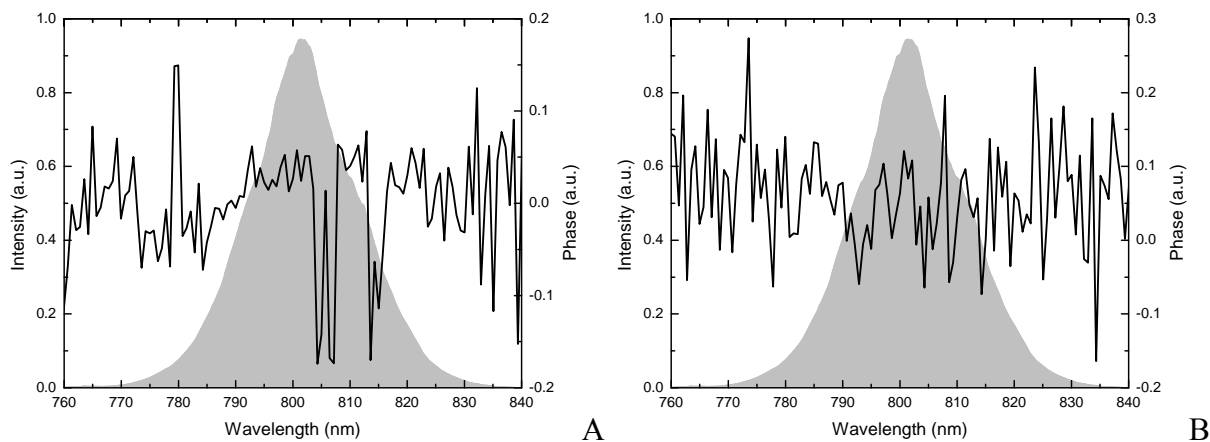


Figure 7-5. A) Latent variable 1 (black line). B) Latent variable 2 (black line). Spectrum of the excitation (grey area) pulse.

The first phase latent variable shows two important phase features at 805 and 815 nm, while the second phase latent variable has a spectral phase with no recognizable features are observed. Although both components contribute significantly to the partial least squares model of the fitness, the first phase latent variable represents the process with the greatest influence over the fitness. The second phase latent variable is needed to produce the initial changes observed in the fitness. The regression model found by partial least squares for the phase agrees with the models that are found with the same methodology to describe second harmonic spectrum and temporal autocorrelation evolutions. Moreover, the first latent variable agrees with the spectral phase retrieved from the experimental optimal pulse (see Chapter 6), corroborating that these pulse features are responsible for achieving quantum control.

Discussion

All the statistical analysis results agree with the experimental observations presented in Chapter 6. For instance, it has been demonstrated that the process is phase dependent and that the

second order spectrum of the excitation does not play a major role in the energy transfer efficiency optimization. This is also observed in the evolution of the spectrum of second harmonic of the best pulse, since no shrinking or shifting of the spectrum of the second harmonic is observed during the optimization. In addition, the Fourier transform analysis of the autocorrelation reveals subtle changes in the temporal profiles of the autocorrelation. These changes observed over the autocorrelation are the actual control features that the genetic algorithm is optimizing, confirming that the achieved control mechanism is not based on modulating the second order power spectrum of the excitation source.

While the change in the frequency components of the autocorrelation are well correlated to the changes in the experimental fitness, the initial randomness of the optimization does not allow us to confirm whether those frequency components must be optimized to achieve control or whether they are optimized because the initial random population does not have them. In other words, is the critical step just moving a random phase to a well defined smooth function? Would we obtain the same frequency components if we were starting from a non-random pulse (e.g. transform limited pulse)? These questions need to be addressed in future work.

The trends of the best individual spectrum of second harmonic, applied phase, and autocorrelation statistically modeled with partial least squares have to include a second latent variable to produce a correct partial least squares model of the fitness. Since partial least squares produces local models,⁸⁹ the second latent variable is always necessary to explain the outliers, i.e. points far away from the center of the hyperplane defined by the global variables (see Appendix C). In our experiments, these outliers represent the initially random pulse created in the optimization. This implies that the system must be optimizing two different processes that they are not strictly correlated with the process investigated. For instance, in the evolution of the

spectrum of the second harmonic, the system finishes with a second harmonic spectrum with a bandwidth close to that of a transform limited pulse, but because of the genetic algorithm is initiated with a random set of pulses, the optimization must first compress the pulse to produce a second harmonic spectrum close to one of a transform limited pulse and then the modifications necessary to achieve control. This evolution model strongly agrees with the pathway observed in both optimizations, where the optimizations initially share a common pathway in the variable space and then they separate to accomplish their own objective.

Summary

We have applied statistics tool to evaluate the results observed in the experiments of quantum control of the energy transfer. These results not only provided new insight into the process (e.g. Fourier components of the autocorrelation) but also confirmed the conclusions obtained from the experimental data. This indicates that statistical analysis is a great tool to be used in the analysis of data produced by closed loop optimizations.

Variable Space Reduction

To further understand how to utilize statistical data reduction analysis, this section aims to investigate how different effects (e.g. phase unwrapping) affect the predicted model when the multivariate analysis is used. The goal of this section is to use multivariate analysis to reproduce the experimental results of the energy transfer optimal control experiments.

Variable Space Size Effect

In a recent work by Damrauer and coworkers, all the phase parameterizations tested during a closed loop experiment were used to infer a set of global variables that control the two-photon induced emission of a ruthenium complex in solution.^{88,89} The question that arises from this study is whether the total number of tested phase parameterizations is truly necessary to extract the global variables affecting the experiment. To investigate this effect we apply partial least

squares to all the phase encodings (all individuals in all generations) as well as to only the phase parameterization of best individuals of each generation tested during the experiment of maximization of energy transfer efficiency presented in Chapter 6. The effect of the sampling is inferred by comparing the global variables obtained with each different set of parameterization. The results of this analysis are presented in Figure 7-6.

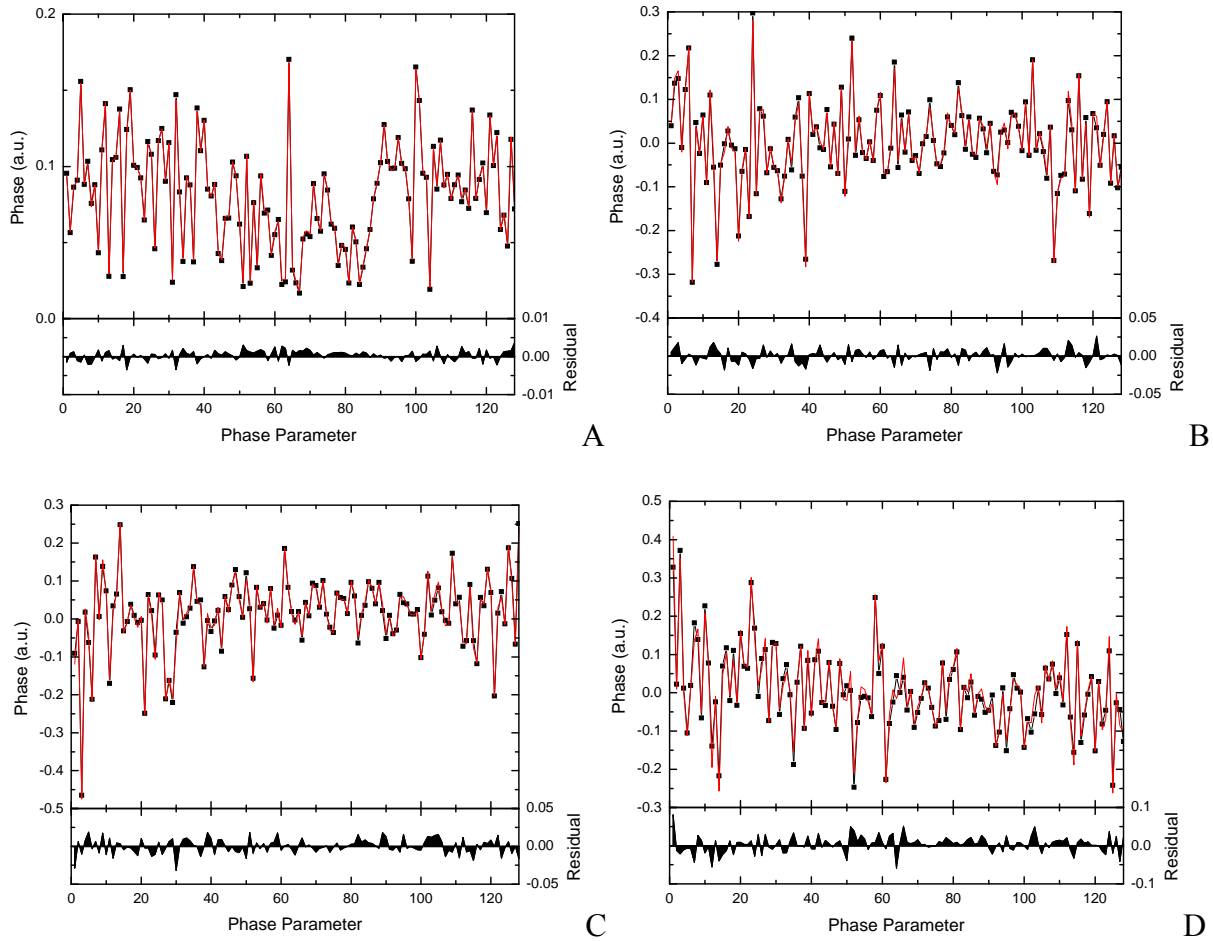


Figure 7-6. Latent variables for the best individuals of each of the 200 generations (red line) and total population (black line and squares). A) Latent variable 1. B) Latent variable 2. C) Latent variable 3. D) Latent variable 4.

Figure 7-6 presents the first four latent variables. The latent variables obtained with both analyses have the same features, suggesting that the statistical analysis can be performed directly on the best pulses parameterization of each optimization.

Statistical Methodology Effect

The next investigation involves the study of the different statistical techniques to model the data. As stated before, partial least squares differs from principal components analysis because it includes the correlation with the molecular response. It is expected that principal component analysis will be outperformed by partial least squares methodology in data modeling.

To investigate whether those two statistical methodologies produce different factorizations, a model produced with only one global component is compared for the two multivariate analysis techniques (partial least squares and principal components). In this test the wrapped phases of the best individuals in each generation are analyzed. The results of this analysis are presented in Figure 7-8 (A).

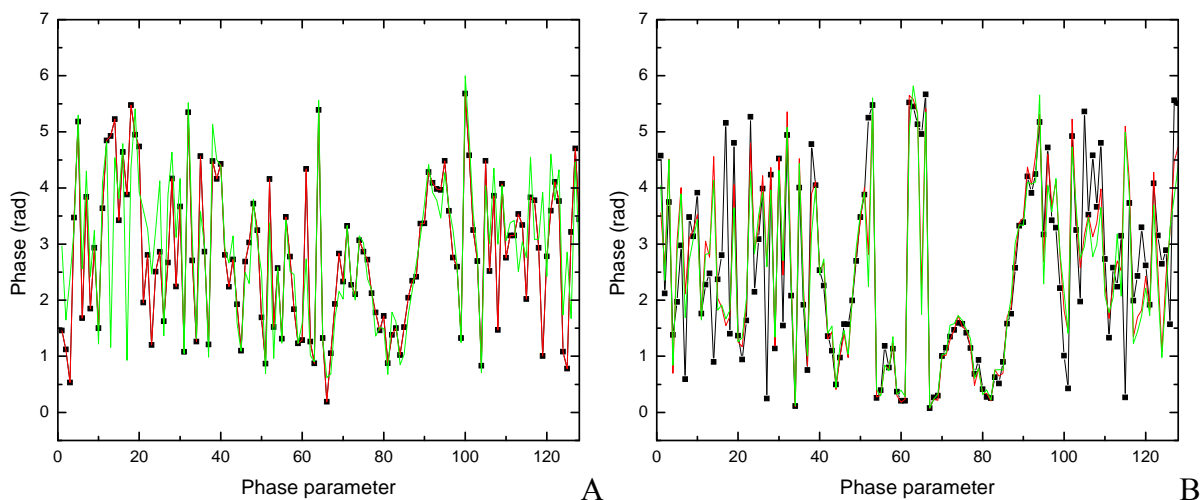


Figure 7-8. Comparison of the model predicted by different statistical methodologies and the optimal phase. A) Energy transfer optimization. B) Fluorescence maximization. Each graphs shows: original data (black line and squares), the partial least squares model (green line), and the principal component analysis model (red line).

Principal components as well as partial least squares model accurately the optimal phase. Surprisingly, the root mean square error is higher for partial least squares than for principal components analysis (Table 7-1).

Table 7-1. Root mean square for the different statistical methodologies.

Statistic methodology	Root mean square error
Principal components analysis	4.10^{-4}
Partial least squares	0.8

To discard a possible effect over the statistical factorization produced by the large data redundancy observed in experiments with the rapid convergence, such as maximization of the energy transfer efficiency, a similar analysis is performed with the data of the maximization of fluorescence alone. In this particular case the fitness changes significantly in at least 130 of the 200 generations. Analysis of this data set displays a similar result, thus discarding an effect due to any rapid convergence which could favor the localization of the partial least squares model. Since the two statistical analyses perfectly match the experimental data, principal component analysis as well as partial least squares can be used to model the data in terms of global variables. To conclude which one produces better phase predictors, it is necessary to perform an experiment where the experimental value of the fitness corresponding to the predicted phase for both methodologies are measured and compared.

Theoretical Phase Unwrapping Effect

The last analysis involves the effect of the unwrapping of the phase before performing the statistical analysis. The closed loop optimization with spatial light modulators explores the effect produced by phases with values in the range from 0 to 2π (see Chapter 3). Unwrapping the phase (so it goes from 0 to $n\pi$) produced in the optimization experiments causes many problems associated with the statistical factorization. For example if a pixel with negligible contribution to the fitness suddenly produces a jump in the phase bigger than π , the unwrapping process will take it into consideration and will increase the variability of the phase parameterization even though this points does not contribute to the fitness. To correctly analyze the optimal phase obtained by the algorithm we need to consider only those parameters in which the spectral

intensity is appreciable, otherwise the phase unwrapping cannot be applied before performing the statistical studies. Most times it is difficult to determine which pixels have sufficient intensity to contribute to the optimization or whether the pixels with low intensities have any effect on the fitness or not.

We use all the phase variables (128 for the energy transfer experiment) to show how the effect of the unwrapping over the phase parameterization results when the statistical analysis is performed. The model of the phase using only one global variable is compared to the actual phase of the 200th generation.

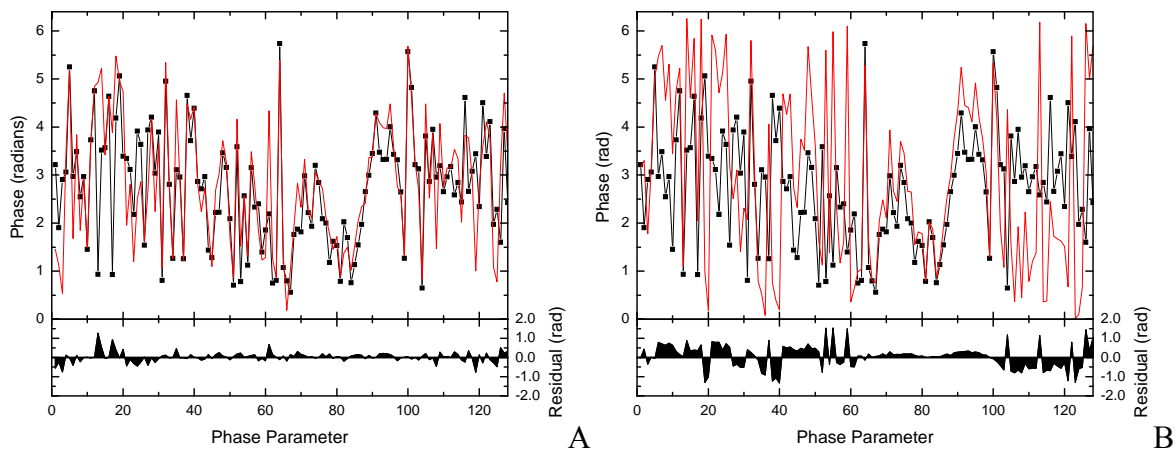


Figure 7-9. Comparison between the model of the optimal phase (red line) and the experimental optimal phase (black line and points). A) Without phase unwrapping. B) With phase unwrapping.

Figure 7-9(A) shows that the phase is well reproduced with only one global variable when the phase is not unwrapped. In contrast, when the phase is unwrapped before the analysis, the model presents very different features compared to the actual phase (Figure 7-9(B)). The phase unwrapping clearly induces more variability in the sample. A similar behavior is obtained for the phase analysis of the unwrapped and wrapped phases even when only the phase variables with more than 5 % of the intensity at the maximum are considered (Figure 7-10). Hence, phase

unwrapping introduces an unnecessary variability to the phase which affects the performance of the statistical analysis.

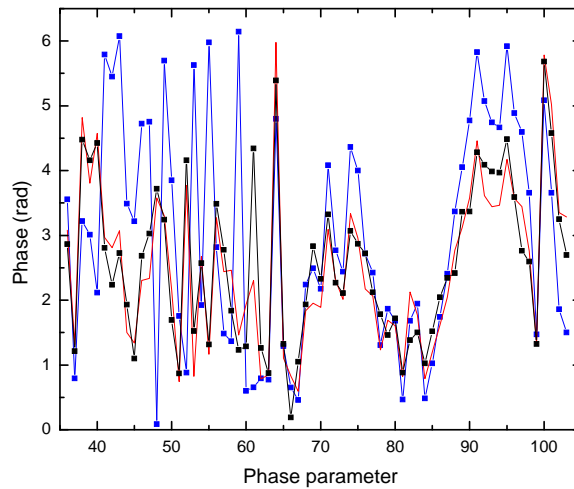


Figure 7-10. Comparison among modeling of the optimal phase without unwrapping (red line) and with unwrapping (blue line), and the experimental optimal phase (black line).

Experimental Phase Unwrapping Effect

We present here an experimental implementation to show the effect of the number of components used to reconstruct the data with or without phase unwrapping.

First we run an optimization and then we use principal component analysis to extract the principal components of the wrapped or unwrapped experimental phase of the best individuals of each generation. Choosing the first, the second, or both principal components that explained the phase, we reconstruct the experimental phase data. We apply each of the reconstructed optimal phases (phase of the 200th generation) to the phase modulator. The signals obtained by the real optimal phase are compared with those obtained by using one or two components.

Table 7-2 and Table 7-3 show raw results and results normalized to the transform limited pulse, respectively.

The fitness is perfectly reproduced with models containing one or two components when the phase is wrapped. On the contrary, the fitness is poorly predicted when the phase is unwrapped, which agrees with the theoretical unwrapping effect previously presented.

Table 7-2. Experimental signal and fitness values for multiple components.

Pulse	Signal					
	SHG	σ_{SHG}	FL	σ_{FL}	FL/SHG	$\sigma_{\text{FL/SHG}}$
Transform limited	3.56	0.06	4.40	0.11	1.24	0.04
Optimal	1.00	0.03	1.41	0.05	1.41	0.07
PC1 unwrapped	0.98	0.03	1.31	0.05	1.34	0.06
PC2 unwrapped	0.57	0.02	0.68	0.04	1.20	0.07
PC1 and PC2 unwrapped	0.47	0.01	0.54	0.03	1.15	0.07
PC1 wrapped	1.12	0.03	1.60	0.06	1.44	0.06
PC2 wrapped	1.10	0.02	1.53	0.05	1.40	0.06
PC1 and PC2 wrapped	0.99	0.02	1.38	0.05	1.39	0.06

Table 7-3. Experimental normalized fitness values for multiple components.

Pulse	Response normalized with respect to transform limited pulse	
	FL/SHG	
Transform limited	1.00	
Optimal	1.14	
PC1 unwrapped	1.08	
PC2 unwrapped	0.96	
PC1 and PC2 unwrapped	0.92	
PC1 wrapped	1.16	
PC2 wrapped	1.12	
PC1 and PC2 wrapped	1.12	

Discussion

In this section, we demonstrated that the dimensionality reduction is not affected either by considering only the best individuals of the population instead of the total population or by the selected multivariate analysis chosen to reconstruct the optimal phase. Since both methodologies are based on correlating the change on the covariance matrix, it is not expected that principal components will produce different results than partial least squares. The reason for this behavior is the heuristic algorithm used for the optimization. Genetic algorithms are based on inheritance and natural selection. Extrapolated to the optimal control experiments, it means that the algorithm is indeed evolving through a space in which the best variables are kept until new and

improved variables are found. It is not surprising that the fitness of the best individual has a monotonous improvement in the space of variables, ultimately causing a matching between the phase optimization direction and the fitness change.

Finally, the phase unwrapping effect is demonstrated to have detrimental characteristics if applied before performing the statistical analysis. It is known that phase wrapping produces errors in the ultrafast generated laser field, which can be exploited by the genetic algorithm to optimize the photoprocess.^{55, 162} We conclude that phase unwrapping should not have to be performed before the statistical analysis.

Summary

We have demonstrated the utility of multivariate data analysis to extract the global components affecting the evolution of the phase variables during the optimization. Surprisingly, neither the selected methodology nor the number of individuals used in the analysis affect significantly the result of the global component analysis. Also, we find that the phase unwrapping process not only is unnecessary but also complicates the statistical factorization of the data. Finally, a very challenging and yet very interesting experiment should be an optimization in which after a certain number of generations without reaching convergence the global variables obtained from a global analysis of the phases are used as a basis set to continue the optimization.

CHAPTER 8 AZOBENZENE EXCITED STATE DYNAMICS WITH TWO-PHOTON EXCITATION

Introduction

Azobenzene and its derivatives are photochromic molecules exhibiting a *trans-cis* photoisomerization. Their photochromism makes azobenzene-like compounds very attractive to investigate fundamental photochemistry processes and to industrial and scientific applications. Some of the proposed applications include light-triggered optical switches and optical data-storage media.¹⁶³ Recently, an azobenzene derivative has been successfully used as an ultrafast molecular trigger in protein folding.¹⁶⁴ To further develop the applications of azobenzene, its molecular rearrangement process needs to be understood.

Azobenzene dynamics have been extensively investigated using many different time resolved as well as steady state spectroscopic techniques.¹⁶⁵⁻¹⁷² However, the mechanism and dynamics of the molecular rearrangement are still controversial. The most debated question in the azobenzene rearrangement is whether the isomerization takes place through an inversion or a rotation pathway.^{173, 174} New experimental approaches are necessary to investigate this molecule and solve the longstanding controversy.

Several experiments have probed the possibility of coherently controlling isomerization processes.^{82, 84-86} While some of these studies were focused on proof of principle,^{82, 85} others used the coherent control methodology to gain insights on the molecular process.^{84, 86} For instance, using an unmodulated pump and a modulated dump pulse Gerber and coworkers studied the dynamics of bacteriorhodopsin isomerization in the excited state potential energy surface close to the conical intersection.⁸⁶ Another optimal control study focused on the isomerization of cyanine dye has uncovered the molecular motion produced in the excited state, and consequently the understanding of the cyanine isomerization process.⁸⁴ The maturity of the coherent control field

has reached a point in which we can envision using modulated pulses to further understand molecular processes in which molecular rearrangements are involved.

The following chapter describes the preliminary experiments performed to seek the feasibility of quantum control of the isomerization of azobenzene. It focuses on establishing if a two-photon excitation of azobenzene is possible and on studying possible changes in the excited state dynamics caused by multiphoton excitation. The ultimate goal of this study is to set the necessary foundations of a two-photon excitation for coherently controlling the photoisomerization of azobenzene with a modulated 800 nm excitation source.

Azobenzene

Azobenzene has two benzene rings linked via two double bonded nitrogen atoms, the azo group. The molecule presents two possible conformations: the thermally stable *trans* form and the metastable *cis* form (Figure 8-1(A)).¹⁷⁵

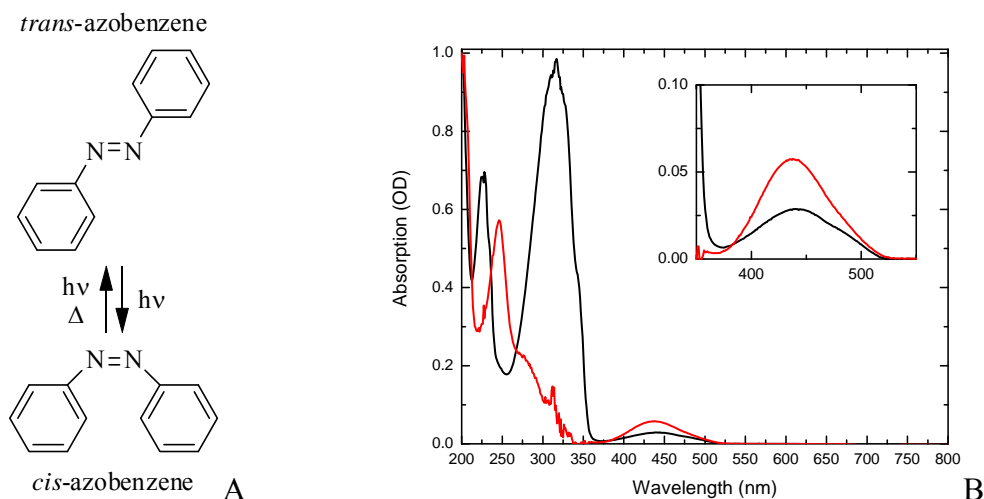


Figure 8-1. A) Isomerization of azobenzene. B) Ground state absorption of azobenzene samples: *trans* (black line) and *cis* (red line).

Since the azo group presents a lone pair of electrons on the nitrogen atoms, the molecule exhibits two low lying electronic transitions, $n\pi^*$ and $\pi\pi^*$, found in the UV-visible spectral region. In the *trans* isomer the two transitions are located at 440 nm ($n\pi^*$) and 330 nm ($\pi\pi^*$),

while for the *cis* isomer the $\pi\pi^*$ transition is observed at the same wavelength and the $\pi\pi^*$ transition is shifted to the blue (Figure 8-1(B)). The cause of this spectral shift is the non-planar structure of the *cis* isomer which decreases p-orbital overlap responsible for π conjugation. The $\pi\pi^*$ transition is one photon allowed in both isomers ($\epsilon_{cis}\sim 10^4$, $\epsilon_{trans}\sim 3\times 10^4\text{ M}^{-1}\text{cm}^{-1}$) whereas the $n\pi^*$ transition is one photon forbidden for the *trans* isomer ($\epsilon_{trans}\sim 400\text{ M}^{-1}\text{cm}^{-1}$) and allowed for the *cis* isomer ($\epsilon_{cis}\sim 1500\text{ M}^{-1}\text{cm}^{-1}$).¹⁶⁶

Due to the similarities with stilbene two possible mechanisms of isomerization have been proposed for azobenzene: one is based on the inversion around one nitrogen atom while maintaining the rings in the same molecular plane; the other involves a rotation of a benzene ring around the nitrogen double bond (Figure 8-2).¹⁷⁵

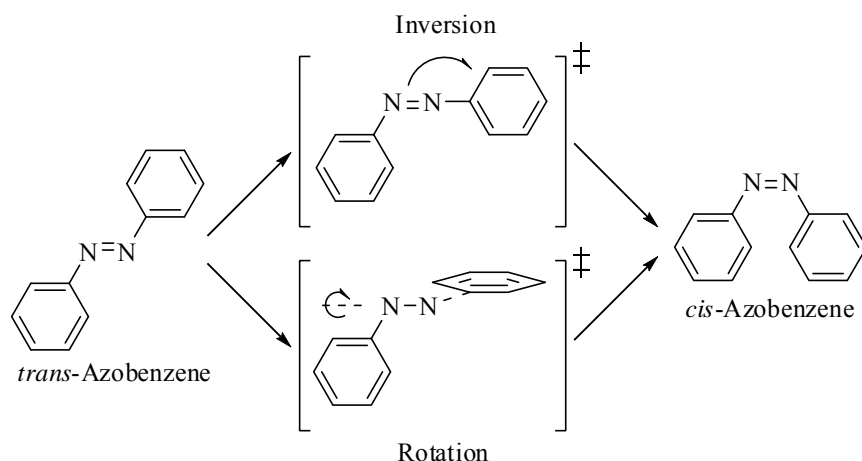


Figure 8-2. Rotation and inversion pathways of azobenzene isomerization. Adapted from work by Diau.¹⁷⁶

Early steady state measurements of the *trans* to *cis* isomerization quantum yield showed an excitation wavelength dependence in which the rearrangement quantum yields are 0.23 and 0.12 for the $n\pi^*$ and $\pi\pi^*$ transitions, respectively.¹⁷² The wavelength dependence of the quantum yield of the isomerization indicates diverse isomerization mechanisms and/or deactivation pathways taking place on different excited states. Rau and coworkers performed a quantum yield

study on a rotationally blocked azobenzene. In those experiments the isomerization quantum yields did not vary significantly ($\phi_{\text{isom}}(n\pi^*)$ is 0.24 and $\phi_{\text{isom}}(\pi\pi^*)$ is 0.21).¹⁷³ Since the bridge blocking the rotation pathways did not produce significant changes in the electronic structure of the azo derivate, the authors proposed a mechanism in which the *trans* to *cis* isomerization proceeds through inversion and the rotation coordinate serves for the excited state relaxation without isomerization.

Recently, several time-resolved experiments have been carried out to study the dynamics of this photoisomerization. These experiments focused on the *trans* to *cis* isomerization dynamics exciting the molecule in either the $n\pi^*$ or $\pi\pi^*$ transitions. Ultrafast studies on the deactivation dynamics after an $n\pi^*$ excitation showed biexponential decay kinetics in which the time constants were solvent dependent.¹⁷¹ All studies agree on biexponential dynamics with time scales of the subpicoseconds (~ 0.3 ps in ethanol) and picoseconds (~ 2.1 ps in ethanol).¹⁶⁶ The ultrafast dynamics component is assigned to the initial evolution of excited state out of the Franck-Condon region and the picosecond component is due to a diffusive motion of the excited state wave function towards the conical intersection where the system will transfer back to the electronic ground state.¹⁷¹ In addition, a slower process with a time scale of 5 to 20 ps was observed in some studies¹⁷⁷ and this has been assigned to the vibrational cooling of vibrationally hot ground state molecules.¹⁷¹

The dynamics following the $\pi\pi^*$ excitation have also been investigated.¹⁷¹ The general picture of the dynamics includes four different relaxation constants. The first time constant represents the radiationless relaxation process from the second excited state, S_2 , to the first, S_1 , in a subpicosecond time scale (~ 120 fs).¹⁷¹ Due to the similar time values ($\tau_2 \sim 0.5$ fs, $\tau_3 \sim 3$ ps and $\tau_4 \sim 20$ ps) all the other constants have been assigned to processes occurring in the first excited

and ground states. The amplitudes of these kinetic steps significantly differ with those observed after the $n\pi^*$ transition.¹⁷¹ These differences led researchers to conclude that the deactivation of the S_2 state involves a population transfer to S_1 where the isomerization takes place. In addition the difference in quantum yield is explained with the difference in the amplitude values of different processes, which is interpreted as different positioning of the excited state wave function upon relaxation to the first excited state.¹⁷¹

All these studies have shown the time constants of the photoprocess but they do not discriminate between an isomerization occurring through an inversion or a rotation mechanism. Two experimental studies supporting an inversion pathway are time resolved picosecond Raman¹⁶⁸ and steady state spectroscopy using rotationally blocked azobenzenes.¹⁷³ The first study shows that the N-N double bond character is maintained during the photoprocess.¹⁶⁸ The second study demonstrates the lack of wavelength dependence of the isomerization quantum yield when a rotational block azobenzene is excited using either transition, $n\pi^*$ or $\pi\pi^*$.¹⁷³

With these experimental precedents, most of the experimental literature considered the isomerization to occur via the inversion pathway. However, the isomerization through the rotational mechanism has been gaining support from numerous theoretical studies.^{176, 178-181} In these studies, the inversion coordinate is challenged as the isomerization coordinate because it is not predicted to be energetically barrierless.¹⁸⁰ In addition, the barrierless rotational coordinate is inferred to lead the excited state close to a conical intersection between S_0 and S_1 , near to the midpoint of the rotation pathway. From the theoretical point of view, this suggests a propitious isomerization via the rotational pathway. A time resolved fluorescence study supports this theoretical prediction for solvents with low viscosity and suggests an inversion mechanism in high viscosity solvents.¹⁸²

Recently, two experiments add more confusion to the unsolved isomerization problem. Using sub ten femtosecond transient absorption experiments with chirped pulses, Kobayashi and coworkers followed the isomerization of an azobenzene derivative (DMAAB).¹⁸³ The experiments indicate that the N-N and C-N stretching modes are coupled through at least one vibrational mode. The authors concluded that the isomerization mechanism cannot be described either as a pure rotation or pure inversion, but both happening simultaneously. Stollow and coworkers used time resolved photoelectron spectroscopy exciting at 330 nm to study the molecule in the gas phase.¹⁸⁴ Two photoelectron bands with distinct lifetimes were identified (170 fs and 420 fs) and assigned to degenerate excited $\pi\pi^*$ states. Following the mechanism proposed by Tajara,¹⁶⁹ Stolow suggested that one of these degenerated states leads to the deactivation of the S_2 to S_1 and the other directly relaxes the system from $S_{n\neq 1,2}$ to S_0 , explaining the difference in the isomerization quantum yield.

Experimental

Transient absorption experiments were performed using a two-photon excitation. Azobenzene sample was purchased from Aldrich Corp. (~99% purity) and used without further purification. Azobenzene solutions with a 5.2 mM concentration are prepared with n-hexane (Fisher, HPLC grade). The sample is held in a 2 mm optical path quartz cell with magnetic stirring to ensure fresh sample for each excitation pulse. Since the two-photon cross section is much smaller than the linear cross section,¹⁸⁵ high optical densities (OD=0.45 in 2 mm) at the probe wavelength 440 nm were used. In addition, the solutions were checked for photoproduct build up before and after the experiments by measuring their absorption spectrum.

The experimental setup utilized in this experiment is a femtosecond time resolved transition absorption setup (Figure 8-3).

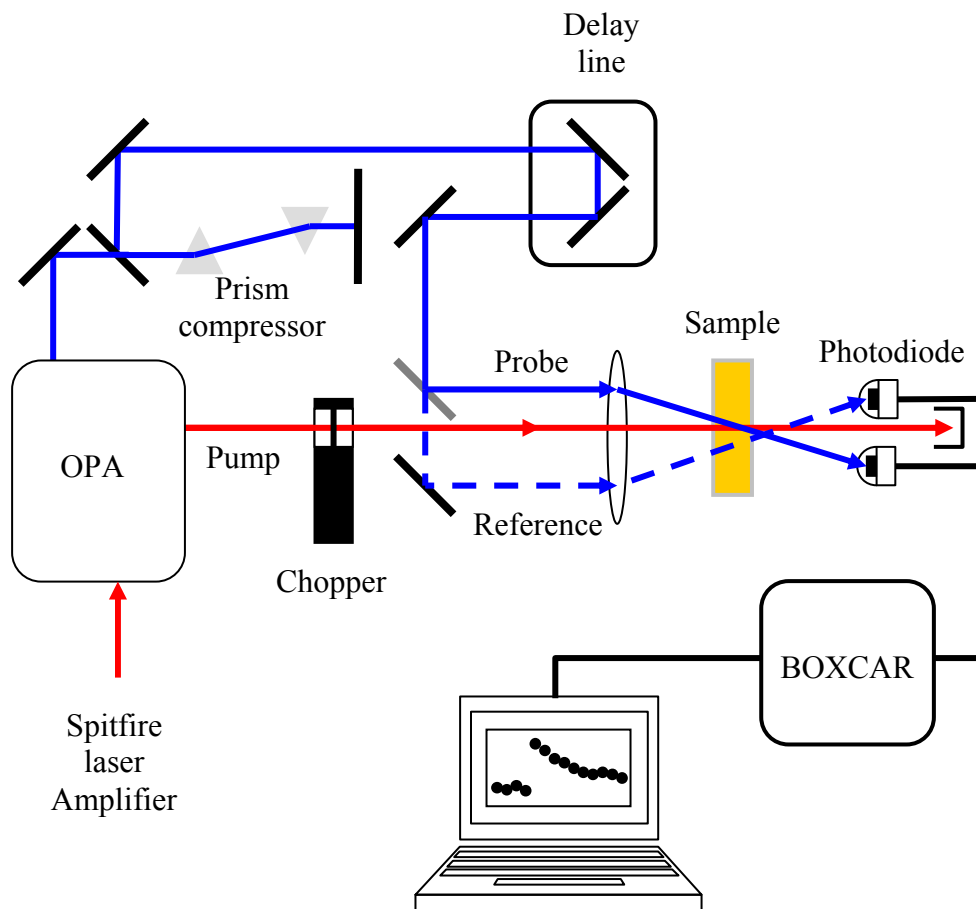


Figure 8-3. Experimental setup for transient absorption experiment probing with UV. nIR pump pulses are obtained from the residual fundamental of the OPA. A chopper wheel is used to compare the signal with and without pump.

The laser source is commercially chirped pulse amplifier system (Spitfire, Spectra physics®), which delivers sub 45 fs pulses centered at 800 nm with a repetition rate of 1kHz and a pulse energy of 800 μJ . Approximately 350 μJ of this laser source are used to pump an optical parametric amplifier (OPA) which generates the probe wavelengths used in this experiment, 440 nm and 480 nm. A 65 μJ excitation beam is obtained from the leftover fundamental beam of the OPA. An optical chopper is placed in the excitation pathway to perform double referenced experiments.

The sample is excited with 800 nm and the transient absorption signals are measured with a single color probe and reference in two independent photodiodes (Thorlabs 210). To avoid the detection of scattered light from the sample, color filters (BG39) are used. The photocurrent produced in the detector is further processed with a boxcar gated integrator (SRS 250) and acquired with a data acquisition card (National Instruments®, PCI-MIO-16E-4).

In the data presented herein every point at a fixed delay time is the average of 16000 individual laser shots. The transient absorption signal produced by the pure solvent is later subtracted from the sample signal. Characterization of the instrument response function is achieved using the Raman signal arising from methanol as well as dichloromethane.

Results and Discussion

The dynamics of the transient absorption signals of azobenzene following two-photon excitation (220 fs FWHM, 800 nm) and probe at 440 nm and 480 nm are investigated. This excitation frequency does not induced one photon absorption: the excitation occurs via two-photon absorption in the spectral region equivalent to 25000 cm^{-1} which correspond to the blue side of the $n\pi^*$ transition of *trans* azobenzene.

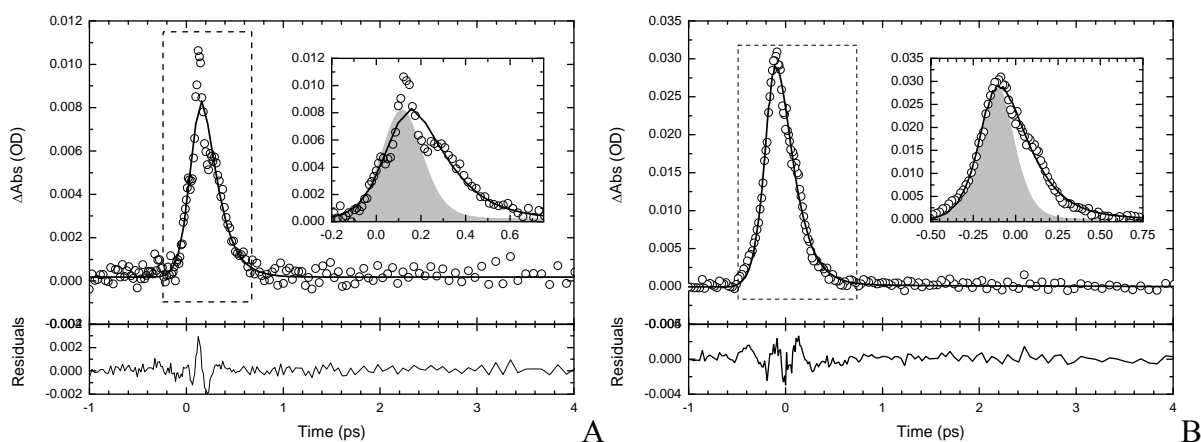


Figure 8-4. Transient evolution of the absorption changes for azobenzene where open circles and black line represent the data and fitting model and the grey plots show the instrument response function. A) Probe at 440 nm. B) Probe at 480 nm.

Transient absorption data of *trans*-azobenzene with the two probe wavelengths are shown in Figure 8-4. The signals depicted in these experiments correspond to the excited state absorption following formation of the excited state, S₁. At both probe wavelengths, the initial absorption is followed by a fast decay. Photoinduced excited state absorptions completely vanish after 1 ps. The model used to describe this data includes two independent decay times convoluted with the instrument response function.

$$\Delta A = IRF \otimes f(t) \quad (8-1)$$

$$IRF = A_{IRF} \exp(-t^2/\sigma_{IRF}) \quad (8-2)$$

$$f(t) = \sum_i A_i \exp(-t/\sigma_i), \quad (8-3)$$

where ΔA is the transition absorption signal, IRF is the instrument response function, A_{IRF} and σ_{IRF} are the amplitude and standard deviation of the instrument response function, A_i and σ_i are the amplitudes and decay times of the model. The time evolution probed at 440 nm has to be modeled with a biexponential function; the decay probed at 480 nm is correctly modeled with a single exponential. The results of the modeled dynamics as well as literature reported values are presented in Table 8-1.

Table 8-1. Experimental and literature decay times.

Excitation	λ_{exc} (nm)	λ_{prb} (nm)	τ_1 (fs)	τ_2 (ps)	IRF	Solvent
Two-photon excitation*	790(395)	440	150	2.5	220	Hexane
Two-photon excitation*	790(395)	480	150	--	200	Hexane
One photon ¹⁶⁶	435	440-750	320	2.1	500	Ethanol
One photon ¹⁷⁰	480	370-590	340	3.0	80	DMSO
One photon ¹⁶⁷	420	350-550	600	2.6	180	Hexane

*from this work

Our results show good agreement with the literature values indicating that the dynamics are independent of the type of initial excitation used in the experiment (one-photon or two-

photons). This result suggests a similar localization of the one and two-photon Franck-Condon areas which would result in similar dynamics.¹⁷¹

The lack of a biexponential behavior at 480 nm shows that this wavelength only probes the excited state population close to the initial Franck-Condon area. In contrast at 440 nm, the excited state is probed during the whole residence time in the excited state, which includes the initial Franck-Condon region and the wave packet movement towards the conical intersection. This interpretation agrees with the most accepted kinetic model of trans-azobenzene.

Summary

We employ two-photon excitation transient absorption to investigate the excited state dynamics of azobenzene in hexane. The transient signal reveals similarities between the dynamics observed with one-photon and two-photon excitations. This allows us to infer that the system reaches the same potential energy surfaces as well as similar Franck-Condon regions for the two different excitations. This opens the possibility of using a two-photon excitation source to coherently control the isomerization rearrangement in azobenzene.

APPENDIX A PULSE SHAPER ALIGNMENT

The quality of the modulation for this apparatus strongly depends on the quality of the alignment. Because of the reflective mode configuration, the alignment procedure is highly simplified (i.e. only one grating angle is necessary to be aligned). The experiment has two distinctive parts: the polarization splitter and beam steering, and the compressor.

The polarization splitter must be setup in a linear arrangement of the following elements: polarizer, Faraday rotator, and $\lambda/2$ waveplate. After these parts are aligned, two mirrors are setup to steer the laser into the compressor. Two iris apertures are set up in between these mirrors for the alignment of the compressor.

The compressor alignment is a difficult task because it involves the construction of a zero dispersion compressor with a $4f$ configuration. Therefore, a recipe for the alignment is given below.

Define the Fourier plane (mask position) and place a translation stage ($S1$) away from that position at a distance equal to the cylindrical mirror focal length (f). Place an aperture ($A1$) at the end point of this stage.

1. Place the grating's rotation stage (RS) close to $S1$. To meet the $4f$ configuration, a second translation stage ($S2$) must be set such that the distance from the grating to this stage plus the distance from $S2$ to the cylindrical mirror is approximately f . Place another aperture ($A2$) on one side of $S2$.

2. With the help of a He-Ne laser place two more apertures ($A3$ and $A4$) in the back of the mask (one close to the back of the mask and the second one as far away as possible) position and check that the aperture height is the same for all of them (beam path parallel to the table).

3. Place the steering mirrors to bring the femtosecond laser beam into the compressor and align the laser beam through $A1$ and $A2$.

4. Place the grating in the RS and check that the grating surface and the rulings are perpendicular to the plane of the optical table. This can be achieved by setting the height of all the grating diffraction orders to the same height at different distances (parallel to the optical table). Align the angle of the grating with $A2$ and then remove $A2$.

5. Place the folding mirror in $S2$ without changing the rotation angle of RS , tilt the vertical angle of the grating such that the beam is reflected in this mirror.

6. Place the cylindrical mirror in $S1$. Use aperture $A3$ and $A4$ to align the folding mirror and the cylindrical mirror. To check the position of the cylindrical mirror, place a regular mirror where the back of the spatial light modulator will be placed, and make the incoming and outgoing beams to be the same size. Having the incoming and outgoing beams collimated and with the same size guarantees that the distance between the cylindrical mirror and the mask's back mirror is equal to f .

7. Block the beam (be careful, it is focusing at the mask position) and place the spatial light modulator in the Fourier plane. Before allowing the beam in the pulse shaper rotate the grating to the Littrow angle (this angle can be calculated using the grating equation). Unblock the beam and place the first diffraction order close to the middle of the mask array. Rotate the mask array until the outgoing beam goes through the entrance aperture ($A5$).

8. With an autocorrelator or other technique (i.e. FROG), slowly move the first stage to minimize the pulse width. If the pulse presents a lot of temporal structure, minimize the pulse width and then rotate the grating. This rotation will minimize the temporal distortion. Repeat this step until the shortest structureless pulse is obtained.

9. After this alignment, the pulse must be analyzed spatially to verify that the beam does not have spatial chirp. If spatial chirp is present, rotate the optical axis of the cylindrical mirror until the effect disappears.

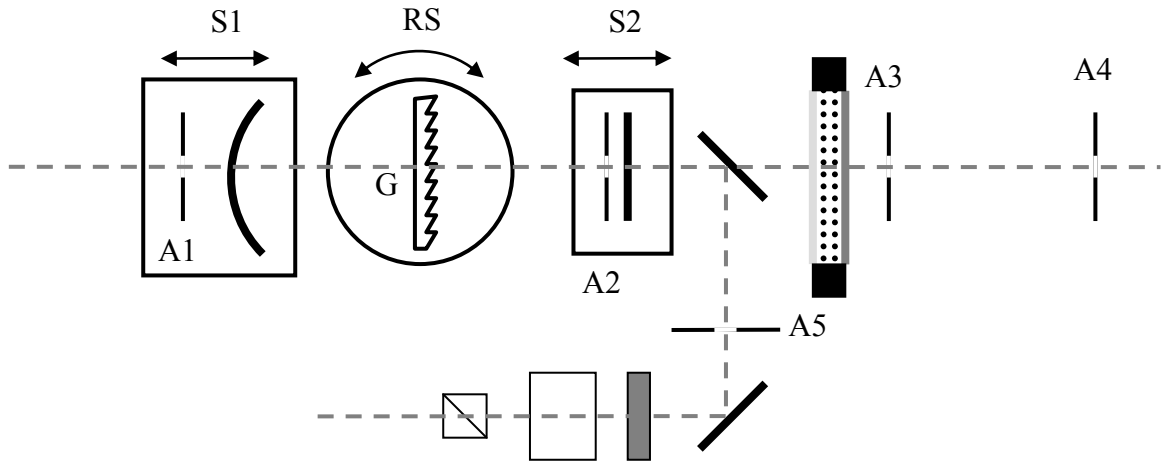


Figure A-1. Scheme of the setup with the apertures and translation stages. S1 and S2: translation stages; RS: rotation stage; A1, A2, A3, A4, and A5: iris apertures; M1, M2 steering mirrors; FM, folding mirror.

APPENDIX B
TIME DEPENDENCE PERTURBATION THEORY

A quantum system in the absence of any interaction can be described by the time-independent Hamiltonian

$$\hat{H}^0 |\psi_k^0\rangle = E_k^0 |\psi_k^0\rangle \quad (\text{B-1})$$

where E_k^0 and ψ_k^0 are the eigenvalues (energies) and eigenfunctions (wave functions) of H^0 .

When a time-dependent perturbation is applied to the system, the time dependence wave function evolution is expressed by the time-dependent Schrödinger equation

$$-\frac{\hbar}{i} \frac{\partial |\Psi\rangle}{\partial t} = \hat{H} |\Psi\rangle. \quad (\text{B-2})$$

Here, H is the total Hamiltonian and contains both the unperturbed and the perturbation operators. Thus,

$$\hat{H} = \hat{H}^0 + \hat{H}'. \quad (\text{B-3})$$

Assuming no perturbation, the time-dependent Schrödinger equation is

$$-\frac{\hbar}{i} \frac{\partial |\Psi\rangle}{\partial t} = \hat{H}^0 |\Psi\rangle \quad (\text{B-4})$$

$$|\Psi\rangle = \sum_k c_k |\psi_k^0\rangle \quad (\text{B-5})$$

Since Ψ can always be expressed in the complete basis set of ψ_k^0

$$-\frac{\hbar}{i} \frac{\partial \sum_k c_k |\psi_k^0\rangle}{\partial t} = \hat{H}^0 \sum_k c_k |\psi_k^0\rangle = \sum_k E_k^0 c_k |\psi_k^0\rangle. \quad (\text{B-6})$$

Projecting this equation in the basis set of ψ_k^0

$$-\frac{\hbar}{i} \frac{\partial \sum_k c_k \langle \psi_k^0 | \psi_k^0 \rangle}{\partial t} = \sum_k E_k^0 c_k \langle \psi_k^0 | \psi_k^0 \rangle \quad (\text{B-7})$$

$$-\frac{\hbar}{i} \frac{\partial \sum_k c_k}{\partial t} = \sum_k E_k^0 c_k. \quad (\text{B-8})$$

This differential equation can be solved for each coefficient individually

$$c_k(t) = c_k \exp(-iE_k^0 t/\hbar). \quad (\text{B-9})$$

Replacing this result in equation B-5, we obtain

$$|\Psi(t)\rangle = \sum_k c_k(t) |\psi_k^0\rangle = \sum_k c_k \exp(-iE_k^0 t/\hbar) |\psi_k^0\rangle. \quad (\text{B-10})$$

Now the Schrödinger equation with the perturbation is

$$-\frac{\hbar}{i} \frac{\partial \sum_k c_k(t) \exp(-iE_k^0 t/\hbar) |\psi_k^0\rangle}{\partial t} = \hat{H} \sum_k c_k(t) \exp(-iE_k^0 t/\hbar) |\psi_k^0\rangle. \quad (\text{B-11})$$

Note that because the Hamiltonian is time-dependent, the state function will evolve with time and the coefficients of the linear combination have to evolve with time, too.

Equation B-11 can be simplified to

$$-\frac{\hbar}{i} \partial \sum_k \frac{\partial c_k(t)}{\partial t} \exp(-iE_k^0 t/\hbar) |\psi_k^0\rangle = \sum_k c_k(t) \exp(-iE_k^0 t/\hbar) \hat{H}' |\psi_k^0\rangle. \quad (\text{B-12})$$

Again projecting in the complete basis set ψ_k^0

$$-\frac{\hbar}{i} \partial \sum_k \frac{\partial c_k(t)}{\partial t} \exp(-iE_k^0 t/\hbar) \delta_{mk} = \sum_k c_k(t) \exp(-iE_k^0 t/\hbar) \langle \psi_m^0 | \hat{H}' | \psi_k^0 \rangle. \quad (\text{B-13})$$

Since δ_{mk} is 1 when k is equal to m , the sum of the left side reduces to

$$\frac{\partial c_m(t)}{\partial t} = \frac{-i}{\hbar} \sum_k c_k(t) \exp(i(E_m^0 - E_k^0)t/\hbar) \langle \psi_m^0 | \hat{H}' | \psi_k^0 \rangle. \quad (\text{B-14})$$

Thus the N^{th} order solution is

$$\frac{\partial c_m^{(N+1)}(t)}{\partial t} = \frac{-i}{\hbar} \sum_k c_m^{(N)}(t) \exp(i(E_m^0 - E_k^0)t/\hbar) \langle \psi_m^0 | \hat{H}' | \psi_k^0 \rangle. \quad (\text{B-15})$$

Assuming that the system is unperturbed in a state ψ_i^0 before the perturbation, the solution of these equations are,

$$c_m^{(0)}(t) = \delta_{mk} \quad (\text{B-16})$$

$$c_m^{(1)}(t) = \frac{-i}{\hbar} \int_{-\infty}^t \exp(i(E_m^0 - E_k^0)t'/\hbar) \langle \psi_m^0 | \hat{H}'(t') | \psi_k^0 \rangle dt' \quad (\text{B-17})$$

$$c_m^{(2)}(t) = \frac{-i}{\hbar} \sum_n \int_{-\infty}^t \exp(i(E_m^0 - E_n^0)t'/\hbar) \langle \psi_m^0 | \hat{H}'(t') | \psi_n^0 \rangle c_n^{(1)}(t') dt'. \quad (\text{B-18})$$

Then the second order time dependent perturbation theory coefficient is

$$c_m^{(2)}(t) = \frac{-1}{\hbar^2} \sum_n \int_{-\infty}^t \exp(i\omega_{mn}t'') H_{mn}(t'') \int_{-\infty}^t \exp(i\omega_{nk}t') H_{nk}(t') dt' dt'' \quad (\text{B-19})$$

where

$$H_{ij}(t) = \langle \psi_i^0 | \hat{H}'(t) | \psi_j^0 \rangle \quad (\text{B-20})$$

$$\omega_{ij} = (E_i^0 - E_j^0)/\hbar. \quad (\text{B-21})$$

For an ultrafast laser field, the perturbation is expressed as

$$\hat{H}'(t) = Q_i x_i E(t). \quad (\text{B-22})$$

Thus, replacing the perturbation on the second order coefficient, the following expression is obtained

$$c_m^{(2)}(t) = \frac{-1}{\hbar^2} \sum_n \mu_{fn} \mu_{ng} \int_{-\infty}^t \int_{-\infty}^t E(t') E(t'') \exp(i\omega_{mn}t'') \exp(i\omega_{nk}t') dt' dt''. \quad (\text{B-23})$$

APPENDIX C PARTIAL LEAST SQUARES

Partial least squares, PLS, is a multi-dimensional linear regression. Like any linear regression, partial least squares describes the relationship between the variable predictor, \mathbf{X} , and variable response, \mathbf{Y} , so that,

$$\mathbf{Y} = \mathbf{X}\mathbf{B} + \mathbf{F} \quad (\text{C-1})$$

where \mathbf{B} represents the matrix of regression coefficients, and \mathbf{F} the residual matrix. Like principal component analysis, partial least squares is a matrix orthogonal linear transformation, which relies on diagonalizing the \mathbf{X} matrix, or its covariance matrix, to extract a new orthogonal basis set based on its variance. Each eigenvector (latent variable) in the basis set is a linear combination of the independent variables, x_i . As any basis set, the latent variables do not have correlation among them. Therefore, \mathbf{X} is decomposed in,

$$\mathbf{T} = \mathbf{X}\mathbf{W} \quad (\text{C-2})$$

Here, \mathbf{T} and \mathbf{W} are matrices containing the collective variable coefficients and their weight, respectively. \mathbf{T} elements are selected such that they represent good approximations of \mathbf{X} and \mathbf{Y} .

$$\mathbf{X} = \mathbf{T}\mathbf{P}' + \mathbf{E} \quad (\text{C-3})$$

$$\mathbf{Y} = \mathbf{T}\mathbf{C}' + \mathbf{F} \quad (\text{C-4})$$

Here, the regression coefficients of \mathbf{P}' and \mathbf{C}' are calculated so that they make the matrices \mathbf{E} and \mathbf{F} small.

$$\mathbf{Y} = \mathbf{X}\mathbf{W}\mathbf{C}' + \mathbf{F} = \mathbf{X}\mathbf{B} + \mathbf{F} \quad (\text{C-5})$$

However, unlike other multilinear regression methods such as principal component regression, PLS finds the minimum number of independent variable sets by including the covariance structure between \mathbf{X} and \mathbf{Y} in the calculation of the weight matrix, \mathbf{W} . In other words,

the criteria for selecting latent variables not only includes the maximization of the explained variance in the independent variable data, \mathbf{X} , but also the maximum possible correlation with the dependent variables, \mathbf{Y} . Hence, partial least squares as multivariate data analysis models dependent variables, \mathbf{Y} , in terms of a set of independent variables, x_i , with the maximum correlation with \mathbf{Y} .

Topologically, this represents a projection of the n^{th} -dimension of the laser parameterization to a hyper-plane with N dimensions (or N latent variables) in such a way that the projection coordinates are good approximations of the molecular response. In other words, latent variables are a new set of coordinates in the independent variable space, where the projection of the actual x_i components points to the direction with maximum correlation with the values of \mathbf{Y} (Figure C-1, d vector).

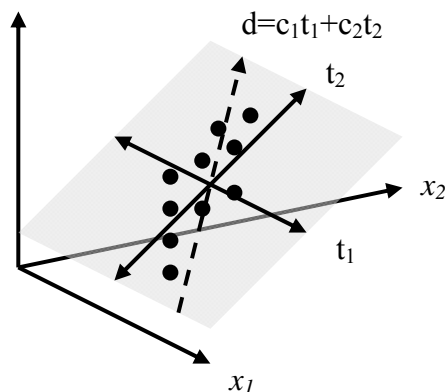


Figure C-1. Geometrical representation of partial least squares model.

APPENDIX D
PARTIAL LEAST SQUARES ANALYSIS RESULTS

Partial Least Squares Regression for The Autocorrelation Evolution

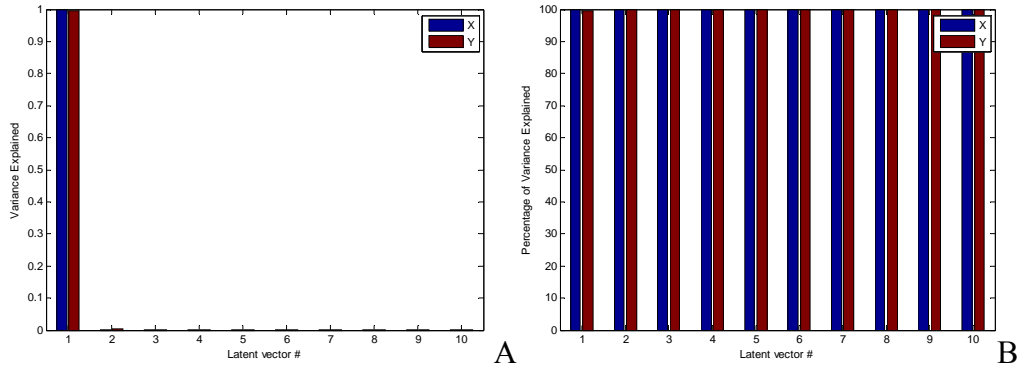


Figure D-1. A) Variance explained by each latent variable. B) Cumulative variance explained. Autocorrelation model (Blue bars). Fitness model (red bars).

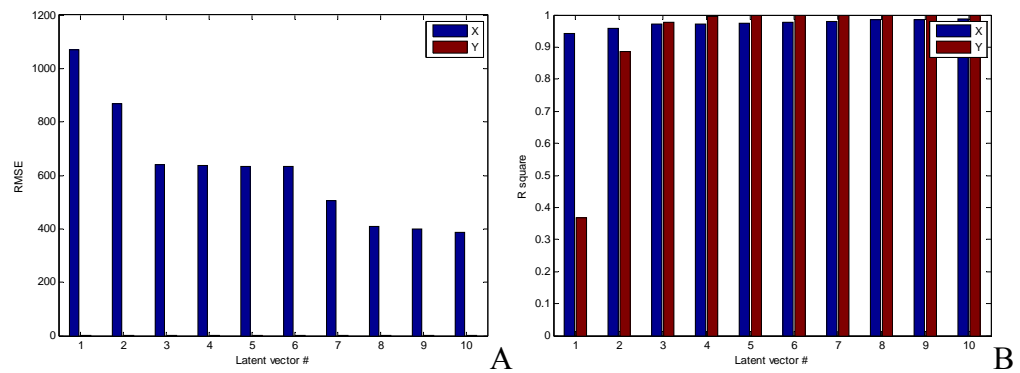


Figure D-2. A) RMSE error and B) Linear correlation (R^2) for the fitness model versus the number of latent variables used in the model. Autocorrelation model (Blue bars). Fitness model (red bars).

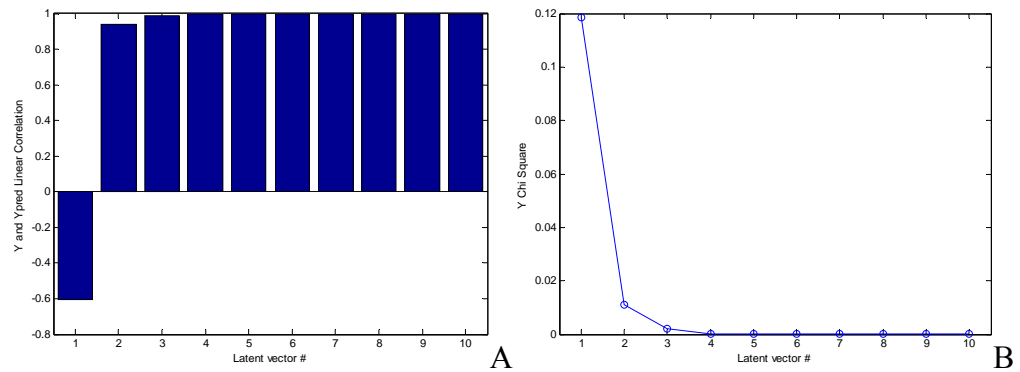


Figure D-3. Error of the fitness model: A) Linear correlation and B) Chi square.

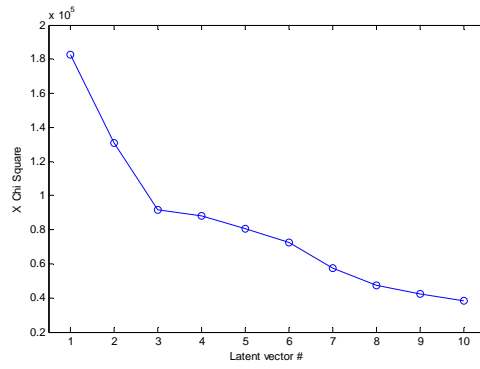


Figure D-4. Chi square error of the autocorrelation model.

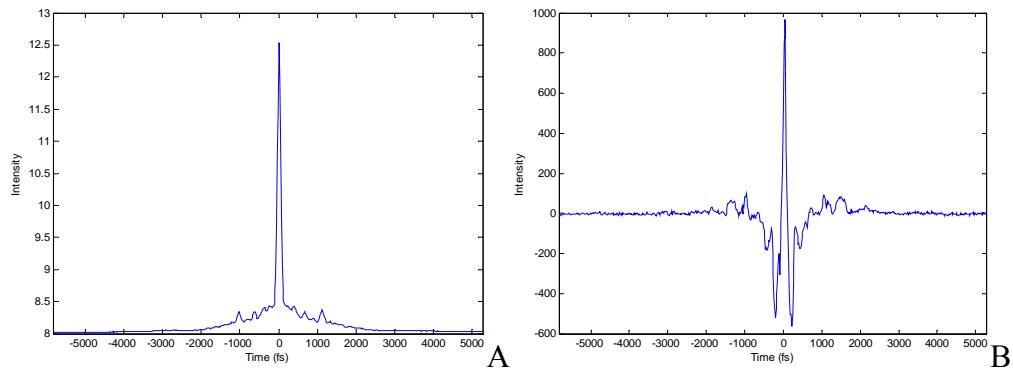


Figure D-5. Autocorrelation latent variables: A) First and B) Second.

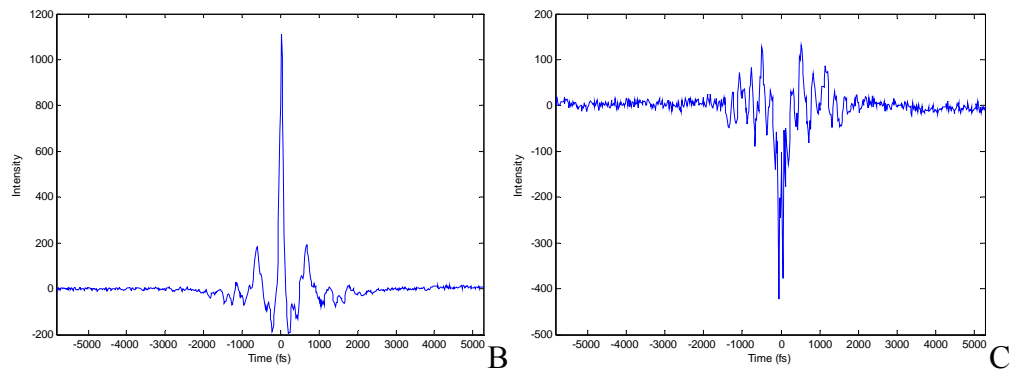


Figure D-6. Autocorrelation latent variables: A) Third and B) Forth.

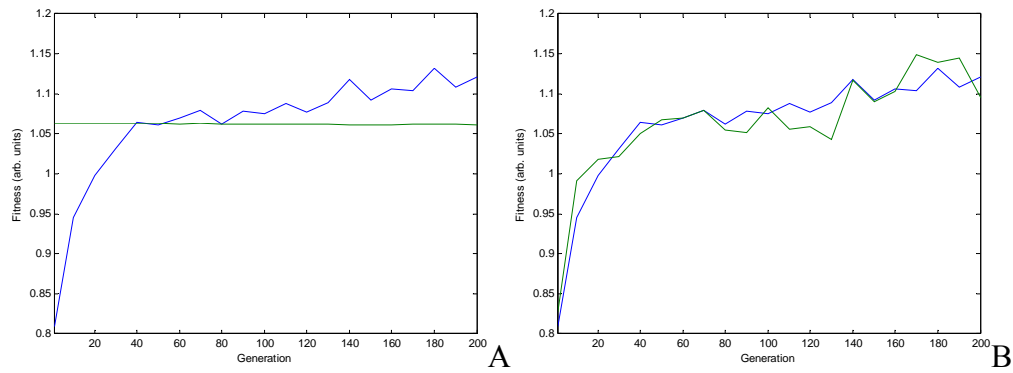


Figure D-7. Fitness (blue line) and PLS linear model (green line). A) With one latent variable. B) With two latent variables.

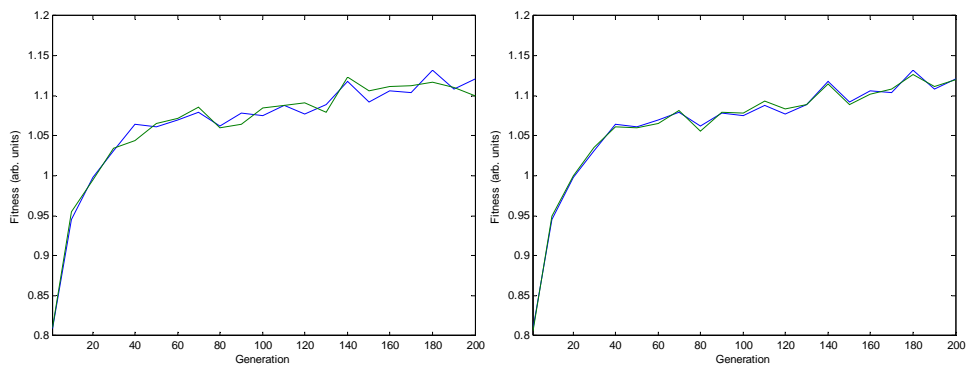


Figure D-8. Fitness (blue line) and PLS linear model (green line). A) With three latent variables. B) With four latent variables.

Partial Least Squares Regression for the Spectral Evolution

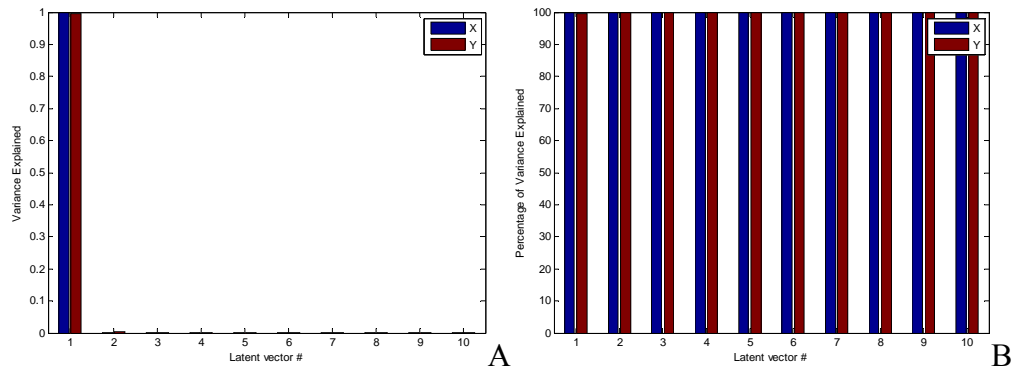


Figure D-9. A) Variance explained by each latent variable. B) Cumulative variance explained. Spectral model (Blue bars). Fitness model (red bars).

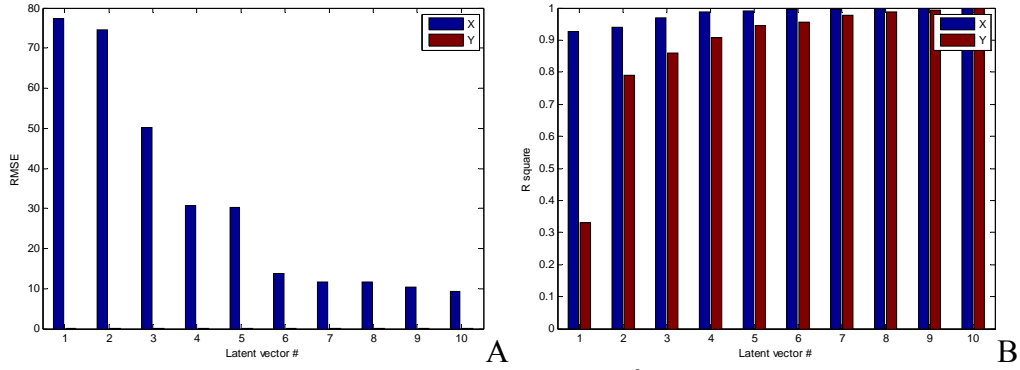


Figure D-10. A) RMSE error and B) Linear correlation (R^2) for the fitness model versus the number of latent variables used in the model. Spectral model (Blue bars). Fitness model (red bars).

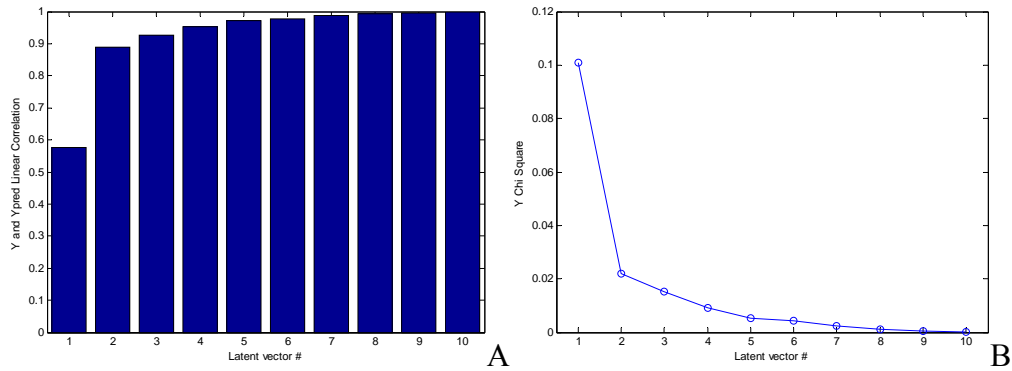


Figure D-11. Error of the fitness model: A) Linear correlation and B) Chi square.

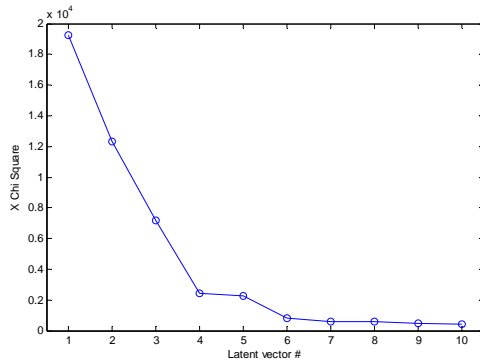


Figure D-12. Chi square error of the spectral model.

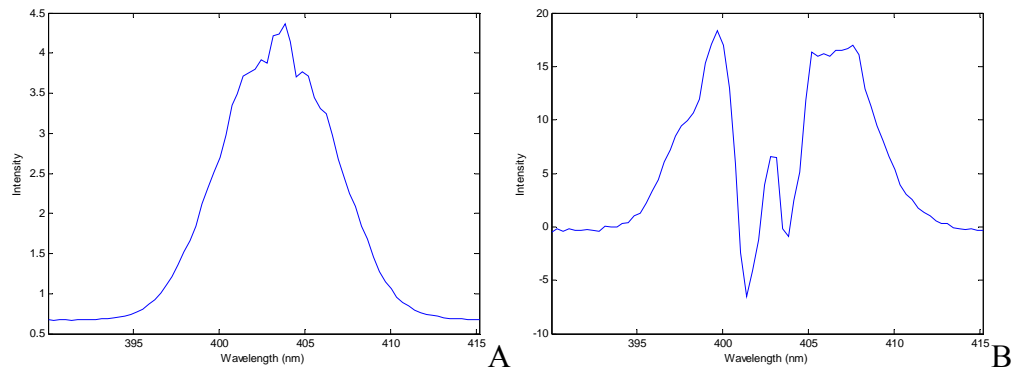


Figure D-13. Spectral latent variables: A) First and B) Second.

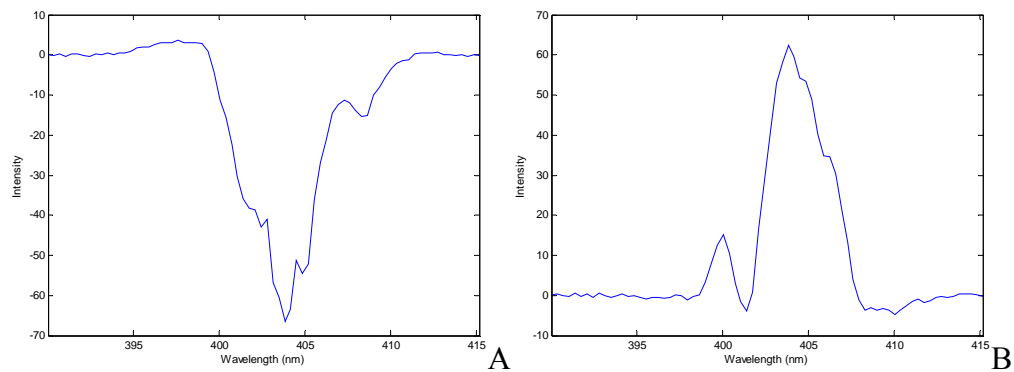


Figure D-14. Spectral latent variables: A) Third and B) Forth.

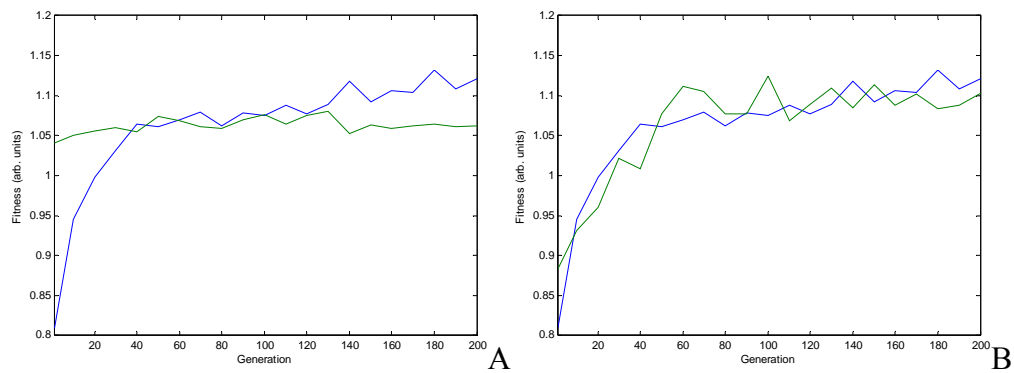


Figure D-15. Fitness (blue line) and PLS linear model (green line). A) With one latent variable. B) With two latent variables.

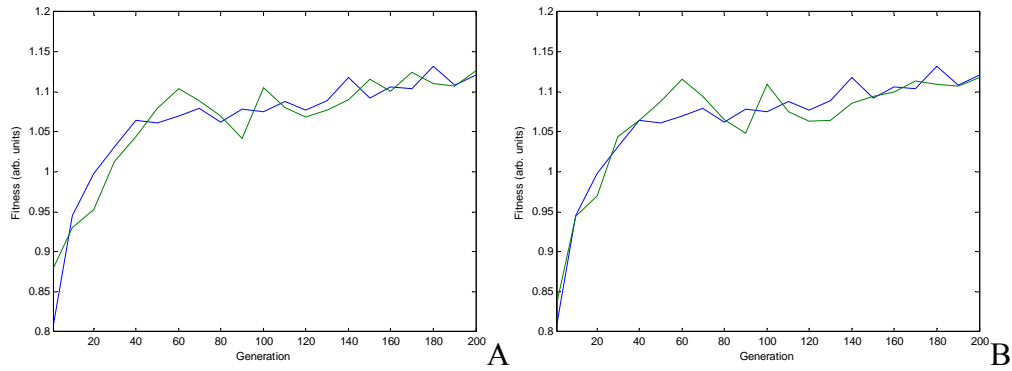


Figure D-16. Fitness (blue line) and PLS linear model (green line). A) With three latent variables. B) With four latent variables.

Partial Least Squares Regression for the Phase Evolution

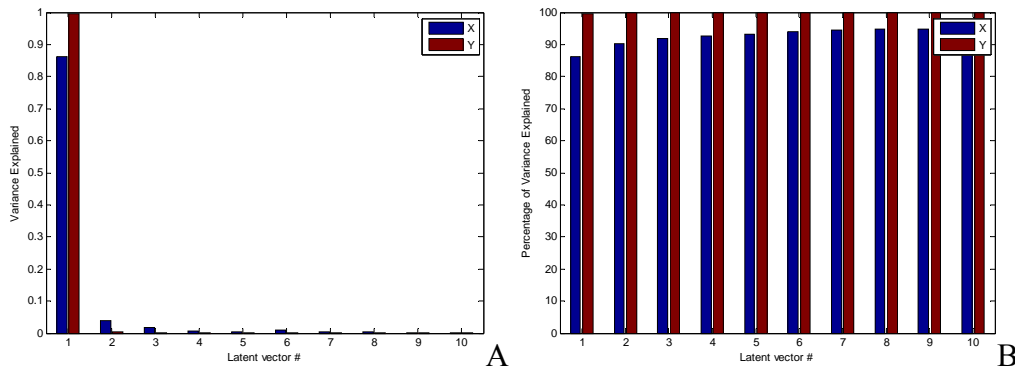


Figure D-17. A) Variance explained by each latent variable. B) Cumulative variance explained. Phase model (Blue bars). Fitness model (red bars).

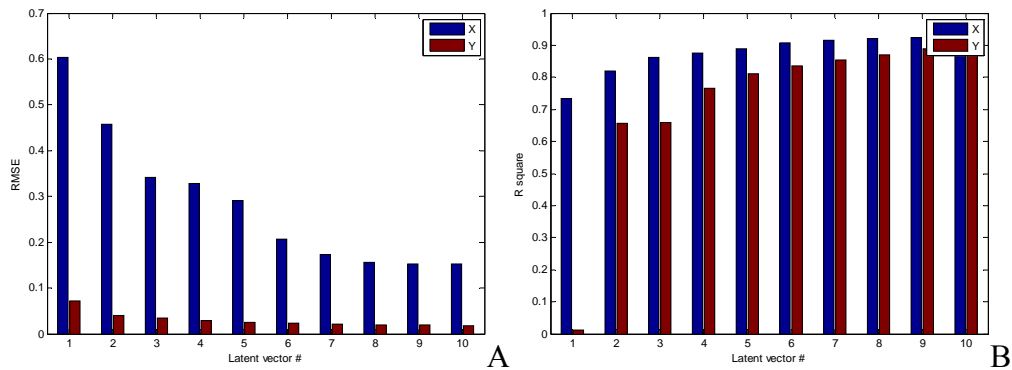


Figure D-18. A) RMSE error and B) Linear correlation (R^2) for the fitness model versus the number of latent variables used in the model. Phase model (Blue bars). Fitness model (red bars).

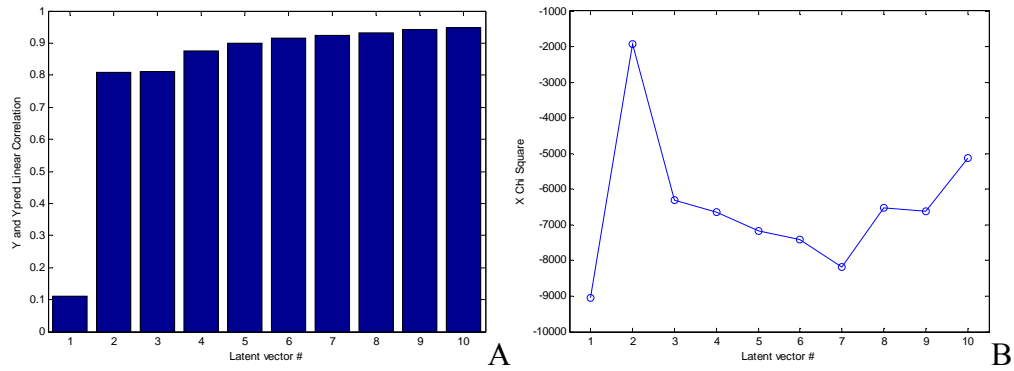


Figure D-19. Error of the fitness model: A) Linear correlation and B) Chi square.

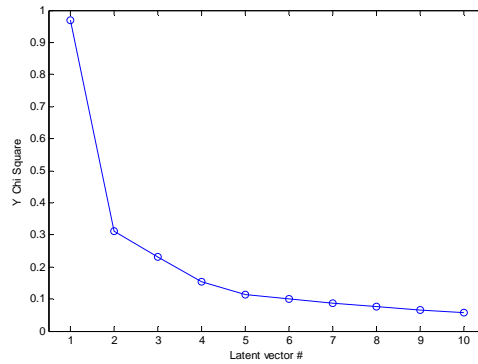


Figure D-20. Chi square error of the phase model.

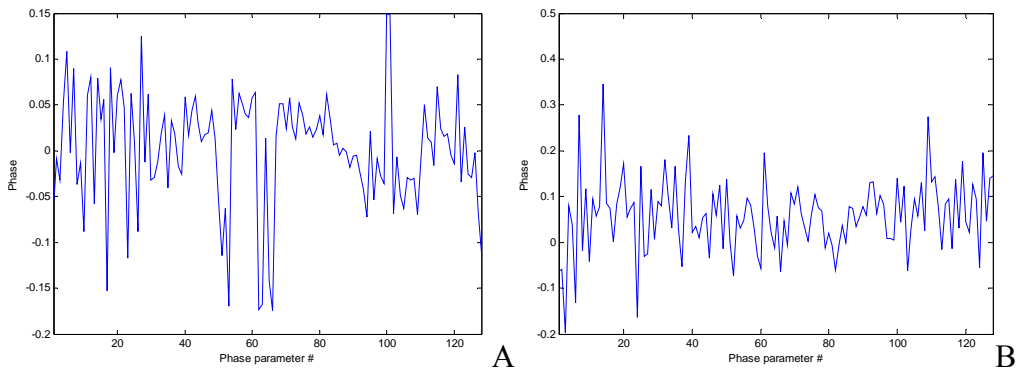


Figure D-21. Phase latent variables: A) First and B) Second.

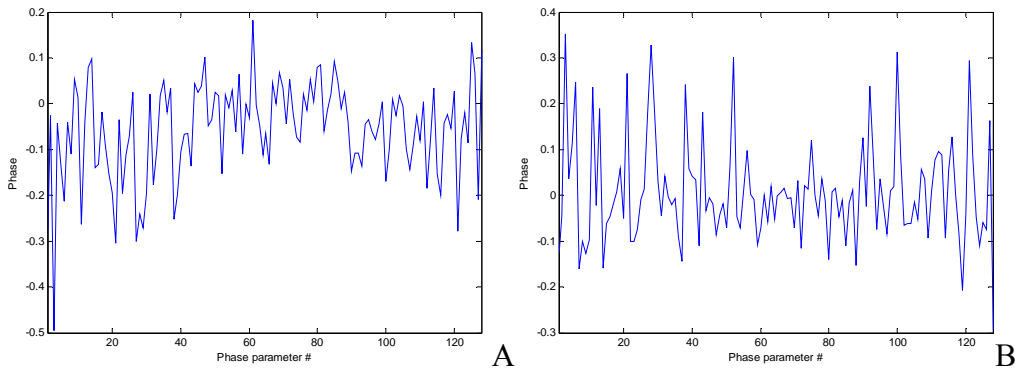


Figure D-22. Phase latent variables: A) Third and B) Forth.

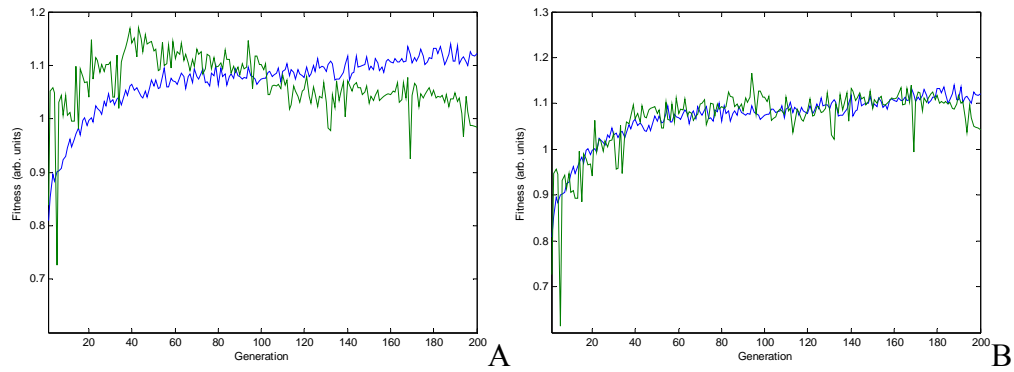


Figure D-23. Fitness (blue line) and PLS linear model (green line). A) With one latent variable. B) With two latent variables.

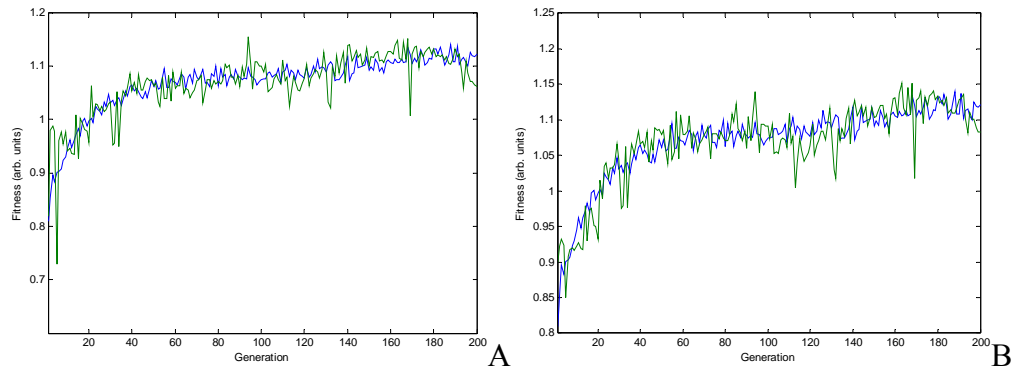


Figure D-24. Fitness (blue line) and PLS linear model (green line). A) With three latent variables. B) With four latent variables.

APPENDIX E
SPATIAL LIGHT MODULATOR CHARACTERIZATION

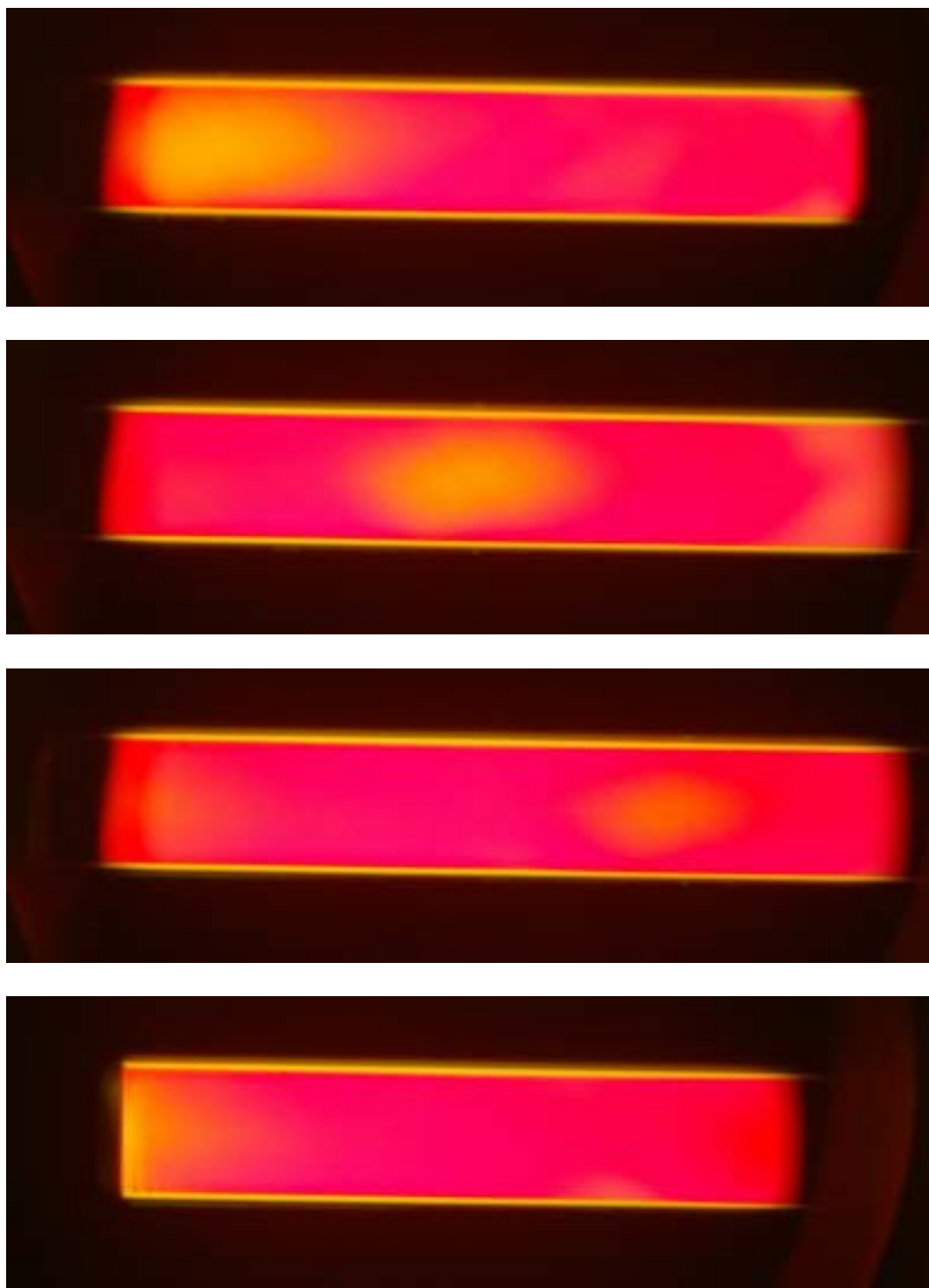


Figure E-1. Spatial light modulator mask pixel inhomogeneity for mask 1 at level 4095 and mask 2 and level 600.

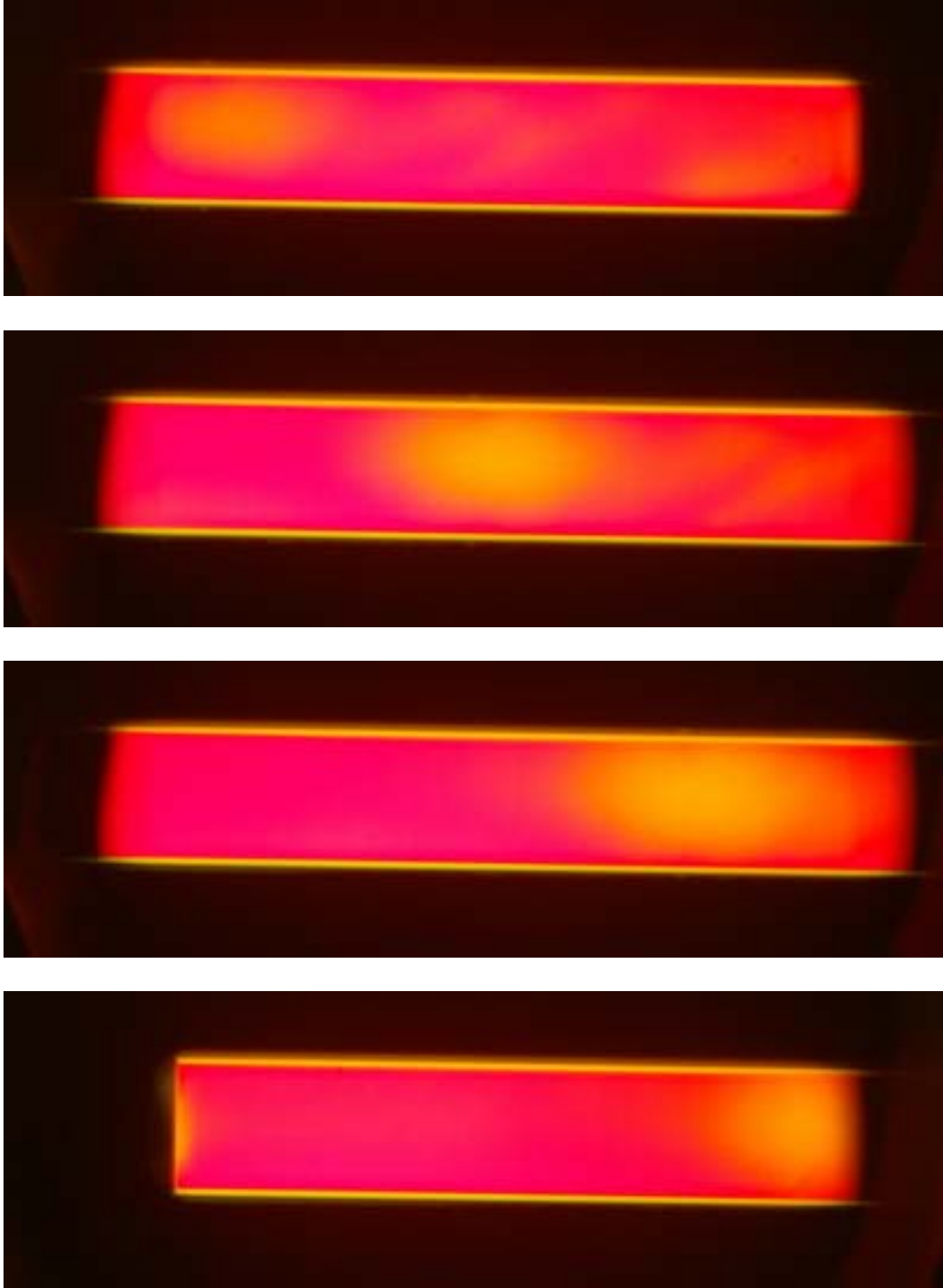


Figure E-2. Spatial light modulator mask pixel inhomogeneity for mask 1 at level 600 and mask 2 and level 4095.

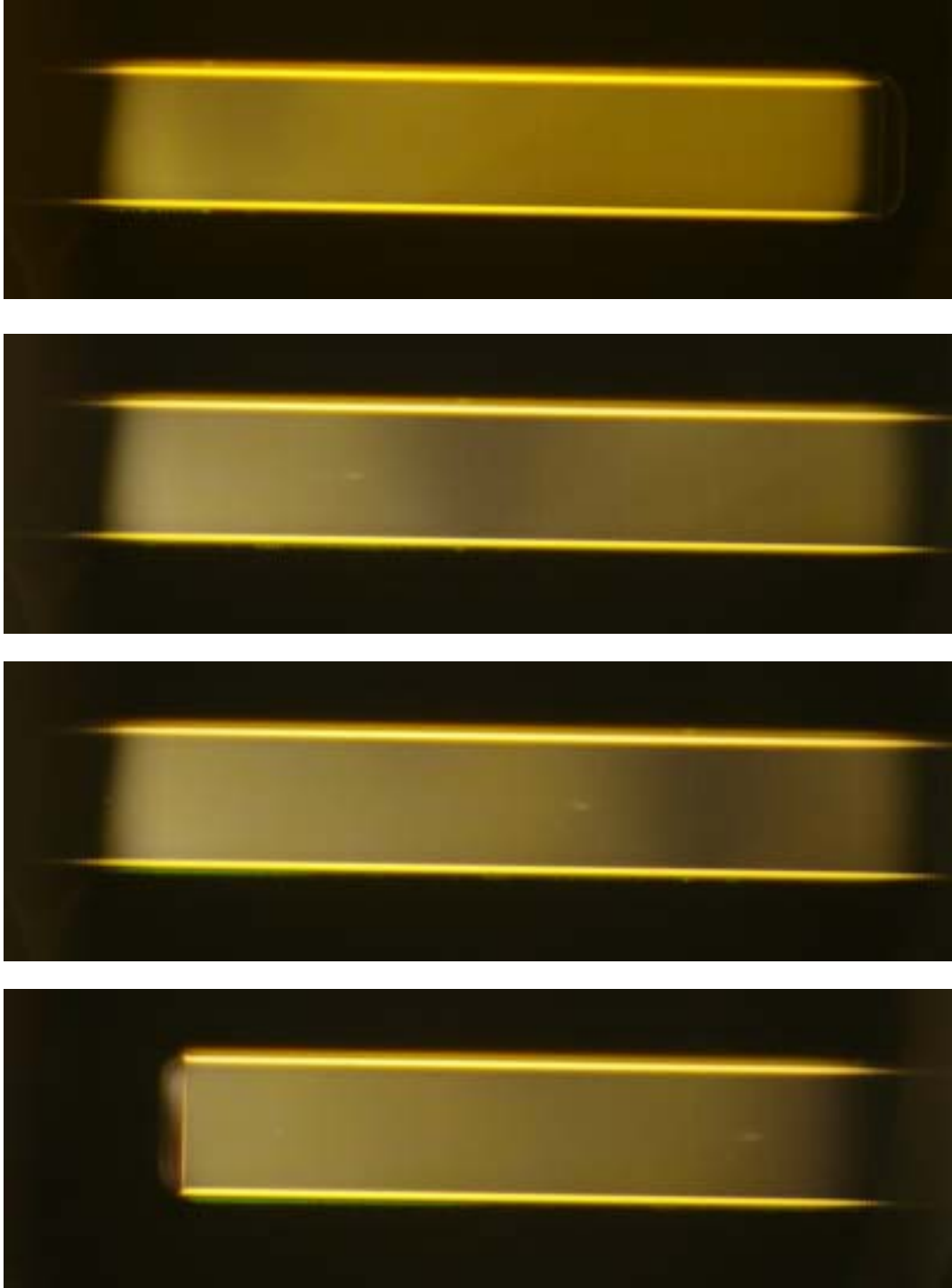


Figure E-3. Spatial light modulator mask pixel inhomogeneity for mask 1 at level 3500 and mask 2 and level 4095.

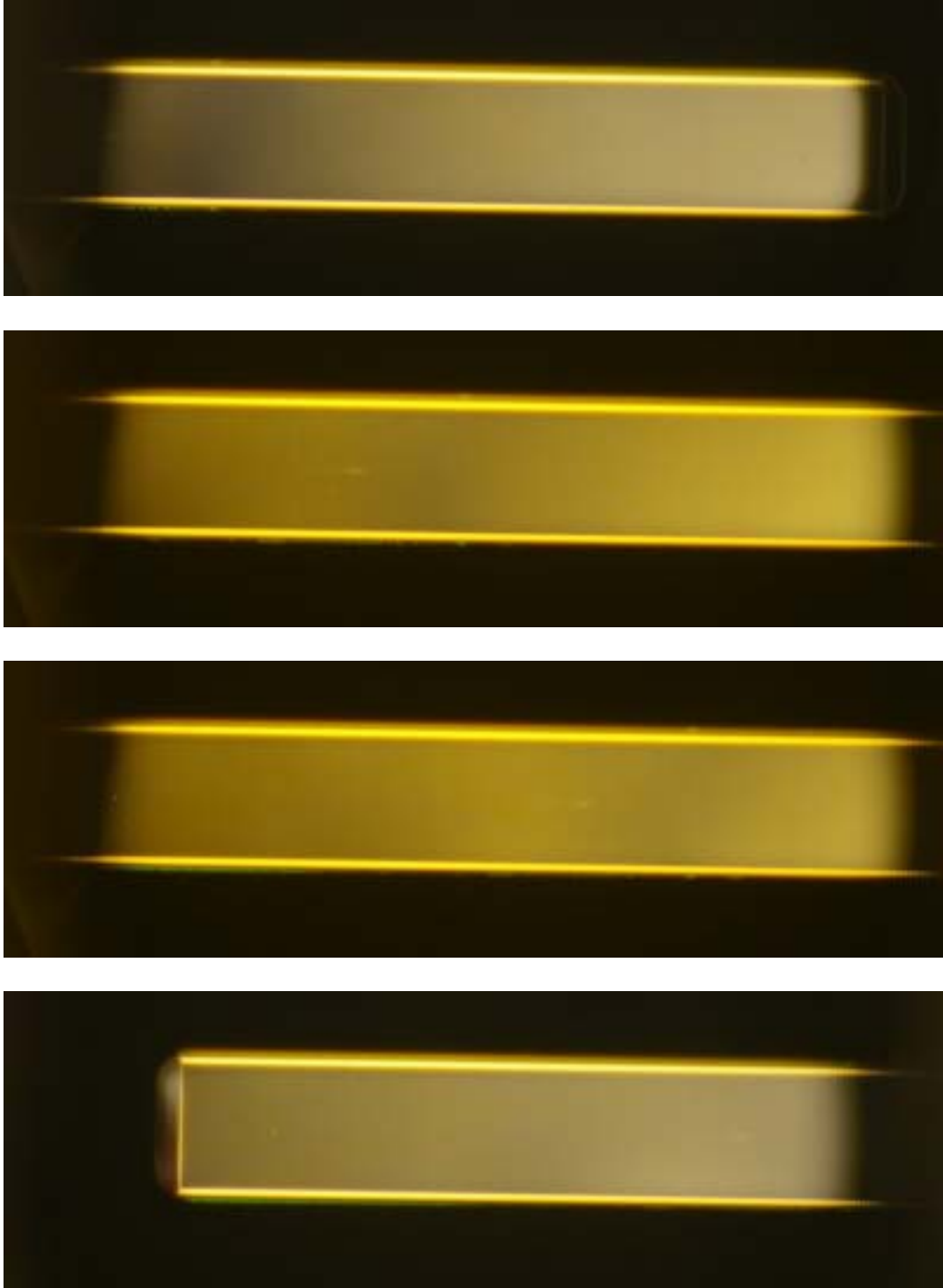


Figure E-4. Spatial light modulator mask pixel inhomogeneity for mask 1 at level 4095 and mask 2 and level 3500.

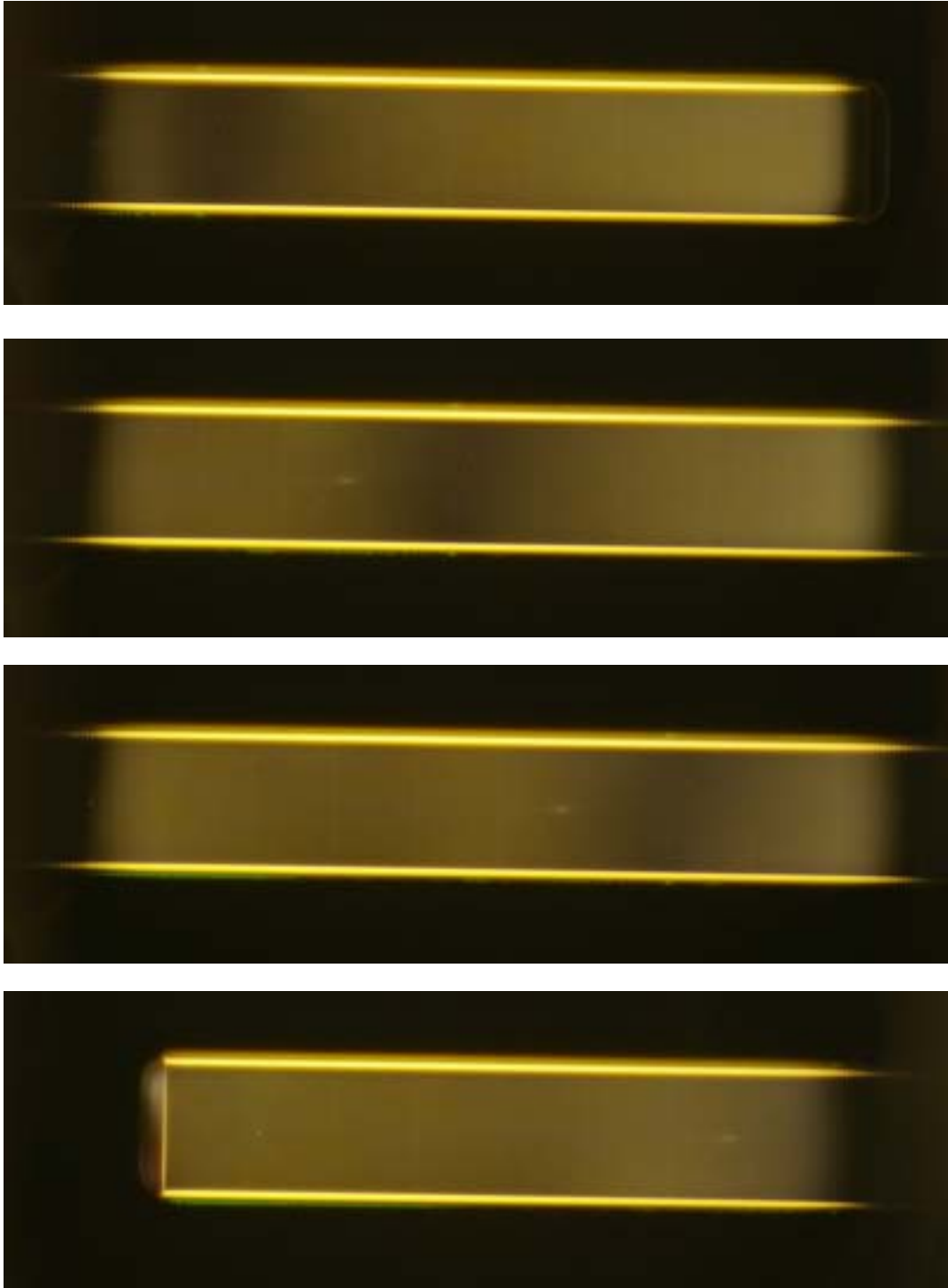


Figure E-5. Spatial light modulator mask pixel inhomogeneity for mask 1 at level 4095 and mask 2 and level 4095.

LIST OF REFERENCES

1. P. Brumer and M. Shapiro, "Control of unimolecular reactions using coherent-light," *Chem. Phys. Lett.* **126**(6), 541-546 (1986).
2. D. J. Tannor and S. A. Rice, "Control of selectivity of chemical reaction via control of wave packet evolution," *J. Chem. Phys.* **83**(10), 5013-5018 (1985).
3. N. Bloembergen and E. Yablonovitch, "Infrared-laser-induced unimolecular reactions," *Phys. Today* **31**(5), 23-30 (1978).
4. A. H. Zewail, "Laser selective chemistry: Is it possible?," *Phys. Today* **33**(11), 27-33 (1980).
5. N. Bloembergen and A. H. Zewail, "Energy redistribution in isolated molecules and the question of mode-selective laser chemistry revisited," *J. Phys. Chem.* **88**(23), 5459-5465 (1984).
6. T. Elsaesser and W. Kaiser, "Vibrational and vibronic relaxation of large polyatomic-molecules in liquids," *Annu. Rev. Phys. Chem.* **42**, 83-107 (1991).
7. Y. Ohtsuki, K. Nakagami, Y. Fujimura, W. S. Zhu, and H. Rabitz, "Quantum optimal control of multiple targets: Development of a monotonically convergent algorithm and application to intramolecular vibrational energy redistribution control," *J. Chem. Phys.* **114**(20), 8867-8876 (2001).
8. C. S. Parmenter, "Introductory lecture. Vibrational redistribution within excited electronic states of polyatomic molecules," *Faraday Discuss.*, 7-22 (1983).
9. M. Dantus and V. V. Lozovoy, "Experimental coherent laser control of physicochemical processes," *Chem. Rev. (Washington, DC, U. S.)* **104**(4), 1813-1859 (2004).
10. M. Shapiro, J. W. Hepburn, and P. Brumer, "Simplified laser control of unimolecular reactions: Simultaneous (ω_1, ω_3) excitation," *Chem. Phys. Lett.* **149**(5-6), 451-454 (1988).
11. C. Chen, Y. Y. Yin, and D. S. Elliott, "Interference between optical transitions," *Phys. Rev. Lett.* **64**(5), 507-510 (1990).
12. V. D. Kleiman, L. C. Zhu, J. Allen, and R. J. Gordon, "Coherent control over the photodissociation of CH_3I ," *J. Chem. Phys.* **103**(24), 10800-10803 (1995).
13. V. D. Kleiman, L. C. Zhu, X. N. Li, and R. J. Gordon, "Coherent Phase-Control of the Photoionization of H_2S ," *J. Chem. Phys.* **102**(14), 5863-5866 (1995).
14. L. C. Zhu, V. Kleiman, X. N. Li, S. P. Lu, K. Trentelman, and R. J. Gordon, "Coherent laser control of the product distribution obtained in the photoexcitation of HI," *Science (Washington, DC, U. S.)* **270**(5233), 77-80 (1995).

15. P. Brumer and M. Shapiro, "Laser control of molecular processes," *Annu. Rev. Phys. Chem.* **43**, 257-282 (1992).
16. D. J. Tannor, R. Kosloff, and S. A. Rice, "Coherent pulse sequence induced control of selectivity of reactions : Exact quantum-mechanical calculations," *J. Chem. Phys.* **85**(10), 5805-5820 (1986).
17. T. Baumert, M. Grosser, R. Thalweiser, and G. Gerber, "Femtosecond time-resolved molecular multiphoton ionization: The Na₂ system," *Phys. Rev. Lett.* **67**(27), 3753-3756 (1991).
18. E. D. Potter, J. L. Herek, S. Pedersen, Q. Liu, and A. H. Zewail, "Femtosecond laser control of a chemical reaction," *Nature (London, U. K.)* **355**(6355), 66-68 (1992).
19. C. J. Bardeen, J. W. Che, K. R. Wilson, V. V. Yakovlev, P. J. Cong, B. Kohler, J. L. Krause, and M. Messina, "Quantum control of NaI photodissociation reaction product states by ultrafast tailored light pulses," *J. Phys. Chem. A* **101**(20), 3815-3822 (1997).
20. N. F. Scherer, A. J. Ruggiero, M. Du, and G. R. Fleming, "Time resolved dynamics of isolated molecular systems studied with phase-locked femtosecond pulse pairs," *J. Chem. Phys.* **93**(1), 856-857 (1990).
21. N. F. Scherer, R. J. Carlson, A. Matro, M. Du, A. J. Ruggiero, V. Romerorochin, J. A. Cina, G. R. Fleming, and S. A. Rice, "Fluorescence-detected wave packet interferometry: Time resolved molecular-spectroscopy with sequences of femtosecond phase-locked pulses," *J. Chem. Phys.* **95**(3), 1487-1511 (1991).
22. U. Gaubatz, P. Rudecki, M. Becker, S. Schiemann, M. Kulz, and K. Bergmann, "Population switching between vibrational levels in molecular-beams," *Chem. Phys. Lett.* **149**(5-6), 463-468 (1988).
23. M. M. T. Loy, "Observation of population inversion by optical adiabatic rapid passage," *Phys. Rev. Lett.* **32**(15), 814-817 (1974).
24. P. Nuernberger, G. Vogt, T. Brixner, and G. Gerber, "Femtosecond quantum control of molecular dynamics in the condensed phase," *Phys. Chem. Chem. Phys.* **9**(20), 2470-2497 (2007).
25. G. M. Huang, T. J. Tarn, and J. W. Clark, "On the controllability of quantum-mechanical systems," *J. Math. Phys.* **24**(11), 2608-2618 (1983).
26. R. S. Judson and H. Rabitz, "Teaching lasers to control molecules," *Phys. Rev. Lett.* **68**(10), 1500-1503 (1992).
27. A. M. Weiner, "Femtosecond pulse shaping using spatial light modulators," *Rev. Sci. Instrum.* **71**(5), 1929-1960 (2000).

28. T. Brixner and G. Gerber, "Femtosecond polarization pulse shaping," *Opt. Lett.* **26**(8), 557-559 (2001).
29. C. J. Bardeen, V. V. Yakovlev, K. R. Wilson, S. D. Carpenter, P. M. Weber, and W. S. Warren, "Feedback quantum control of molecular electronic population transfer," *Chem. Phys. Lett.* **280**(1-2), 151-158 (1997).
30. T. Brixner and G. Gerber, "Quantum control of gas-phase and liquid-phase femtochemistry," *ChemPhysChem* **4**(5), 418-438 (2003).
31. T. Brixner, N. H. Damrauer, B. Kiefer, and G. Gerber, "Liquid-phase adaptive femtosecond quantum control: Removing intrinsic intensity dependencies," *J. Chem. Phys.* **118**(8), 3692-3701 (2003).
32. D. Meshulach and Y. Silberberg, "Coherent quantum control of two-photon transitions by a femtosecond laser pulse," *Nature (London, U. K.)* **396**(6708), 239-242 (1998).
33. R. A. Bartels, M. M. Murnane, H. C. Kapteyn, I. Christov, and H. Rabitz, "Learning from learning algorithms: Application to attosecond dynamics of high-harmonic generation," *Phys. Rev. A* **70**(4), 043404 (2004).
34. R. E. Carley, E. Heesel, and H. H. Fielding, "Femtosecond lasers in gas phase chemistry," *Chem. Soc. Rev.* **34**(11), 949-969 (2005).
35. R. J. Gordon and S. A. Rice, "Active control of the dynamics of atoms and molecules," *Annu. Rev. Phys. Chem.* **48**, 601-641 (1997).
36. H. Rabitz, R. de Vivie-Riedle, M. Motzkus, and K. Kompa, "Chemistry: Whither the future of controlling quantum phenomena?," *Science (Washington, DC, U. S.)* **288**(5467), 824-828 (2000).
37. M. Shapiro and P. Brumer, "Quantum control of chemical reactions," *J. Chem. Soc., Faraday Trans.* **93**(7), 1263-1277 (1997).
38. T. C. Weinacht and P. H. Bucksbaum, "Using feedback for coherent control of quantum systems," *J. Opt. B Quantum S. O.* **4**(3), R35-R52 (2002).
39. M. Wollenhaupt, V. Engel, and T. Baumert, "Femtosecond laser photoelectron spectroscopy on atoms and small molecules: Prototype studies in quantum control," *Annu. Rev. Phys. Chem.* **56**, 25-56 (2005).
40. R. J. Levis, G. M. Menkir, and H. Rabitz, "Selective bond dissociation and rearrangement with optimally tailored, strong-field laser pulses," *Science (Washington, DC, U. S.)* **292**(5517), 709-713 (2001).
41. R. L. Fork, C. V. Shank, C. Hirlimann, R. Yen, and W. J. Tomlinson, "Femtosecond white-light continuum pulses," *Opt. Lett.* **8**(1), 1-3 (1983).

42. D. Meshulach and Y. Silberberg, "Coherent quantum control of multiphoton transitions by shaped ultrashort optical pulses," *Phys. Rev. A* **60**(2), 1287-1292 (1999).
43. J. P. Ogilvie, K. J. Kubarych, A. Alexandrou, and M. Joffe, "Fourier transform measurement of two-photon excitation spectra: applications to microscopy and optimal control," *Opt. Lett.* **30**(8), 911-913 (2005).
44. M. A. Montgomery and N. H. Damrauer, "Elucidation of control mechanisms discovered during adaptive manipulation of [Ru(dpb)₃](PF₆)₂ emission in the solution phase," *J. Phys. Chem. A* **111**(8), 1426-1433 (2007).
45. L. Nikowa, D. Schwarzer, and J. Troe, "Transient hot UV spectra in the collisional deactivation of highly excited trans-stilbene in liquid solvents," *Chem. Phys. Lett.* **233**(3), 303-308 (1995).
46. S. L. Logunov, V. V. Volkov, M. Braun, and M. A. El-Sayed, "The relaxation dynamics of the excited electronic states of retinal in bacteriorhodopsin by two-pump-probe femtosecond studies," *Proc. Natl. Acad. Sci. U. S. A.* **98**(15), 8475-8479 (2001).
47. D. S. Larsen, I. H. M. van Stokkum, M. Vengris, M. A. van der Horst, F. L. de Weerd, K. J. Hellingwerf, and R. van Grondelle, "Incoherent manipulation of the photoactive yellow protein photocycle with dispersed pump-dump-probe spectroscopy," *Biophys. J.* **87**(3), 1858-1872 (2004).
48. A. Rundquist, A. Efimov, and D. H. Reitze, "Pulse shaping with the Gerchberg-Saxton algorithm," *J. Opt. Soc. Am. B* **19**(10), 2468-2478 (2002).
49. A. M. Weiner, D. E. Leaird, G. P. Wiederrecht, and K. A. Nelson, "Femtosecond pulse sequences used for optical manipulation of molecular motion," *Science (Washington, DC, U. S.)* **247**(4948), 1317-1319 (1990).
50. W. Wohlleben, T. Buckup, J. L. Herek, and M. Motzkus, "Coherent control for spectroscopy and manipulation of biological dynamics," *ChemPhysChem* **6**(5), 850-857 (2005).
51. J. L. Herek, W. Wohlleben, R. J. Cogdell, D. Zeidler, and M. Motzkus, "Quantum control of energy flow in light harvesting," *Nature (London, U. K.)* **417**(6888), 533-535 (2002).
52. W. Wohlleben, T. Buckup, J. L. Herek, R. J. Cogdell, and M. Motzkus, "Multichannel carotenoid deactivation in photosynthetic light harvesting as identified by an evolutionary target analysis," *Biophys. J.* **85**(1), 442-450 (2003).
53. G. Vogt, P. Nuernberger, R. Selle, F. Dimler, T. Brixner, and G. Gerber, "Analysis of femtosecond quantum control mechanisms with colored double pulses," *Phys. Rev. A* **74**(3), 033413 (2006).
54. G. Cerullo, C. J. Bardeen, Q. Wang, and C. V. Shank, "High-power femtosecond chirped pulse excitation of molecules in solution," *Chem. Phys. Lett.* **262**(3-4), 362-368 (1996).

55. T. C. Gunaratne, X. Zhu, V. V. Lozovoy, and M. Dantus, "Symmetry of nonlinear optical response to time inversion of shaped femtosecond pulses as a clock of ultrafast dynamics," *Chem. Phys.* **338**(2-3), 259-267 (2007).
56. T. Hellerer, A. M. K. Enejder, and A. Zumbusch, "Spectral focusing: High spectral resolution spectroscopy with broad-bandwidth laser pulses," *Appl. Phys. Lett.* **85**(1), 25-27 (2004).
57. K. P. Knutsen, J. C. Johnson, A. E. Miller, P. B. Petersen, and R. J. Saykally, "High spectral resolution multiplex CARS spectroscopy using chirped pulses," *Chem. Phys. Lett.* **387**(4-6), 436-441 (2004).
58. T. Chen, A. Vierheilig, P. Waltner, M. Heid, W. Kiefer, and A. Materny, "Femtosecond laser-controlled selective excitation of vibrational modes on a multidimensional ground state potential energy surface," *Chem. Phys. Lett.* **326**(5-6), 375-382 (2000).
59. V. D. Kleiman, S. M. Arrivo, J. S. Melinger, and E. J. Heilweil, "Controlling condensed-phase vibrational excitation with tailored infrared pulses," *Chem. Phys.* **233**(2-3), 207-216 (1998).
60. T. Witte, J. S. Yeston, M. Motzkus, E. J. Heilweil, and K. L. Kompa, "Femtosecond infrared coherent excitation of liquid phase vibrational population distributions ($\nu > 5$)," *Chem. Phys. Lett.* **392**(1-3), 156-161 (2004).
61. L. Windhorn, T. Witte, J. S. Yeston, D. Proch, M. Motzkus, K. L. Kompa, and W. Fuss, "Molecular dissociation by mid-IR femtosecond pulses," *Chem. Phys. Lett.* **357**(1-2), 85-90 (2002).
62. L. Windhorn, J. S. Yeston, T. Witte, W. Fuss, M. Motzkus, D. Proch, K. L. Kompa, and C. B. Moore, "Getting ahead of IVR: A demonstration of mid-infrared induced molecular dissociation on a sub-statistical time scale," *J. Chem. Phys.* **119**(2), 641-645 (2003).
63. T. Brixner, N. H. Damrauer, P. Niklaus, and G. Gerber, "Photosensitive adaptive femtosecond quantum control in the liquid phase," *Nature (London, U. K.)* **414**(6859), 57-60 (2001).
64. J. P. Ogilvie, D. Debarre, X. Solinas, J. L. Martin, E. Beaurepaire, and M. Joffre, "Use of coherent control for selective two-photon fluorescence microscopy in live organisms," *Opt. Express* **14**(2), 759-766 (2006).
65. K. A. Walowicz, I. Pastirk, V. V. Lozovoy, and M. Dantus, "Multiphoton intrapulse interference. 1. Control of multiphoton processes in condensed phases," *J. Phys. Chem. A* **106**(41), 9369-9373 (2002).
66. J. M. Dela Cruz, I. Pastirk, V. V. Lozovoy, K. A. Walowicz, and M. Dantus, "Multiphoton intrapulse interference 3: Probing microscopic chemical environments," *J. Phys. Chem. A* **108**(1), 53-58 (2004).

67. I. Pastirk, J. M. Dela Cruz, K. A. Walowicz, V. V. Lozovoy, and M. Dantus, "Selective two-photon microscopy with shaped femtosecond pulses," *Opt. Express* **11**(14), 1695-1701 (2003).
68. T. Okada, I. Otake, R. Mizoguchi, K. Onda, S. S. Kano, and A. Wada, "Optical control of two-photon excitation efficiency of alpha-perylene crystal by pulse shaping," *J. Chem. Phys.* **121**(13), 6386-6391 (2004).
69. I. Otake, S. S. Kano, and A. Wada, "Pulse shaping effect on two-photon excitation efficiency of alpha-perylene crystals and perylene in chloroform solution," *J. Chem. Phys.* **124**(1), 014501 (2006).
70. C. Ventalon, J. M. Fraser, M. H. Vos, A. Alexandrou, J. L. Martin, and M. Joffre, "Coherent vibrational climbing in carboxyhemoglobin," *Proc. Natl. Acad. Sci. U. S. A.* **101**(36), 13216-13220 (2004).
71. H. S. Tan, E. Schreiber, and W. S. Warren, "High-resolution indirect pulse shaping by parametric transfer," *Opt. Lett.* **27**(6), 439-441 (2002).
72. T. C. Weinacht, J. L. White, and P. H. Bucksbaum, "Toward strong field mode-selective chemistry," *J. Phys. Chem. A* **103**(49), 10166-10168 (1999).
73. B. J. Pearson, J. L. White, T. C. Weinacht, and P. H. Bucksbaum, "Coherent control using adaptive learning algorithms," *Phys. Rev. A* **6306**(6), 063412 (2001).
74. J. Konradi, A. K. Singh, and A. Materny, "Mode-focusing in molecules by feedback-controlled shaping of femtosecond laser pulses," *Phys. Chem. Chem. Phys.* **7**(20), 3574-3579 (2005).
75. J. Konradi, A. K. Singh, A. V. Scaria, and A. Materny, "Selective spectral filtering of molecular modes of beta-carotene in solution using optimal control in four-wave-mixing spectroscopy," *J. Raman Spectrosc.* **37**(6), 697-704 (2006).
76. S. H. Shim, D. B. Strasfeld, E. C. Fulmer, and M. T. Zanni, "Femtosecond pulse shaping directly in the mid-IR using acousto-optic modulation," *Opt. Lett.* **31**(6), 838-840 (2006).
77. D. B. Strasfeld, S. H. Shim, and M. T. Zanni, "Controlling vibrational excitation with shaped mid-IR pulses," *Phys. Rev. Lett.* **99**(3), 038102 (2007).
78. B. P. Krueger, G. D. Scholes, R. Jimenez, and G. R. Fleming, "Electronic excitation transfer from carotenoid to bacteriochlorophyll in the purple bacterium *Rhodospseudomonas acidophila*," *J. Phys. Chem. B* **102**(12), 2284-2292 (1998).
79. A. N. Macpherson, J. B. Arellano, N. J. Fraser, R. J. Cogdell, and T. Gillbro, "Efficient energy transfer from the carotenoid S₂ state in a photosynthetic light-harvesting complex," *Biophys. J.* **80**(2), 923-930 (2001).

80. V. Sundstrom, T. Pullerits, and R. van Grondelle, "Photosynthetic light-harvesting: Reconciling dynamics and structure of purple bacterial LH2 reveals function of photosynthetic unit," *J. Phys. Chem. B* **103**(13), 2327-2346 (1999).
81. H. Kawano, Y. Nabekawa, A. Suda, Y. Oishi, H. Mizuno, A. Miyawaki, and K. Midorikawa, "Attenuation of photobleaching in two-photon excitation fluorescence from green fluorescent protein with shaped excitation pulses," *Biochem. Biophys. Res. Commun.* **311**(3), 592-596 (2003).
82. G. Vogt, G. Krampert, P. Niklaus, P. Nuernberger, and G. Gerber, "Optimal control of photoisomerization," *Phys. Rev. Lett.* **94**(6), 068305 (2005).
83. K. Hoki and P. Brumer, "Mechanisms in adaptive feedback control: Photoisomerization in a liquid," *Phys. Rev. Lett.* **95**(16), 168305 (2005).
84. B. Dietzek, B. Bruggemann, T. Pascher, and A. Yartsev, "Mechanisms of molecular response in the optimal control of photoisomerization," *Phys. Rev. Lett.* **97**(25), 258301 (2006).
85. V. I. Prokhorenko, A. M. Nagy, S. A. Waschuk, L. S. Brown, R. R. Birge, and R. J. D. Miller, "Coherent control of retinal isomerization in bacteriorhodopsin," *Science* (Washington, DC, U. S.) **313**(5791), 1257-1261 (2006).
86. G. Vogt, P. Nuernberger, T. Brixner, and G. Gerber, "Femtosecond pump-shaped-dump quantum control of retinal isomerization in bacteriorhodopsin," *Chem. Phys. Lett.* **433**(1-3), 211-215 (2006).
87. D. Cardoza, C. Trallero-Herrero, F. Langhojer, H. Rabitz, and T. Weinacht, "Transformations to diagonal bases in closed-loop quantum learning control experiments," *J. Chem. Phys.* **122**(12), 124306-124307 (2005).
88. M. A. Montgomery, R. R. Meglen, and N. H. Damrauer, "General method for the dimension reduction of adaptive control experiments," *J. Phys. Chem. A* **110**(20), 6391-6394 (2006).
89. M. A. Montgomery, R. R. Meglen, and N. H. Damrauer, "General method for reducing adaptive laser pulse-shaping experiments to a single control variable," *J. Phys. Chem. A* **111**(24), 5126-5129 (2007).
90. J. L. White, B. J. Pearson, and P. H. Bucksbaum, "Extracting quantum dynamics from genetic learning algorithms through principal control analysis," *J. Phys. B: At., Mol. Opt. Phys.* **37**(24), L399-L405 (2004).
91. F. Langhojer, D. Cardoza, M. Baertschy, and T. Weinacht, "Gaining mechanistic insight from closed loop learning control: The importance of basis in searching the phase space," *J. Chem. Phys.* **122**(1), 014102 (2005).

92. T. H. Maiman, "Stimulated optical radiation in Ruby," *Nature* (London, U. K.) **187**(4736), 493-494 (1960).
93. H. Abramczyk, *Introduction to laser spectroscopy*, 1st ed. (Elsevier, Amsterdam ; Boston, 2005), pp. xiii, 317.
94. J.-C. Diels and W. Rudolph, *Ultrashort laser pulse phenomena : fundamentals, techniques, and applications on a femtosecond time scale*, 2nd ed. (Academic Press, Burlington, MA, 2006), pp. xxi, 652.
95. R. W. Boyd, *Nonlinear optics* (Academic Press, Boston, 1992), pp. xiii, 439.
96. P. F. Moulton, "Spectroscopic and laser Characteristics of Ti-Al₂O₃," *J. Opt. Soc. Am. B* **3**(1), 125-133 (1986).
97. I. D. Jung, F. X. Kartner, N. Matuschek, D. H. Sutter, F. MorierGenoud, G. Zhang, U. Keller, V. Scheuer, M. Tilsch, and T. Tschudi, "Self-starting 6.5-fs pulses from a Ti:Sapphire laser," *Opt. Lett.* **22**(13), 1009-1011 (1997).
98. J. D. Kafka, M. L. Watts, and J. W. J. Pieterse, "Picosecond and femtosecond pulse generation in a regeneratively mode-locked Ti:Sapphire laser," *IEEE J. Quantum Electron.* **28**(10), 2151-2162 (1992).
99. D. Strickland and G. Mourou, "Compression of amplified chirped optical pulses," *Opt. Commun.* **55**(6), 447-449 (1985).
100. R. Trebino, *Frequency resolved optical gating : the measurement of ultrashort laser pulses* (Kluwer Academic, Boston, 2000), pp. xvii, 425.
101. C. Iaconis and I. A. Walmsley, "Spectral phase interferometry for direct electric-field reconstruction of ultrashort optical pulses," *Opt. Lett.* **23**(10), 792-794 (1998).
102. C. W. Hillegas, J. X. Tull, D. Goswami, D. Strickland, and W. S. Warren, "Femtosecond laser-pulse shaping by use of microsecond radiofrequency pulses," *Opt. Lett.* **19**(10), 737-739 (1994).
103. E. Zeek, R. Bartels, M. M. Murnane, H. C. Kapteyn, S. Backus, and G. Vdovin, "Adaptive pulse compression for transform-limited 15-fs high-energy pulse generation," *Opt. Lett.* **25**(8), 587-589 (2000).
104. A. M. Weiner, J. P. Heritage, and J. A. Salehi, "Encoding and decoding of femtosecond pulses," *Opt. Lett.* **13**(4), 300-302 (1988).
105. A. M. Weiner, J. P. Heritage, and E. M. Kirschner, "High-resolution femtosecond pulse shaping," *J. Opt. Soc. Am. B* **5**(8), 1563-1572 (1988).

106. O. E. Martinez, "3000 Times grating compressor with positive group-velocity dispersion: Application to fiber compensation in 1.3-1.6 μm Region," *IEEE J. Quantum Electron.* **23**(1), 59-64 (1987).
107. S. D. Jacobs, K. A. Cerqua, K. L. Marshall, A. Schmid, M. J. Guardalben, and K. J. Skerrett, "Liquid-crystal laser optics: Design, fabrication, and performance," *J. Opt. Soc. Am. B* **5**(9), 1962-1979 (1988).
108. M. Schadt and W. Helfrich, "Voltage-dependent optical activity of a twisted nematic liquid crystal," *Appl. Phys. Lett.* **18**(4), 127-128 (1971).
109. A. M. Weiner, D. E. Leaird, J. S. Patel, and J. R. Wullert, "Programmable shaping of femtosecond optical pulses by use of 128-element liquid-crystal phase modulator," *IEEE J. Quantum Electron.* **28**(4), 908-920 (1992).
110. W. Demtröder, *Laser spectroscopy : basic concepts and instrumentation*, Springer series in chemical physics ; v. 5 (Springer-Verlag, Berlin ; New York, 1981), pp. xiii, 694.
111. M. Born and E. Wolf, *Principles of optics : electromagnetic theory of propagation, interference and diffraction of light*, 7th expanded ed. (Cambridge University Press, Cambridge ; New York, 1999), pp. xxxiii, 952.
112. A. M. Weiner, D. E. Leaird, J. S. Patel, and J. R. Wullert, "Programmable femtosecond pulse shaping by use of a multielement liquid-crystal phase modulator," *Opt. Lett.* **15**(6), 326-328 (1990).
113. M. M. Wefers and K. A. Nelson, "Analysis of programmable ultrashort waveform generation using liquid-crystal spatial light modulators," *J. Opt. Soc. Am. B* **12**(7), 1343-1362 (1995).
114. A. Efimov, C. Schaffer, and D. H. Reitze, "Programmable shaping of ultrabroad-bandwidth pulses from a Ti:Sapphire laser," *J. Opt. Soc. Am. B* **12**(10), 1968-1980 (1995).
115. H. Wang, Z. Zheng, D. E. Leaird, A. M. Weiner, T. A. Dorschner, J. J. Fijol, L. J. Friedman, H. Q. Nguyen, and L. A. Palmaccio, "20-fs pulse shaping with a 512-element phase-only liquid crystal modulator," *IEEE J. Sel. Top. Quantum Electron.* **7**(4), 718-727 (2001).
116. A. Prakelt, M. Wollenhaupt, A. Assion, C. Horn, C. Sarpe-Tudoran, M. Winter, and T. Baumert, "Compact, robust, and flexible setup for femtosecond pulse shaping," *Rev. Sci. Instrum.* **74**(11), 4950-4953 (2003).
117. A. Monmayrant and B. Chatel, "New phase and amplitude high resolution pulse shaper," *Rev. Sci. Instrum.* **75**(8), 2668-2671 (2004).

118. B. W. Xu, J. M. Gunn, J. M. Dela Cruz, V. V. Lozovoy, and M. Dantus, "Quantitative investigation of the multiphoton intrapulse interference phase scan method for simultaneous phase measurement and compensation of femtosecond laser pulses," *J. Opt. Soc. Am. B* **23**(4), 750-759 (2006).
119. A. V. Oppenheim, R. W. Schaffer, and J. R. Buck, *Discrete-time signal processing*, 2nd ed. (Prentice Hall, Upper Saddle River, N.J., 1999), pp. xxvi, 870.
120. D. J. Tannor and S. A. Rice, "Coherent pulse sequence control of product formation in chemical reactions," *Adv. Chem. Phys.* **70**, 441-523 (1988).
121. J. M. Geremia, W. S. Zhu, and H. Rabitz, "Incorporating physical implementation concerns into closed loop quantum control experiments," *J. Chem. Phys.* **113**(24), 10841-10848 (2000).
122. M. Mitchell and NetLibrary Inc., *An introduction to genetic algorithms*, Complex adaptive systems (MIT Press, Cambridge, MA., 1996), pp. viii, 205.
123. J. H. Holland, *Adaptation in natural and artificial systems : an introductory analysis with applications to biology, control, and artificial intelligence*, 1st MIT Press ed., Complex adaptive systems (MIT Press, Cambridge, Mass., 1992), pp. xiv, 211.
124. A. M. Srb, R. D. Owen, and R. S. Edgar, *General genetics*, 2d ed. (W., San Francisco., 1965), pp. x, 557.
125. J. D. Watson and F. H. C. Crick, "Molecular structure of nucleic acids: a structure for deoxyribose nucleic acid," *Nature (London, U. K.)* **171**(4356), 737-738 (1953).
126. T. Baumert, T. Brixner, V. Seyfried, M. Strehle, and G. Gerber, "Femtosecond pulse shaping by an evolutionary algorithm with feedback," *Appl. Phys. B: Lasers Opt.* **65**(6), 779-782 (1997).
127. D. Yelin, D. Meshulach, and Y. Silberberg, "Adaptive femtosecond pulse compression," *Opt. Lett.* **22**(23), 1793-1795 (1997).
128. D. Zeidler, S. Frey, K. L. Kompa, and M. Motzkus, "Evolutionary algorithms and their application to optimal control studies," *Phys. Rev. A* **64**(2), 023420 (2001).
129. W. Xiufeng, W. Xiufeng, and M. Elbuluk, "Neural network control of induction machines using genetic algorithm training," presented at the Industry Applications Conference, 1996. Thirty-First IAS Annual Meeting, IAS '96., Conference Record of the 1996 IEEE, 1996.
130. A. Jullien, L. Canova, O. Albert, D. Boschetto, L. Antonucci, Y. H. Cha, J. P. Rousseau, P. Chaudet, G. Cheriaux, J. Etchepare, S. Kourtev, N. Minkovski, and S. M. Saltiel, "Spectral broadening and pulse duration reduction during cross-polarized wave generation: influence of the quadratic spectral phase," *Appl. Phys. B: Lasers Opt.* **87**(4), 595-601 (2007).

131. A. F. Bartelt, M. Roth, M. Mehendale, and H. Rabitz, "Assuring robustness to noise in optimal quantum control experiments," *Phys. Rev. A* **71**(6), 063405 (2005).
132. W. Schade, J. Preusser, D. L. Osborn, Y. Y. Lee, J. deGouw, and S. R. Leone, "Spatially resolved femtosecond time correlation measurements on a GaAsP photodiode," *Opt. Commun.* **162**(4-6), 200-204 (1999).
133. V. I. Gavrilenko and M. A. Noginov, "Ab initio study of optical properties of Rhodamine 6G molecular dimers," *J. Chem. Phys.* **124**(4), 044301 (2006).
134. W. T. Silfvast, *Laser fundamentals* (Cambridge University Press, Cambridge, Eng. ; NY, 1996), pp. xxii, 521.
135. M. A. Albota, C. Xu, and W. W. Webb, "Two-photon fluorescence excitation cross sections of biomolecular probes from 690 to 960 nm," *Appl. Opt.* **37**(31), 7352-7356 (1998).
136. C. Eggeling, A. Volkmer, and C. A. M. Seidel, "Molecular photobleaching kinetics of Rhodamine 6G by one- and two-photon induced confocal fluorescence microscopy," *ChemPhysChem* **6**(5), 791-804 (2005).
137. A. Fischer, C. Cremer, and E. H. K. Stelzer, "Fluorescence of coumarins and xanthenes after two-photon absorption with a pulsed titanium-sapphire laser," *Appl. Opt.* **34**(12), 1989-2003 (1995).
138. S. Reindl and A. Penzkofer, "Triplet quantum yield determination by picosecond laser double-pulse fluorescence excitation," *Chem. Phys.* **213**(1-3), 429-438 (1996).
139. G. Angel, R. Gagel, and A. Laubereau, "Femtosecond relaxation dynamics in the electronic ground state of dye molecules studied by polarization-dependent amplification spectroscopy," *Chem. Phys. Lett.* **156**(2-3), 169-174 (1989).
140. P. C. Beaumont, D. G. Johnson, and B. J. Parsons, "Photophysical properties of laser dyes: Picosecond laser flash photolysis studies of Rhodamine 6G, Rhodamine B and Rhodamine 101," *J. Chem. Soc., Faraday Trans.* **89**(23), 4185-4191 (1993).
141. W. Falkenstein, A. Penzkofer, and W. Kaiser, "Amplified spontaneous emission in Rhodamine dyes: Generation of picosecond light pulses and determination of excited state absorption and relaxation," *Opt. Commun.* **27**(1), 151-156 (1978).
142. B. Kopainsky and W. Kaiser, "Investigation of intramolecular and intermolecular transfer processes by picosecond fluorescence gating," *Opt. Commun.* **26**(2), 219-224 (1978).
143. M. M. Malley and G. Mourou, "Picosecond time-resolved fluorescence spectrum of Rhodamine 6G," *Opt. Commun.* **10**(4), 323-326 (1974).
144. A. Penzkofer, W. Falkenstein, and W. Kaiser, "Vibronic relaxation in S₁ state of rhodamine dye solutions," *Chem. Phys. Lett.* **44**(1), 82-87 (1976).

145. C. V. Shank, E. P. Ippen, and O. Teschke, "Sub-picosecond relaxation of large organic molecules in solution," *Chem. Phys. Lett.* **45**(2), 291-294 (1977).
146. M. C. Gazeau, V. Wintgens, P. Valat, J. Kossanyi, D. Doizi, G. Salvetat, and J. Jaraudias, "New experimental method for determining the S₁-S_n absorption spectrum of highly fluorescent dyes " *Can. J. Phys.* **71**(1-2), 59-65 (1993).
147. P. R. Ojeda, I. A. K. Amashta, J. R. Ochoa, and I. L. Arbeloa, "Excitonic treatment and bonding of aggregates of Rhodamine 6G in ethanol," *J. Chem. Soc., Faraday Trans.* **84**, 1-8 (1988).
148. A. Baltuska, M. S. Pshenichnikov, and D. A. Wiersma, "Second-harmonic generation frequency-resolved optical gating in the single-cycle regime," *IEEE J. Quantum Electron.* **35**(4), 459-478 (1999).
149. B. Valeur, *Molecular fluorescence : principles and applications* (Wiley-VCH, Weinheim, 2002), pp. xiv, 387.
150. Z. H. Peng, J. S. Melinger, and V. Kleiman, "Light harvesting unsymmetrical conjugated dendrimers as photosynthetic mimics," *Photosynth. Res.* **87**(1), 115-131 (2006).
151. E. Atas, Z. H. Peng, and V. D. Kleiman, "Energy transfer in unsymmetrical phenylene ethynylene dendrimers," *J. Phys. Chem. B* **109**(28), 13553-13560 (2005).
152. Z. H. Peng, Y. C. Pan, B. B. Xu, and J. H. Zhang, "Synthesis and optical properties of novel unsymmetrical conjugated dendrimers," *J. Am. Chem. Soc.* **122**(28), 6619-6623 (2000).
153. D. Kuroda and V. D. Kleiman, "Quantum control of two-photon Fluorescence in solution," in *Springer Series in Chemical Physics* (Springer-Berlin, 2007), pp. 226-228.
154. U. Siegner, M. Haiml, J. Kunde, and U. Keller, "Adaptive pulse compression by two-photon absorption in semiconductors," *Opt. Lett.* **27**(5), 315-317 (2002).
155. D. J. Kane and R. Trebino, "Characterization of arbitrary femtosecond pulses using frequency resolved optical gating," *IEEE J. Quantum Electron.* **29**(2), 571-579 (1993).
156. B. L. Davis, J. S. Melinger, D. McMorrow, Z. H. Peng, and Y. C. Pan, "Aggregation effects on the optical properties of a light harvesting phenylacetylene dendrimer in non-polar solution," *J. Lumin.* **106**(3-4), 301-311 (2004).
157. S. F. Swallen, R. Kopelman, J. S. Moore, and C. Devadoss, "Dendrimer photoantenna supermolecules: energetic funnels, exciton hopping and correlated excimer formation," *J. Mol. Struct.* **486**, 585-597 (1999).
158. D. Meshulach, D. Yelin, and Y. Silberberg, "Adaptive ultrashort pulse compression and shaping," *Opt. Commun.* **138**(4-6), 345-348 (1997).

159. A. Assion, T. Baumert, M. Bergt, T. Brixner, B. Kiefer, V. Seyfried, M. Strehle, and G. Gerber, "Control of chemical reactions by feedback-optimized phase-shaped femtosecond laser pulses," *Science* (Washington, DC, U. S.) **282**(5390), 919-922 (1998).
160. C. Daniel, J. Full, L. Gonzalez, C. Lupulescu, J. Manz, A. Merli, S. Vajda, and L. Woste, "Deciphering the reaction dynamics underlying optimal control laser fields," *Science* (Washington, DC, U. S.) **299**(5606), 536-539 (2003).
161. S. Wold, M. Sjostrom, and L. Eriksson, "PLS-regression: a basic tool of chemometrics," *Chemom. Intell. Lab. Syst.* **58**(2), 109-130 (2001).
162. J. W. Wilson, P. Schlup, and R. A. Bartels, "Ultrafast phase and amplitude pulse shaping with a single, one-dimensional, high-resolution phase mask.," *Opt. Express* **15**(14), 8979-8987 (2007).
163. T. Ikeda and O. Tsutsumi, "Optical switching and image storage by means of azobenzene liquid-crystal films," *Science* (Washington, DC, U. S.) **268**(5219), 1873-1875 (1995).
164. S. Sporlein, H. Carstens, H. Satzger, C. Renner, R. Behrendt, L. Moroder, P. Tavan, W. Zinth, and J. Wachtveitl, "Ultrafast spectroscopy reveals subnanosecond peptide conformational dynamics and validates molecular dynamics simulation," *Proc. Natl. Acad. Sci. U. S. A.* **99**(12), 7998-8002 (2002).
165. I. K. Lednev, T. Q. Ye, R. E. Hester, and J. N. Moore, "Femtosecond time-resolved UV-visible absorption spectroscopy of trans-azobenzene in solution," *J. Phys. Chem.* **100**(32), 13338-13341 (1996).
166. T. Nagele, R. Hoche, W. Zinth, and J. Wachtveitl, "Femtosecond photoisomerization of cis-azobenzene," *Chem. Phys. Lett.* **272**(5-6), 489-495 (1997).
167. I. K. Lednev, T. Q. Ye, P. Matousek, M. Towrie, P. Foggi, F. V. R. Neuwahl, S. Umaphathy, R. E. Hester, and J. N. Moore, "Femtosecond time-resolved UV-visible absorption spectroscopy of trans-azobenzene: dependence on excitation wavelength," *Chem. Phys. Lett.* **290**(1-3), 68-74 (1998).
168. T. Fujino and T. Tahara, "Picosecond time-resolved Raman study of trans-azobenzene," *J. Phys. Chem. A* **104**(18), 4203-4210 (2000).
169. T. Fujino, S. Y. Arzhantsev, and T. Tahara, "Femtosecond time-resolved fluorescence study of photoisomerization of trans-azobenzene," *J. Phys. Chem. A* **105**(35), 8123-8129 (2001).
170. H. Satzger, S. Sporlein, C. Root, J. Wachtveitl, W. Zinth, and P. Gilch, "Fluorescence spectra of trans- and cis-azobenzene - mission from the Franck-Condon state," *Chem. Phys. Lett.* **372**(1-2), 216-223 (2003).
171. H. Satzger, C. Root, and M. Braun, "Excited-state dynamics of trans- and cis-azobenzene after UV excitation in the $\pi\pi^*$ band," *J. Phys. Chem. A* **108**(30), 6265-6271 (2004).

172. T. Pancur, F. Renth, F. Temps, B. Harbaum, A. Kruger, R. Herges, and C. Nather, "Femtosecond fluorescence up-conversion spectroscopy of a rotation-restricted azobenzene after excitation to the S_1 state," *Phys. Chem. Chem. Phys.* **7**(9), 1985-1989 (2005).
173. H. Rau, "Further evidence for rotation in the $\pi\pi^*$ and inversion in the $n\pi^*$ photoisomerization of azobenzenes," *J. Photochem. Photobiol., A* **26**(2-3), 221-225 (1984).
174. H. Rau and E. Luddecke, "On the rotation-inversion controversy on photo-isomerization of azobenzenes: experimental proof of inversion," *J. Am. Chem. Soc.* **104**(6), 1616-1620 (1982).
175. H. Bouas-Laurent, *Photochromism : molecules and systems* (Elsevier ; Distributors for the, Amsterdam ; New York, NY, 1990), pp. xxii, 1068.
176. E. W. G. Diau, "A new trans-to-cis photoisomerization mechanism of azobenzene on the $S_1(n\pi^*)$ surface," *J. Phys. Chem. A* **108**(6), 950-956 (2004).
177. P. Hamm, S. M. Ohline, and W. Zinth, "Vibrational cooling after ultrafast photoisomerization of azobenzene measured by femtosecond infrared spectroscopy," *J. Chem. Phys.* **106**(2), 519-529 (1997).
178. A. Cembran, F. Bernardi, M. Garavelli, L. Gagliardi, and G. Orlandi, "On the mechanism of the cis-trans isomerization in the lowest electronic states of azobenzene: S_0 , S_1 , and T_1 ," *J. Am. Chem. Soc.* **126**(10), 3234-3243 (2004).
179. C. Ciminelli, G. Granucci, and M. Persico, "The photoisomerization mechanism of azobenzene: A semiclassical simulation of nonadiabatic dynamics," *Chem. Eur. J.* **10**(9), 2327-2341 (2004).
180. C. R. Crecca and A. E. Roitberg, "Theoretical study of the isomerization mechanism of azobenzene and disubstituted azobenzene derivatives," *J. Phys. Chem. A* **110**(26), 8188-8203 (2006).
181. T. Ishikawa, T. Noro, and T. Shoda, "Theoretical study on the photoisomerization of azobenzene," *J. Chem. Phys.* **115**(16), 7503-7512 (2001).
182. C. W. Chang, Y. C. Lu, T. T. Wang, and E. W. G. Diau, "Photoisomerization dynamics of azobenzene in solution with S_1 excitation: A femtosecond fluorescence anisotropy study," *J. Am. Chem. Soc.* **126**(32), 10109-10118 (2004).
183. T. Saito and T. Kobayashi, "Conformational change in azobenzene in photoisomerization process studied with chirp-controlled sub-10-fs pulses," *J. Phys. Chem. A* **106**(41), 9436-9441 (2002).

184. T. Schultz, J. Quenneville, B. Levine, A. Toniolo, T. J. Martinez, S. Lochbrunner, M. Schmitt, J. P. Shaffer, M. Z. Zgierski, and A. Stolow, "Mechanism and dynamics of azobenzene photoisomerization," *J. Am. Chem. Soc.* **125**(27), 8098-8099 (2003).
185. L. De Boni, J. J. Rodrigues, D. S. dos Santos, C. H. T. P. Silva, D. T. Balogh, O. N. Oliveira, S. C. Zilio, L. Misoguti, and C. R. Mendonca, "Two-photon absorption in azoaromatic compounds," *Chem. Phys. Lett.* **361**(3-4), 209-213 (2002).

BIOGRAPHICAL SKETCH

Daniel Kuroda was born on May 24, 1977, in Buenos Aires city, Argentina, where he spent his childhood and youth until he moved to the United State to pursue a PhD degree in chemistry. After attending Don Zeno School for 5 years, he began his undergraduate studies in the spring of 1996 at Universidad de Buenos Aires, in Buenos Aires city, Argentina. With an intense physical chemistry background and a special interest in quantum mechanics and chemical kinetics, he came to the University of Florida, Department of Chemistry in the August of 2002 to begin doctoral studies under the supervision of Professor Valeria Kleiman in the area of coherent control of light matter interactions. His professional career as a Ph.D. will continue in Philadelphia where he plans to take a post doctoral position.